DEVELOPMENT OF AIR-TO-AIR HEAT PUMP SIMULATION PROGRAM WITH ADVANCED HEAT EXCHANGER CIRCUITRY ALGORITHM

by

IP SENG IU

Bachelor of Science/Electromechanical Engineering
The University of Macau
Taipa, Macau SAR
1999

Master of Science/Mechanical Engineering
Oklahoma State University
Stillwater, OK
2002

Submitted to the Faculty of the
Graduate College of the
Oklahoma State University
in partial fulfillment of
the requirements for
the Degree of
DOCTOR OF PHILOSOPHY
May 2007

DEVELOPMENT OF AIR-TO-AIR HEAT PUMP SIMULATION PROGRAM WITH ADVANCED HEAT EXCHANGER CIRCUITRY ALGORITHM

Dissertation Approved:

Daniel E. Fisher

Dissertation Advisor

Jeffrey D. Spitler

Afshin J. Ghajar

J. Robert Whiteley

A. Gordon Emslie

Dean of the Graduate College

ACKNOWLEDGMENTS

There are many people I would like to thank for their supports for this accomplishment. Without any one of them I am not sure if I am able to come to this point to write the acknowledgments. My family members are supportive all the way. My parents raised all of us during the tough time but I did not realize that when I was kid. I had a really good time in the childhood. Thank you all. This dissertation is dedicated to my late father, Son Iu. I always like to be around with him and hope that he can feel the joy with me in another world.

My wife, Kahori and her family are also very supportive. Mr. and Mrs. Matsunaga always treat me like their son. I still thought I could marry with Kahori when I was a student is a generous gift from them. Kahori is the real director of this dissertation. I would have just gone to another direction if without her support.

When I was still a student in the University of Macau, Dr. Tam always talked about all the funs he had at OSU. I was intrigued by him and decided to come here some day. I had a rough start at OSU but Dr. Ghajar was willing to help me through. I always think that I owe him this one.

My academic advisor, Dr. Fisher, has guided me through my Master and Doctoral studies. He has made me realize how important and useful FORTRAN is. The computer language that I used to despise. I guess right now I cannot live without it anymore. It is a

roller coaster ride with him in the last seven years. It is a great learning experience though. I have learned a lot from him. He also reminds me the joy of being in a big family.

Dr. Spitler is the first professor that I was referred to by Dr. Tam. I am glad he is in my committee. He is a very knowledgeable professor. I should have realized his academic greatness earlier. OSU is very fortunate to have him around.

I really appreciate my outside committee member, Dr. Whiteley for reading all of my writings. I had no clue what kind of professor he is when I asked him to join my committee. Thank you Dr. Fisher for the recommendation. Dr. Whiteley is an outside committee member like no others. I am glad I can have him in my committee.

Dr. Bansal and Dr. Rees are two former visiting professors at OSU. They provided great help at the beginning of this research. If without their help, I would not know what I would be writing for this research.

Ben Alexander is a very skillful technician. He helped me in several different projects and set up the pseudo psychometric room. He seemed enjoyed working at OSU but I believe he deserves something better than that. If I am looking for someone to help in the future, he will be the first on my list.

I also like to thank the people at York, now Johnson Controls, Inc. for their technical support. Charles Obosu started this project and helped me set up all the experiment in the lab. Nathan Weber always provided me valuable inputs to improve the simulation program. He has been fun to work with since we worked together at OSU. John Knight took over the project later and he has brought the simulation program to another level. I have learned a lot from him in the practical perspective. He has also

helped me find all the resources that I need to finish this work. Steven Jones helped me run all the experiment patiently. He was even willing to squeeze his work schedule to get the data for me. I really appreciate his help.

I guess I cannot say enough thank you to all of them but than you all!

TABLE OF CONTENTS

LIST OF TABLES

LIST OF FIGURES

NOMENCLATURE

Alphabet

$a_1, a_2, ...$	Empirical coefficients for compressor mass flow rate
A	Area, m^2 (ft^2)
$b_1, b_2, ...$	Empirical coefficients for compressor power
bo	Pierre boiling number
$c_1, c_2, ...$	Empirical coefficients for the short tube model
C_1, C_2	Intermediate variables for refrigerant pressure drop calculation
C	Correction factor
$\dot{C}$	Heat capacity rate, $W.K^{-1}$ ($Btu.hr^{-1}.R^{-1}$)
C_r	Ratio of heat capacity rate
c_p	Specific heat, $j.kg^{-1}.K^{-1}$ ($Btu.lbm^{-1}.R^{-1}$)
$d_1, d_2, ...$	Empirical coefficients for the short tube two-phase correction
D	Diameter, m (ft)
e	Measurement uncertainty
e'	Fractional uncertainty
$e_1, e_2, ...$	Empirical coefficients for short tube two-phase correction
f	Friction factor
$f_1, f_2, ...$	Empirical coefficients for friction factor
F	Weighting factor
$F_1, F_2, ...$	Intermediate parameter for evaporative heat transfer coefficient
Fr	Froude number
Ft	Froude rate
g	Gravitational acceleration, 9.8 $m.s^{-2}$ or 32 $ft.s^{-2}$
$g_1, g_2, ...$	Empirical coefficients for TXV capacity calculation
G	Mass flux, $kg.s^{-1}.m^{-2}$ ($lbm.hr^{-1}.m^{-2}$)

h	Heat transfer coefficient, $W.m^{-2}.K^{-1}$ ($Btu.hr^{-1}.ft^{-2}.R^{-1}$)
h'	Dimensionless heat transfer coefficient
$h_1, h_2, ...$	Empirical coefficients for accumulator model
H	Height, m (ft)
HB	Heat balance, %
i	Enthalpy, $j.kg^{-1}$ ($Btu.lbm^{-1}$)
j	j-factor
$j_1, j_2, ...$	Empirical coefficients for j-factor calculation
$j_{1,1}, j_{1,2}, ...$	Admittance matrix entries
J	Flow admittance or conductance, $m.s^{-1}$ ($ft.s^{-1}$)
$\boldsymbol{J}$	Admittance matrix
$k_1, k_2, ...$	Empirical coefficients for distributor model
k	Thermal conductivity, $W.m^{-1}.K^{-1}$ ($Btu.hr^{-1}.ft^{-1}.R^{-1}$)
K_{H_1}	Intermediate parameter for void fraction calculation
K_{H_2}	Intermediate parameter for void fraction calculation
K_i	Heat exchanger entrance loss coefficient
K_e	Heat exchanger exit loss coefficient
$K_{\Delta P}$	K-factor for pressure drop calculation
L	Length, m (ft)
L_h	Louver height, m (ft)
L_p	Louver pitch, m (ft)
$\dot{m}$	Mass flow rate, $kg.s^{-1}$ ($lbm.hr^{-1}$)
$m_1, m_2, ...$	Entries of mass flow rate vector, $kg.s^{-1}$ ($lbm.hr^{-1}$)
m	Intermediate parameter for fin efficiency calculation
M	Refrigerant mass, charge, inventory, kg (lbm)
$\boldsymbol{M}$	Mass flow rate vector
MIN	Minimum
$n_1, n_2, ...$	Empirical coefficients for heat transfer correlation
N	Number of ...
Nu	Nusselt number, $h D_h / k$
NTU	Number of transfer unit
$p_1, p_2, ...$	Pressure vector entries, kPa (psi)

P	Pressure, kPa (psi)
$\boldsymbol{P}$	Pressure vector
P_f	Heat exchanger fin density, fins.m^{-1} (fins.in^{-1})
P_r	Heat exchanger longitudinal row pitch, center to center spacing, m (ft)
P_t	Heat exchanger transverse tube pitch, center to center spacing, m (ft)
Pr	Prandtl number
$\dot{q}$	Heat flux, W.m^{-2} (Btu.hr^{-1}.ft^{-2})
$\dot{Q}$	Heat, energy, capacity, W (Btu.hr^{-1})
r	Radius, m (ft)
r_r	Radius ratio for fin efficiency calculation
R	Derived result in uncertainty analysis
Re	Reynolds number
S	Spacing, m (ft)
SSE	Sum of squared error
T	Temperature, °C (°F) or K (R) in uncertainty analysis
T'	Wet bulb temperature, °C (°F)
U	Overall heat transfer coefficient, W.m^{-2}.K^{-1} (Btu.hr^{-1}.ft^{-2}.R^{-1})
v'	Dimensionless velocity
$\dot{V}$	Volumetric flow rate, m^3.s^{-1} (CFM)
V	Volume, m^3 (ft^3)
W	Molecular weight, kg.kmol^{-1} (lbm.kmol^{-1})
$\dot{W}$	Power consumption, W
x	Refrigerant quality
x^+	Pseudo entrance length
X'	Dimensionless heat exchanger parameters
X_L	Geometry parameter for fin efficiency calculation, m (ft)
X_M	Geometry parameter for fin efficiency calculation, m (ft)
X_{tt}	Lockhart-Martinelli parameter
Y	Intermediate parameter for short tube model
Z	Depth, m (ft)

Greek Symbols

α	Void fraction
β	Intermediate parameter for void fraction model
δ	Thickness, m (ft)
Δ	Difference, change
ϵ	Effectiveness
γ	Intermediate parameter for coil effectiveness calculation
Γ	Distributor loading
ϕ	Intermediate parameter for fin efficiency calculation
ϕ_{TP}	Two-phase correction factor
ψ	Flow rate per ton, $kg.s^{-1}.kW^{-1}$ ($lbm.hr^{-1}.ton^{-1}$)
Ψ	Mole fraction
μ	Dynamic viscosity, $kg.m^{-1}.s^{-1}$ ($lbm.ft^{-1}.hr^{-1}$)
η	Efficiency
ν	Independent variable
ρ	Density, $kg.m^{-3}$ ($lbm.ft^{-3}$)
θ	Wavy fin angle, deg
σ	Area ratio for heat exchanger air side pressure drop calculation
τ	Coil velocity deviation from mean face velocity
ω	Oil mass fraction
$\xi_1, \xi_2, \xi_3, \ldots$	Intermediate parameters for U-bend pressure drop calculation

Subscripts

1^{st}	First portion of heat exchanger transition element
absolute	Absolute
accel	Acceleration
accum	Accumulator
act	Actual condition
air	Air

avg	Average
bare	Bare tube
cb	Convective boiling
chamfer	Orifice chamfer
ckt	Circuit
cmp	Compressor
cmprsn	Compression
coil	Coil, heat exchanger
collar	Fin collar
cor	Corrected
crit	Critical
cross	Cross-sectional
diff	Difference
dis	Compressor discharge
disln	Discharge line
eq	Equivalent
equation	Equation
est	Estimated
evp	Evaporator
fic	Fictitious
fin	Fin
filter	Filter drier
flow	Flow rate through filter drier
fric	Friction
front	Heat exchanger front
grav	Gravitation
h	Hydraulic
hole	Accumulator tube hole
in	Inlet, inside
isen	Isentropic
liq	Liquid refrigerant
liqln	Liquid line
local	Local

low	Lower
max	Maximum
mea	Measured
min	Minimum
mix	Mixture
nb	Nucleate boiling
net	Net
nom	Nominal
noz	Distributor nozzle
oil	Oil
orifice	Short tube orifice
out	Outlet, outside
overall	Overall
rated	Rating condition
r	Heat exchanger row
ratio	Ratio
rbr	Row-by-Row
ref	Refrigerant
reference	Reference
RTD	Resistance Temperature Detector
sat	Saturated
seg	Heat exchanger tube segment
sub	Subcooled
suc	Compressor suction
sucln	Suction line
surf	Surface
TC	Thermocouple
TP	Two-phase
tot	Total
TXV	Thermal expansion valve
tube	Tube (distributor, coil, or accumulator)
Ubend	U-bend
up	Upper

vap	Vapor refrigerant
w	Water

1. INTRODUCTION

1.1. Background

Vapor compression cycle based heat pump systems are commonly used for both heating and cooling purposes in the United States. These systems are typically charged with ozone-depleting refrigerants, such as R-22, that is being phased out in the near future. There is a critical need in the industry to design the next-generation heat pump systems using ozone-safe refrigerants. However, the ozone-safe refrigerants, such as R-410A, have substantially different characteristics than R-22. This presents a challenging problem for heat pump design engineers because of a lack of empirical data and product development experience with the new refrigerants. To reduce the cost of designing the next-generation heat pump systems, computer simulation increasingly drives design procedures in the heat pump industry.

Although computer simulation programs vary both in terms of complexity and computational intensity, the unique requirements of the design procedure are often not considered in selecting a simulation tool. Often these tools use simple heat exchanger models without due consideration of their impact on the design process. The simple models may not be adequate for the following aspects of the heat pump design.

Heat exchanger circuiting: For plate-fin-tube heat exchangers, circuiting refers to the connections of coil tubes. It is an important aspect in system design but is universally

ignored in simple models. A number of studies have demonstrated that circuit design has a significant impact to coil capacity and pressure drop (Ellison *et al.* 1981; Domanski and Didion 1983; Liang *et al.* 1998; Jiang *et al.* 2002, 2006; Wang *et al.* 1999a). Simple models rely on the experience of design engineers and some trial and error in the test room to optimize the heat exchanger circuit design.

Refrigerant mixtures: The use of refrigerant mixtures is increasingly popular in heat pump systems. However unlike pure refrigerants, refrigerant mixtures experience temperature glide in the saturation region. Simple models rely on average saturation temperature in the heat transfer calculation that cannot account for the temperature change in the saturation region.

Local air side heat transfer coefficient: For multi-row coils, Rich (1975) showed that the air side heat transfer coefficient varies from row to row. For a four-row heat exchanger, the first row heat transfer coefficient can be 30% higher than the last row at a given air flow rate. Simple models are based on global analysis that cannot account for the variation of air side heat transfer coefficient.

Detailed heat exchanger models divide the heat exchanger into small elements and calculate the elements one-by-one along the refrigerant flow direction. Computer simulation with detailed heat exchanger models may require considerably more computation time, but has the ability to:

- Analyze different circuiting schemes.
- Account for the temperature glide of refrigerant mixtures.
- Incorporate the local air side heat transfer coefficient in the heat transfer

calculations.

All of these features are closely related to each other and are governed by the element-by-element analysis. A circuiting algorithm that can analyze all kinds of circuitry can be used to determine the local boundary conditions for each heat exchanger element. The temperature glide in the saturation region for refrigerant mixtures can be easily accounted for if the local refrigerant boundary conditions for each element are determined by the circuiting algorithm. With the elemental analysis, the variation of air side heat transfer coefficients can be also easily accommodated in each element calculation. As a result, the local heat transfer for each element can be more accurately calculated.

However, due to coil circuitry can be very complicated in real life and simple circuiting algorithms have limitations and cannot be used to analyze complex circuitries, an ideal circuiting algorithm that can analyze all kinds of circuiting is required in the elemental heat exchanger analysis. It is necessary to relax the constraints in the simple circuitry models and develop a simulation strategy that is "generic" in nature and can simulate any kind of heat exchanger circuitry.

Local air side heat transfer correlations are rare in the literature but they are required for the detailed heat exchanger models for more accurate analysis. The local heat transfer coefficients together with the circuiting algorithm can determine the local boundary conditions for each heat exchanger element. As a result, the temperature glide in refrigerant mixtures can be accounted for.

1.2. Objectives

The main objective of this research is to develop a deterministic heat pump

simulation program. It is capable of:

1. Simulating pure refrigerants and refrigerant mixtures. The program allows users to select a variety of refrigerants to perform heat pump simulations.
2. Simulating complicated heat exchanger circuiting, including split and joined circuits. The program provides heat pump design engineers the flexibility to design their own heat exchanger circuits.

Each heat pump component is developed as a stand alone program. The models are also integrated into a single program to simulate overall system operations. The aim is then to eventually incorporate a refrigerant property library and a flexible heat exchanger circuit model in the simulation environment for the assessment of overall system performance.

A local air side heat transfer correlation is experimentally developed and used in the heat pump program. The heat pump program is experimentally validated under various boundary conditions and system configurations. To access the individual performance of the component models and the integrated system performance, validation tests are conducted at two levels:

- **Component level:** Component models are simulated one-by-one using experimental data for the model inputs.
- **System level:** All component models are linked together to simulate the heat pump operation. The inputs of each component model are the simulated outputs from other components.

The new heat pump program developed under the proposed research is intended to be a design and simulation tool for the industry. Heat pump design engineers can specify the

boundary conditions and let the program calculate the component size. If all components are defined, it can allow users to simulate the system under both design and off-design conditions.

1.3. Unique Contributions

A heat exchanger model with a unique circuiting algorithm is developed in this project. The circuiting algorithm is used to determine the refrigerant distribution in the heat exchanger. The circuiting algorithm is able to solve the heat exchanger circuit network and calculate the local refrigerant flow rate in each circuit branch according to the circuit pressure drop. It is capable of modeling split, joined, and other complicated circuits.

The elemental method, which divides the heat exchanger coil into tube segments, is used to calculate the refrigerant pressure drop and heat transfer of the heat exchanger. The saturation refrigerant temperature in each segment is calculated locally according to the refrigerant condition. Therefore, the temperature glide experienced by refrigerant mixtures in the saturation region can be automatically accounted for in the elemental heat exchanger models.

Previously developed row-by-row heat transfer correlations are for flat fins, e.g. Rich (1975), Ganguli and Breber (1988), and Yang (1999, 2002). A new set of row-by-row heat transfer correlations for louvered fins is experimentally developed in this research. Currently, the overall heat transfer coefficient for the entire heat exchanger is used as the local coefficient (Ellison *et al.* 1981; Liang *et al.* 1998; Jiang *et al.* 2002, 2006), however, it has been shown that the air side heat transfer coefficient varies from

row to row (Rich 1975). Row effect to louvered fins is investigated in this research. The row-by-row heat transfer analysis results for louvered fins support the elemental heat exchanger model and minimize the modeling uncertainties.

1.4. Overview

Chapter 2 is a survey of the literature to identify what has been done, and what needs to be done for this research. Mathematical models for the heat pump components and heat transfer correlations, etc. are selected in this chapter.

Chapter 3 presents the mathematical models that are selected for this investigation from the published literature. It also presents the new heat exchanger circuiting algorithm developed from this research.

Chapter 4 evaluates the performance of the implemented models for a range of boundary conditions. This is imperative because some of the models are developed on an empirical or semi-empirical basis, the evaluation is able to verify the models and identify possible problems before comparing the modeling results to experimental data.

Chapter 5 presents the development of the row-by-row heat transfer coefficients for louvered fins. The experimental method, data reduction and validation procedures, and an analysis of the row-by-row heat transfer coefficients for louvered fins are presented in this chapter. A new row-by-row air side heat transfer correlation is presented based on the data from louvered fin coils. In addition, a conversion method to convert the overall heat transfer correlation to the row-by-row form is presented.

Chapter 6 discusses the experimental validation of the models. The experimental method used to collect the validation data is presented. Both component and system level

validation results are presented. Validation data are collected from the experiments conducted at Oklahoma State University and the York laboratory in Norman, Oklahoma. Overall 100 data points are used for the validation.

Chapter 7 summarizes the objectives and findings of the research. A list of future work that extends the scope of this research is proposed. The recommended topics intend to eliminate the input requirements and assumptions of the simulation program in this research.

The reference, bibliography, and appendix are shown in chapter 8, 9, and 10, respectively. All of the cited publications in this report are shown in the reference chapter. Additional publications related to this research are presented in the bibliography chapter. The appendix shows complementary data and other information that has been omitted from the main body of this report.

2. REVIEW OF LITERATURE

The development of a heat pump simulation program involves a variety of models that range from the refrigerant side heat transfer coefficient to compressor operations. The large body of literature that exists for each of these models is listed in the bibliography section. This review only covers elements that are directly related to the research objectives. The heat pump component models, the solution algorithm to integrate these models, refrigerant property calculations, circuiting algorithms, and local air side heat transfer correlations are discussed in this Chapter.

2.1. Component Models

There are four major components in a typical heat pump system: compressor, condenser, expansion device, and evaporator. The compressor is a pumping device which transports the refrigerant from the low pressure side to the high pressure side of the system. The condenser transfers heat from the refrigerant to the environment while the evaporator transfers heat from the environment to the refrigerant. The expansion device is a metering device that regulates the refrigerant flow rate in the system.

2.1.1. Compressors

Most commonly used compressors in heat pump systems are either reciprocating or scroll types. The most widely used reciprocating compressor model is the volumetric

efficiency model as documented by McQuiston *et al.* (2000). This model shows the relationship among the important compressor variables, e.g. clearance factor, polytropic exponent, piston displacement, mass flow rate, and power consumption, etc. It is used as the basis for a number of detailed compressor models (Fischer *et al.* 1998; Domanski and Didion 1983). These models use the 1st principle approach that accounts for the energy balances inside and outside of reciprocating compressors. However, these models require many input parameters that are only known to compressor manufacturers (such as the clearance factor). In addition, experimental data are often required to determine the volumetric efficiency. The volumetric efficiency model is also used as the basis for parameter-estimation compressor models (Popovic and Shapiro 1995; Kim and Bullard 2001) that require experimental data to estimate the compressor parameters. The requirement of detailed compressor inputs and experimental data are the downsides of the detailed compressor models. It is not convenient for heat pump design and is not adopted in this research.

Detailed modeling of the scroll compressor is rather complex. When two scrolls mate together, it forms several crescent shaped pockets. Gas refrigerant is compressed simultaneously in several pockets as the scroll moves. Schein and Radermacher (2001) presented a simulation model to study the internal leakage between scrolls. The mass and energy balances are modeled in each compression pocket. The model was not experimentally validated but intended to be an analytical tool to predict scroll compressor performance. This model requires input of scroll geometry that is only known to manufacturer. It is suitable for compressor analysis but is too complex to be used in a heat pump design programs.

The scroll compressor model by Chen *et al.* (2002a) defines the scroll movement into suction, compression and discharge chambers. It models the entire compression process according to the mass and energy balances in each chamber. This compressor model is used with an overall energy balance model (Chen *et al.* 2002b) around the compressor to determine the compressor mass flow rate, power consumption, and discharge temperature. Lee (2002) used the same approach to develop a similar scroll compressor model based on the heat balance. This model was validated with experimental data and had satisfactory results. However, both the Chen *et al.* and Lee's models require detailed input parameters such as the scroll geometry which are only known to the manufacturer. These models are too complex to be used in heat pump design simulations and are more suitable for compressor design purposes.

Winandy *et al.* (2002a) presented a simple scroll compressor model that divides the compressor operation into four control volumes: heating-up, isentropic compression, compression at a fixed volume and cooling down. Heat transfer equations are applied to each control volume. Experimental data were used to estimate the heat transfer coefficients in the heat transfer equations of the model. This model avoids the problem of requiring compressor geometry. Winandy *et al.* (2002b) applied the same model to an open-type reciprocating compressor and showed promising results. However, since this model is a parameter-estimation model, experimental data are required. It is therefore not suitable for heat pump design purposes.

The ARI model (1999) is a simple, yet satisfactory compressor model. It is an empirical model that generalizes the compressor performance in a 10-coefficient polynomial equation. This model can apply to any type of compressor, e.g. scroll,

reciprocating. The coefficients in the equation can be generated from the compressor performance data published by manufacturers. Some compressor manufacturers such as Bristol and Copeland also publish the polynomial coefficients to be used with the ARI model. The major disadvantage of the empirical model is that it lacks physical and thermodynamic details related to compressor operation. Application of the model outside the rated operation range can be problematic. However the coefficients are highly accessible and the compressor rating conditions cover a large range of saturation temperatures (ARI 1999) to make it suitable for heat pump design purposes. In addition, a correction method (Dabiri and Rice 1981; Mullen *et al.* 1998) that extends this model to off-design conditions is available as described in Section 3.1. The ARI model is adopted in this research.

2.1.2. Heat Exchangers

Common heat exchanger models differ in the level of discretization imposed on the heat transfer surface, as well as in the assumptions and procedures used in each calculation domain. When considering the level of discretization, heat exchanger models can be classified into three categories, namely zone-by-zone, tube-by-tube and segment-by-segment models. Both the tube-by-tube and segment-by-segment models are sufficiently detailed to analyze heat exchanger circuit design, account for temperature glide of refrigerant mixtures, and accommodate the use of row-by-row air side heat transfer coefficients. Zone-by-zone models do not have these capabilities but are more computationally efficient. Figure 2.1 illustrates the three heat exchanger models, which are discussed in the following sections.

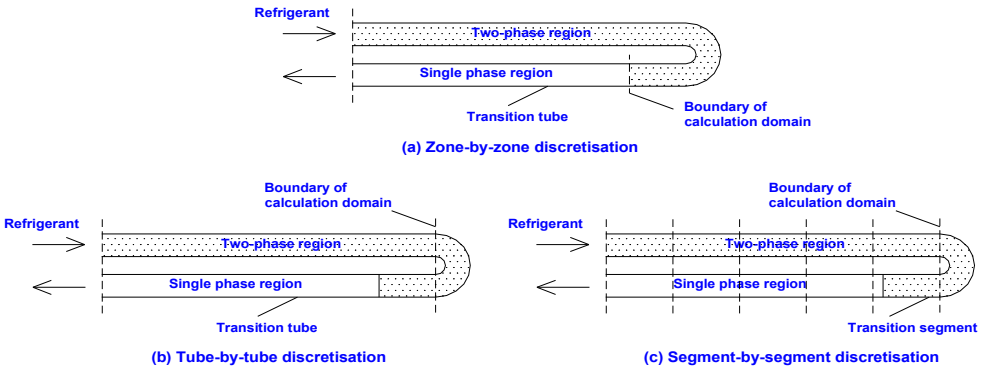

Figure 2.1 Discretization of heat exchanger tubes.

2.1.2.1. Zone-by-Zone Model

This model (Fischer *et al.* 1998; Mullen *et al.* 1998) divides the heat exchanger into "zones", which are defined according to the state of the refrigerant, i.e. superheated, two-phase and/or subcooled. Each zone is treated as an isolated heat exchanger where the inlet refrigerant condition is equal to the outlet refrigerant condition at the previous zone or the coil inlet. The air side boundary condition at the front row of the heat exchanger is applied to all succeeding rows regardless of the heat exchange between the air and refrigerant in the preceding rows, as a result, the heat exchanger capacity is always over predicted. This model assumes that the circuiting in all tube branches are the same and each circuit branch performs equivalently. This “equivalent circuit” assumption is illustrated in Figure 2.2. Figure 2.2a is an example that is close to the equivalent-circuit heat exchanger, because both circuits are identical in terms of the number of tubes and circuiting. If the refrigerant flow rates are identical in each circuit and airside conditions at the coil face are uniform, both circuits perform similarly. In practice, the circuit inlets are splits from the coil header, and the circuit outlets are joined to another junction at the coil outlet. This should result in the same pressure drop in each

circuit. For the circuit shown in Figure 2.2a, since both circuits are identical in length, the refrigerant mass flow rates are likely distributed equally to the circuits.

The equivalent circuit assumption becomes problematic for the circuiting shown in Figure 2.2b. Note that the circuits are not equivalent because there are more tubes in circuit 1 compared to circuit 2. If the refrigerant flow rates are identical in each circuit, circuit 1 is expected to have a higher heat transfer capacity and refrigerant pressure drop.

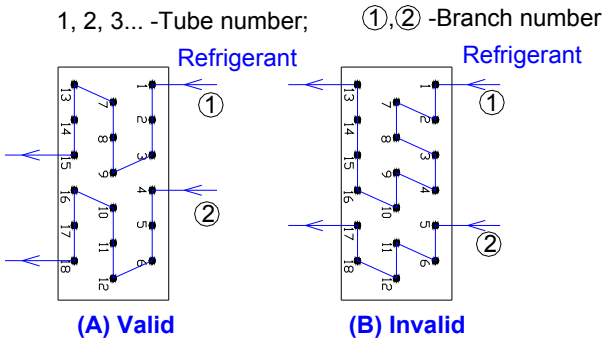

Figure 2.2 Zone-by-zone method: Equivalent circuit assumption.

On the other hand, if the pressure drop in each circuit is the same, circuit 1 will have lower refrigerant flow rate. The "equivalent circuit" assumption clearly proscribes the use of the zone-by-zone model for circuit design. System designs based on this coil model must depend on experimental measurements to optimize the coil performance. In addition, due to the lack of circuiting detail, the refrigerant conditions at the coil return bends are unknown, and the pressure drops in the return bends cannot be calculated precisely. The zone-by-zone model is not suitable for this research because of its weakness in handling coil circuiting.

2.1.2.2. Tube-by-Tube Model

This model (Domanski and Didion 1983; Liang *et al.* 1998) defines each single

coil tube as a calculation domain. The equivalent circuit assumption is not used in the tube-by-tube models. Each tube is treated as an isolated heat exchanger and calculated one-by-one. Constant refrigerant properties are assumed throughout each tube. The calculation is performed sequentially along the refrigerant flow direction until it reaches the coil outlet. The air side boundary condition for each tube is obtained from the calculation results of the upstream tubes. However, due to the tube arrangement in the heat exchanger circuit, the upstream tube on the air side may not be always the upstream tube on the refrigerant side. As a result, an iterative procedure is usually used in the tube-by-tube model to determine the air side boundary condition for each tube. This approach results in significantly longer computation time but is more accurate compared to the zone-by-zone models. In addition, the tube-by-tube calculation may experience calculation error in the "transition tube", where both single phase and two-phase refrigerants exist as shown in Figure 2.1b. In this tube, calculation error may be introduced due to the application of a single heat transfer correlation to the entire tube.

2.1.2.3. Segment-by-Segment Model

This model, also known as the elemental method, (Rossi and Braun 1995; Jiang *et al.* 2002, 2006; Ragazzi and Pedersen 1991; Vardhan and Dhar 1998) defines a small segment of a tube as the calculation domain. The calculation procedure is the same as the tube-by-tube method in that each segment is calculated one-by-one along the refrigerant flow direction. This model shares the advantages of the tube-by-tube model; moreover, the refined discretization can minimize the problems that may be encountered in transition tube of tube-by-tube models. Figure 2.1c shows that the transition region can be reduced in the segmented discretization. However, depending on the number of

segments defined in each tube, this method can be computationally expensive.

Despite the penalty in computation time, the segment-by-segment model is adopted in this research because it accommodates both the circuiting algorithm and local air side heat transfer coefficients in the heat exchanger calculations. In addition, due to the local refrigerant side boundary conditions are known in each segment, the local saturation temperature for each segment can be determined. As a result, the refrigerant temperature change in the saturation region can be accounted for in the segment-by-segment calculations. The segment-by-segment model can also be naturally extended to the tube-by-tube model by defining the entire tube as a segment. In small tonnage system, tube-by-tube discretization is adequate for the calculation and can save computation time.

2.1.3. Expansion Devices

Capillary tubes, short tube orifices, and thermal expansion valves (TXV) are all used in heat pump systems. Capillary tubes and short tube orifices are constant flow area expansion devices, while the TXV is a "variable open area orifice" that controls the superheat level at the evaporator outlet by adjusting the TXV opening. A larger valve opening allows more refrigerant flow, which in turn yields higher superheat at the evaporator outlet. Heat pumps that use TXV expansion devices are more energy efficient because the refrigerant flow rate of the system adjusts to the air side boundary conditions. Capillary tubes and short tube orifices do not have this capability but are relatively simple and cheap. Since short tube orifices and TXV are more commonly used in heat pump systems, the following sections only cover the models for these two expansion devices.

2.1.3.1. Short Tube Orifice

Mei (1982) introduced a semi-empirical model based on the standard orifice relation as shown below (ASHRAE 2005):

$$\dot{m}_{ref} = C_{orifice} A_{orifice} \sqrt{2 \cdot \rho \cdot \Delta P} \tag{2.1}$$

where ΔP is the pressure drop across the short tube orifice; and $C_{orifice}$ is the orifice coefficient as determined by experimental data. R-22 data were used to develop the model. Mei correlated the orifice coefficient to both the pressure drop and subcooling at the orifice inlet. This model has the restriction that it is only applicable to subcooled inlet conditions. For two-phase or low subcooled inlet conditions, it is not sufficiently accurate for heat pump simulation.

Aaron and Domanski (1990) developed another semi-empirical model based on the same standard orifice relation. This model also takes all orifice geometries into account for the mass flow rate calculation. In addition, Aaron and Domanski found that the orifice pressure drop should be correlated to the difference between the inlet pressure and the pressure before the refrigerant flushes across the orifice. The flush pressure was correlated with subcooling, saturation and outlet pressures, and orifice geometry using the R-22 data obtained in their experiment. However, this model is also only applicable to subcooled inlet conditions and is therefore not suitable for heat pump simulation.

Kim and O'Neal (1994) found that the Aaron and Domanski model underpredicted their experimental data for low subcooling conditions. They extended the range of experimental data to include the two-phase inlet conditions. Kim *et al.* (1994) introduced a two-phase correction factor for the Aaron and Domanski model to handle the two-phase inlet conditions. This short tube orifice model is semi-empirical in that it

relies on experimental data to determine the unknown coefficients in the model equations. Those coefficients are empirical and are refrigerant dependent. O'Neal and co-workers conducted experiments to determine the coefficients for the most common refrigerants and refrigerant mixtures: R-22 (Kim and O'Neal 1994), R-12 and R-134a (Kim *et al.* 1994), R-407C (Payne and O'Neal 1998), R-410A (Payne and O'Neal 1999). This model can be used for this research but is not adopted.

Choi *et al.* (2004) and Payne and O'Neal (2004) applied the Buckingham Pi theorem (Buckingham 1914) to develop a dimensionless correlation for the short tube orifice. They re-organized the parameters in the semi-empirical model (Kim and O'Neal 1994) into dimensionless groups that have physical meanings. These models are also semi-empirical and are dependent on experimental data to determine the empirical coefficients in the models. Choi *et al.* (2004) and Payne and O'Neal (2004) determined a set of universal empirical coefficients that can be used for most common refrigerants. This model is adopted for this research.

2.1.3.2. Thermal Expansion Valve

Modeling of the TXV is also based on the standard orifice relation (Fischer *et al*. 1998). The orifice coefficient is related to the TXV bleed factor and the rated superheat. Bleed factor is analogous to the orifice diameter in the orifice model. The variable open area characteristic of the TXV results in dynamic behavior. For steady-state heat pump operation, the TXV operates just like a short tube orifice and the orifice model can be used to model the TXV with "pseudo" orifice geometry parameters. Tandon (1999) showed an example that used experimental data and an orifice model to estimate the pseudo orifice parameters. The requirement of experimental data to simulate the TXV

steady state operation is inconvenient for heat pump design purpose, this modeling approach is not used in the research.

Sporlan (1998) presented a TXV sizing procedure for selecting the TXV size according to the pressure drop across the TXV. The pressure drop across the TXV can be determined by other components in a heat pump system. It is relatively convenient to use because it does not require experimental data. This method is used to determine the appropriate TXV size for the system. For TXV steady state simulation, the desired system superheat is specified by design engineers. The TXV controls the system superheat by varying the valve opening. The change of valve opening also affects the system subcooling. A bigger valve opening allows more refrigerant flow through the TXV and the system subcooling increases (Kim and O'Neal 1994). This method does not require too many TXV parameters and can be easily used in TXV system simulation. This method is adopted in this research.

2.2. System Simulation Algorithms

System performance changes according to the boundary conditions. For heat pump applications, since the fluid flow and heat transfer dynamics are much faster than the load dynamics, steady-state system simulation is appropriate for heat pump design and simulation (Rossi and Braun 1995). This section discusses the steady-state simulation algorithms presented in the literature.

The system simulation algorithm integrates the system component models and calculates system performance at specified boundary conditions. For air-to-air heat pumps, the boundary conditions are air side temperatures, flow rates, and the refrigerant

charge of the system. The simulation must satisfy the boundary conditions and establish momentum, energy and mass balances in the system. Constraints for each balance equation are shown below.

Momentum Balance: The refrigerant pressure rise across the compressor must be equal to the pressure drop across the rest of the system. The refrigerant mass flow rate is always the same in all components.

Energy Balance: The energy input to the system through the evaporator, low pressure refrigerant lines, and compressor must be equal to the energy rejected by the system through the condenser, compressor shell, and high pressure refrigerant lines.

Mass Balance: Assuming there is no refrigerant leakage, the refrigerant charge remains the same regardless of the change in air side boundary conditions.

2.2.1. Successive Substitution Method

The successive substitution method simulates the system components one-by-one along the refrigerant flow direction. Initial values of three parameters are required to start the system simulation. These parameters are adjusted during the simulation to establish the steady-state momentum, energy, and mass balances in the system. The successive substitution method in the ORNL heat pump model (Fischer *et al.* 1998) requires an initial value for condensing temperature, evaporating temperature, and system superheat as shown in Figure 2.3. The solution logic is divided into high pressure, low pressure and system mass calculations. These calculations are three nested iteration loops in the algorithm that correspond to the momentum, energy and mass balance equations.

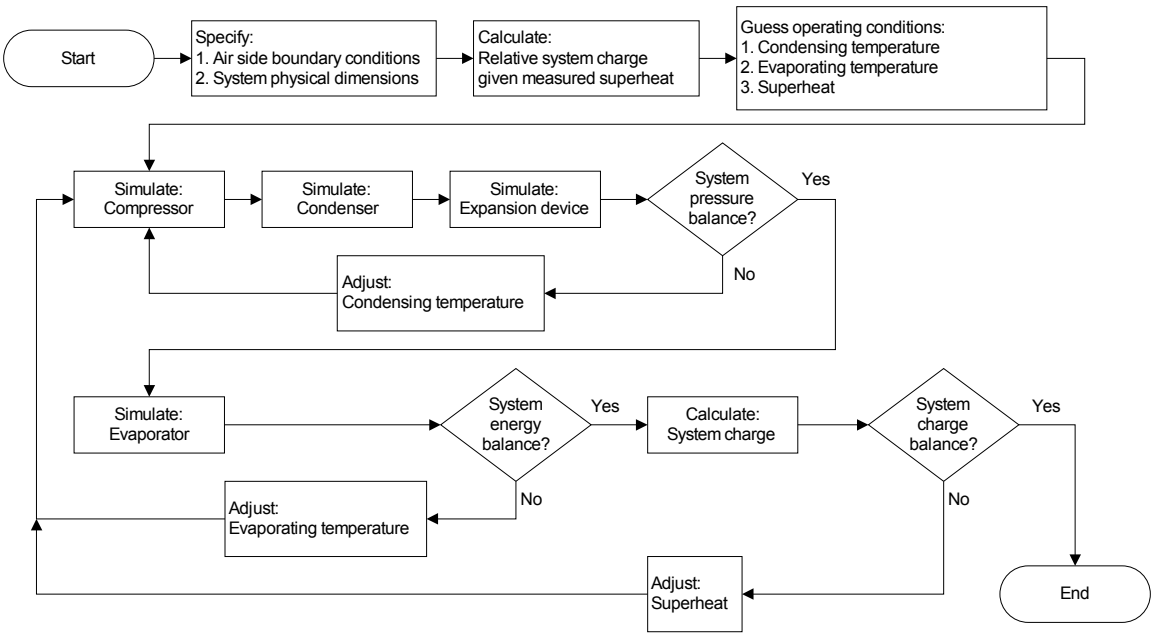

Figure 2.3 Successive substitution: System simulation algorithm.

High Pressure Calculation: The momentum balance is established in the high pressure calculation that includes the compressor, condenser and expansion device models. While keeping other estimated variables unchanged, the condensing temperature is adjusted in the high pressure iteration. The condensing temperature is proportional to the expansion device mass flow rate, but is inversely proportional to the compressor mass flow rate. Therefore, these two flow rates can be matched by adjusting the condensing temperature. The resulting refrigerant mass flow rate is used for the rest of the component calculations.

Low Pressure Calculation: The energy balance is established in the low pressure calculation which includes only the evaporator of the system. Only the evaporating temperature is adjusted to match the calculated and guessed superheats. A higher evaporating temperature results in a lower superheat, and vice versa. A match in superheat implies that the energy rejected from the system is equal to the energy supplied to the system, i.e. an energy balance is established. Note that once the evaporating temperature is changed, the mass flow rate calculation in the high pressure calculation is

affected and the momentum balance is violated. As a result, for each change of evaporating temperature, the simulation returns to the high pressure calculation to re-establish the momentum balance, then re-starts the low pressure calculation until both momentum and energy are balanced in the system.

System Charge Calculation: The mass balance is established in the charge calculation where the calculated system charge is compared to the specified charge. The superheat is adjusted to find the desired refrigerant inventory in the system. The higher superheat implies more refrigerant vapor and less refrigerant by weight in the system. Therefore, by adjusting the system superheat, the mass balance can be achieved. However, once the initial value of superheat is changed, the momentum and energy balances must both be re-established. The high and low pressure, and the system charge calculations are therefore three nested loops for the system simulation. The overall simulation finishes when the mass balance is established.

Domanski and Didion (1983) found that the refrigerant charge tends to be underpredicted due to the uncertainty in system internal volume in the charge calculation. To avoid the uncertainty, they introduced the relative charge simulation where the calculated charge is used as a boundary condition instead of the actual charge. The relative charge is calculated based on the actual system superheat. The relative charge calculation is similar to the system simulation as shown in Figure 2.3 but without the outer mass balance loop. Note that the relative charge must be calculated before starting the system simulation. Shen *et al.* (2006) introduced a two-point tuning method to account for the uncertainties in refrigerant charge calculation. The method calculates a relative charge based on the charges calculated at two different boundary conditions.

They showed that the two-point tuning method performs better then the single point tuning method that Domanski and Didion (1983) used.

In addition to system simulation, the successive substitution method can be used for system design calculations. The ORNL program has an option to perform design calculations where the desired system subcooling and superheat are specified boundary conditions. In this simulation, the refrigerant charge and the size of the expansion device are calculated. Figure 2.4 shows the design calculation logic.

Note that only condensing and evaporating temperatures are initial guesses to start the calculation. In addition, there are also other changes in the algorithm for design calculation:

1. In the high pressure calculation, since the system subcooling is specified instead of the expansion device, the momentum balance matches the calculated and desired subcooling instead of mass flow rate. The condensing temperature is still the only variable being adjusted to find the momentum balance.
2. In the low pressure calculation, since superheat is no longer a guessed variable, the energy balance matches the calculated and specified superheats. The interaction between the high and low pressure calculations remains unchanged, i.e. once the evaporating temperature is changed in the low pressure calculation, the high pressure calculation is re-visited with updated evaporating temperature. When both momentum and energy are balanced in the calculation, the size of the expansion device and the system charge are calculated according to the calculated refrigerant conditions.

The successive substitution method is also used in many other system simulation

programs such as HPSIM (Domanski and Didion 1983), ACMODEL (Rossi and Braun 1995), and Tandon (1999), etc. Their simulation logic is essentially the same as the ORNL heat pump program but with a few variations. For example, HPSIM uses compressor suction and discharge pressures as initial guesses instead of evaporating and condensing temperatures. The ACMODEL updates all guessed variables simultaneously after the algorithm executes all component models. The algorithm becomes a multi-dimensional search method.

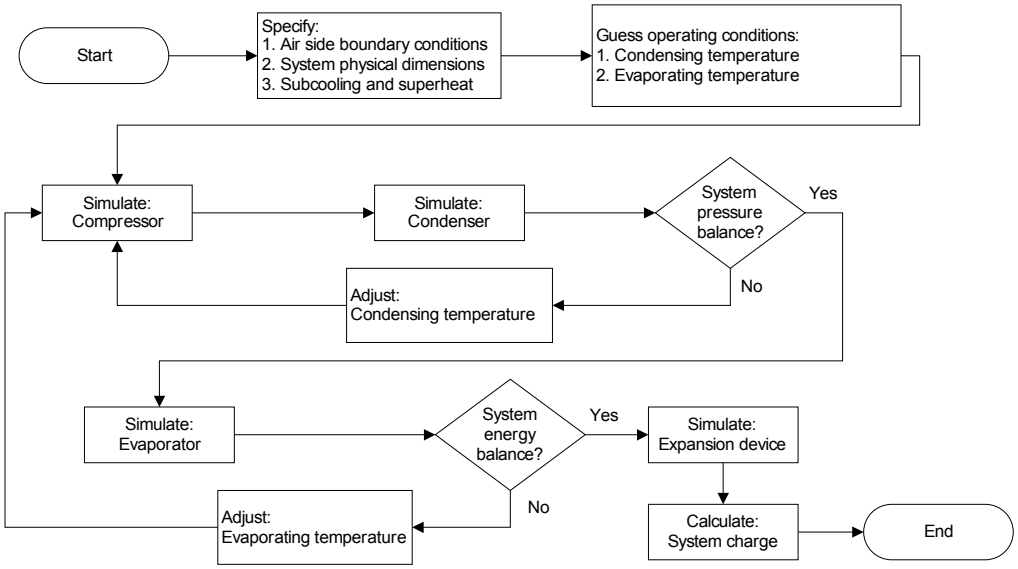

Figure 2.4 Successive substitution: System design calculation.

The ORNL method is adopted in this research because of its known robustness. In addition, the use of evaporating and condensing temperatures as initial guesses is advantageous. While refrigerant operating pressures can be dramatically different depending on the refrigerant in the system, the saturation temperatures are always similar and are bounded by the air side boundary condition. As a result, evaporating and condensing temperatures are easier to guess to start the simulation.

2.2.2. Newton Raphson Method

Besides the successive substitution method, the Newton-Raphson method is also used for system simulations. Mullen *et al.* (1998) developed the ACRC solver that uses the Newton-Raphson method to simulate room air conditioning units. Special care must be exercised with the Newton-Raphson method in the situation where the solution alternates between the single phase and two-phase regions in each iteration. The ACRC solver uses a different set of residual equations to handle the single and two-phase alternating problems. The solver checks the refrigerant condition after every iteration to decide which set of residual equations to use. If the refrigerant properties are out of range, the solver repeats the previous iteration with half step length. The implementation of these two features improves the robustness of Newton-Raphson method and makes it more applicable for system simulations.

The Newton-Raphson method has the flexibility in both system simulation and design calculation. Mullen *et al.* (1998) introduced a "swapping parameters and variables" feature in the ACRC solver to perform different calculations. Unlike the successive substitution method that only calculates certain outputs according to the program logic, the ACRC solver allows users to choose their own output parameters. Outputs such as required heat exchanger length that cannot be easily calculated in the successive substitution method can be easily produced by the Newton Raphson solver. The residual equations in the Newton-Raphson method are solved simultaneously, the parameters and variables in the residual equations can be freely swapped as long as the number of residual equations is equal to the number of unknown variables. The computation time is another advantage of the Newton-Raphson method. All residual

equations are solved simultaneously without the nested loop iteration required by the successive substitution method. As a result, the Newton-Raphson method is less computationally intensive.

The downside of the Newton-Raphson method is that more initial values are required to start the simulation (Mullen *et al.* 1998). For the basic vapor compression cycle with four major components: compressor, condenser, expansion device, and evaporator, there are at least nine initial conditions required. The initial guesses are refrigerant pressure and enthalpy at the each component inlet, as well as the refrigerant mass flow rate in the system. Depending on the refrigerant and air side boundary conditions, reasonable initial guesses are not always easy to specify. All the initial guesses must be reasonably close to the final values or the simulation may not converge. As a result the Newton-Raphson method is less robust than the successive substitution method for heat pump simulation, and is not adopted in this research.

2.3. Refrigerant Properties

The refrigerant property database, REFPROP (McLinden *et al.* 1998) is commonly used for refrigerant property calculations (Domanski 1999; Liaw *et al.* 2002; Jiang *et al.* 2002, 2006; Wang *et al.* 1999a). The REFPROP package comes with a graphic user interface, and FORTRAN routines that can be used for program development such as heat pump system simulations. REFPROP is able to calculate the thermodynamic and transport properties for common refrigerants and refrigerant mixtures. In addition, it also allows users to define their own refrigerant mixtures. A sample driver program that comes with the package demonstrates the property

calculations for pure refrigerant and refrigerant mixtures.

Since refrigerant property calculations are used everywhere in system simulations, the accumulated time for the property calculations can be prohibitively long if the property calculation is inefficient. Domanski (1999) found that the FORTRAN routines in REFPROP are too time consuming for his tube-by-tube heat exchanger program, EVSIM, because of too many property calls in the program and the calculation algorithms of the REFPROP routines. Every time the REFPROP routines are called, they generate the refrigerant saturation curve first before doing other calculations. Instead of using the REFPROP routines, EVSIM uses a table look-up method for the refrigerant property calculations. Refrigerant properties at discrete states are pre-calculated and stored in look-up tables. When the property calculation is called, the refrigerant property is retrieved from the tables. If the refrigerant property is between the pre-calculated discrete states, linear interpolation is used to approximate the refrigerant property. The table look-up method is more efficient than the calculation procedures in REFPROP because it does not need to generate the saturation curve. It is also used in the EnergyPlus program (Crawley *et al.* 1998) for system simulations.

Another advantage of the table look-up method is that it can be easily updated with other refrigerant property databases. As long as the format of the look-up tables is compatible with the table look-up routines, the method can be used with the most updated refrigerant properties including databases for new refrigerant mixtures. The table look-up method is used for this research to save the computation time from refrigerant property calculations.

2.4. Refrigerant Oil Mixture

The use of oil in heat pump systems is to lessen the surface to surface wear on the moving parts in the compressor. However, a certain amount of oil is always discharged from the compressor and circulated in the heat pump systems (Cremaschi 2004). The addition of oil in the refrigerant affects the refrigerant heat transfer and pressure drop in the condenser and evaporator.

Eckels *et al.* (1994a, 1994b, 1998a) developed heat transfer and pressure drop correction correlations to account for the oil. They found that the existence of oil in the heat pump systems decreases the refrigerant heat transfer and increases the pressure drop. Their correlations were derived from experimental data at limited test conditions and may not be generally applicable.

Shen and Groll (2005) conducted an extensive review of the effect of the refrigerant-oil mixture on heat transfer and pressure drop. Their findings agreed with the Eckels *et al.* results, i.e. the oil in the refrigerant decreases the heat transfer and increases the pressure drop. However, they concluded that the most reliable way to model the oil effect is to take the oil properties into account in the refrigerant property calculations. This modeling approach is used in this research.

2.5. Circuiting Algorithms

Circuiting, which is used to address refrigerant maldistribution in heat exchangers can be simulated with an appropriate algorithm in the elemental heat exchanger models, i.e. tube-by-tube and segment-by-segment models, to determine local air and refrigerant side boundary conditions for each heat exchanger element. Desirable circuiting

algorithms should be able to solve for refrigerant maldistribution in complicated coil circuitries, such as splitting and joining circuits. For the development of circuiting algorithm, there are two crucial parts that need to be considered:

1. The refrigerant flow path for each circuit and all split and joined locations must be kept track of.
2. The refrigerant flow rate at each circuit branch must be calculated and the refrigerant flow maldistribution in the coil must be determined.

Ellison *et al.* (1981) used 3-dimensional arrays to keep track of the tube connections. Table 2.1 shows the array values for the circuit shown in Figure 2.5. Each tube is assigned eight 3-dimensional arrays to keep track of the tube location, and the joined and split locations. Four of the arrays are used for the inlet connections, and the other four are used for the outlet connections. The first two array indices of all eight arrays are the same; they store the horizontal and vertical locations of the current tube. The last array index is either 1 or 2 to represent the 1st or 2nd connection. This limits the method to no more than 2 split or joined connections. The arrays store the horizontal or vertical location of the connecting tubes. For example, at the tube (1,1) outlet, it splits to tubes (2,1) and (1,2), the outlet arrays are:

OUTX(1,1,1) = 2; OUTY(1,1,1) = 1

OUTX(1,1,2) =1; OUTY(1,1,2) = 2

The values -1 and 99 in the table represent the tubes connecting to the coil inlet and outlet, respectively. If the array value is zero, it means there is no 2nd tube connection, such as tube (2,1).

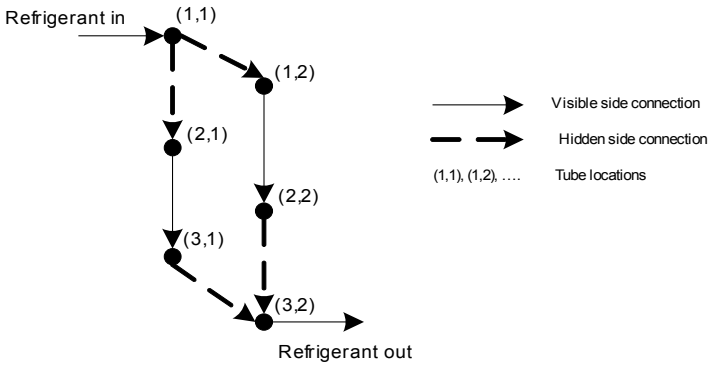

Figure 2.5 Sample circuit (Ellison *et al.* 1981)

Table 2.1 Connection arrays for the sample circuit of Ellison *et al.* (1981).

Tube Locations		Connection Arrays							
I	J	INX (I, J, 1)	INY (I, J, 1)	INX (I, J, 2)	INY (I, J, 2)	OUTX (I, J, 1)	OUTY (I, J, 1)	OUTX (I, J, 2)	OUTY (I, J, 2)
1	1	-1	-1	0	0	2	1	1	2
2	1	1	1	0	0	3	1	0	0
3	1	2	1	0	0	3	2	0	0
1	2	1	1	0	0	2	2	0	0
2	2	1	2	0	0	3	2	0	0
3	2	3	1	2	2	99	99	0	0

Refrigerant mass flow rate in each circuit branch is solved according to the circuiting connections. It is only possible to calculate the refrigerant mass flow rate for each circuit if the split and joined locations are known. For joined circuits, the mass flow rate is the sum of the incoming circuits. For split circuits, the mass flow rate is a fraction of the upstream flow rate that is determined by the pressure drop of the current circuit branch. However, due to the enormous number of circuiting possibilities, a generic circuiting algorithm that is able to solve the mass flow rate distribution for all possible circuits is not straight forward. Ellison *et al*. (1981) used an iterative method to solve the refrigerant maldistribution problem. It is a circuit-by-circuit calculation that starts from the coil inlet along the refrigerant flow direction. If the circuit outlet is joined with other

circuits, the calculation starts from the inlet of the joining circuit until all joining circuits are calculated. If the circuit inlet is a split, the mass flow rate is apportioned by the down stream pressure drop that is calculated from the previous iteration. The iteration continues until the calculated mass flow rates converge.

The circuiting algorithm by Ellison *et al*. is a fundamental approach to analyze heat exchanger circuits. However, they assumed that a tube cannot have more than two joined tubes at the inlet, and in turn cannot have more than two split tubes at the outlet. This assumption limits the flexibility of algorithm for analyzing multi-junction circuiting. Therefore, it is not used in this research.

Liang *et al.* (1998) used the two-dimensional adjacency matrix in graph theory (Chartrand 1985) to store the coil circuitry information. For the sample circuit shown in Figure 2.5, since there are six tubes, the adjacency matrix is a 6×6 matrix. Table 2.2 shows the corresponding adjacency matrix. The element in the adjacency matrix is either one or zero. The ones represent connections with adjacent tube, while zeros represent no split or joined connection. Note that the diagonal of the adjacency matrix represents the tube connecting to itself; it is therefore always zero.

Similar to Ellison *et al.*, Liang *et al.* assumed that there is no more than two-way split and joined circuits. The refrigerant mass flow rate in each circuit branch is solved using an iterative method. The calculation sequence is from circuit-to-circuit according to the adjacency matrix. In each circuit branch, the tube-by-tube or segment-by-segment method can be performed in the direction of refrigerant flow.

Although the Liang *et al.* model has the same limitation as the Ellison *et al.* model, the use of the adjacency matrix is an easier and more flexible way to store the

circuiting connections. The adjacency matrix method can be used as part of the circuiting model development but is not adopted in this research.

Table 2.2 Adjacency matrix for the sample circuit of Ellison *et al.* (1981).

	Tube (1, 1)	Tube (2, 1)	Tube (3, 1)	Tube (1, 2)	Tube (2, 2)	Tube (3, 2)
Tube (1, 1)	0	1	0	1	0	0
Tube (2, 1)	1	0	1	0	0	0
Tube (3, 1)	0	1	0	0	0	1
Tube (1, 2)	1	0	0	0	1	0
Tube (2, 2)	0	0	0	1	0	1
Tube (3, 2)	0	0	1	0	1	0

Domanski (1999) also used an iterative method in his heat exchanger program, EVSIM. Refrigerant flow rate in each circuit branch is apportioned according to its respective pressure drop in the previous iteration. The calculation is considered converged when the refrigerant pressures are the same at all outlet circuits. Compared to the Ellison *et al.* model, this program is able to analyze multi-junction circuiting. However, it assumes that there is either split or joined circuitry in the coil. A circuit that splits from an upstream circuit and joins to another downstream circuits cannot be analyzed. This assumption limits the flexibility of the circuiting analysis and therefore is not used in this research.

Liaw *et al.* (2002) used the same 3-D array method as Ellison *et al.* (1981) in their air-conditioning system model to compare the system performance for different circuitries. No split or joined circuiting was considered. The mass flow rate in each circuit branch is solved using the Newton-Raphson method. The residual equations are set up according to the refrigerant mass and momentum balances, i.e.:

$$\dot{m}_1 + \dot{m}_2 + \cdots + \dot{m}_n = \dot{m}_{tot} \tag{2.2}$$

$$\Delta P_1 = \Delta P_2 = \cdots = \Delta P_n \tag{2.3}$$

where n is the number of circuit branches. Note that equation (2.3) is only valid for non-splitting and non-joining circuitry. It is suitable for modeling coils with different circuit branch lengths such as the coil in Figure 2.2b but is not suitable for this research.

Jiang *et al.* (2002, 2006) adopted the analogy of electric circuit to heat exchanger circuit. The refrigerant pressure drops and mass flow rates are treated as electric voltages and currents, respectively. The equivalent electrical circuit for Figure 2.5 is shown in Figure 2.6. Note that each tube is represented as a resistor in the circuit. The junction numbers in the circuit are used to construct the junction-tube connectivity matrix which stores the circuiting information in the model. Table 2.3 shows the junction-tube connectivity matrix for this circuit. The numbers "1" and "-1" represent the junction before and after the tube, respectively, and "0" means the junction is not directly connected to the tube.

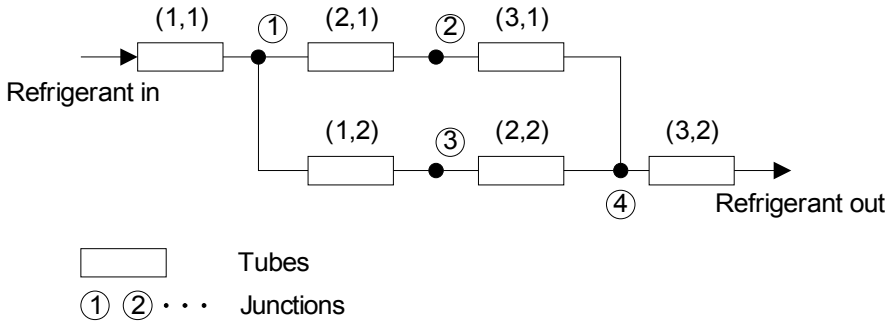

Figure 2.6 Equivalent electrical circuit for the sample heat exchanger circuit.

The Jiang *et al.* model is able to model split and joined circuiting because of the electrical circuit analogy approach. The Newton-Raphson method is used to solve for the mass flow rate in each circuit branch. This model relaxes the circuiting limitations of previous models but has the requirement that both inlet and outlet refrigerant pressures

are inputs to the mass flow rate calculations. The pressure inputs are not necessarily required for an ideal circuiting algorithm because the refrigerant pressure drop across the coil can be calculated with only the inlet pressure as an input. Therefore, this model is not adopted for this research. Since all available circuiting models have significant limitations, a new model has been developed as part of this research. The new model is presented in Section 3.4.6.

Table 2.3 Junction-tube connectivity matrix for the sample circuit.

	Tube					
Junction	(1,1)	(2,1)	(3,1)	(1,2)	(2,2)	(3,2)
1	-1	1	0	0	0	0
2	0	-1	1	1	0	0
3	0	0	0	-1	1	0
4	0	0	-1	0	-1	1

2.6. Local Air Side Heat Transfer Coefficients

In elemental heat exchanger models, a local air side heat transfer coefficient is required for each element calculation. For each element, the air side heat transfer coefficient should be calculated according to the local air temperature and air velocity. If uniform air temperature and velocity is assumed, the local heat transfer coefficient is the same for all elements at a given coil row. Figure 2.7 shows the typical heat exchanger geometry for heat pump systems. Plate fins and staggered tubes are used for this kind of heat exchangers. Air travels outside the tubes and is in the parallel direction with the fins, while refrigerant travels inside the tubes.

Rich (1975) showed that air side heat transfer coefficients vary from row-to-row for this kind of heat exchangers. He presented a row-by-row heat transfer correlation

based on a four-row coil experiment as shown in Figure 2.8. The correlation is presented in terms of the j-factor, which is a dimensionless number representing the air side heat transfer coefficient. At low Reynolds numbers, Rich suggested that there could be stable vortices behind the tubes that affect the air temperature distribution of the downstream rows. Therefore, row 1 has the highest heat transfer coefficient. But as the Reynolds number increases, the vortices start to break up, and the result in better air mixing in the downstream rows. The heat transfer coefficients in the downstream rows are higher.

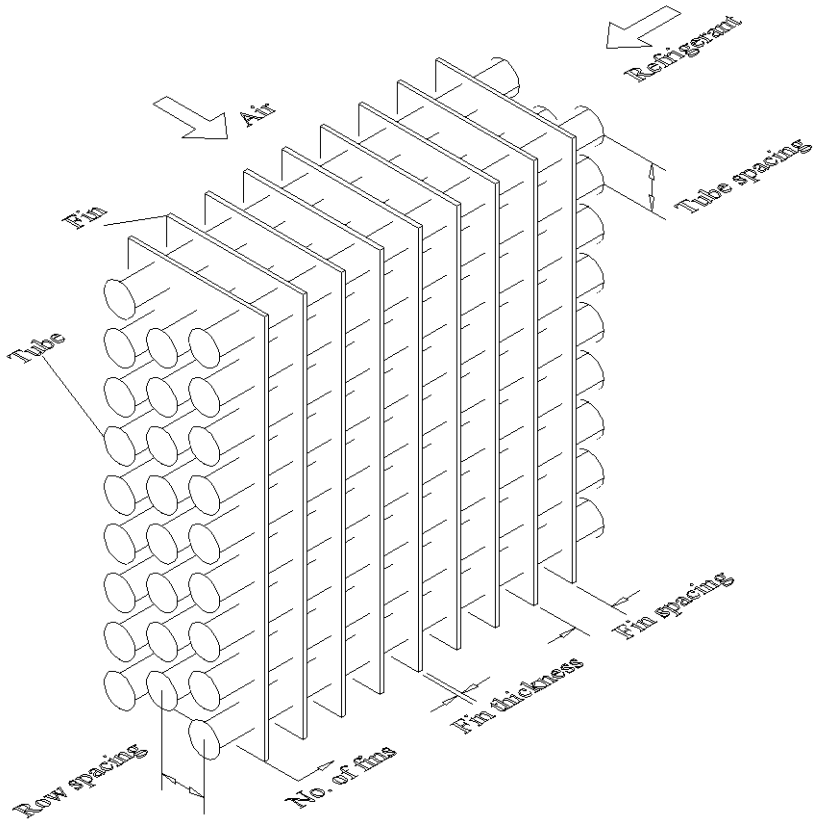

Figure 2.7 Heat exchanger geometry.

Bell (2006) postulated that Rich's low Reynolds number data are still in the laminar regime. He suggested using different characteristic length to present the data. Halici *et al.* (2001) studied the tube row effect on heat transfer coefficients. Their air velocity range was about half of Rich's range. Their experimental data also showed that

row 1 had the highest j-factor in their 1 to 4 row coil tests.

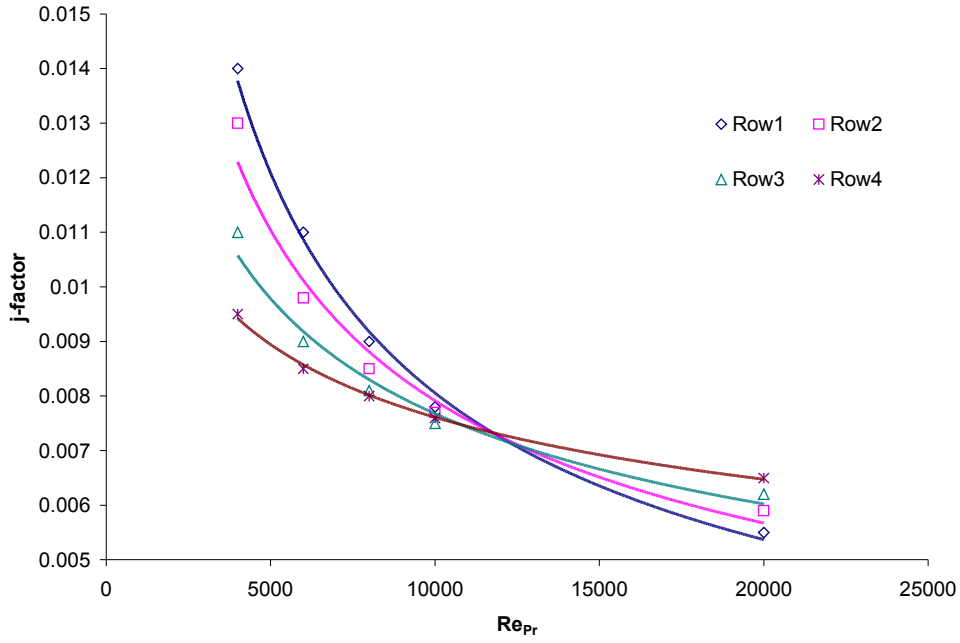

Figure 2.8 Row-by-row j-factor (Rich 1975).

However, their data were presented in terms of Reynolds number with the coil hydraulic diameter as the characteristic length and the Reynolds number ranges from 400 to 1800. Webb (1994) and Wang (2006) believed that the variation of j-factor in the low Reynolds number range is due to the entrance length effect, i.e. the air flow is not fully developed in the flow channels of the front rows and the heat transfer coefficients are higher. The entrance length effect is a characteristic of laminar flow. All of the above analyses confirm that the variation of j-factor for low Reynolds numbers is due to laminar flow.

Ganguli and Breber (1988) and Yang (1999, 2002) studied the row effect to heat transfer coefficient for high Reynolds number. They developed row correction correlations to account for the variation of heat transfer coefficients from row-to-row. The correlations project higher correction factors and higher heat transfer coefficients for

the deeper rows. Their findings agree with Rich's data for high Reynolds number.

All of the research results agree that the heat transfer coefficient varies row by row and is related to Reynolds number. Rich's correlation is suitable for elemental heat exchanger models because it can account for the row-by-row effect on the air side heat transfer coefficient. However, Rich's correlation was developed for smooth flat fins, which are rarely used nowadays. Enhanced fins, such as louvered and lanced fins, are currently favored by the industry. Rich's correlation is therefore not suitable for heat pump design.

Aside from Rich's correlation, row-by-row heat transfer correlations are rarely available in the literature. Air side heat transfer correlations are often presented for the overall coil (McQuiston *et al.* 2000; Gray and Webb 1986; Wang *et al.* 1999b). Domanski (1991) assumed that each row equally affected the overall correlation. He adjusted the overall correlation according to the number of rows to obtain row-by-row heat transfer coefficients. However, Rich (1975) showed that the row-by-row heat transfer coefficient varies according to the entering air velocity. Therefore, Domanski's assumption is not used for this research.

Pirompugd *et al.* (2005) proposed a tube-by-tube data reduction procedure to derive a representative heat transfer coefficient for all row numbers. The row effect on the heat transfer coefficient is accounted for in the data reduction result by using a representative value. However, j-factor correlations from this data reduction procedure are rare in the literature, and the true row effect is hidden in the data reduction result. Therefore, this method is not used in this research.

Overall heat transfer coefficients are often used in elemental heat exchanger

models (Ellison *et al.* 1981; Liang *et al.* 1998; Liaw *et al.* 2002). They assumed that the local heat transfer coefficient is equal to the overall coefficient and is applied to all coil elements. Since this is a relatively rough assumption and row-by-row correlations for louvered fins are not available in the literature, a limited set of experiments is performed to experimentally determine row-by-row correlations for louvered fins.

3. MATHEMATICAL MODELS

Since the system simulation model is intended to be a design tool for heat pump manufacturers, the model should only require user accessible input data and minimize the need for experimental data. In addition, it should be capable of modeling complex heat exchanger circuit designs. The simulation program includes the models of four major components (compressor, condenser, expansion device, and evaporator), and minor components (interconnecting pipes, accumulator and filter drier). Each component model is implemented as a stand-alone module that can be used to analyze the individual component performance, and can be integrated to simulate the overall system operation. The following sections describe the component models that are used for the system simulation.

3.1. Compressor

The compressor is modeled with the ARI 10-coefficient polynomial model (ARI 1999). This model calculates the refrigerant mass flow rate and the power consumption based on the compressor suction and discharge saturation temperatures as shown below:

Mass Flow Rate:

$$\dot{m}_{cmp,rated} = a_1 + a_2 T_{sat,suc} + a_3 T_{sat,dis} + a_4 T^2_{sat,suc} + a_5 T_{sat,suc} T_{sat,dis} + a_6 T^2_{sat,dis} + a_7 T^3_{sat,suc} + a_8 T_{sat,dis} T^2_{sat,suc} + a_9 T_{sat,suc} T^2_{sat,dis} + a_{10} T^3_{sat,dis} \quad (3.1)$$

Power Consumption:

$$\dot{W}_{cmp,rated} = b_1 + b_2 T_{sat,suc} + b_3 T_{sat,dis} + b_4 T^2_{sat,suc} + b_5 T_{sat,suc} T_{sat,dis} + b_6 T^2_{sat,dis} + b_7 T^3_{sat,suc} + b_8 T_{sat,dis} T^2_{sat,suc} + b_9 T_{sat,suc} T^2_{sat,dis} + b_{10} T^3_{sat,dis} \quad (3.2)$$

The coefficients, $a_1, a_2, ..., a_{10}$, and $b_1, b_2, ..., b_{10}$ are published by compressor manufacturers according to the ARI standard 540 (1999). They are derived from the compressor performance data under specific rating conditions. If the compressor is operating at other conditions, the use of the ARI model becomes questionable. Dabiri and Rice (1981), and Mullen *et al.* (1998) found that the mass flow rate and power consumption for off rating conditions can be corrected using the density and isentropic power ratios, respectively:

$$\dot{m}_{cmp,act} = \left(\frac{\rho_{ref}}{\rho_{ref,rated}} \right) \dot{m}_{cmp,rated} \quad (3.3)$$

$$\dot{W}_{cmp,act} = \left(\frac{\dot{m}_{cmp,act}}{\dot{m}_{cmp,rated}} \right) \left(\frac{\Delta i_{ref,isen}}{\Delta i_{ref,isen,rated}} \right) \dot{W}_{cmp,rated} \quad (3.4)$$

The major function of the compressor model is to calculate refrigerant mass flow rate, power consumption, and the refrigerant state at the compressor outlet. Since the outlet pressure (which can be approximated by the discharge saturation temperature) is an input to the ARI model, if the temperature or enthalpy at the compressor outlet is known, the outlet refrigerant state can be determined. According to the heat balance across the compressor, the outlet enthalpy is calculated by:

$$i_{ref,out} = \frac{\dot{W}_{cmp,act} - \dot{Q}_{net}}{\dot{m}_{cmp,act}} + i_{ref,in} \quad (3.5)$$

where $\dot{Q}_{net}$ is net energy loss across the compressor, which includes shell heat loss and

mechanical friction loss. The amount of net energy loss differs for each type of compressor (e.g. scroll, reciprocating), and the surrounding air and refrigerant conditions. It is usually less than 25% of the compressor power consumption (Weber 2005). The energy loss can be determined from Equation (3.5) if the refrigerant mass flow rate, compressor power consumption, suction and discharge refrigerant states are available from measurements.

3.2. Expansion Device

For the expansion devices, both the short tube orifice and the thermal expansion valve (TXV) are modeled because they are commonly used in heat pump systems. The function of the expansion device models is to calculate the amount of refrigerant allowed to travel through the expansion valve, i.e. refrigerant mass flow rate.

In the short tube orifice model, the refrigerant mass flow rate is calculated using the dimensionless equation given by Payne and O'Neal (2004). For subcooled inlet conditions, the mass flow rate is defined as:

$$\pi_1 = \frac{c_1 + c_2\pi_2 + c_3\pi_4 + c_4\pi_3 + c_5 \ln \pi_5}{1 + c_6\pi_2 + c_7(\pi_4)^2} \tag{3.6}$$

where the c_1, c_2, ... are empirical coefficients, and the dimensionless groups are:

$$\pi_1 = \frac{G}{\sqrt{\rho_{liq} P_{crit} \cdot 1000}} \tag{3.7}$$

$$\pi_2 = \frac{P_{in} - P_{sat}}{P_{crit}} \tag{3.8}$$

$$\pi_3 = \frac{\rho_{vap}}{\rho_{liq}} \tag{3.9}$$

$$\pi_4 = \frac{\Delta T_{sub}}{T_{crit} + 273.15} \tag{3.10}$$

$$\pi_5 = \frac{L_{orifice}}{D_{orifice}} \tag{3.11}$$

For two-phase inlet conditions, a two-phase correction factor is introduced to correct the model as shown below:

$$\pi_{1,TP} = C_{TP}\pi_{1,sat} \tag{3.12}$$

where $\pi_{1,sat}$ is the dimensionless mass flow rate at saturated condition. The two-phase correction factor is defined as:

$$C_{TP} = \frac{d_1\pi_6 + d_2\pi_6^{\,2} + d_3(\ln\pi_6)^2 + d_4(\ln\pi_{10})^2 + d_5(\ln\pi_8)^2 + d_6(\ln\pi_5)^2}{1 + d_7\pi_6 + d_8\pi_9 + d_9\pi_7^3} \tag{3.13}$$

where d_1, d_2, ... are empirical coefficients, and the dimensionless groups are:

$$\pi_6 = \frac{\rho_{avg,in}}{\rho_{liq}} \tag{3.14}$$

$$\pi_7 = \frac{P_{in}}{P_{crit}} \tag{3.15}$$

$$\pi_8 = \frac{P_{crit} - P_{in}}{P_{crit}} \tag{3.16}$$

$$\pi_9 = \frac{x_{in}}{1 - x_{in}}\left(\frac{\rho_{liq}}{\rho_{vap}}\right)^{1/2} \tag{3.17}$$

$$\pi_{10} = \frac{P_{crit} - P_{sat}}{P_{crit}} \tag{3.18}$$

The average density is defined as:

$$\rho_{avg,in} = \left[\frac{x_{in}}{\rho_{vap}} + \frac{(1-x_{in})}{\rho_{liq}} \right]^{-1} \tag{3.19}$$

The coefficients c_1, c_2, c_3, ... and d_1, d_2, d_3, ... are derived from experimental data for different refrigerants and a variety of boundary conditions. Table 3.1 shows the empirical coefficients presented by Payne and O'Neal (2004).

Table 3.1 Empirical coefficients for the short tube model Payne and O'Neal (2004).

c_1	3.8811E-01	d_1	1.1831E+00
c_2	1.1427E+01	d_2	-1.4680E+00
c_3	-1.4194E+01	d_3	-1.5285E-01
c_4	1.0703E+00	d_4	-1.4639E+01
c_5	-9.1928E-02	d_5	9.8401E+00
c_6	2.1425E+01	d_6	-1.9798E-02
c_7	-5.8195E+02	d_7	-1.5348E+00
		d_8	-2.0533E+00
		d_9	-1.7195E+01

Thermal expansion valve (TXV) controls the system superheat by adjusting the TXV opening. Once the superheat is maintained and the system is operating at steady state conditions, the TXV performs like a short tube orifice. If a TXV is used in the system simulation, it keeps the system superheat unchanged but varies the subcooling. The refrigerant mass flow rate from the TXV model is not necessary for steady state simulation. However, for design calculations, it is desirable to size the expansion device based on the system operating conditions. The TXV sizing calculation is described in the Sporlan literature (1998) as follows. For a specific evaporating temperature, the TXV capacity is calculated as:

$$\dot{Q}_{TXV,rated} = g_1 \cdot \dot{Q}_{nom} + g_2 \tag{3.20}$$

where $\dot{Q}_{nom}$ is the nominal capacity of the system, which is equal to the rated capacity

of the compressor. The TXV capacity is usually presented for some typical evaporating temperatures in the catalog. Interpolation or extrapolation is used when the operating condition is not listed in the catalog.

The TXV capacity is rated at a specific refrigerant liquid temperature and pressure drop. When selecting the appropriate TXV size, correction factors should be applied to account for deviations from the specified liquid temperature and pressure drop. The actual TXV size is calculated as:

$$\dot{Q}_{TXV,act} = C_{T_{liq}} \cdot C_{\Delta P} \cdot \dot{Q}_{TXV,rated} \tag{3.21}$$

where the correction factors for liquid temperature and pressure drop are:

$$C_{T_{liq}} = g_3 \cdot T_{liq} + g_4 \tag{3.22}$$

$$C_{\Delta P} = g_5 \cdot \Delta P^{g_6} \tag{3.23}$$

A pressure drop correction factor is also presented at discrete evaporating temperatures. Interpolation or extrapolation is used to approximate the correction factor for other temperatures.

The above four equations describe the TXV sizing algorithm. Note that all the boundary conditions in the equations are calculated at the end of the system design calculation. The coefficients $g_1, g_2, ..., g_6$ are curve-fit coefficients that are derived from the catalog data.

3.3. Distributor

Expansion devices such as the short tube orifice and TXV are usually used with a distributor for multi-circuit coils. A distributor consists of a nozzle and multiple

distributor tubes. The function of the nozzle is to uniformly distribute the refrigerant to all heat exchanger circuits through the distributor tubes (Sporlan 1999). The use of a distributor introduces an extra pressure drop between the expansion device and the heat exchanger. This pressure drop is calculated using the equation fit method presented in the ORNL heat pump model (Fischer *et al.* 1998).

The nozzle pressure drop is:

$$\Delta P_{noz} = k_1 \cdot \Gamma_{noz}^{k_2} \tag{3.24}$$

where Γ_{noz} is called the "nozzle loading" (Sporlan 1999). It is defined as the ratio of the actual nozzle capacity to the rated nozzle capacity:

$$\Gamma_{noz} = \frac{\dot{Q}_{noz,act}}{\dot{Q}_{noz,rated}} \tag{3.25}$$

where the actual capacity is the evaporator capacity, and the rated capacity is obtained from catalog data and is given by:

$$\dot{Q}_{noz,rated} = k_5 C_{noz} \exp\left(\frac{T_{sat,evp}}{k_6}\right) \tag{3.26}$$

where C_{noz} is a correction factor that is equal to unity when applying the rated evaporating temperatures listed in the catalog. For other evaporating temperatures, C_{noz} is calculated using the following equation:

$$C_{noz} = 10^{\left(\frac{T_{liq,rated} - T_{liq,act}}{k_9}\right)} \tag{3.27}$$

Similar to the distributor nozzle, the pressure drop across the distributor tube is calculated by:

$$\Delta P = k_3 \Gamma_{tube}^{k_4} \tag{3.28}$$

where Γ_{tube} is the "tube loading" of the distributor (Sporlan 1999), it is defined as:

$$\Gamma_{tube} = \frac{\dot{Q}_{tube,act}}{\dot{Q}_{tube,rated}} \tag{3.29}$$

The actual tube capacity is a fraction of the actual nozzle capacity as shown below:

$$\dot{Q}_{tube,act} = \frac{\dot{Q}_{noz,act}}{N_{ckt}} \tag{3.30}$$

and the rated tube capacity is obtained from the catalog data using the following correlation:

$$\dot{Q}_{tube,rated} = k_7 C_{noz} C_{tube} \exp\left(\frac{T_{sat,evp}}{k_8}\right) \tag{3.31}$$

where the tube correction factor, C_{tube} is defined as:

$$C_{tube} = \left(\frac{L_{tube,rated}}{L_{tube,act}}\right)^{k_{10}} \tag{3.32}$$

Note that if the rated tube length is the same as the actual tube length, the tube correction factor is unity. The coefficients $k_1, k_2, ..., k_{10}$ in the distributor model are curve fit coefficients that can be derived from manufacturer's catalog data.

3.4. Heat Exchangers

Both condenser and evaporator heat exchangers are modeled using the discrete segment method. The heat exchangers are discretized into small elements (Ragazzi and Pedersen 1991). This method is capable of modeling the effects of coil circuiting. Each elemental length can be as long as a single tube, i.e. a tube-by-tube discretization, or a

small segment of a tube, i.e. a segment-by-segment discretization. Figure 3.1 depicts the segment-by-segment discretization for a heat exchanger coil. The dashed lines represent the discretization boundaries. Note that the U-bend is not part of the discretization, since the U-bend is not exposed to the air stream, the heat transfer at the U-bends is negligible (Ragazzi and Pedersen 1991; Domanski 1999). However, the U-bends do introduce a significant refrigerant pressure drop in the heat exchanger, so the U-bend pressure drop is taken into account in the heat exchanger calculation. Each discretized element is treated as a single-tube cross-flow heat exchanger as shown in Figure 3.2.

For each element, the heat transfer capacity is calculated using the ε-NTU method. It is defined as:

$$\dot{Q} = \epsilon \dot{C}_{min} (T_{ref,in} - T_{air,in}) \tag{3.33}$$

where:

$$\dot{C}_{min} = MIN(\dot{C}_{air}, \dot{C}_{ref}) \tag{3.34}$$

$$\dot{C}_{air} = \dot{m}_{air} c_{p,air} \tag{3.35}$$

$$\dot{C}_{ref} = \dot{m}_{ref} c_{p,ref} \tag{3.36}$$

$\dot{m}_{air}$ is the air mass flow rate across each element. It is weighted by the element length and the coil frontal tube length:

$$\dot{m}_{air} = \dot{m}_{coil} \frac{L_{seg}}{L_{front}} \cdot \tau \tag{3.37}$$

τ is the velocity deviation from the mean face velocity. It is a user input that accounts for the air maldistribution at the coil surface.

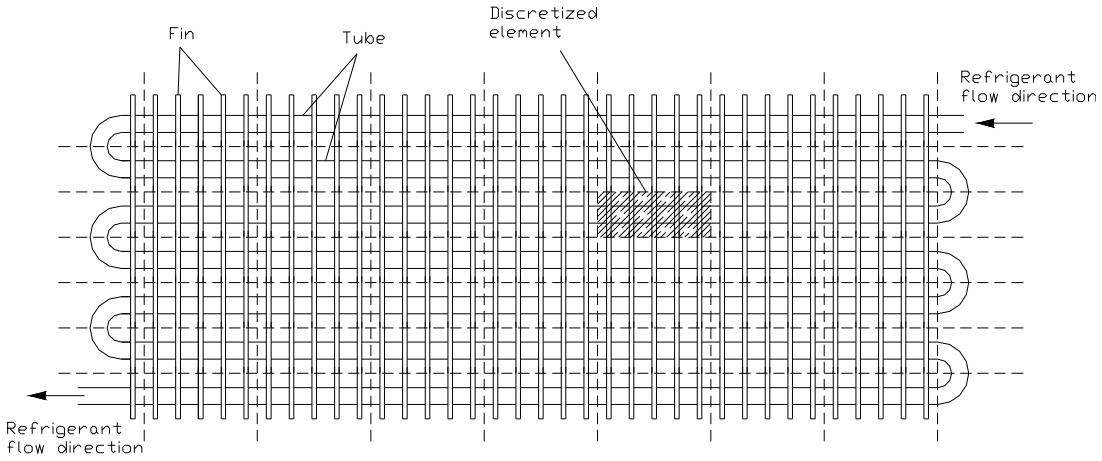

Figure 3.1 Heat exchanger segment-by-segment discretization.

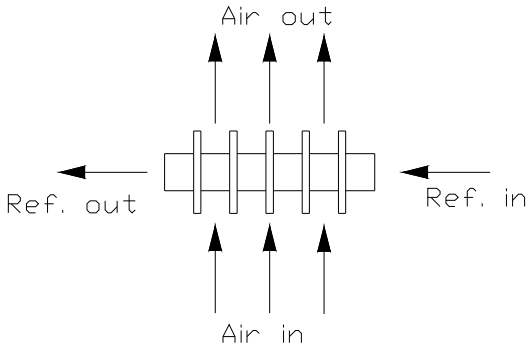

Figure 3.2 Heat exchanger element

The coil effectiveness is calculated differently depending on the operating conditions.

For a single-phase refrigerant:

If $\dot{C}_{min} = \dot{C}_{ref}$:

$$\epsilon = \frac{1}{C_r}\left(1 - \exp\left\{-C_r\left[1 - \exp(-NTU)\right]\right\}\right) \tag{3.38}$$

If $\dot{C}_{min} = \dot{C}_{air}$:

$$\epsilon = 1 - \exp\left\{-\frac{1}{C_r}\left[1 - \exp(-C_r \cdot NTU)\right]\right\} \tag{3.39}$$

For a two-phase refrigerant:

$$\epsilon = 1 - \exp(-NTU) \tag{3.40}$$

where:

$$NTU = \frac{UA}{C_{min}} \tag{3.41}$$

$$C_r = \frac{\dot{C}_{min}}{\dot{C}_{max}} \tag{3.42}$$

Assuming negligible inside and outside fouling resistances, the overall heat transfer coefficient is the total of the refrigerant side, tube wall, and air side resistances as shown below:

$$\frac{1}{UA} = \frac{1}{h_{ref} A_{in}} + \frac{\ln(\frac{D_{out,tube}}{D_{in,tube}})}{2\pi k_{tube} L_{tube}} + \frac{1}{\eta_{surf} h_{air} A_{out}} \tag{3.43}$$

where the surface efficiency is:

$$\eta_{surf} = 1 - \frac{A_{fin}}{A_{out}}(1 - \eta_{fin}) \tag{3.44}$$

The fin efficiency is calculated using Schmidt's method (1949), which is defined as:

$$\eta_{fin} = \frac{\tanh(m \cdot r_{collar} \cdot \phi)}{m \cdot r_{collar} \cdot \phi} \tag{3.45}$$

where r_{collar} is the tube outside radius including the fin collar, and:

$$m = \sqrt{\frac{2 \cdot h_{air}}{k_{fin} \delta_{fin}}} \tag{3.46}$$

$$\phi = (r_r - 1)\left[1 + 0.35 \ln(r_r)\right] \tag{3.47}$$

For staggered tubes, the radius ratio is defined as:

$$r_r = 1.27 \frac{X_M}{r_{collar}} \left[\frac{X_L}{X_M} - 0.3 \right]^{1/2} \tag{3.48}$$

where X_L and X_M are geometric parameters that are correlated to the tube pitch (P_t) and row pitch (P_r) as follows:

$$X_M = \frac{P_t}{2} \quad \text{if} \quad X_M \le P_r$$
$$X_M = P_r \quad \text{if} \quad X_M > P_r \tag{3.49}$$

$$X_L = \frac{1}{2} \sqrt{\left(\frac{P_t}{2} \right)^2 + P_r^{\,2}} \tag{3.50}$$

Each heat exchanger element is calculated one-by-one along the refrigerant flow path from the coil inlet to outlet. The inlet condition of each element is equal to the outlet condition of the previous element. For the elements located at the coil inlet, the inlet condition is equal to the coil inlet condition.

On the air side, the inlet condition varies depending on the element location. If the element is in the front row of the heat exchanger, the inlet condition is the same as the coil inlet condition. If the element is not at the front row, the inlet condition is the average of the outlet conditions of two nearest upstream elements. For the staggered tube arrangement shown in Figure 3.3, if tube-by-tube discretization is used, the inlet condition for tube number 3 is:

$$T_{3,air,in} = \frac{\left(T_{1,air,out} + T_{2,air,out} \right)}{2} \tag{3.51}$$

Note that since the calculation sequence is along the refrigerant flow direction, the upstream air outlet conditions may not be immediately available depending on the coil

circuiting. It is assumed that the air outlet condition for each element is equal to the coil entering condition at the beginning of the calculation. Iteration is performed to update the air outlet conditions until the calculated coil capacity converges.

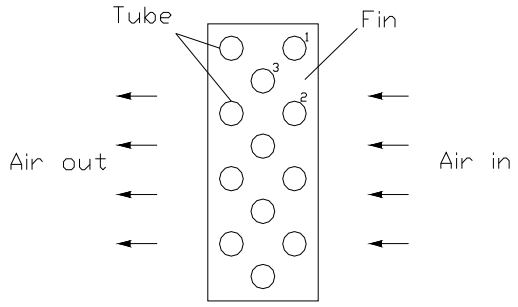

Figure 3.3 Side view of heat exchanger showing staggered tube pattern.

3.4.1. Dehumidification

The dehumidification process only occurs on the evaporator coil, where cold refrigerant circulates inside the coil tubes and hot air flows outside the coil. When the coil surface temperature is less the entering air dew point temperature, the heat exchanger dehumidifies the moisture content of the entering air and the coil surface becomes "wet". For wet surface heat exchanger elements, the dehumidification model from Harms *et al.* (2003) is used. This model is analogous to the traditional ε-NTU method as shown below:

$$\dot{Q} = \epsilon_{wet} \dot{m}_{air} (i_{air,in} - i_{ref,in,sat}) \tag{3.52}$$

where $i_{ref,in,sat}$ is the saturation enthalpy at refrigerant inlet temperature. ϵ_{wet} is the wet surface effectiveness which is calculated using the traditional ε-NTU equations but with the following terms in place:

$$\dot{C}_{air} = \dot{m}_{air} c_{p,sat} \quad \text{for the heat capacity rate of air} \tag{3.53}$$

$$h_{air,wet} = \frac{h_{air} c_{p,sat}}{c_{p,air}} \quad \text{for the air side heat transfer coefficient} \tag{3.54}$$

The saturation specific heat is defined as:

$$c_{p,sat} = \frac{\Delta i_{ref,sat}}{\Delta T_{ref}} \tag{3.55}$$

Also note that the driving potential in this model is the enthalpy to account for both sensible and latent heats.

For each heat exchanger element, if the surface temperature from the dry surface calculation is less then the entering air dew point temperature, the wet surface heat transfer is calculated. Due to the fact that the coil tube material is usually highly conductive, the inlet refrigerant temperature is used instead of the surface temperature to determine if dehumidification occurs. This approach is also used in the HVAC2 Toolkit (Brandemuehl 1993) and can avoid the calculation of surface temperature that is an unknown at the beginning of the calculation.

3.4.2. Air Side Heat Transfer Coefficient

According to Rich's experimental results (1975), the air side heat transfer coefficient varies from row to row of the heat exchanger. It is desirable to use the local heat transfer coefficient for the calculation of each heat exchanger element. However, row-by-row heat transfer correlations are rare. Most air side heat transfer correlations published in the literature are for the entire coil. The following shows some updated overall coil correlations for different fin types. The development and analysis of row-by-row coefficients for the louvered fin are presented in Chapter 5.

Published air side heat transfer correlations for the entire coil are usually presented in terms of the j-factor, as given by:

$$h_{air} = j \cdot c_{p,air} \cdot G_{air} \cdot Pr_{air}^{-2/3} \tag{3.56}$$

where G_{air} is the mass flux of the air based on the minimum free flow area of the heat exchanger. The j-factor is an empirical correlation that is derived from experimental data. Each fin pattern has it own j-factor correlation. Plain fin, wavy fin, and louvered fin correlations are included below.

Plain fin (Wang *et al.* 2000a):

If $N_r = 1$:

$$j = 0.108\, Re_{D_{collar}}^{-0.29} \left(\frac{P_t}{P_r}\right)^{j_1} \left(\frac{1}{P_{fin} D_{collar}}\right)^{-1.084} \left(\frac{1}{P_{fin} D_h}\right)^{-0.786} \left(\frac{1}{P_{fin} P_t}\right)^{j_2} \tag{3.57}$$

where:

$$j_1 = 1.9 - 0.23 \ln\left(Re_{D_{colloar}}\right) \tag{3.58}$$

$$j_2 = -0.236 + 0.126 \ln\left(Re_{D_{collar}}\right) \tag{3.59}$$

The hydraulic diameter is:

$$D_h = \frac{4 A_{min} N_r P_r}{A_{out}} \tag{3.60}$$

If $N_r > 1$:

$$j = 0.086\, Re_{D_{collar}}^{j_3} N_r^{j_4} \left(\frac{1}{P_{fin} D_{collar}}\right)^{j_5} \left(\frac{1}{P_{fin} D_h}\right)^{j_6} \left(\frac{1}{P_{fin} P_t}\right)^{-0.93} \tag{3.61}$$

where:

$$j_3 = -0.361 - 0.042\frac{N_r}{\ln(Re_{D_{collar}})} + 0.1581 \cdot \ln\left[N_r\left(\frac{1}{P_{fin} D_{collar}}\right)^{0.41}\right] \tag{3.62}$$

$$j_4 = -1.224 - \frac{0.076}{\ln(Re_{D_{collar}})}\left(\frac{P_r}{D_h}\right)^{1.42} \tag{3.63}$$

$$j_5 = -0.083 + 0.058\frac{N_r}{\ln Re_{D_{collar}}} \tag{3.64}$$

$$j_6 = -5.735 + 1.211\ln\left(\frac{Re_{D_{collar}}}{N_r}\right) \tag{3.65}$$

The Reynolds number is based on fin collar diameter and is calculated as:

$$Re_{D_{collar}} = \frac{G_{air} \cdot D_{collar}}{\mu_{air}} \tag{3.66}$$

This correlation is valid for the following ranges:

$$200 \le Re_{D_{collar}} \le 20000$$

$$1 \le N_r \le 6$$

$$6.35\,mm \le D_{collar} \le 12.7\,mm$$

$$1.19\,mm \le P_{fin} \le 8.7\,mm$$

$$17.7\,mm \le P_t \le 31.75\,mm$$

$$12.4\,mm \le P_r \le 27.5\,mm$$

Wavy fin (Wang *et. al* 2002):

If $Re_{D_{collar}} < 1000$:

$$j = 0.882\, Re_{D_{collar}}{}^{j_1} \left(\frac{D_{collar}}{D_h}\right)^{j_2} \left(\frac{S_{fin}}{P_t}\right)^{j_3} \left(\frac{S_{fin}}{D_{collar}}\right)^{-1.58} (\tan\theta)^{-0.2} \tag{3.67}$$

where:

$$j_1 = 0.0045 - 0.491\, Re_{D_{collar}}{}^{-0.0316 - 0.0171 \ln(N_r \tan\theta)} \left(\frac{P_r}{P_t}\right)^{-0.109 \ln(N_r \tan\theta)} \left(\frac{D_{collar}}{D_h}\right)^{0.542 + 0.0471 N_r} \left(\frac{S_{fin}}{D_{collar}}\right)^{0.984} \left(\frac{S_{fin}}{P_t}\right)^{-0.349} \tag{3.68}$$

$$j_2 = -2.72 + 6.84 \tan\theta \tag{3.69}$$

$$j_3 = 2.66 \tan\theta \tag{3.70}$$

If $Re_{D_{collar}} \geq 1000$:

$$j = 0.0646\, Re_{D_{collar}}{}^{j_1} \left(\frac{D_{collar}}{D_h}\right)^{j_2} \left(\frac{S_{fin}}{P_t}\right)^{-1.03} \left(\frac{P_r}{D_{collar}}\right)^{0.432} \tan\theta^{-0.692}\, N_r{}^{-0.737} \tag{3.71}$$

where:

$$j_1 = -0.0545 - 0.0538 \tan\theta - 0.302\, N_r{}^{-0.24} \left(\frac{S_{fin}}{P_r}\right)^{-1.3} \left(\frac{P_r}{P_t}\right)^{0.379} \left(\frac{P_r}{D_h}\right)^{-1.35} (\tan\theta)^{-0.256} \tag{3.72}$$

$$j_2 = -1.29 \left(\frac{P_r}{P_t}\right)^{1.77 - 9.43 \tan\theta} \left(\frac{D_{collar}}{D_h}\right)^{0.229 - 1.43 \tan\theta} N_r{}^{-0.166 - 1.08 \tan\theta} \left(\frac{S_{fin}}{P_t}\right)^{-0.174 \ln(0.5 N_r)} \tag{3.73}$$

This correlation is valid for the following ranges:

$$500 \leq Re_{D_{collar}} \leq 10000$$

$$1 \leq N_r \leq 6$$

$$7.66\, mm \leq D_{collar} \leq 16.85\, mm$$

$$1.1\,mm \le S_{fin} \le 6.2\,mm$$

$$21\,mm \le P_t \le 38.1\,mm$$

$$19.05\,mm \le P_r \le 33\,mm$$

$$5.3^o \le \theta \le 34.7^o$$

Louvered fin (Wang *et al.* 1999b):

If $Re_{D_{collar}} < 1000$:

$$j = 14.3117\, Re_{D_{collar}}{}^{j_1} \left(\frac{1}{P_{fin} D_{collar}}\right)^{j_2} \left(\frac{L_h}{L_p}\right)^{j_3} \left(\frac{1}{P_{fin} P_r}\right)^{j_4} \left(\frac{P_r}{P_t}\right)^{-1.724} \tag{3.74}$$

where:

$$j_1 = -0.991 - 0.1055 \left(\frac{P_r}{P_t}\right)^{3.1} \ln\left(\frac{L_h}{L_p}\right) \tag{3.75}$$

$$j_2 = -0.7344 + 2.1059 \left[\frac{N_r{}^{0.55}}{\ln(Re_{D_{collar}}) - 3.2}\right] \tag{3.76}$$

$$j_3 = 0.08485 \left(\frac{P_r}{P_t}\right)^{-4.4} N_r{}^{-0.68} \tag{3.77}$$

$$j_4 = -0.1741 \ln N_r \tag{3.78}$$

If $Re_{D_{collar}} \ge 1000$:

$$j = 1.1373\, Re_{D_{collar}}{}^{j_5} \left(\frac{1}{P_{fin} P_r}\right)^{j_6} \left(\frac{L_h}{L_p}\right)^{j_7} \left(\frac{P_r}{P_t}\right)^{j_8} N_r{}^{0.3545} \tag{3.79}$$

where:

$$j_5 = -0.6027 + 0.02593\left(\frac{P_r}{D_h}\right)^{0.52} N_r^{-0.5} \ln\left(\frac{L_h}{L_p}\right) \tag{3.80}$$

$$j_6 = -0.4776 + 0.40774\left[\frac{N_r^{0.7}}{\ln(Re_{D_{collar}}) - 4.4}\right] \tag{3.81}$$

$$j_7 = -0.58655\left(\frac{1}{P_{fin} D_h}\right)^{2.3}\left(\frac{P_r}{P_t}\right)^{-1.6} N_r^{-0.65} \tag{3.82}$$

$$j_8 = 0.0814\left[\ln(Re_{D_{collar}}) - 3\right] \tag{3.83}$$

This correlation is valid for the following ranges:

$$250 \le Re_{D_{collar}} \le 8000$$

$$1 \le N_r \le 6$$

$$6.93\,mm \le D_{collar} \le 10.42\,mm$$

$$1.22\,mm \le P_{fin} \le 2.49\,mm$$

$$17.7\,mm \le P_t \le 25.4\,mm$$

$$12.7\,mm \le P_r \le 19.05\,mm$$

$$0.79\,mm \le L_h \le 1.4\,mm$$

$$1.7\,mm \le L_p \le 3.75\,mm$$

3.4.3. Refrigerant Side Heat Transfer Coefficient

The refrigerant side heat transfer coefficient is defined according to the refrigerant condition (single-phase or two-phase), and the heat transfer process (condensation or evaporation). It is calculated using the following correlations:

For single-phase condensation and evaporation (Gnielinski 1976):

$$h_{ref} = \frac{(Re_{D_{in}} - 1000)\, Pr_{ref}\, (f/2)}{1 + 12.7\sqrt{f/2}\,(Pr_{ref}^{0.67} - 1)} \frac{k_{ref}}{D_{in}} \tag{3.84}$$

where:

$$f = [1.58 \ln(Re_{D_{in}}) - 3.28]^{-2} \tag{3.85}$$

For two-phase condensation (Dobson 1994):

$$h_{ref} = 2.61 \frac{h_{liq}}{X_{tt}^{0.8}} \tag{3.86}$$

where h_{liq} is the Dittus-Boelter (1930) single-phase correlation for condensation:

$$h_{liq} = 0.023\, Re_{D_{in}}^{0.8}\, Pr_{liq}^{0.3} \frac{k_{liq}}{D_{in}} \tag{3.87}$$

X_{tt} is the Lockhart-Martinelli parameter, which is defined as:

$$X_{tt} = \left(\frac{\rho_{vap}}{\rho_{liq}}\right)^{0.5} \left(\frac{\mu_{liq}}{\mu_{vap}}\right)^{0.125} \left(\frac{1 - x_{ref}}{x_{ref}}\right)^{0.875} \tag{3.88}$$

This correlation is valid for $x_{ref} \geq 0.17$. Interpolation between single and two-phase correlations is used for $x_{ref} < 0.17$.

For two-phase evaporation (Wattelet 1990):

$$h_{ref} = \left(h_{nb}^{2.5} + h_{cb}^{2.5}\right)^{\frac{1}{2.5}} \tag{3.89}$$

The nucleate boiling term is related to the refrigerant molecular weight (W) and circumferential heat flux ($\dot{q}$), which is given by:

$$h_{nb} = 55\, W^{-0.5}\, \dot{q}^{0.67}\, Pr_{ref}^{0.12} (-\log Pr_{ref})^{-0.55} \tag{3.90}$$

and the convective boiling term is given by:

$$h_{cb} = F_1 h_{liq} F_2 \tag{3.91}$$

where:

$$F_1 = 1 + 1.925\, X_{tt}^{-0.83} \tag{3.92}$$

$$h_{liq} = 0.023\, Re_{D_{in}}^{0.8}\, Pr_{liq}^{0.4} \frac{k_{liq}}{D_{in}} \tag{3.93}$$

$$F_2 = 1 \quad \text{if} \quad Fr_{liq} \geq 0.25$$

$$F_2 = 1.32\, Fr_{liq}^{0.2} \quad \text{if} \quad Fr_{liq} < 0.25 \tag{3.94}$$

The liquid phase Froude number is defined as:

$$Fr_{liq} = \frac{G_{ref}^{\ 2}}{\rho_{liq}^{\ 2}\, g\, D_{in}} \tag{3.95}$$

This correlation is valid for $x_{ref} < 0.8$. For $x_{ref} \geq 0.8$, interpolation is used between the single phase and two-phase correlations.

The correlations presented in this section are for smooth tubes. An enhancement factor can be used to scale the smooth tube coefficients to predict enhanced tube performance. Eckels *et al.* (1994a; 1994b; 1998a) presented some enhancement factor correlations for enhanced tubes. However, due to the fact that different tube manufacturers have different tube types, enhancement factor correlations must generally be obtained from the manufacturer.

3.4.4. Air Side Pressure Drop

The air side pressure drop correlation is usually presented in terms of the friction

factor as follows:

$$\Delta P_{air} = \frac{G_{air}^{\ 2}}{2\rho_{in}}\left[\left(K_i + 1 - \sigma^2\right) + 2\left(\frac{\rho_{in}}{\rho_{out}} - 1\right) + f\left(\frac{A_{out}}{A_{min}}\right)\left(\frac{\rho_{in}}{\rho_{out}}\right) - (1 - \sigma^2 - K_e)\frac{\rho_{in}}{\rho_{out}}\right] \tag{3.96}$$

where:

$$\sigma = \frac{A_{min}}{A_{front}} \tag{3.97}$$

The entrance and exit loss coefficients are obtained from McQuiston *et al.* (2000):

$$K_i = -0.404\,\sigma + 0.494 \tag{3.98}$$

$$K_e = -1.272\,\sigma + 0.8726 \tag{3.99}$$

Wang *et al.* (1999b, 2000a, and 2002) also presented fiction factor correlations for different fin types. The fiction factor correlations are presented below. Note that the application ranges for these friction factor correlations are the same as the corresponding j-factor correlations.

Plain fin (Wang *et al.* 2000a):

$$f = 0.0267\,Re_{D_{collar}}^{\ f_1}\left(\frac{P_t}{P_r}\right)^{f_2}\left(\frac{1}{P_{fin}D_{collar}}\right)^{f_3} \tag{3.100}$$

where:

$$f_1 = -0.764 + 0.739\frac{P_t}{P_r} + \frac{0.177}{P_{fin}D_{collar}} - \frac{0.00758}{N_r} \tag{3.101}$$

$$f_2 = -15.689 + \frac{64.021}{\ln\left(Re_{D_{collar}}\right)} \tag{3.102}$$

$$f_3 = 1.696 - \frac{15.695}{\ln\left(Re_{D_{collar}}\right)} \tag{3.103}$$

Wavy fin (Wang *et al.* 2002):

If $Re_{D_{collar}} < 1000$:

$$f = 4.37\, Re_{D_{collar}}{}^{f_1} \left(\frac{S_{fin}}{D_h}\right)^{f_2} \left(\frac{P_r}{P_t}\right)^{f_3} \left(\frac{D_{collar}}{D_h}\right)^{0.2054} N_r{}^{f_4} \tag{3.104}$$

where:

$$f_1 = -0.574 - 0.137\left(\ln(Re_{D_{collar}}) - 5.26\right)^{0.245} \left(\frac{P_t}{D_{collar}}\right)^{-0.765} \left(\frac{D_{collar}}{D_h}\right)^{-0.243} \left(\frac{S_{fin}}{D_h}\right)^{-0.474} (\tan\theta)^{-0.217} N_r{}^{0.035} \tag{3.105}$$

$$f_2 = -3.05 \tan\theta \tag{3.106}$$

$$f_3 = -0.192\, N_r \tag{3.107}$$

$$f_4 = -0.646 \tan\theta \tag{3.108}$$

If $Re_{D_{collar}} \geq 1000$:

$$f = 0.228\, Re_{D_{collar}}{}^{f_1} (\tan\theta)^{f_2} \left(\frac{S_{fin}}{P_r}\right)^{f_3} \left(\frac{P_r}{D_{collar}}\right)^{f_4} \left(\frac{D_{collar}}{D_h}\right)^{0.383} \left(\frac{P_r}{P_t}\right)^{-0.247} \tag{3.109}$$

where:

$$f_1 = -0.141 \left(\frac{S_{fin}}{P_r}\right)^{0.0512} (\tan\theta)^{-0.472} \left(\frac{P_r}{P_t}\right)^{0.35} \left(\frac{P_t}{D_h}\right)^{0.449\tan\theta} N_r{}^{-0.049 + 0.237\tan\theta} \tag{3.110}$$

$$f_2 = -0.562 \ln(Re_{D_{collar}})^{-0.0923} N_r{}^{0.013} \tag{3.111}$$

$$f_3 = 0.302\, Re_{D_{collar}}{}^{0.03} \left(\frac{P_t}{D_{collar}}\right)^{0.026} \tag{3.112}$$

$$f_4 = -0.306 + 3.63 \tan\theta \tag{3.113}$$

Louvered fin (Wang *et al.* 1999b):

If $N_r = 1$:

$$f = 0.00317\, Re_{D_{collar}}^{\;f_1} \left(\frac{P_{fin}}{P_r}\right)^{f_2} \left(\frac{D_h}{D_{collar}}\right)^{f_3} \left(\frac{L_h}{L_p}\right)^{f_4} \left(\ln\left(\frac{A_{out}}{A_{bare}}\right)\right)^{-6.0483} \tag{3.114}$$

where:

$$f_1 = 0.1691 + 4.4118 \left(\frac{P_{fin}}{P_r}\right)^{-0.3} \left(\frac{L_h}{L_p}\right)^{-2.0} \ln\left(\frac{P_r}{P_t}\right) \left(\frac{P_{fin}}{P_t}\right)^{3.0} \tag{3.115}$$

$$f_2 = -2.6642 - 14.3809 \left[\frac{1}{\ln\left(Re_{D_{collar}}\right)}\right] \tag{3.116}$$

$$f_3 = -0.6816 \ln\left(\frac{P_{fin}}{P_r}\right) \tag{3.117}$$

$$f_4 = 6.4668 \left(\frac{P_{fin}}{P_t}\right)^{1.7} \ln\left(\frac{A_{out}}{A_{bare}}\right) \tag{3.118}$$

If $N_r \geq 1$:

$$f = 0.06393\, Re_{D_{collar}}^{\;f_5} \left(\frac{P_{fin}}{D_{collar}}\right)^{f_6} \left(\frac{D_h}{D_{collar}}\right)^{f_7} \left(\frac{L_h}{L_p}\right)^{f_8} N_r^{\;f_9} \left[\ln\left(Re_{D_{collar}}\right) - 4.0\right]^{-1.093} \tag{3.119}$$

where:

$$f_5 = 0.1395 - 0.0101 \left(\frac{P_{fin}}{P_r}\right)^{0.58} \left(\frac{L_h}{L_p}\right)^{-2} \ln\left(\frac{A_{out}}{A_{bare}}\right) \left(\frac{P_r}{P_t}\right)^{1.9} \tag{3.120}$$

$$f_6 = -6.4367 \left[\frac{1}{\ln\left(Re_{D_{collar}}\right)}\right] \tag{3.121}$$

$$f_7 = 0.07191 \cdot \ln\left(Re_{D_{collar}}\right) \tag{3.122}$$

$$f_8 = -2.0585\left(\frac{P_{fin}}{P_t}\right)^{1.67} \ln\left(Re_{D_{collar}}\right) \tag{3.123}$$

$$f_9 = 0.1036 \ln\left(\frac{P_r}{P_t}\right) \tag{3.124}$$

3.4.5. Refrigerant Side Pressure Drop

The refrigerant side pressure drop is also calculated in the heat exchanger models, although it is relatively insignificant compared to the pressure drop across the expansion device. The refrigerant pressure drop in each heat exchanger tube segment is due to friction, acceleration, and gravitation forces (Ragazzi and Pedersen 1991):

$$\Delta P_{ref} = \Delta P_{fric} + \Delta P_{accel} + \Delta P_{grav} \tag{3.125}$$

3.4.5.1. Frictional Pressure Drop

The frictional pressure drop is the dominant component. For single-phase flow, it is calculated in terms of the friction factor:

$$\Delta P_{fric} = \frac{2 f G_{ref}^{\ 2}}{\rho_{ref} D_{in}} L_{seg} \tag{3.126}$$

where:

$$f = \frac{16}{Re_{D_{in}}} \quad \text{for} \quad Re_{D_{in}} \le 2300 \tag{3.127}$$

$$f = \frac{0.046}{\left(Re_{D_{in}}\right)^{0.2}} \quad \text{for} \quad 1E5 \ge Re_{D_{in}} > 2300 \quad \text{vapor refrigerant} \tag{3.128}$$

$$f = \frac{0.079}{(Re_{D_{in}})^{0.25}} \quad \text{for} \quad 1E5 \geq Re_{D_{in}} > 2300 \quad \text{liquid refrigerant} \tag{3.129}$$

$$f = \frac{0.0032 + 0.221(Re_{D_{in}})^{-0.237}}{4} \quad \text{for} \quad Re_{D_{in}} > 1E5 \tag{3.130}$$

For two-phase flow, following Souza *et al.* (1993), the frictional pressure drop is given by:

$$\Delta P_{fric} = \Delta P_{liq} \cdot \phi_{liq}^2 \tag{3.131}$$

where ΔP_{liq} is the frictional pressure drop in liquid phase, and the ϕ_{liq} is a two-phase correction factor. It is defined as:

$$\phi_{liq}^2 = 1.376 + \frac{C_1}{X_{tt}^{C_2}} \tag{3.132}$$

X_{tt} is the Lockhart-Martinelli parameter as defined in section Equation (3.88), and C_1 and C_2 are related to the liquid Froude number:

$$\begin{aligned} C_1 &= 7.242 \quad \text{if} \quad Fr_{liq} \geq 0.7 \\ C_2 &= 1.655 \end{aligned} \tag{3.133}$$

$$\begin{aligned} C_1 &= 4.172 + 5.48\, Fr_{liq} - 1.564\, Fr_{liq}^2 \quad \text{if} \quad Fr_{liq} < 0.7 \\ C_2 &= 1.773 - 0.169\, Fr_{liq} \end{aligned} \tag{3.134}$$

where the liquid Froude number is defined in Equation (3.95).

3.4.5.2. Accelerational Pressure Drop

Accelerational pressure drop is also calculated differently according to the phase of the refrigerant. For single-phase refrigerant, the acceleration pressure drop is

calculated as:

$$\Delta P_{accel} = G_{ref}{}^2 \left(\frac{1}{\rho_{ref,in}} - \frac{1}{\rho_{ref,out}} \right) \tag{3.135}$$

For two-phase refrigerant, it is calculated as:

$$\Delta P_{accel} = G_{ref}^2 \left(\frac{x_{ref}^2}{\alpha \rho_{vap}} + \frac{(1-x_{ref})^2}{(1-\alpha)\rho_{liq}} \right) \tag{3.136}$$

where the void fraction is calculated using Zivi's correlation (1964):

$$\alpha = \frac{1}{1 + \frac{1-x_{ref}}{x_{ref}} \left(\frac{\rho_{vap}}{\rho_{liq}} \right)^{2/3}} \tag{3.137}$$

3.4.5.3. Gravitational Pressure Drop

The gravitational pressure drop is the least significant component. It is often neglected in heat exchanger calculations. In this heat exchanger model, it is assumed that all heat exchanger elements share an equal amount of gravitation pressure drop throughout the entire coil (Ragazzi and Pedersen 1991). The pressure drop is calculated as:

$$\Delta P_{grav} = \rho_{ref} \, g \, L_{seg} \frac{H_{coil}}{L_{coil}} \tag{3.138}$$

3.4.5.4. U-Bend Pressure Drop

The above pressure drop calculations are for straight tubes. For U-bends, the pressure drop is calculated using the Paliwoda (1992) model:

For single-phase refrigerant:

$$\Delta P_{Ubend} = \frac{1}{2} K_{\Delta P} \frac{G_{ref}^{\ 2}}{\rho_{ref}} \tag{3.139}$$

where $K_{\Delta P}$ is the curve fit correction factor:

$$K_{\Delta P} = \frac{1}{3.426 \cdot \ln\left(\frac{P_t}{2 D_{in}}\right) + 3.8289} \tag{3.140}$$

For two-phase refrigerant:

$$\Delta P_{Ubend} = \Delta P_{Ubend,vap} \xi_1 \tag{3.141}$$

where $\Delta P_{Ubend,vap}$ is the U-bend pressure drop for vapor refrigerant. ξ_1 is a correction factor which is defined as:

$$\xi_1 = (\xi_2 + 3(1-\xi_2) x_{ref})(1-x_{ref})^{0.333} + x_{ref}^{2.276} \tag{3.142}$$

$$\xi_2 = \frac{\rho_{vap}}{\rho_{liq}} \left(\frac{\mu_{liq}}{\mu_{vap}} \right)^{0.25} \tag{3.143}$$

All of the above correlations are for smooth tubes. The refrigerant side pressure for enhanced tube is scaled by the "penalty factor", so called because the tube enhancement increases the refrigerant pressure drop and it is not desirable. The penalty factor correlations from Eckels *et al.* (1994a; 1994b; 1998a) can be used to adjust the refrigerant pressure drop for enhanced tubes, but for this research, penalty factor correlations are acquired from the tube manufacturer.

3.4.6. Circuiting Algorithm

Heat exchanger circuiting determines the refrigerant flow distribution in the coil.

It is important to know the local refrigerant mass flow rate at each heat exchanger element in order to determine the heat transfer and pressure drop accurately. The proposed circuiting algorithm consists of two parts: the circuit table and the solution algorithm.

A unique circuit table is proposed to store the circuiting information. This circuit table not only shares the flexibility of the adjacency matrix that is used by Liang *et al.* (1998), but it is also more intuitively interpreted. The sample circuit shown in Figure 2.5 can be used to demonstrate the use of circuit table. In order to use the circuit table, the tubes in the circuit are numbered as shown in Figure 3.4.

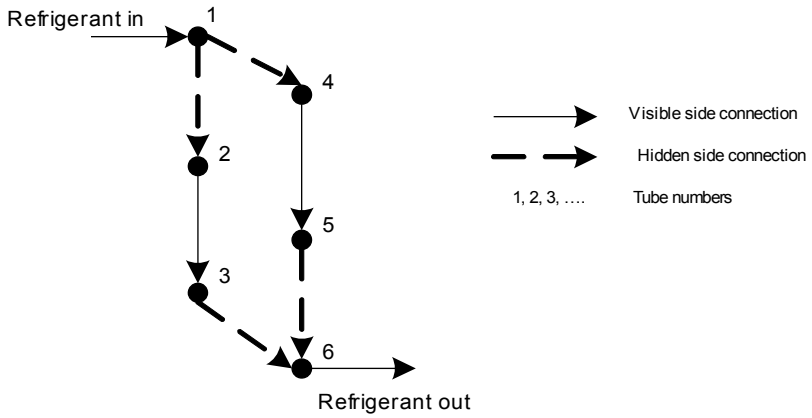

Figure 3.4 Sample circuit with re-assigned tube numbers.

Table 3.2 shows the circuit table for this circuit. From the circuit table, it is easy to determine that there are two circuit branches in the coil. Each circuit branch has a different flow path as shown under the "Tube Sequence" in the table. The tube numbers for the first and last tubes are the split and joined connection indicators, respectively. Note that both circuit branches start from tube 1 and end at tube 6, which means that they both start from the same inlet (tube 1) and join together at the same outlet (tube 6). The construction of the circuit table is simple and straightforward. It can be expanded to store

any kind of complex circuiting without limitations.

Table 3.2 Circuit table for the sample circuit.

Branch No.	Tube Sequence			
	1st	2nd	3rd	4th
1	1	2	3	6
2	1	4	5	6

The proposed circuiting algorithm determines the mass flow rate distribution in the circuit branches. The following conservation equations are used in the algorithm:

For the joining circuit shown in Figure 3.5a:

$$\dot{m}_4 = \dot{m}_1 + \dot{m}_2 + \dot{m}_3 \tag{3.144}$$

$$P_{4,in} = P_{1,out} = P_{2,out} = P_{3,out} \tag{3.145}$$

$$i_{4,in} = \frac{\sum_{i=1}^{3} \dot{m}_i i_{i,out}}{\sum_{i=1}^{3} \dot{m}_i} \tag{3.146}$$

where i is the refrigerant enthalpy. For the splitting circuit shown in Figure 3.5b:

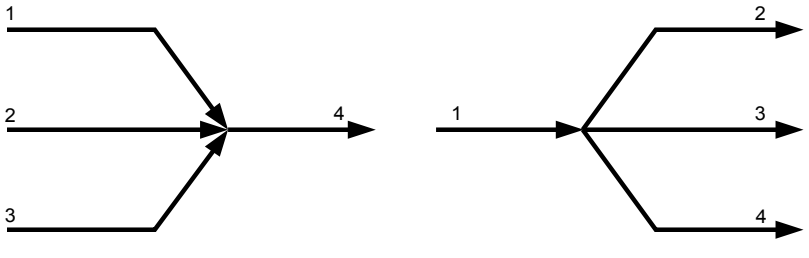

Figure 3.5 Joining and splitting circuits.

$$\dot{m}_1 = \dot{m}_2 + \dot{m}_3 + \dot{m}_4 \tag{3.147}$$

$$P_{1,out} = P_{2,in} = P_{3,in} = P_{4,in} \tag{3.148}$$

$$i_{1,out} = i_{2,in} = i_{3,in} = i_{4,in} \tag{3.149}$$

The mass flow rate in each circuit branch is calculated according to the refrigerant pressure drop and flow admittance (J) as follows:

$$\dot{m}_{ckt} = J_{ckt} \cdot \left(P_{in,ckt} - P_{out,ckt} \right) \tag{3.150}$$

The nodal admittance formulation (Vlach and Singhal 1993) is proposed to determine the mass flow rate in each circuit. This method was initially designed for electrical circuits and has never been used for heat exchanger circuits. It is derived from the Kirchhoff current law (KCL) that states that the algebraic sum of all currents leaving any junction is zero. Considering the analogy of electrical voltage and current to refrigerant pressure and mass flow rate, the nodal admittance formulation can be conveniently applied to heat exchanger circuits.

The circuiting in a heat exchanger coil is described by the following matrix equation:

$$\mathbf{M} = \mathbf{J} \cdot \mathbf{P} \tag{3.151}$$

where **J** is the admittance (conductance) matrix. It is a square matrix and its order is equal to the number of circuit junctions (split and joined). The coil outlet is also considered as a junction in heat exchanger circuits. The diagonal entries of **J** are positive and are equal to the sum of the circuit admittances connected to the same junction:

$$j_{i,i} = \sum^{m} J_q \quad \text{for } i = 1, 2, ..., n \tag{3.152}$$

where i is the current junction number, q is the branch number, m is the number of circuit branches connected to junction i, and n is total number of junctions in the circuit, including the coil outlet. The off-diagonal entries of the **J** matrix are non-positive and are

equal to the sum of admittances between the neighboring junctions. It is given by:

$$j_{i,k} = -\sum^{n} J_q \quad \text{for } i,\ k = 1, 2, ..., n; \text{ and } i \neq k \tag{3.153}$$

Note that if junctions i and k are not neighbors, the value of $j_{i,k}$ is zero. Therefore, for each junction i, Equations (3.152) and (3.153) calculate the entries for each row of the **J** matrix. Equation (3.153) also implies that **J** is an $n \times n$ symmetric matrix, so only half of the off-diagonal entries must be calculated.

M is an n-dimension column vector. The number of entries is equal to the number of junctions. Its entries have the same unit as mass flow rate but they are not the mass flow rate at the junctions. They are calculated differently according to the junction location:

For the coil outlet junction:

$$m_i = P_{in,coil} \sum^{m'} J_q - \dot{m}_{tot} \quad \text{for } i = 1, 2, ..., n \tag{3.154}$$

For other junctions in the coil:

$$m_i = P_{in,coil} \sum^{m'} J_q \quad \text{for } i = 1, 2, ..., n \tag{3.155}$$

where m' is the number of circuit branches connected to the coil inlet.

P is simply a column vector for refrigerant pressure. Its entries are the refrigerant pressure at each circuit junction, and its dimension is the same as the vector **M**.

Since the circuit admittances and junction pressures are unknown at the beginning of the calculation, the nodal admittance method requires an iterative procedure. The procedure is summarized as follows:

1. Initialize the circuit mass flow rates to start the iteration.
2. Calculate the junction pressures using the refrigerant pressure drop correlations in section 3.4.5.
3. Calculate the circuit admittances using Equation (3.150).
4. Calculate the vector **M** using Equations (3.154) and (3.155).
5. Calculate the admittance matrix **J** using Equations (3.152) and (3.153).
6. Calculate the junction pressure vector **P** using Equation (3.151). If the calculated junction pressures are similar to the results obtained in step 2 within a small value, the iteration terminates. The circuit mass flow rates are found. Otherwise, go to next step.
7. Update the circuit mass flow rates using Equation (3.150). Go to step 2.

The following example illustrates how the **J**, **M**, and **P** matrices are calculated. Consider the complex circuitry shown in Figure 3.6, it is a rather uncommon circuitry but can demonstrate the capability of the circuiting algorithm. There are 10 circuit branches with arbitrarily assigned branch numbers as shown in the figure. The branches are connected by 5 different junctions, i.e. tubes 2, 6, 7, 9, and the coil outlet. For example, branches 1, 2, 4 and 5 are connected to tube 2. Let's arbitrarily number the junctions as shown in Table 3.3 to calculate the matrices.

Since there are 5 junctions, **J** is a 5×5 matrix. The first row of the **J** matrix is with respect to the first junction, i.e. tube 2. Therefore the diagonal entry $j_{1,1}$ is the sum of circuit admittances connected to tube 2, which is:

$$j_{1,1}=J_1+J_2+J_4+J_5$$

Table 3.3 Junction numbering for the sample circuit in Figure 3.6.

Junction Number	Location
1	Tube 2
2	Tube 6
3	Tube 7
4	Tube 9
5	Coil Outlet

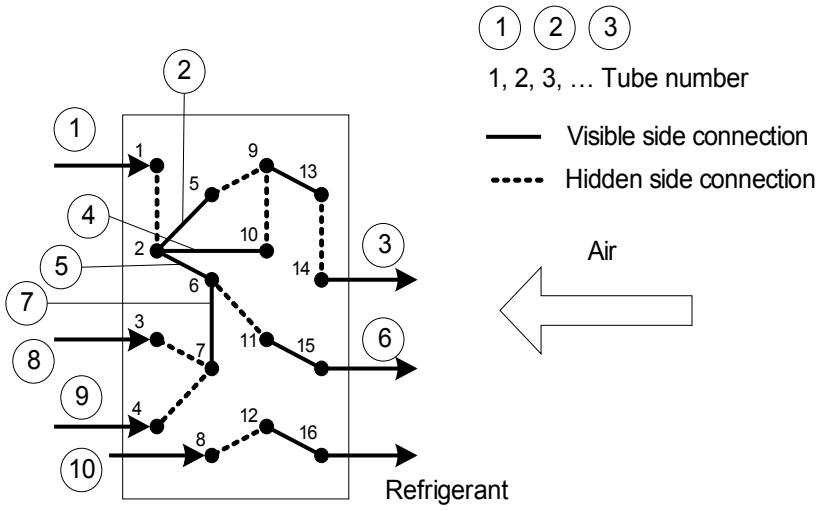

Figure 3.6 Illustrative example for the nodal admittance formulation method.

Note that the subscript for J is the branch number. The off-diagonal entries $j_{1,2}$, $j_{1,3}$, ..., and $j_{1,5}$ are the negative sum of the circuit admittances between neighboring junctions, which are:

$$j_{1,2}=-J_5 \quad ; \quad j_{1,3}=0 \quad ; \quad j_{1,4}=-(J_2+J_4) \quad ; \quad j_{1,5}=0$$

Since junction 1 (tube 2) and junction 3 (tube 7) are separated by junction 2 (tube 6), they are not neighboring junctions and the value of $j_{1,3}$ is zero. Similarly, junction 1 (tube 2) and junction 5 (coil outlet) are separated by other junctions, the value of $j_{1,5}$ is also zero.

The rest of the matrix entries are determined similarly. The resulting **J** matrix for this circuit is shown below:

$$\boldsymbol{J}=\begin{bmatrix} J_1+J_2+J_4+J_5 & -J_5 & 0 & -(J_2+J_4) & 0 \\ -J_5 & J_5+J_6+J_7 & -J_7 & 0 & -J_6 \\ 0 & -J_7 & J_7+J_8+J_9 & 0 & 0 \\ -(J_2+J_4) & 0 & 0 & J_2+J_3+J_4 & -J_3 \\ 0 & -J_6 & 0 & -J_3 & J_3+J_6+J_{10} \end{bmatrix}$$

As expected, the matrix is symmetric and only half of the off-diagonal entries must be calculated.

For the vector **M**, since junction 1 (tube 2) is directly connected to the coil inlet through branch 1, according to Equation (3.155), the value of this entry is:

$$m_1=P_{in,coil}\cdot J_1$$

Note that the subscript for *J* is the branch number and the subscript for *m* is the junction number. For junctions 2 and 4 (tubes 6 and 9) that are not directly connected to coil inlet because of the separation by other junctions, the number of inlet branches are zero and the values of these entries are also zero:

$$m_2=m_4=0$$

Junction 3 (tube 7) has two circuit branches (8 and 9) directly connected to the coil inlet, therefore the value of this entry is:

$$m_3=P_{in,coil}\cdot(J_8+J_9)$$

Junction 5 is the coil outlet, it has one branch (i.e. branch 10) directly connected to the coil inlet. According to Equation (3.154), this entry is:

$$m_5=P_{in,coil}\cdot J_{10}-\dot{m}_{tot}$$

Since there are only 5 five junctions, the resulting **M** vector is:

$$\boldsymbol{M} = \begin{bmatrix} P_{in,coil} \cdot J_1 \\ 0 \\ P_{in,coil} \cdot (J_8 + J_9) \\ 0 \\ P_{in,coil} \cdot J_{10} - \dot{m}_{tot} \end{bmatrix}$$

The pressure vector **P** is the easiest one to determine. It stores the refrigerant pressure at each junction, i.e. tubes 2, 6, 7, 9, and the coil outlet, as shown below:

$$\boldsymbol{P} = \begin{bmatrix} p_1 \\ p_2 \\ p_3 \\ p_4 \\ p_5 \end{bmatrix} = \begin{bmatrix} P_2 \\ P_6 \\ P_7 \\ P_9 \\ P_{out,coil} \end{bmatrix}$$

where the subscript for *p* is the junction number, and the subscript for *P* is the junction location.

3.4.7. Transition Element

In the elemental heat exchanger model, it is possible to have an element that consists of both single and two-phase refrigerants. For this "transition element", if either the single-phase or two-phase equations are used, error will be introduced. The error can be significant if the element is long. More segments can be used to minimize the problem but this will increase the computational time. Moreover, the fundamental "transition element" problem still exists. Therefore, a transition element algorithm was developed to eliminate the transition element problem.

The heat exchanger model divides the transition element into single and two-phase portions, and applies the corresponding heat transfer equations to each portion. The calculation procedures for the transition element are summarized as follows:

1. Assume constant refrigerant properties in the entire element and apply either single-phase or two-phase heat transfer equations to calculate the capacity.

2. Compare the refrigerant properties at the element inlet and outlet to determine if there is a phase change between the single-phase and two-phase regions. If there is a phase change, determine the location of the transition. It is either near the condenser inlet, the condenser outlet, or the evaporator outlet.

3. Calculate the capacity for the 1st portion of the element according to the element location.

$$\dot{Q}_{1^{st}} = \dot{m}_{ref}\left(i_{ref,in} - i_{sat,vap}\right) \quad \text{for condenser inlet} \tag{3.156}$$

$$\dot{Q}_{1^{st}} = \dot{m}_{ref}\left(i_{ref,in} - i_{sat,liq}\right) \quad \text{for condenser outlet} \tag{3.157}$$

$$\dot{Q}_{1^{st}} = -\dot{m}_{ref}\left(i_{ref,in} - i_{sat,vap}\right) \quad \text{for evaporator outlet} \tag{3.158}$$

4. Guess the length of the 1st portion. It should be between zero and the total element length.

5. Compute the 1st portion capacity using the ε-NTU method. If the element is near the condenser inlet, use the single-phase heat transfer equations. Otherwise use the two-phase equations.

6. Compare the capacities calculated in steps (3) and (5). If they do not match, adjust the guessed length and repeat step (5). Note that the length is proportional to the capacity and is bounded. Therefore, it is well-suited for any one-dimensional search method.

7. Subtract the length of the 1st portion from the total element length to obtain the length of the 2nd portion.

8. Compute the capacity for the 2nd portion. If the element is near the condenser inlet, use the two-phase equations. Otherwise, use the single-phase equations.

9. Add the capacities of the 1st and 2nd portions from steps (5) and (8), respectively. The result is the total capacity of the transition element.

3.4.8. Heat Exchanger Solution Algorithm

The heat exchanger solution algorithm involves several iterative procedures as shown in Figure 3.7. The calculation starts by breaking the heat exchanger into elements. For each element, the average refrigerant property of the inlet and outlet conditions is used in the heat transfer and pressure drop calculations. It usually takes 2 to 3 iterations to converge. After each element calculation, the inlet and outlet refrigerant qualities are compared to determine if a transition element calculation is needed. The element-by-element calculation is performed along the refrigerant flow direction for all tubes and all circuits of the heat exchanger.

At the beginning of the heat exchanger calculation, it is assumed that the inlet air conditions for all heat exchanger elements are the same as the inlet air conditions to the coil. The inlet air conditions are updated once all elements have been calculated. This iteration process is considered converged when the total coil capacity remains unchanged within ±1%.

The calculation of the refrigerant flow rate distribution is another iterative procedure of the heat exchanger calculation. Uniform refrigerant distribution is assumed at the beginning of the calculation. The refrigerant flow rate in each circuit is updated using the proposed circuiting algorithm once the air side has converged. The flow rate

iteration is considered converged when the coil outlet pressure remains unchanged within ±0.07 kPa (±0.01 psi).

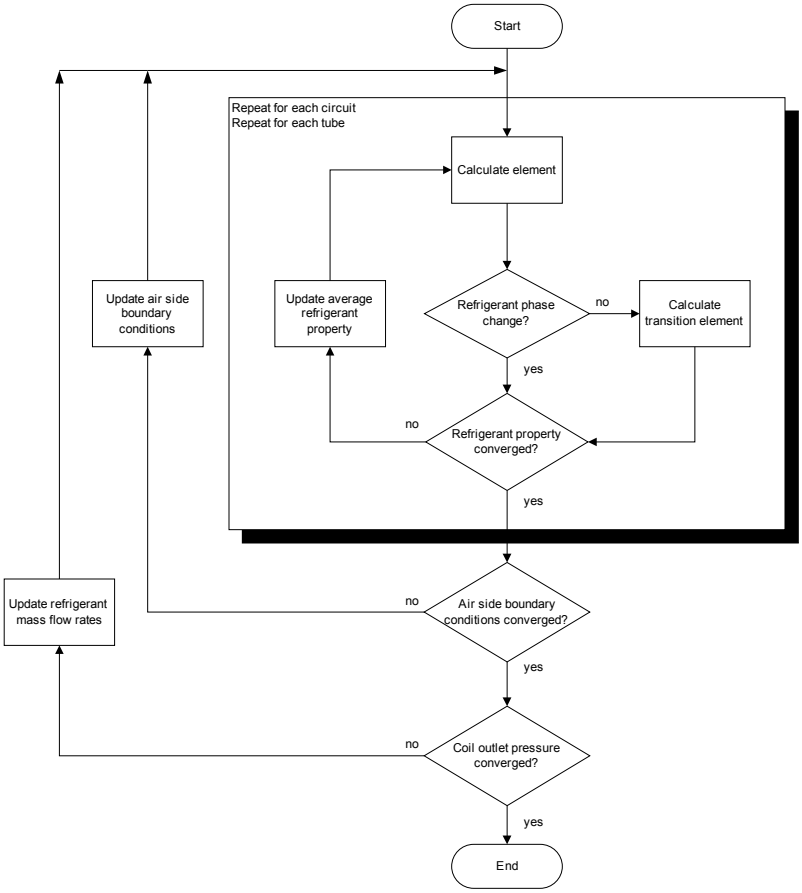

Figure 3.7 Algorithm for heat exchanger model.

3.5. System Charge

System charge is one of the boundary conditions in the system simulation. It is the total of the refrigerant inventories in all heat pump components. For single-phase refrigerant, the refrigerant inventory is calculated by:

$$M = \rho_{ref} \cdot V \tag{3.159}$$

For two-phase refrigerant, it is related to the void fraction as given by:

$$M = \left[\alpha \rho_{vap} + (1-\alpha) \rho_{liq} \right] V \tag{3.160}$$

where the void fraction is the volume fraction that is occupied by vapor refrigerant. Using the Graham *et al.* (1998) correlation, the void fraction is:

$$\alpha = 1 - \exp[-1 - 0.3 \cdot \ln Ft - 0.0328 \cdot (\ln Ft)^2] \quad \text{if} \quad Ft > 0.01031$$
$$\alpha = 0 \quad \text{if} \quad Ft \le 0.01031 \tag{3.161}$$

where Ft is the Froude rate and is defined as:

$$Ft = \left[\frac{x_{ref}^3 G_{ref}^2}{\rho_{vap}^2 \cdot g \, D_{in} (1 - x_{ref})} \right]^{1/2} \tag{3.162}$$

3.6. Interconnecting Pipes

The system components are connected to each other by interconnecting pipes. Both heat transfer and pressure drop across the piping are taken into account in the system simulation. The piping calculations are treated as part of the heat exchanger calculation, however heat transfer or temperature change across the pipes is a user input. Pressure drop across the pipes is calculated in the same way as the heat exchanger element, where pressure drop due to friction, acceleration, and gravitation changes are calculated.

3.7. Filter Drier

The filter drier collects and holds excess water in the refrigeration system (ARI 2004). The use of a filter drier introduces an extra refrigerant pressure drop. This pressure drop is assumed proportional to the refrigerant mass flow rate and is correlated

to the catalog data as shown below:

$$\Delta P_{filter} = \frac{\Delta P_{rated}}{\dot{Q}_{flow,rated}\Psi_{flow}} \dot{m}_{ref} \tag{3.163}$$

where the rated pressure drop ΔP_{rated}, and flow capacity $\dot{Q}_{flow,rated}$ are published in the manufacturer's catalog, and the "flow rate per ton" Ψ_{flow} is constant according to the ARI standard 710 (2004). Table 3.4 shows the Ψ_{flow} values for typical refrigerants.

Table 3.4 Flow rate per ton for different refrigerants (ARI 2004).

Refrigerant	Ψ_{flow} (kg.s^{-1}.kW^{-1})
R-22	0.0064
R-134A	0.0067
R-407C	0.0064
R-410A	0.0060

3.8. Accumulator

The function of the accumulator is to trap the liquid refrigerant such that only vapor refrigerant can flow into the compressor. A typical accumulator geometry is shown in Figure 3.8. If there is two-phase refrigerant coming into the accumulator, the vapor refrigerant will travel out of the accumulator through the J-tube. While the liquid refrigerant will be trapped at the bottom of the accumulator due to its heavier weight. The two tiny holes on the J-tube are used to drain the liquid phase refrigerant out of the J-tube in case the liquid refrigerant is carried over into to the J-tube by the incoming pressure. This mechanism allows the accumulator to avoid liquid refrigerant going into the compressor. The upper hole on the J-tube is a "backup" hole. It provides a secondary outlet for the liquid refrigerant when the liquid level in the accumulator is higher than the

J-tube outlet. Note that some accumulators only have the lower hole in the J-tube, but the length of the J-tube is longer and its outlet is closer to the top of the accumulator.

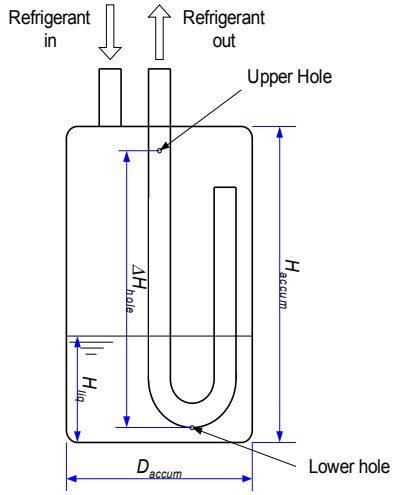

Figure 3.8 Geometry definitions for the accumulator model.

The function of the accumulator is especially important when a heat pump system switches from cooling to heating mode. The sudden change in operation results in refrigerant not fully vaporized through the evaporator. Liquid refrigerant is trapped in the accumulator during the operation change. However, if the system is properly charged, the liquid refrigerant in the accumulator will be eventually evaporated when the system operation becomes steady. The evaporated refrigerant migrates to the condenser outlet and becomes subcooled refrigerant because of conservation of mass (Knight 2005).

However, if the system is over charged, it is possible that there is two-phase refrigerant in the accumulator even at steady state conditions. This is not desirable because it can damage the compressor in the long term. The amount of refrigerant in the accumulator is also taken into account in the system charge calculation. It is calculated according to the liquid level in the accumulator (Domanski and Didion 1983). This model is based on the accumulator geometry as shown in Figure 3.8. If the accumulator

outlet is superheated vapor, there is only vapor in the accumulator, and the refrigerant mass is:

$$M_{accum} = V_{accum}\rho_{vap} \tag{3.164}$$

If there is liquid refrigerant in the accumulator, the liquid height in the accumulator is used to calculate the refrigerant inventory. It is calculated by:

$$M_{accum} = A_{accum}\left[H_{liq}\rho_{liq} + (H_{accum} - H_{liq})\rho_{vap}\right] \tag{3.165}$$

On the right hand side of the equation, the first part is the mass of liquid refrigerant, and the second part is the mass of vapor refrigerant. The liquid height is determined according to the pressure balance in the accumulator. If the accumulator only has the lower hole, the liquid height is:

$$H_{liq} = \frac{\left(P_{hole} - P_{tube}\right)}{\rho_{liq} g} \tag{3.166}$$

where:

$$P_{hole} = \frac{1}{2\rho_{liq}}\left(\frac{\dot{m}_{liq}}{A_{hole}}\right)^2 \tag{3.167}$$

$$P_{tube} = \frac{1}{2\rho_{vap}}\left(\frac{x_{ref}\dot{m}_{ref}}{A_{tube}}\right)^2 \tag{3.168}$$

$$\dot{m}_{liq} = (1 - x_{ref})\dot{m}_{ref} \tag{3.169}$$

It is assumed the lower hole is very close to the bottom of the accumulator, so the liquid height in the accumulator is the same as the liquid height above the lower hole, i.e. $H_{liq} = H_{liq,low}$. Note that if the accumulator has the upper hole but the calculated liquid height is less than the hole distance, ΔH_{hole} , these equations are still valid.

However, if the calculated liquid height is higher than the upper hole, a mass balance across both holes and the tube is used to determine the actual liquid height in the accumulator:

$$\dot{m}_{liq} = \dot{m}_{hole,low} + \dot{m}_{hole,up} \tag{3.170}$$

where:

$$\dot{m}_{hole,low} = A_{hole,low}\sqrt{2\rho_{liq}P_{hole,low}} \tag{3.171}$$

$$\dot{m}_{hole,up} = A_{hole,up}\sqrt{2\rho_{liq}P_{hole,up}} \tag{3.172}$$

The hole pressures are calculated from pressure balance:

$$P_{hole,low} = \rho_{liq} g H_{liq,low} + P_{tube} \tag{3.173}$$

$$P_{hole,up} = \rho_{liq} g H_{liq,up} + P_{tube} \tag{3.174}$$

where the liquid height above the upper hole is:

$$H_{liq,up} = H_{liq,low} - \Delta H_{hole} \tag{3.175}$$

In addition to trapping liquid refrigerant, the accumulator also introduces a refrigerant pressure drop. The pressure drop is calculated based on the manufacturer's catalog data. Assuming the pressure drop is proportional to the mass flow rate, which is in turn proportional to the system capacity, it is calculated by:

$$\Delta P_{accum} = \frac{\dot{Q}_{rated}}{\dot{Q}_{max}} \Delta P_{rated} \tag{3.176}$$

where $\dot{Q}_{rated}$ is the compressor rated capacity. $\dot{Q}_{max}$ is the maximum rated capacity of the accumulator which is correlated to the catalog data as follows:

$$\dot{Q}_{max} = h_1 T_{sat,evp} + h_2 \tag{3.177}$$

Note that some manufacturers publish accumulator data based on the change in saturation temperature instead of pressure. This is converted to a pressure change in the pressure drop calculation.

3.9. Refrigerant Properties

The REFPROP Fortran routines (McLinden *et al.* 1998) were initially considered for the refrigerant property calculations. However, as discussed in the section 2.3 these Fortran routines are impractical when a large number of refrigerant property calculations are required. The EnergyPlus (Crawley *et al.* 1998) table look-up method is used in this heat pump simulation program because it is more computationally efficient. Its table format is divided into three sections according to the refrigerant state: superheated, saturated, and subcooled. In the single phase sections (superheated and subcooled), since the refrigerant properties do not change dramatically, a 4 K (7.2 R) temperature increment is used to generate the table entries, while a more refined 2 K (3.6 R) increment is used for the saturation properties.

The refrigerant database REFPROP 6.0 (McLinden *et al.* 1998) is used to generate the refrigerant property tables. REFPROP, which is maintained by the National Institute of Standards and Technology (NIST), includes properties for both natural and pure refrigerants. It also includes some common refrigerant mixtures and allows users to define their own refrigerant mixtures. The refrigerant tables currently available in this heat pump simulation program are propane, R-22, R-134A, R410A, and R407C.

Due to the temperature glide characteristic of refrigerant mixtures, at a given saturation temperature, the liquid and vapor saturation pressures are different. The

format of the refrigerant tables are designed to accommodate both pure refrigerant and refrigerant mixtures. Both the liquid and vapor saturation pressures are stored in the tables. For pure refrigerants, both saturation pressures are the same at a given saturation temperature. The utility program from Tang (2005) can be used to generate new refrigerant tables from the REFPROP database.

3.10. Refrigerant-Oil Mixture

The amount of oil circulating in the heat pump systems alters the refrigerant properties. These refrigerant-oil mixture properties are calculated using the models recommended by Shen and Groll (2005). The absolute oil mass fraction circulating in the system can be best defined at the liquid line (Cremaschi 2004):

$$\omega_{absolute} = \frac{\dot{m}_{oil}}{\dot{m}_{ref} + \dot{m}_{oil}} \tag{3.178}$$

It is usually less than 1% for heat pump applications (Copeland 2006, Bristol 2006, Cremaschi 2006). The local oil mass fraction in the heat exchangers are defined as:

$$\omega_{local} = \frac{\omega_{absolute}}{1 - x_{mix}} \tag{3.179}$$

where x_{mix} is the quality of the refrigerant-oil mixture. The local oil mass fraction is the key parameter to determine the refrigerant-oil properties as shown in the following equations.

Specific heat: Jensen and Jackman (1984) present the following weighting method to calculate the specific heat based on the local oil mass fraction:

$$c_{p,mix} = \omega_{local} c_{p,oil} + (1 - \omega_{local}) c_{p,liq} \tag{3.180}$$

where the oil specific heat is calculated as:

$$c_{p,oil} = \frac{4.186 \cdot [0.388 + 0.00045(1.8\,T_{ref} + 32)]}{\sqrt{\rho_{oil}/\rho_w}} \tag{3.181}$$

The density of water in the above equation is evaluated at a reference temperature of 15.6 °C.

Density: From Baustian *et al.* (1986), the refrigerant-oil mixture density is calculated by:

$$\rho_{mix} = \left[\frac{w_{local}}{\rho_{oil}} + \frac{1 - w_{local}}{\rho_{liq}} \right]^{-1} \tag{3.182}$$

Dynamic viscosity: From Yokozeki (1992), the dynamic viscosity is:

$$\mu_{mix} = \exp\left(F_{liq} \cdot \ln \mu_{liq} + F_{oil} \cdot \ln \mu_{oil} \right) \tag{3.183}$$

where the weighting factor is defined as:

$$F_{oil} = \frac{W_{oil}^{0.58} \Psi_{oil}}{W_{oil}^{0.58} \Psi_{oil} + W_{liq}^{0.58} \Psi_{liq}} \tag{3.184}$$

$$F_{liq} = 1 - F_{oil} \tag{3.185}$$

The mole fractions are calculated as:

$$\Psi_{oil} = \frac{\omega_{local} \left(\frac{W_{ref}}{W_{oil}} \right)}{1 - \omega_{local} + \omega_{local} \left(\frac{W_{ref}}{W_{oil}} \right)} \tag{3.186}$$

$$\Psi_{ref} = 1 - \Psi_{oil} \tag{3.187}$$

Surface tension: From Jensen and Jackman (1984), the surface tension is calculated by:

$$\sigma_{mix} = \sigma_{liq} + (\sigma_{oil} - \sigma_{liq}) \sqrt{\omega_{local}} \tag{3.188}$$

Thermal conductivity: Also from Jensen and Jackman (1984), the conductivity is:

$$k_{mix} = k_{liq}(1-\omega_{local}) + k_{oil}\omega_{local} - 0.72(k_{oil}-k_{liq})(1-\omega_{local})\omega_{local} \quad (3.189)$$

The oil properties in the above equations can be obtained from the ASHRAE handbook-Refrigeration (2006), compressor manufacturers, or oil suppliers.

3.11. System Simulation Algorithms

The simulation algorithms are designed to meet the needs of heat pump design engineers. Three simulation algorithms have been implemented: "Orifice and TXV Design", "Fixed Orifice Simulation", and "TXV Simulation". All of these algorithms converge on the mass, momentum, and energy conservation equations under specified boundary conditions.

3.11.1. Orifice and TXV Design

This algorithm is used for system design. For given air side boundary conditions, system subcooling, and superheat, it calculates the size of the expansion device (orifice diameter and TXV rated capacity), and system charge. The compressor model coefficients, and the indoor and outdoor coil geometries are required to start the calculation. Figure 3.9 shows the simulation algorithm for the "Orifice and TXV Design" calculation.

Initial guesses for this calculation are the saturation temperatures at the compressor suction and discharge. The algorithm iterates on the saturated discharge temperature on the high pressure side to converge on the specified subcooling. It is considered converged when the subcooling difference is within ±0.006 K (±0.01 R), or the saturated temperature varies within ±0.006 °C (±0.01 °F), whichever comes first in

the iteration. For the low pressure side iteration, the saturated suction temperature is adjusted to converge on the specified superheat. The convergence criterion is similar to the high pressure side iteration. If the superheat difference is within ±0.006 K (±0.01 R) or the change of saturated temperature is within ±0.006 °C (±0.01 °F), the calculation is converged. Once both iterations are converged, the size of the expansion device and system charge are calculated based on the simulated system performance and the overall design calculation is complete.

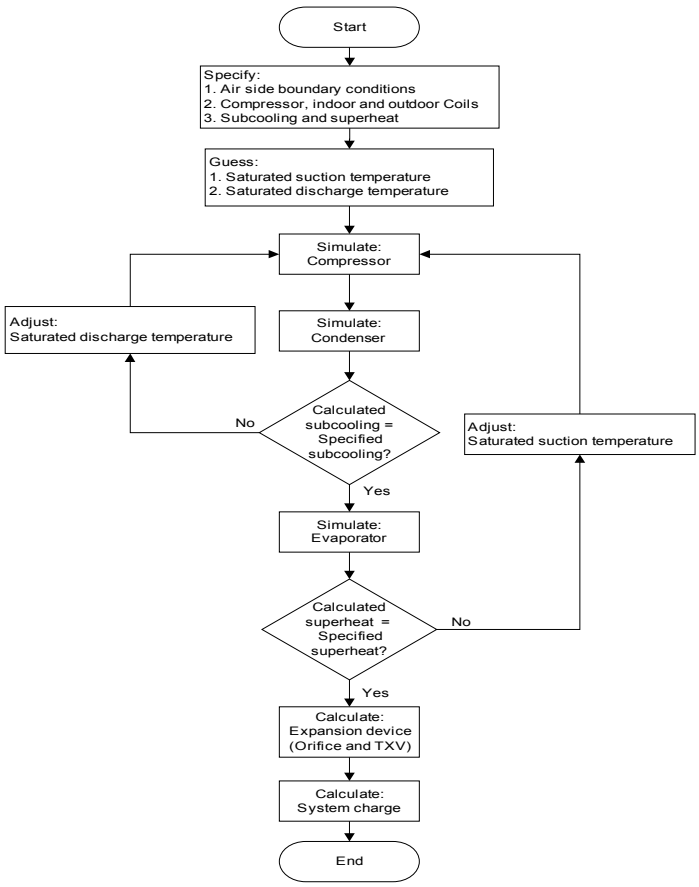

Figure 3.9 Simulation algorithm for Orifice and TXV Design.

3.11.2. Fixed Orifice Simulation

This algorithm is used for simulating a system with a short tube orifice expansion device. The air side conditions and system charge are specified boundary conditions. Compressor, indoor and outdoor coils, and orifice size are required inputs. Figure 3.10 shows the simulation algorithm for the fixed orifice simulation.

In addition to the compressor suction and discharge saturation temperatures, the system superheat is also an initial guess for this calculation. Since the orifice size is specified, the high pressure side iteration matches the refrigerant mass flow rates that are calculated from the compressor and orifice models. The saturated discharge temperature is adjusted in the inner loop. When the saturated temperature varies within ±0.006 °C (±0.01 °F) or the mass flow rate difference is within ±0.005 $kg.hr^{-1}$ (±0.01 $lbm.hr^{-1}$), the iteration is considered converged.

The low pressure side iteration is the same as the "Orifice and TXV Design" calculation, where the saturated suction temperature is adjusted to converge on the superheat. The same convergence criterion applies. However, the superheat is a guessed value in this algorithm. Another iteration loop needed to find the actual superheat based on the specified system charge. The guessed superheat is adjusted until the calculated charge matches the specified charge. The iteration is considered converged when the charge difference is within ±0.005 kg (±0.01 lbm) or the guessed superheat varies within ±0.006 K (±0.01 R). Once the system charge converges, the overall system simulation is finished. This simulation algorithm can be used to study the impact of system charge, and air side conditions on the system performance.

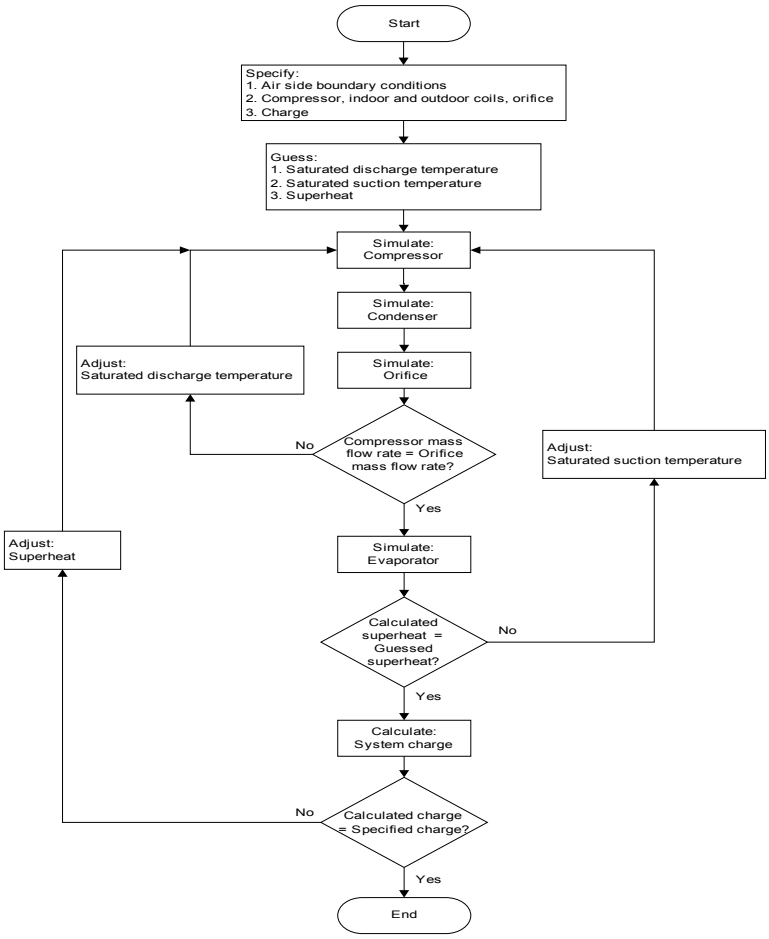

Figure 3.10 Simulation algorithm for fixed orifice simulation.

3.11.3. TXV Simulation

This algorithm is used for simulating a system with a TXV as expansion device. Air side conditions, system charge and TXV superheat setting are specified. Figure 3.11 shows the TXV simulation algorithm. It requires the specification of the compressor, indoor and outdoor coils to start the simulation.

The initial guesses for this simulation are compressor suction and discharge saturation temperatures, and system subcooling. The high and low pressure side iterations are essentially the same as the "Orifice and TXV Design" calculation with the

same convergence criteria.

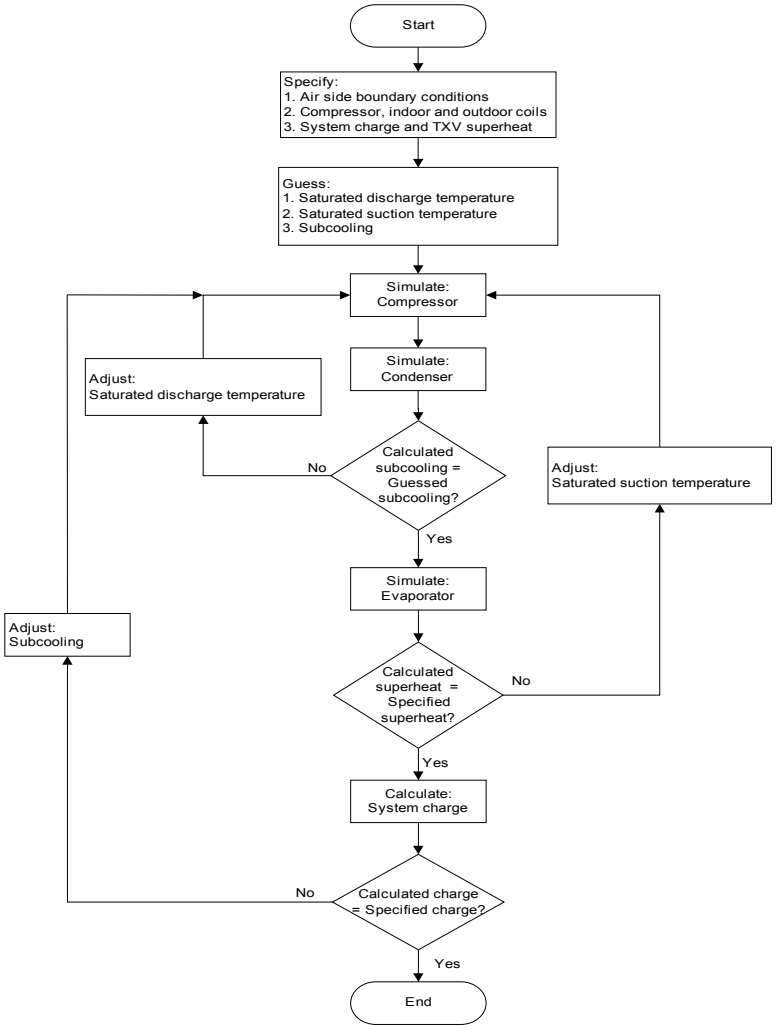

Figure 3.11 Simulation algorithm for TXV simulation.

However, the high pressure side iteration converges by adjusting the guessed subcooling instead of the specified subcooling. Another iteration loop is used to find the actual subcooling based on the specified system charge. The simulation is converged when the calculated charge matches the specified charge within ±0.005 kg (±0.01 lbm) or the subcooling varies within ±0.006 K (±0.01 R). Like the "Fixed Orifice Simulation", this algorithm can be used to study the impact of charge and air side conditions on the system performance.

4. MODEL EVALUATION

The component models and simulation algorithms are implemented in FORTRAN code. It is expected that the code should predict the trend of actual component performance and simulate reasonable system operations. For example, the orifice model should predict a higher refrigerant mass flow rate for a higher upstream refrigerant pressure. The system simulation should predict a lower system capacity for a higher condenser entering air temperature. This section evaluates the implemented component models and simulation algorithms with illustrative examples. The evaluations merely show that the predicted results are consistent with expected trends. Accuracy of the simulation, which requires validation with experimental data, is addressed in Chapter 6.

4.1. Compressor

A Copeland compressor ZP54K3E-PFV is used for the compressor model evaluation. It is a 5-ton (17.5 kW), scroll type compressor and operates with R-410A. During the system simulation, the compressor suction and discharge temperatures are adjusted to find the system performance. The compressor model should react to the changes of the saturation temperatures and predict reasonable compressor performance.

Figure 4.14 shows the predicted mass flow rate for a typical range of saturation temperatures. Note that the entire test was performed for a constant superheat of 11.1 K. The model predicts that the mass flow rate is proportional to the suction saturation

temperature but is inversely proportional to the discharge saturation temperature. For a given discharge saturation temperature, if the suction saturation temperature increases, the refrigerant density becomes higher. As a result, the mass flow rate through the compressor should increase. On the other hand, for a given suction saturation, since the suction refrigerant density is constant, the mass flow rate is affected by the discharge to suction pressure ratio only. The increase of discharge saturation temperature increases the pressure ratio, and thus decreases the mass flow rate. The model is able to predict the mass flow rate consistently with the change of saturation temperatures. In addition, Figure 4.14 shows that the mass flow rate is more sensitive to the change of suction saturation temperature. This characteristic is confirmed with the experimental data presented by Chen *et al.* (2002b).

The predicted power consumption for the same range of saturation temperatures is shown in Figure 4.2. The predicted power consumption increases with the discharge saturation temperature, but decreases with suction saturation temperature. For an increasing discharge to suction pressure ratio, more power input is required. Figure 4.2 shows that the model is able to predict this characteristic. When the difference between the suction and discharge saturation temperatures increases, the pressure ratio increases, and so does the power consumption. Note that the power consumption is more sensitive to the change of discharge saturation temperature. Chen *et al.* (2002b) also showed this trend in their experimental data. If the mass flow rate is relatively constant for the range of discharge saturation temperature, more power input is required to compress the refrigerant to higher pressure.

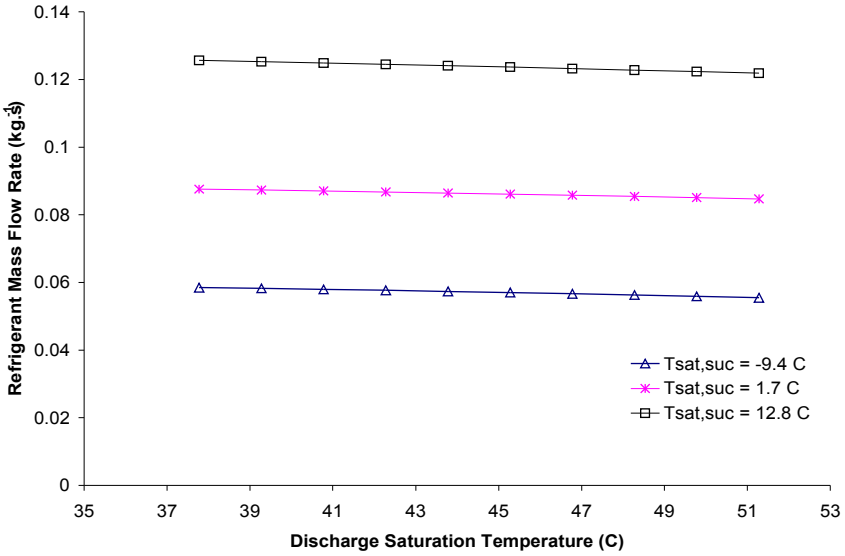

Figure 4.1 Compressor evaluation: Mass flow Rate (Tested at 11.1 K superheat)

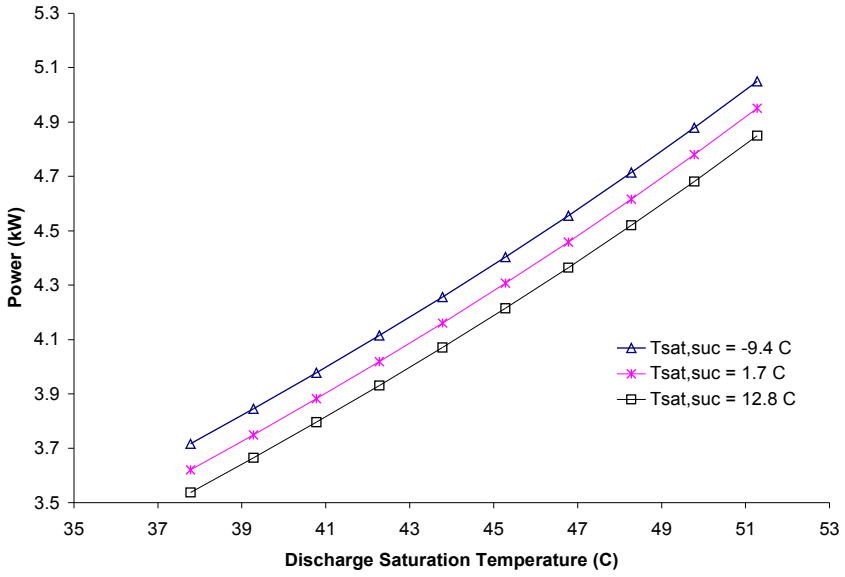

Figure 4.2 Compressor evaluation: Power consumption (Tested at 11.1 K superheat).

4.2. Short Tube Orifice

A short tube orifice with a length of 12.7 mm, and a diameter of 1.9 mm is used to verify the short tube orifice model. Figure 4.3 shows the predicted mass flow rate for a

range of typical refrigerants (R22, R134A, R410A, and R407C). The test is performed at constant entering enthalpy of 255 kJ.kg^{-1}, and 12.8 °C outlet saturation temperature. Note that the slope change in the curves is due to the inlet refrigerant condition changes from two-phase to subcooled condition, a two-phase correction factor is applied to the orifice model for the two-phase inlet conditions. The transition saturation temperature is different for different refrigerants. It is about 44 °C for R22, and 34 °C for R407A, etc. as shown in the figure. For increasing inlet pressure, it is expected that more mass flow is pressed through the orifice. The model is able to predict this trend accordingly for all tested refrigerants.

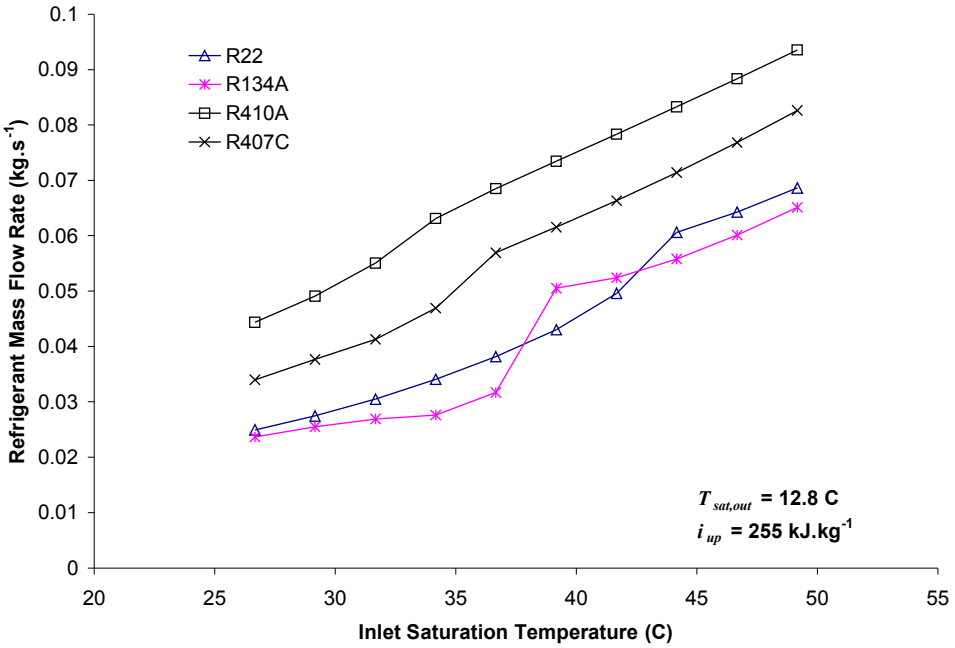

Figure 4.3 Orifice model evaluation: Change of inlet saturation temperature.

Since refrigerant flow through the orifice is nearly choked, the mass flow rate should be relatively independent of the outlet pressure. Payne and O'Neal (2004) did not include the outlet pressure as a correlating parameters in their model. As a result, this

model is totally independent of the outlet pressure.

In the "Orifice and TXV Design" calculation, the orifice diameter is calculated at the end of the algorithm. A larger orifice diameter allows more refrigerant flow through the orifice. This calculation is verified by the example shown in Figure 4.4. Note that the model predicts the trend of mass flow rate consistently for all tested refrigerants. The predicted mass flow rate increases with larger orifice diameter.

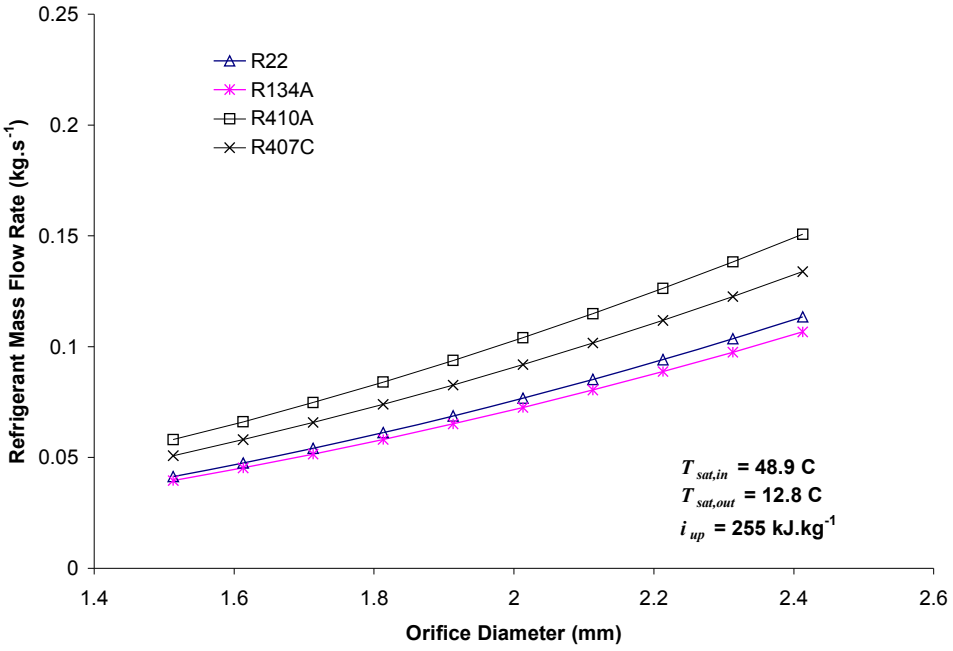

Figure 4.4 Orifice model evaluation: Change of orifice diameter.

Figure 4.4 also shows that the model is able to predict the mass flow rate difference for different refrigerants. For the same orifice diameter, the mass flow rates for the tested refrigerants are different. It is due to the difference in operation pressure. At the same inlet saturation temperature of 48.9 °C, R410A operates at the highest pressure of 2977 kPa, while R134A operates at the lowest pressure of 1282 kPa. As a result, the higher pressure produces more mass flow rate for R410A compared to R134A.

4.3. Condenser

A single-circuit coil shown in Figure 4.5 is used to verify the condenser model performance. The coil tubes are in staggered arrangement and circuited in counter-cross flow pattern. Table 4.1 lists the dimensions of this test coil. The condenser model is tested for a range of saturation temperatures with tube-by-tube discretization.

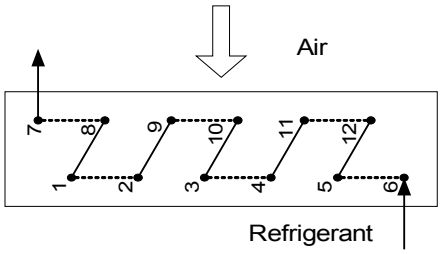

Figure 4.5 Test Coil for heat exchanger model evaluations.

Table 4.1 Test coil geometry.

Coil Width	0.8 m
Coil Height	0.2 m
No. of rows	2
No. of tubes per row	6
Tube OD	10 mm
Tube ID	9.4 mm
Tube Spacing	25.4 mm
Row Spacing	22 mm
Tube Type	Microfin
Fin thickness	0.099 mm
Fin Density	591 fins.m^{-1}
Fin Type	Louver

Figure 4.6 shows the predicted condenser capacity for different refrigerants. Inlet air and refrigerant conditions are fixed as shown in the figure. The predicted capacities are proportional to the saturation temperature because there is more heat transfer in the

two-phase region. As the saturation temperature increases and the refrigerant reaches the subcooled region at the condenser outlet, the change in capacity becomes relatively constant. Figure 4.6 shows that the capacity curves change slope at about 48 °C saturation temperature, where the refrigerant at the condenser outlet is subcooled liquid.

For a specific saturation temperature, Figure 4.6 shows that the capacity varies for different refrigerants. This is due to the difference in saturation region as shown in Figure 4.7. The R410A capacity is higher than other refrigerants at low saturation temperatures because R410A has the widest saturation region, and thus has more two-phase refrigerant in the condenser.

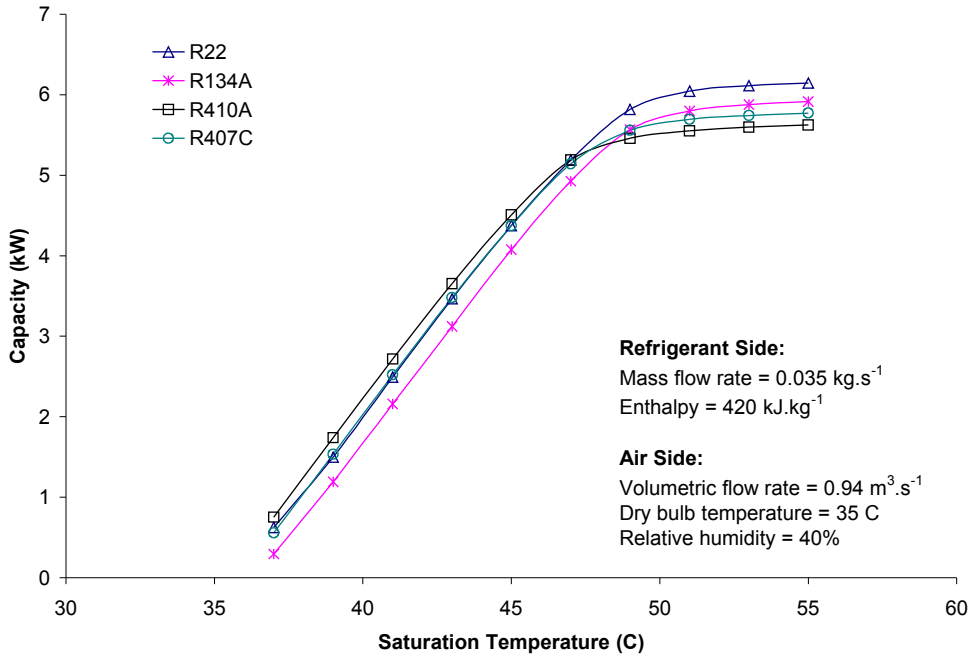

Figure 4.6 Condenser model evaluation: Capacity.

As the saturation temperature increases, the refrigerant in the condenser covers more of the saturation region and results in more heat transfer. But once the saturation temperature reaches the subcooled outlet temperature, the capacity does not change

significantly. The saturation region of R134A is the smallest, therefore its capacity increases the most rapidly with increasing saturation temperature.

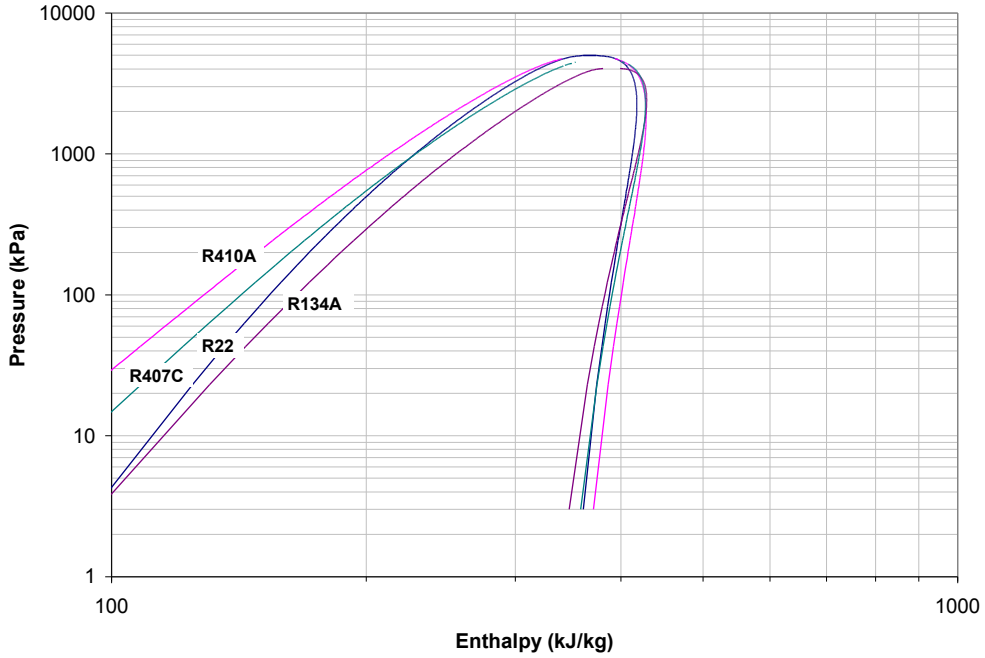

Figure 4.7 Pressure-Enthalpy diagram for different refrigerants.

In system simulation, i.e. the "Fixed Orifice Simulation" and the "TXV Simulation", the system charge is a boundary condition. Since most of the refrigerant resides in the heat exchangers, the charge calculation is important and is evaluated with the same test coil and test conditions. Figure 4.8 shows the change of refrigerant inventory in the condenser due to a change of saturation temperature. Since the condenser capacity increases with saturation temperature, more refrigerant is condensed into the liquid phase and more refrigerant is in the condenser. Note that when there is a subcooled liquid in the condenser, the mass inventory increases more rapidly because of higher refrigerant density.

The compressor, condenser, and short tube orifice evaluations have shown that

the models are able to reflect the change of boundary conditions consistently and conform to the theoretical trends. Higher saturation temperature decreases the compressor mass flow rate, but increases the orifice mass flow rate, condenser capacity, and outlet subcooling. These relationships are useful for adjusting the saturation temperature at the high pressure side iteration of system simulation.

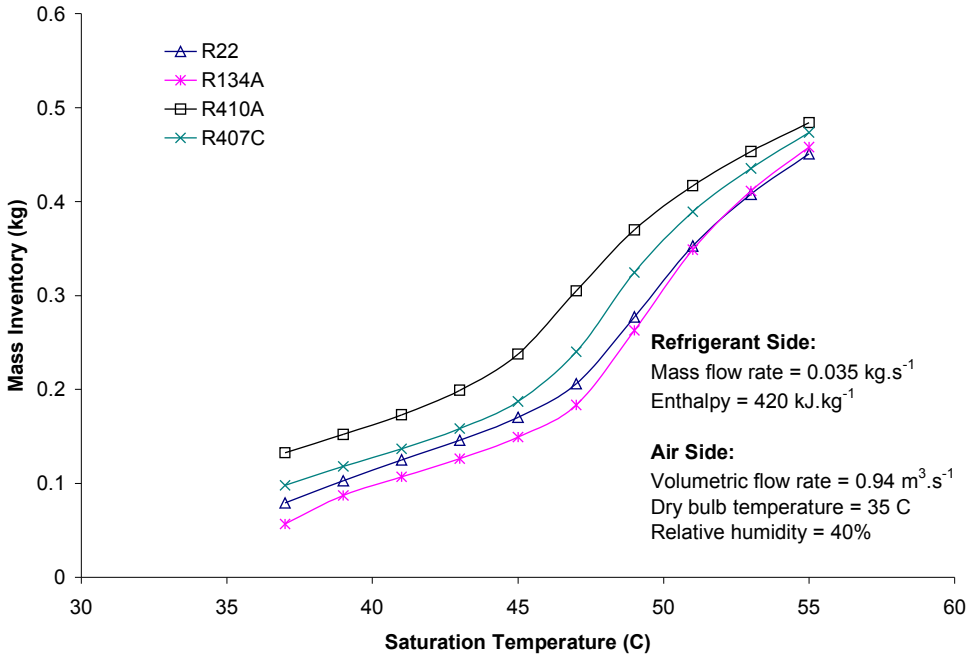

Figure 4.8 Condenser model evaluation: Mass inventory.

4.4. Evaporator

The evaporator model is the major component at the low pressure side iteration. It is tested with the same coil as shown in Figure 4.5. However, boundary conditions are changed to typical evaporator operating conditions in this test. The same tube-by-tube discretization is used to run the evaporator model. Figure 4.9 shows the predicted evaporator capacity for a range of saturation temperatures. The inlet conditions for this

test are fixed as shown in the figure. As the saturation temperature increases, there is less vaporized refrigerant in the evaporator, and the capacity decreases. Figure 4.9 shows when there is no superheated refrigerant in the evaporator (at about 11 °C), the capacity begins to fall more noticeably because the two-phase heat transfer is higher than the single phase heat transfer.

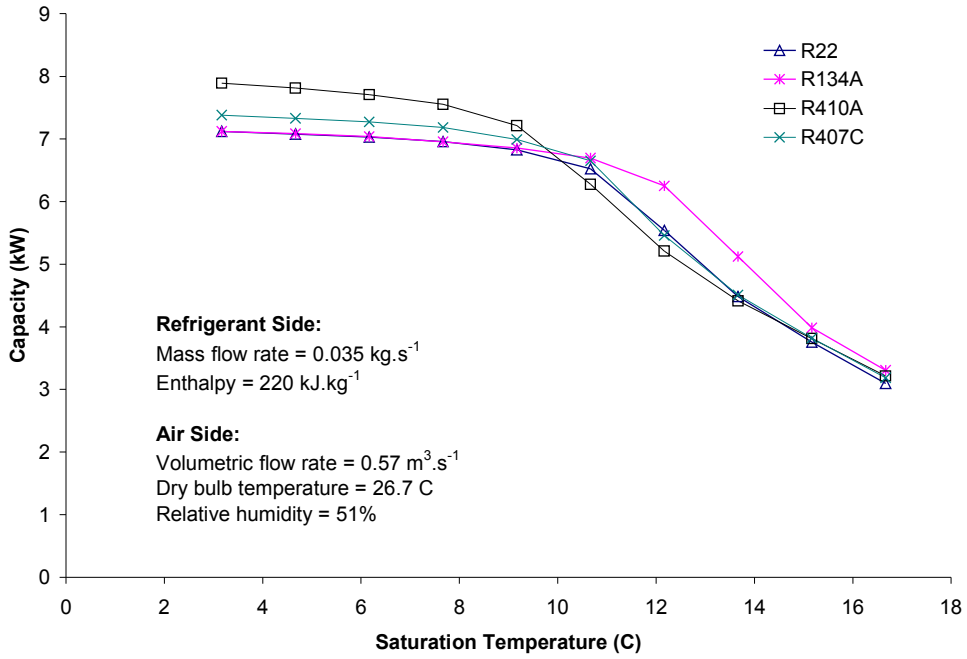

Figure 4.9 Evaporator model evaluation: Capacity.

The capacity for different refrigerants is also compared in Figure 4.9. R410A has the highest capacity for low saturation temperatures because it has the widest saturation region as shown in the pressure-enthalpy diagram (Figure 4.7). As the saturation temperature increases, the R134A capacity becomes the highest because it has the smallest saturation region where more refrigerant can take the advantage of two-phase heat transfer.

The evaporator refrigerant inventory, shown in Figure 4.10, increases with

saturation temperature. Since higher saturation temperature results in less capacity, more liquid refrigerant is in the evaporator, and the mass of refrigerant increases.

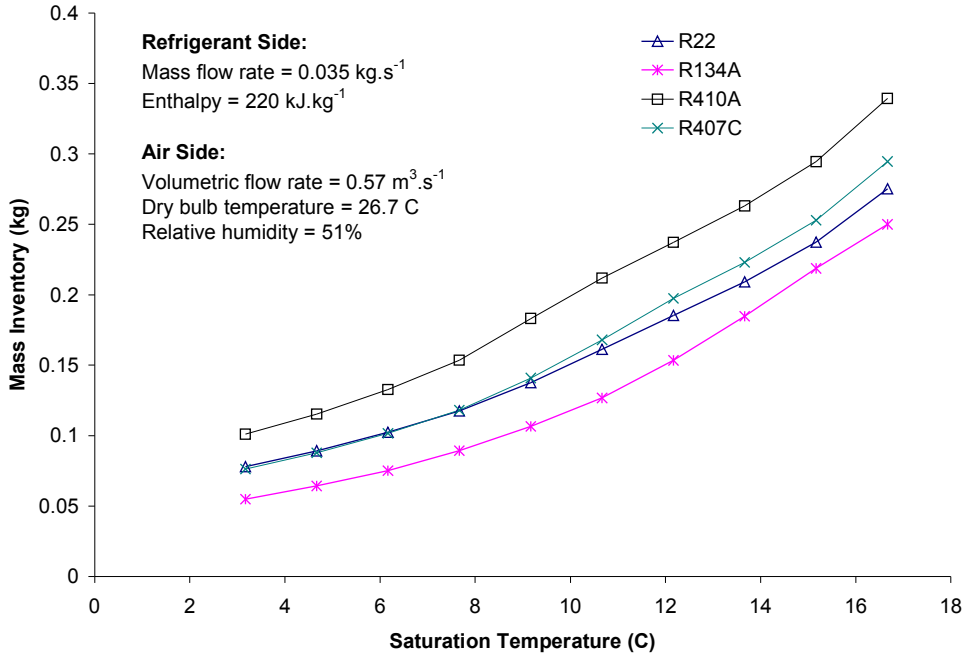

Figure 4.10 Evaporator model evaluation: Mass Inventory.

In the low pressure side calculation, the saturation temperature is adjusted to find the desired superheat. Since the saturation temperature is inversely proportional to the capacity, and higher evaporator capacity means more superheat at the evaporator outlet; these relationships are useful for adjusting the saturation temperature in the low pressure side iteration of system simulation. Once both high and low pressure sides are converged, it is also easy to find the desired superheat because the mass inventory is inversely proportional to the superheat.

4.5. Circuiting

The circuiting algorithm is evaluated for the sample coils shown in Figure 4.11.

All coils have the same geometry but different circuitries. The coil dimensions are shown in Table 4.2. Circuit 1 is a simple circuit with only one branch. Circuit 2 is a split circuit where the refrigerant comes in from branch 1 and splits to branches 2 and 3 at tube 4. Circuit 3 is a joined circuit where the refrigerant comes in from branches 1 and 2 and joins to branch 3 at tube 10. The last circuit is a rather complicated circuit where the refrigerant comes in from branch 1, splits to branches 2, 3, and 4 at tube 8. The portion of refrigerant in branch 4 goes to the coil outlet directly. Another portion goes to branches 2 and 3 and joins to branch 5 at tube 18. It should be noted that existing circuiting algorithms are unable to model this split-joined circuitry.

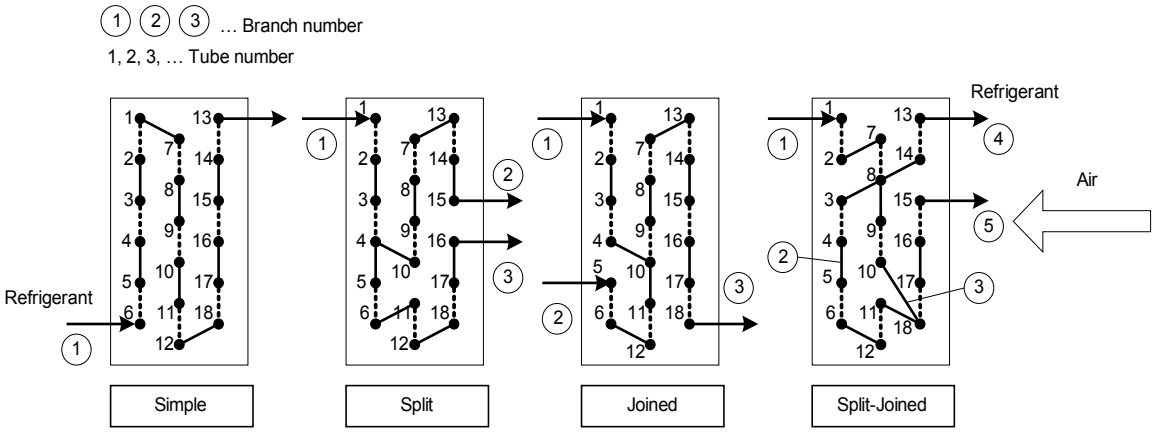

Figure 4.11 Sample circuits for circuiting model evaluations.

The circuits are tested for condenser coils with R22 as the refrigerant. Figure 4.12 shows the predicted coil capacity subject to a change of refrigerant mass flow rate. Other boundary conditions are fixed for the test as shown in the figure. Note that the capacity increases for low refrigerant mass flow rate. As the mass flow rate increases, some of the capacities starts to fall. For example, the simple circuit capacity starts to fall at about 0.04 $kg.s^{-1}$ mass flow rate. This is because the high mass flow rate drives the refrigerant temperature to the air temperature before the refrigerant reaches the coil outlet, the rest of

the coil does not have heat transfer potential but the refrigerant pressure continues to drop which results in a capacity drop.

Table 4.2 Test coil geometry for circuiting algorithm evaluations.

Coil Width	0.8 m
Coil Height	0.2 m
No. of rows	3
No. of tubes per row	6
Tube OD	10 mm
Tube ID	9.4 mm
Tube Spacing	25.4 mm
Row Spacing	22 mm
Tube Type	Microfin
Fin thickness	0.099 mm
Fin Density	591 fins.m^{-1}
Fin Type	Louver

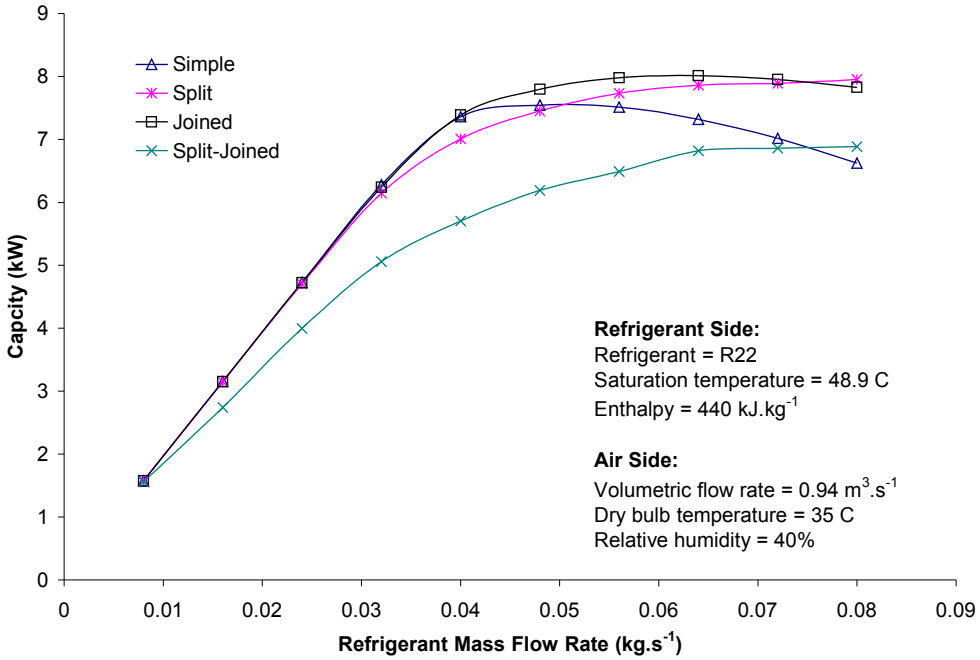

Figure 4.12 Circuiting model evaluation: Capacity.

Figure 4.13 shows the coil pressure drop for each circuit for the same range of

refrigerant mass flow rate. Note that the earlier the coil loses the heat exchange potential, the more liquid refrigerant is in coil and pressure drop starts to rise dramatically. Maximizing capacity and minimizing pressure drop is always a challenge in circuit design. Although for the range of mass flow rate shown, the Split circuit stands out because it has decent capacity but relatively low pressure drop, this conclusion draws from the specific boundary conditions and coil dimensions, and cannot be generalized.

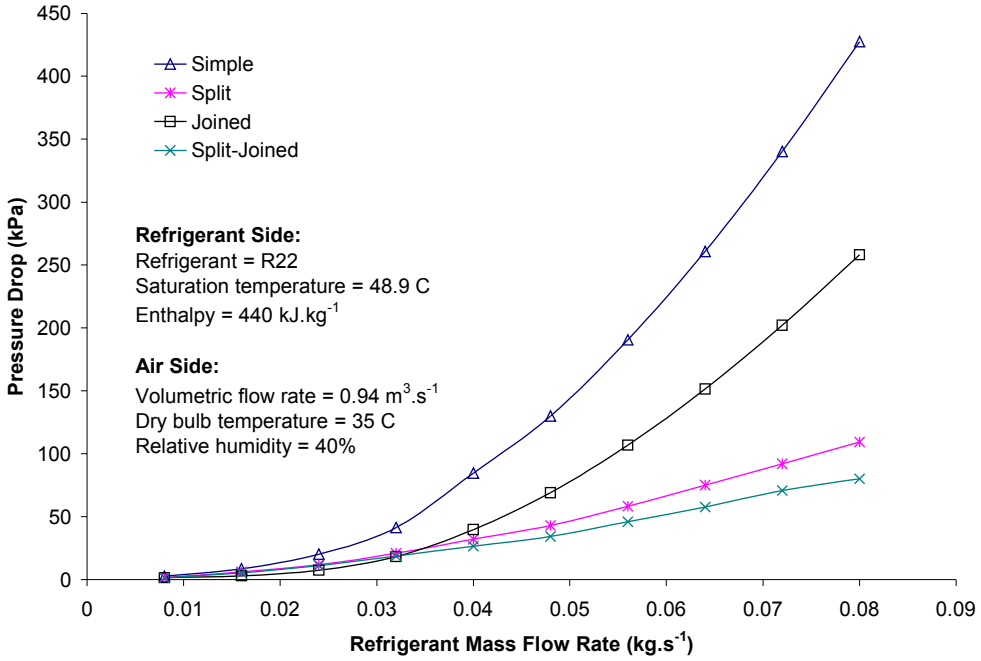

Figure 4.13 Circuiting model evaluation: Pressure drop.

The advantage and major ability of the circuiting model are to analyze the refrigerant distribution in the circuit branches. Knowing the local refrigerant mass flow rate in each branch is beneficial in calculating local heat transfer and pressure drop. Figure 4.14 shows the refrigerant distribution for the test coils when the refrigerant mass flow rate is 0.032 $kg.s^{-1}$. For the simple circuit, 100% of the refrigerant flows through the branch. The Split circuit distributes almost the same amount of refrigerant to branches 2 and 3.

Note that since branches 2 and 3 are connected to the same header at the coil outlet, their pressure drops are the same. The slight difference in refrigerant distribution is due to the difference in heat transfer. Branch 2 is longer; it has more heat transfer potential and results in more liquid refrigerant. Refrigerant prefers going to branch 3 because it has less flow resistance. The Joined circuit has an equal amount of refrigerant coming from branches 1 and 2. Both branches have the same pressure drop because they are connected to the same junctions, i.e. the coil inlet and tube 10.

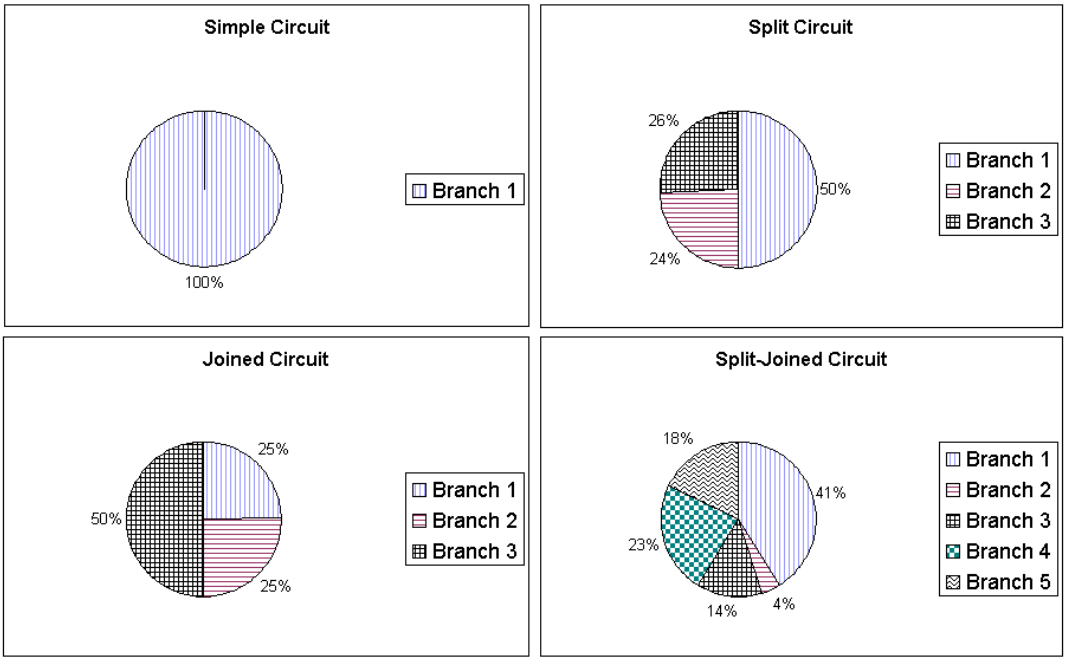

Figure 4.14 Circuiting model evaluation: Refrigerant distribution (mass flow rate = 0.032 kg.s^{-1}).

Although there is a difference in heat transfer, it does not constitute more than 1% of the mass flow rate. The Split-Joined circuit has the most complicated flow distribution. Since the refrigerant always prefers the low resistance path, most of refrigerant stays in branch 1 because there is no liquid refrigerant in it. The refrigerant flow is relatively "choked", which is harmful to the capacity. As shown in Figure 4.12, the Split-Joined circuit has the lowest capacity compared to other circuits. Branches 2 and 3 are both

connected to the same junctions (i.e. tubes 8 and 18). Since branch 2 is a longer path with a higher flow resistance, more refrigerant goes to branch 3. Only a small portion of refrigerant goes to branch 2. The refrigerant leaves the coil from branches 4 and 5. Since branch 4 has a lower resistance, it has higher flow rate.

This example shows that the circuiting algorithm is able to model different kinds of circuitry and predict reasonable results. Because the coil circuiting has a significant effect on coil capacity and pressure drop, the circuiting algorithm supports an important aspect of the system design, which might otherwise be ignored.

4.6. System Simulation

In this section, the system simulation is evaluated for a 4-ton (14.1 kW) air conditioner with a scroll compressor and a short tube orifice. R22 is the refrigerant in this system. The heat exchangers are a 2-row evaporator and a 1-row condenser. They are circuited as shown in Figure 4.15. Detailed configurations and dimensions of this system are shown in Table 4.3. In order to evaluate the system performance for a range of air side boundary conditions, the "Fixed Orifice Simulation" option is used to simulate the system. Tube-by-tube discretization is used in both heat exchanger models. Four air side parameters (i.e. indoor dry bulb temperature, wet bulb temperature, flow rate, and outdoor dry bulb temperature) are changed one at a time from the baseline boundary conditions shown below:

- Indoor air flow rate = 0.6 $m^3.s^{-1}$
- Indoor dry bulb temperature = 27 °C
- Indoor wet bulb temperature = 19 °C

- Outdoor air flow rate = 1.2 $m^3.s^{-1}$
- Outdoor dry bulb temperature = 35 °C

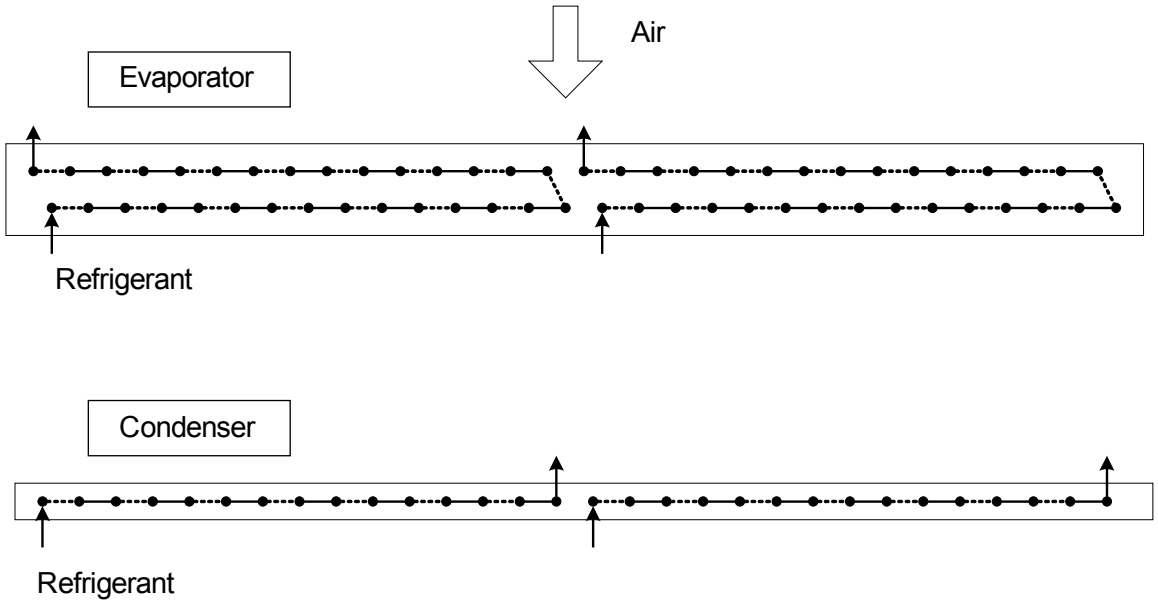

Figure 4.15 Coil circuitry for the sample system.

Table 4.3 Sample system for the evaluations of system simulation.

Compressor		**Expansion Device**			**Condenser**	**Evaporator**
Type	Scroll	**Type**	Short tube orifice	**Coil Width**	1.2 m	0.6 m
				Coil Height	0.95 m	0.95 m
				No. of rows	1	2
Part no.	ZR48K3-PFV	**Short tube length**	12.7 mm	**No. of tubes per row**	30	30
				Tube OD	13.2 mm	
				Tube ID	13.2 mm	
Refrigerant	R22	**Short tube chamfer depth**	zero	**Tube Spacing**	31.6 mm	
				Row Spacing	27.5 mm	
				Tube Type	Smooth	
Charge	3.2 kg	**Orifice diameter**	2.2 mm	**Fin thickness**	0.15 mm	
				Fin Density	571 fins.m^{-1}	
				Fin Type	Smooth	

The simulated system capacity for this condition is 12.5 kW. Figure 4.16 shows the

system capacity subject to different air side parameters. The intersection of the curves represent the baseline condition. Note that the figure shows the fractional change of capacity versus fractional change of air side parameters. The range of air side parameters is selected from the manufacturer's catalog data. The purpose of the fractional presentation is two-fold. It not only shows the relationship between the system capacity and air side parameters, but it also shows the sensitivity of each air side parameters to the system capacity.

Figure 4.16 shows that the system capacity is proportional to the indoor dry bulb and wet bulb temperatures, and the air flow rate, but decreases with increasing outdoor dry bulb temperature. Increasing the indoor dry bulb and wet bulb temperatures increases the heat transfer potential of the evaporator; on the other hand, increasing the indoor air flow rate increases the heat transfer rate at the evaporator. All of these changes enhance the system capacity. When the outdoor dry bulb temperature increases, the heat transfer potential at the condenser is reduced because the air temperature is closer to the refrigerant temperature. The decrease in condenser capacity results in higher entering refrigerant temperatures on the low pressure side, which in turn reduces the heat transfer potential at the evaporator. As a result, the system capacity decreases. The simulation is able to predict all of these air side effects rationally.

On the other hand, the simulation predicts that the system capacity is most sensitive to the indoor wet bulb and outdoor dry bulb temperatures. The indoor air flow rate has a moderate impact. The sensitivity is verified by the catalog data for a York 4-ton heat pump, BHH048 that has the same rating capacity as the simulated system. Figure 4.17 shows the system performance from catalog data that are presented in the

same fashion as shown in Figure 4.16. Note that the catalog data indicates that the system capacity does not change with indoor dry bulb temperature and therefore it is not plotted in the figure. This may be because the system capacity is relatively constant for the range of indoor dry bulb temperatures in this data set.

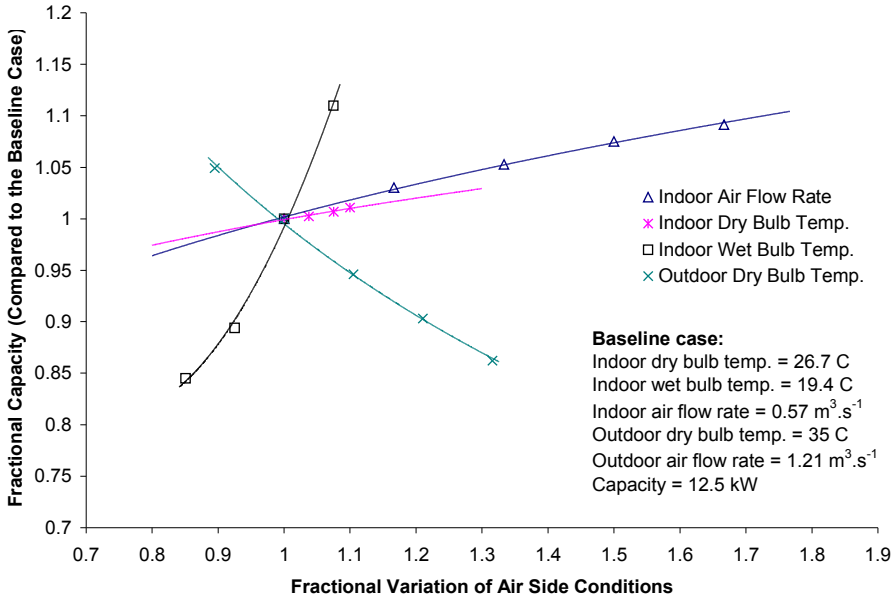

Figure 4.16 Evaluation of system simulation: Capacity.

The catalog data (Figure 4.17) show that the system capacity is sensitive to the change of indoor wet bulb and outdoor dry bulb temperatures. These trends agree with the predicted simulation results shown in Figure 4.16. The catalog system capacity becomes insensitive to the indoor wet bulb temperature when the temperature decreases to about 85% of the baseline value. This is due to the coil surface becomes dry when there is less moisture content in the entering air. The simulation results (Figure 4.16) predict a similar trend but do not have the same abrupt change as the catalog data (Figure 4.17). Since heat pump manufacturers do not run all the test points in the catalog, interpolation and extrapolation are usually used to generate the entire table based on

some rating test points (Knight 2005), the nearly dry coil test point may be a result of approximation.

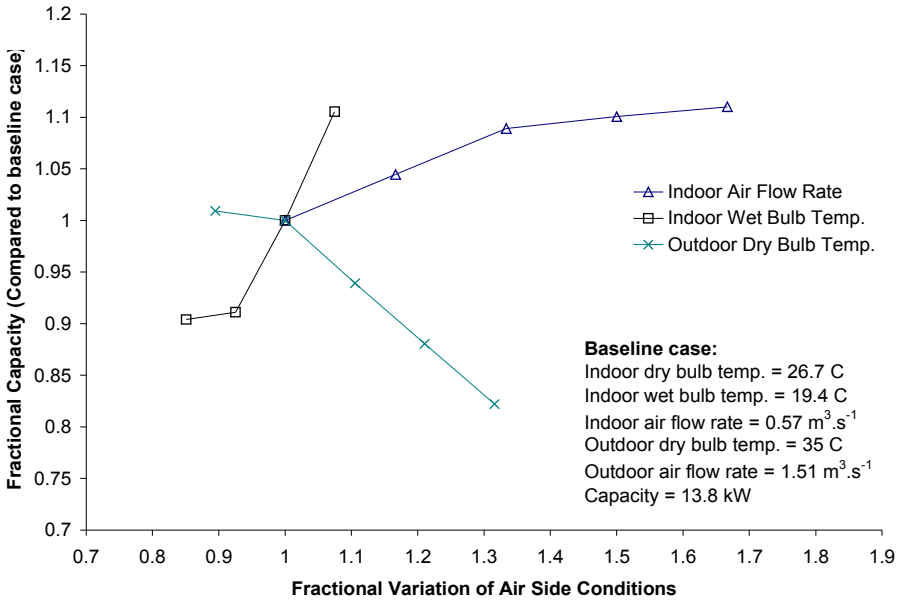

Figure 4.17 Catalog data for the York heat pump BHH048.

4.7. System Simulation with Row-by-Row Heat Transfer Coefficient

It is known that the air side heat transfer coefficient varies from row to row in heat exchangers. Published heat transfer coefficients are usually for the entire coil. The overall heat transfer coefficient was used to obtain the simulation results shown in the above sections. However, Rich (1975) previously published the row-by-row heat transfer coefficients that are applicable to the coil geometry shown in Table 4.3. To estimate the impact of row-by-row coefficients, the system capacity using the row-by-row coefficient is compared to the capacity using the overall coefficient. Since the row-by-row heat transfer coefficient is a strong function of air flow rate, the comparison is shown for a

typical range of air flow rates, which is equivalent to:

$$1300 < Re_{Pr} < 3000$$

Figure 4.18 compares the simulated system capacities. Note that the overall coefficient predicts lower system capacity compared to the row-by-row coefficient.

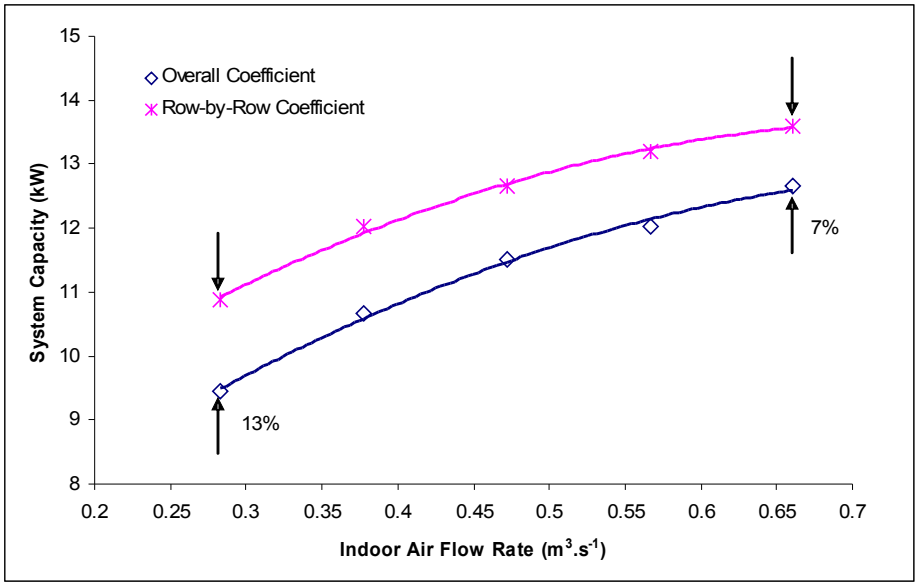

Figure 4.18 Comparison of row-by-row and overall flat fin heat transfer coefficients.

The row effect is more significant at low Reynolds number. As the air flow rate increases, the difference in capacity decreases because the row-by-row coefficients becomes similar as shown in Rich's data (Figure 2.8). The capacity difference changes from 13% to 7% from the lowest flow rate to the highest.

5. DEVELOPMENT OF ROW-BY-ROW HEAT TRANSFER COEFFICIENT

5.1. Experimental Method

Row-by-row heat transfer data are obtained following the experimental procedures described by Rich (1975). The coil calorimeter (Figure 5.1) at the York laboratory in Norman, Oklahoma is used to collect the experimental data.

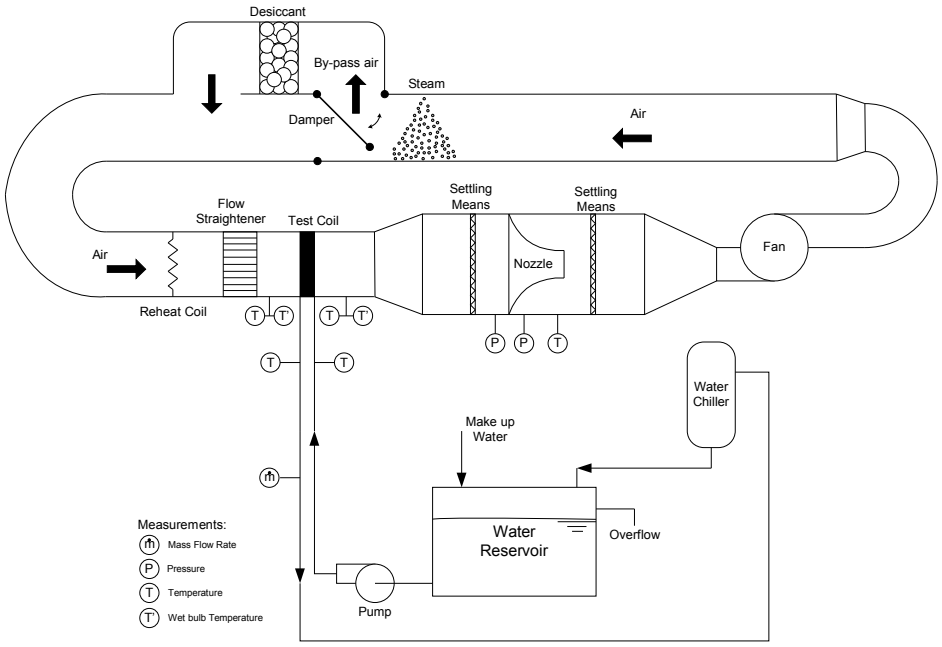

Figure 5.1 Test rig for coil performance measurement.

Different coils are tested in a closed-loop wind tunnel with air blowing across the fins and water circulating inside the coil tubes. Entering air temperature is controlled by an upstream reheat coil, whereas entering water temperature is controlled by a water chiller.

Chilled water is stored in an insulated water reservoir to be drawn into the coil. Air moisture entering the coil is controlled by a steam generator with a desiccant dehumidifier bypass as shown in Figure 5.1.

Coil entering and leaving air temperatures are measured with thermocouple grids at the inlet and outlet of the coil, respectively. Air volumetric flow rate is derived from the differential pressure measurement across a nozzle according to the ANSI/ASHRAE standard 51 (2000). Temperature at the nozzles outlet is measured to calculate the air mass flow rate. The air mass flow rate and temperature measurements are used to calculate the overall coil capacity according to the following heat transfer equation:

$$\dot{Q} = \dot{m} \cdot c_p \cdot \Delta T \tag{5.1}$$

The coil capacity is also calculated from the water side measurements. Thermocouple probes are located at the inlet and outlet coil headers to measure the overall temperature difference. A turbine flow meter is used to measure the water flow rate. These measurements provide enough information to calculate the water side coil capacity using Equation (5.1). Table 5.1 shows the list of measurements and uncertainties. With the measuring instrument shown in the table, the uncertainties for the air side and water side capacities are about ±2% and ±3.5%, respectively. A detailed uncertainty analysis on this experiment is addressed in a later section. For a perfect heat balance, both air side and water side capacities should be the same. However, a ±5% difference in heat balance is generally acceptable (Wang *et al.* 2000b).

Multi-row coils are used for the row-by-row heat transfer experiments. The coils are circuited such that each coil row is a separate circuit, and the circuits are only connected at the inlet and outlet headers. Figure 5.2 shows the instrumentation of a four-

row coil. Thermocouples are glued and insulated on the tube surface at each circuit outlet to measure the leaving water temperatures. It is assumed that the entering water temperatures are the same for all circuits, and the pressure drop for each circuit is measured to derive the water mass flow rate in each circuit. Therefore the water capacity for each individual row can be calculated using Equation (5.1).

Table 5.1 Measuring instruments and uncertainties for the coil tests.

Measurement	Sensor Type	Uncertainty
Air temperature	Thermocouple	±0.1 °C
Nozzle pressure drop	Pressure transducer	±0.25 %
Water temperature	RTD probe	±0.2 °C
Water flow rate	Turbine flow meter	±1 %

The air temperatures between rows are necessary in the data reduction procedures to derive the row-by-row heat transfer coefficient. However, due to the compactness of coil geometry, the air temperatures between rows are difficult to measure. Rich (1975) assumed a perfect heat balance between air and water sides for each row and used the water side capacity at each row to calculate the air temperature between rows. Since the entering air temperature for the first row (entering coil) and the leaving air temperature for the last row (leaving coil) are measured in the experiment, the air temperature calculation can start from the coil inlet along the air flow direction to the coil outlet. The calculated coil outlet temperature should be equal to the measured leaving air temperature. Similarly, the temperature calculation can also start from the coil outlet into the air flow direction to the coil inlet. The calculated inlet temperature should be equal to the measured entering air temperature instead.

However, if a perfect heat balance is assumed in the air temperature calculation,

all of the air to water heat imbalance is either distributed to the first or the last row only depending on the calculation direction. The heat imbalance is contributed by each coil row and should be distributed to all rows in the air temperature calculation. Therefore, it is assumed that the heat imbalance is distributed to each row weighted by the individual row capacity as shown in Equation (5.2). The air temperature between rows is therefore calculated based on the corrected row capacities.

$$\dot{Q}_{cor,i} = \dot{Q}_{mea,i} + \Delta \dot{Q}_{coil} \frac{\dot{Q}_{mea,i}}{\dot{Q}_{coil,w}} \tag{5.2}$$

where the subscripts *i* is the row number. $\dot{Q}_{mea,i}$ is the measured capacity for each row and $\Delta \dot{Q}_{coil}$ is the coil capacity imbalance between air and water:

$$\Delta \dot{Q}_{coil} = \dot{Q}_{coil,air} - \dot{Q}_{coil,w} \tag{5.3}$$

where the water side capacity is calculated from the overall water flow rate and water temperatures measured at the coil headers.

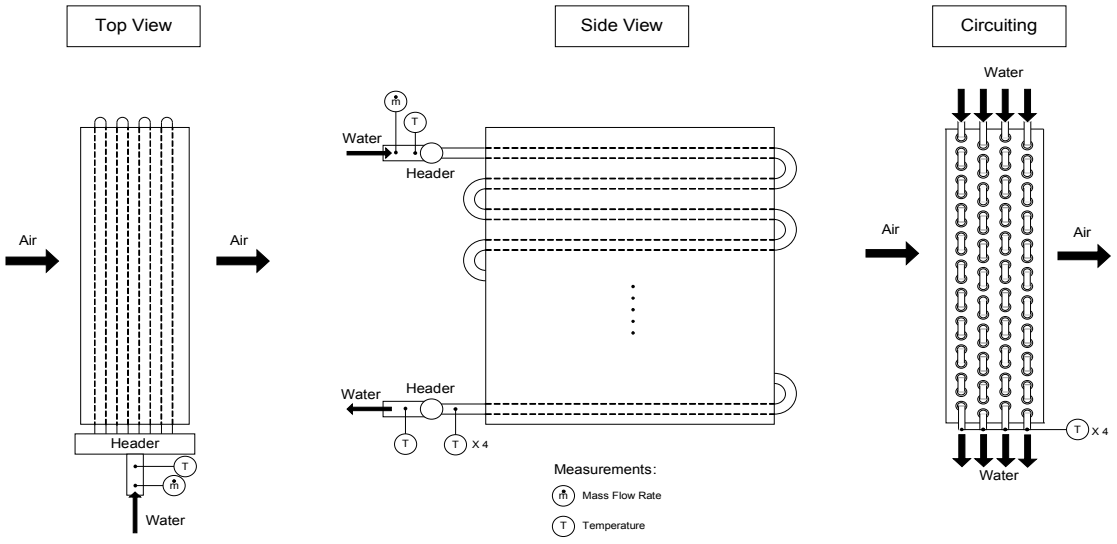

Figure 5.2 Coil instrumentation.

5.2. Test Conditions

Experimental data are collected over a range of coil face velocities to develop the air side heat transfer correlations. Since the heat transfer coefficient is a strong function of the air flow rate, other air side and water side boundary conditions are kept constant in this experiment. The test conditions are:

- Entering air dry bulb temperature: 38 °C
- Entering coil face velocity: 0.8 to 4.1 $m.s^{-1}$
- Entering water temperature: 16 °C
- Entering water flow rate: 1.6 $m^3.hr^{-1}$

The above test conditions are for a dry surface. Wet coils are not measured in these experiments. At least five test points are taken within the face velocity range. For each test point, the difference between the overall air side and water side capacities should be within ±5% (Wang *et al.* 2000b).

Fin density is the easiest parameter to change in the coil manufacturing process. Heat pump design engineers can use different fin densities in the heat exchanger coil to meet the system rating requirement. A number of coils with different fin densities are used to conduct this row-by-row heat transfer experiment. Table 5.2 shows the coil test matrix. The fin densities cover the typical application range for heat pump coils. Louvered fins are used in all coils except coil 7, which is a flat fin coil that has the same specifications as Rich's coil (1975). This coil is run first to verify the test facility and instrumentation. All of the coils have the same face area that is 508 mm high and 762 mm long. The coil tubes are smooth to eliminate the uncertainty of enhanced surfaces

during data reduction. All coils have 4 rows which are enough to derive the row-by-row coefficients from 1 to 4 rows. It was also found that if a coil has more than 4 rows, its heat transfer performance is not enhanced significantly compared to a 4-row coil (McQuiston *et al.* 2000; Incropora and DeWitt 1996; Wang *et al.* 2000b). Therefore, coils with more than 4 rows are not considered in this experiment.

Table 5.2 Coil test matrix.

Coil	Fin type	Fin Thickness	Fin Density	No. of Rows	Tube OD	Tube x Row spacing
1	Louvered	0.11 mm	512 fins.m^{-1}	4	9.5 mm	25.4 x 22 mm
2	Louvered	0.11 mm	551 fins.m^{-1}	4	9.5 mm	25.4 x 22 mm
3	Louvered	0.11 mm	591 fins.m^{-1}	4	9.5 mm	25.4 x 22 mm
4	Louvered	0.11 mm	669 fins.m^{-1}	4	9.5 mm	25.4 x 22 mm
5	Louvered	0.11 mm	709 fins.m^{-1}	4	9.5 mm	25.4 x 22 mm
6	Louvered	0.11 mm	787 fins.m^{-1}	4	9.5 mm	25.4 x 22 mm
7*	Flat	0.15 mm	551 fins.m^{-1}	4	13.2 mm	31.8 x 27.5 mm

* - Rich's coil specifications (1975)

5.3. Derivation of the Heat Transfer Coefficient

The row-by-row measurements are used to derive the row-by-row heat transfer coefficients for the test coils. For each data point, the following information is required:

- **Coil geometry:** Total outside heat transfer area, total inside heat transfer area, number of circuits, tube wall thickness, tube thermal conductivity, fin thickness, and fin thermal conductivity.
- **Air side:** Volumetric flow rate, inlet and outlet temperatures for each coil row.
- **Water side:** Volumetric flow rate, inlet and outlet temperatures for each circuit.

There are different ways to derive the heat transfer coefficient, but the end result should be similar. Rich (1975) used the Wilson plot technique (Wilson 1915) to derive the heat transfer coefficient. In this study the Wang *et al.* (2000b) method is used. Coil capacity

is calculated from both air and water side measurements by Equation (5.1). Average capacity between the air side and water side is used in the data reduction procedures as described below:

Using the effectiveness-NTU method, the capacity is calculated by:

$$\dot{Q} = \epsilon \dot{Q}_{max} \tag{5.4}$$

where:

$$\dot{Q}_{max} = \dot{C}_{min} \cdot (T_{air,in} - T_{w,in}) \tag{5.5}$$

$$\dot{C}_{min} = MIN(\dot{C}_{air}, \dot{C}_w) \tag{5.6}$$

$$\dot{C}_w = \dot{m}_w \cdot c_{p,w} \tag{5.7}$$

$$\dot{C}_{air} = \dot{m}_{air} \cdot c_{p,air} \tag{5.8}$$

Note that the capacity is for one row only. The air temperature between rows is calculated from the row-by-row capacity that is measured on the water side. For mixed air and unmixed water sides, the effectiveness is (Incropera and DeWitt 1996):

$$\epsilon = 1 - \exp\left[\frac{-(1 - e^{-NTU \cdot \dot{C}_r})}{\dot{C}_r}\right] \quad \text{for} \quad \dot{C}_{min} = \dot{C}_{air} \tag{5.9}$$

$$\epsilon = \frac{1}{\dot{C}_r}\left[1 - \exp\left(-\dot{C}_r(1 - e^{-NTU})\right)\right] \quad \text{for} \quad \dot{C}_{min} = \dot{C}_w \tag{5.10}$$

where:

$$\dot{C}_r = \frac{MIN(\dot{C}_{air}, \dot{C}_w)}{MAX(\dot{C}_{air}, \dot{C}_w)} \tag{5.11}$$

$$NTU = \frac{UA}{\dot{C}_{min}} \tag{5.12}$$

Neglecting the contact resistance, and the fouling resistances, the overall heat transfer

coefficient, *UA* is:

$$\frac{1}{UA}=\frac{1}{\eta_{surf} h_{air} A_{out}}+\frac{\ln(\frac{D_{out}}{D_{in}})}{2\pi k_{tube} L_{tube}}+\frac{1}{h_w A_{in}} \tag{5.13}$$

where the surface efficiency is calculated using Schmidt's method (1949) as described in section 3.4. The water side heat transfer coefficient is calculated by Gnielinski's correlation (1976):

$$h_w=\frac{(Re_{D_{in}}-1000)\,Pr_w \frac{f}{2}}{1+12.7\sqrt{\frac{f}{2}}(Pr_w^{\frac{2}{3}}-1)}\frac{k_w}{D_{in}} \tag{5.14}$$

where:

$$f=[1.58\ln(Re_{D_{in}})-32.8]^{(-2)} \tag{5.15}$$

Note that there is no explicit expression for h_{air}, therefore the following iterative procedures are used to calculate h_{air}:

1. Make an initial guess for h_{air}.
2. Compute the overall heat transfer coefficient using Equation (5.13); the coil effectiveness using Equation (5.9) or (5.10); and the coil capacity using Equation (5.4).
3. Compare the calculated capacity to measured capacity. If they are only different by a small number, the iteration terminates and the value for h_{air} is found. Otherwise go to next step.
4. Adjust the value of h_{air} and go to step 2 again. Note that the coil capacity is proportional to the air side heat transfer coefficient and the coil effectiveness must be

between zero and unity.

5.4. Uncertainty Analysis

In Section 5.1, the uncertainties of the direct measurements have been presented. These uncertainties are propagated to other parameters, such as capacity and heat transfer coefficients. This section presents an uncertainty analysis (Kline and McClintock 1953) that translates the uncertainties from direct measurements to derived measurements. A derived measurement can consist of several independent direct measurements, and its uncertainty is defined as:

$$e_R = \pm\sqrt{\left(\frac{\partial R}{\partial \nu_1} e_{\nu_1}\right)^2 + \left(\frac{\partial R}{\partial \nu_2} e_{\nu_2}\right)^2 + \ldots + \left(\frac{\partial R}{\partial \nu_n} e_{\nu_n}\right)^2} \tag{5.16}$$

where e is the measurement uncertainty, R is the derived result, and ν_1, ν_2, ..., ν_n are the independent variables.

5.4.1. Air Side Capacity

From the air side measurements, the air side capacity is calculated as:

$$\dot{Q}_{air} = \rho_{air} \dot{V}_{air} c_{p,air} \Delta T_{air} \tag{5.17}$$

The direct uncertainties are the air flow rate and temperature measurements. If the uncertainty in air properties are negligible because they are evaluated at measured temperature, the uncertainty for the air capacity is:

$$e_{\dot{Q}_{air}} = \pm\rho_{air} c_{p,air} \sqrt{(\Delta T_{air} e_{\dot{V}_{air}})^2 + (\dot{V}_{air} e_{\Delta T_{air}})^2} \tag{5.18}$$

Another common way to present the uncertainties is in terms of fractional values. Dividing Equation (5.18) by Equation (5.17), the fractional uncertainty of the air capacity

is:

$$e'_{\dot{Q}_{air}} = \pm\sqrt{(e'_{\dot{V}_{air}})^2 + \left(\frac{e_{\Delta T_{air}}}{\Delta T_{air}}\right)^2} \tag{5.19}$$

where e' is the fractional uncertainty. The uncertainty for ΔT_{air} is:

$$e_{\Delta T_{air}} = \pm\sqrt{(e_{T_{air,in}})^2 + (e_{T_{air,out}})^2} = \pm\sqrt{0.1^2 + 0.1^2} = \pm 0.14 \quad °C \tag{5.20}$$

The fractional uncertainty for the air flow rate is calculated using the uncertainty analysis in the ASHRAE standard 51 (2000). It is defined as:

$$e'_{\dot{V}_{air}} = \pm\sqrt{(e'_{noz})^2 + (e'_A)^2 + (e'_{fs})^2 + (e'_{\Delta P})^2 + (e'_{SP})^2} \tag{5.21}$$

where:

e'_{noz} = Fractional error in nozzle discharge coefficient

e'_A = Fractional error in area of nozzle

e'_{fs} = Fractional variation in fan speed

$e'_{\Delta P}$ = Fractional error in pressure change across nozzle

e'_{SP} = Fractional error in static pressure

According to the Standard, the fractional errors in nozzle discharge coefficient and area are given by:

$$e'_{noz} = \pm 0.012 \tag{5.22}$$

$$e'_A = \pm 0.005 \tag{5.23}$$

The variation in fan speed is within ±1%, and the error in pressure measurements are ±0.25%. Therefore, the fractional uncertainty for the air flow rate measurement is:

$$e'_{\dot{V}_{air}} = \pm\sqrt{(0.012)^2 + (0.005)^2 + (0.01)^2 + (0.0025)^2 + (0.0025)^2} = \pm 0.017 \tag{5.24}$$

Substituting Equations (5.20) and (5.24) into Equation (5.19), the calculation of fractional uncertainty for the air capacity is simplified to:

$$e'_{\dot{Q}_{air}} = \pm\sqrt{(0.017)^2 + \left(\frac{0.14}{\Delta T_{air}}\right)^2} \tag{5.25}$$

Note that the uncertainty varies depending on the air temperature change. It is higher for smaller temperature changes.

5.4.2. Water Side Capacity

From the water side measurements, the capacity is calculated as:

$$\dot{Q}_w = \rho_w \dot{V}_w c_{p,w} \Delta T_w \tag{5.26}$$

A similar uncertainty analysis to the air side capacity can be applied here, and the resulting fractional uncertainty in water side capacity is:

$$e'_{\dot{Q}_w} = \pm\sqrt{(e'_{\dot{V}_w})^2 + \left(\frac{e_{\Delta T_w}}{\Delta T_w}\right)^2} \tag{5.27}$$

where the fractional uncertainty for water flow rate is:

$$e'_{\dot{V}_w} = \pm 0.01 \tag{5.28}$$

The temperature change uncertainty from the RTD measurements is:

$$e_{\Delta T_w} = \pm\sqrt{(e_{T_{w,in}})^2 + (e_{T_{w,out}})^2} = \pm\sqrt{0.2^2 + 0.2^2} = \pm 0.28 \quad °\text{C} \tag{5.29}$$

The RTD measurements are used to calculate the overall water side capacity. Therefore, the uncertainty for overall water side capacity is calculated by:

$$e'_{\dot{Q}_w} = \pm\sqrt{(0.01)^2 + \left(\frac{0.28}{\Delta T_w}\right)^2} \tag{5.30}$$

Individual row capacity is also calculated by Equation (5.26) but the water mass flow and temperature change are for a single coil row instead. Before the coil test is run in the York coil calorimeter, the pressure drop for each circuit is measured by running a constant water flow rate through each circuit to check the circuit flow resistance. Table 5.3 shows the pressure drop for each circuit at 0.91 $m^3.hr^{-1}$ water flow rate. These pressure drop measurements are used to scale the water flow rate distribution to each circuit in the row capacity calculation.

Table 5.3 Circuit pressure drop at 0.91 $m^3.hr^{-1}$ water flow rate.

Circuit no.	1	2	3	4
Pressure drop (kPa)	176.85	175.89	179.26	179.26

The coil row temperature change is calculated by the entering water temperature measured by the RTD and the leaving water temperature measured by the thermocouple (TC) on the tube surface. The average leaving TC temperature, which is weighted by the mass flow rate of each circuit, should match the leaving water temperature measured by the RTD probe at the coil outlet. Since the RTD probe is directly inserted into the water stream, it is more accurate than the average outlet temperature measured by the thermocouples. The RTD measurements are used to calibrate the TC measurements for the row capacity calculation. Figure 5.3 shows the calibration curve for the TC measurements. Note that the TC measurements predict lower temperature changes because it is approximated by the tube surface temperatures.

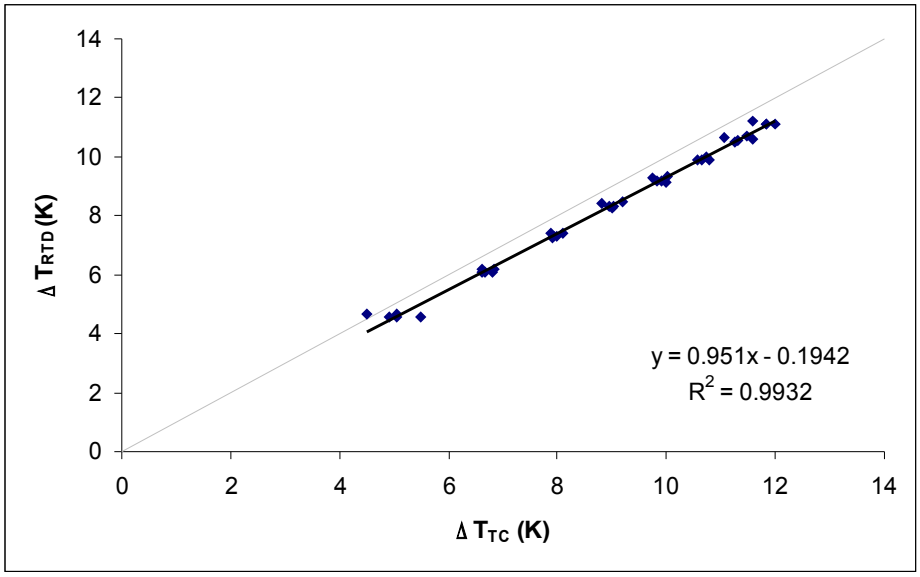

Figure 5.3 Comparison of RTD and TC measurements.

With the calibration, the uncertainty in leaving water temperature for individual row includes both the RTD and TC measurements. It is calculated by:

$$e_{T_{w,out}} = \pm\sqrt{(e_{T_{w,RTD}})^2 + (e_{T_{w,TC}})^2} = \pm\sqrt{0.2^2 + 0.1^2} = \pm 0.22 \quad ^\circ\text{C} \tag{5.31}$$

and the uncertainty for the row temperature change is:

$$e_{\Delta T_w} = \pm\sqrt{(e_{T_{w,in}})^2 + (e_{T_{w,out}})^2} = \pm\sqrt{0.2^2 + 0.22^2} = \pm 0.3 \quad ^\circ\text{C} \tag{5.32}$$

Therefore, the uncertainty for the row capacity is:

$$e'_{\dot{Q}_w} = \pm\sqrt{(0.01)^2 + \left(\frac{0.3}{\Delta T_w}\right)^2} \tag{5.33}$$

5.4.3. j-factor

The j-factor is calculated by the following equation:

$$j = \frac{h_{air}}{c_{p,air} \cdot G_{air} \cdot Pr_{air}^{-2/3}} \tag{5.34}$$

where $c_{p,air}$ and Pr_{air} are air properties that are depending on temperature measurement. G_{air} is the maximum air mass flux and is related to the uncertainty of air flow rate. Therefore, the fractional uncertainty for the j-factor can be calculated by:

$$e'_j = \pm\sqrt{(e'_{h_{air}})^2 + (e'_{\dot{V}_{air}})^2 + (\frac{e_{T_{air}}}{T_{air}})^2} \tag{5.35}$$

Note that the unit for the air temperature in Equation (5.36) is Kelvin (Holman 1971). Substituting the uncertainties for air flow rate and temperature, Equation (5.35) becomes:

$$e'_j = \pm\sqrt{(e'_{h_{air}})^2 + (0.017)^2 + \left(\frac{0.1}{T_{air}}\right)^2} \tag{5.36}$$

The uncertainty for the air side heat transfer coefficient is related to the data reduction procedures in section 5.3. From Equation (5.13), the fractional uncertainty for the heat transfer coefficient is:

$$e'_{h_{air}} = \pm\sqrt{(e'_{h_w})^2 + (e'_{UA})^2} \tag{5.37}$$

From Equation (5.14), h_w is a function of water flow rate and temperature. Hence, the fractional uncertainty is:

$$e'_{h_w} = \pm\sqrt{(e'_{\dot{V}_w})^2 + \left(\frac{e_{T_w}}{T_w}\right)^2} = \pm\sqrt{(0.01)^2 + \left(\frac{0.2}{T_w}\right)^2} \tag{5.38}$$

where T_w is in Kelvin. UA is related to Equations (5.9) to (5.12). Its fractional uncertainty is calculated by:

$$e'_{UA} = \pm\sqrt{(e'_{\epsilon})^2 + (e'_{\dot{C}_r})^2 + (e'_{\dot{C}_{min}})^2} \tag{5.39}$$

From Equations (5.6) and (5.11) the minimum heat rate and heat capacity ratio are functions of flow rates and temperatures at both air and water sides. Their uncertainties are identical as shown below:

$$e'_{\dot{C}_r} = e'_{\dot{C}_{min}} = \pm\sqrt{(e'_{\dot{V}_{air}})^2 + (e'_{\dot{V}_w})^2 + \left(\frac{e_{T_{air}}}{T_{air}}\right)^2 + \left(\frac{e_{T_w}}{T_w}\right)^2} \tag{5.40}$$

$$\text{or} \quad e'_{\dot{C}_r} = e'_{\dot{C}_{min}} = \pm\sqrt{(0.017)^2 + (0.01)^2 + \left(\frac{0.1}{T_{air}}\right)^2 + \left(\frac{0.2}{T_w}\right)^2}$$

where both the air and water temperatures are in Kelvin.

The heat exchanger effectiveness can be calculated by Equations (5.4) to (5.6). Its uncertainty is given by:

$$e'_{\epsilon} = \pm\sqrt{(e'_{\dot{Q}_{avg}})^2 + (e'_{\dot{C}_{min}})^2 + \left(\frac{e_{T_{air,w}}}{\Delta T_{air,w}}\right)^2} \tag{5.41}$$

where $\dot{Q}_{avg}$ is the average capacity of the air and water capacities. $T_{air,w}$ is the temperature difference between air and water. The uncertainties for these two terms are:

$$e'_{\dot{Q}_{avg}} = \pm\sqrt{(e'_{\dot{Q}_{air}})^2 + (e'_{\dot{Q}_w})^2} \tag{5.42}$$

$$e_{T_{air,w}} = \pm\sqrt{(e_{T_{air}})^2 + (e_{T_w})^2} = \pm\sqrt{(0.1)^2 + (0.2)^2} = \pm 0.22 \quad °\text{C} \tag{5.43}$$

Note that the fractional uncertainties for air and water capacities are calculated by Equations (5.25), and (5.30) or (5.33), respectively. Equations (5.36) to (5.43) summarize the calculation procedures for the j-factor uncertainty.

5.5. Verification of Experimental Method

Before proceeding to the experiment for louvered fins, a flat fin coil with the

same specifications as Rich's test coil (1975) is run to verify Rich's row-by-row correlation in the York test facility. This coil is geometrically the same as Rich's coil but with a larger face area to accommodate the York laboratory air loop. The larger face area is not expected to affect the derived heat transfer coefficient because it should be unique for a specific combination of fin type, fin thickness, fin density, tube dimension, and tube pitch. Due to the limitation of the test facility, the test range of Reynolds number is limited to about:

$$5000 < Re_{Pr} < 15000$$

However, it is a typical application range for heat pump systems, and covers most of Rich's test range. This test range provides enough data to verify the test facility and check Rich's results. The same test is repeated 5 times on different dates to check the repeatability of the measurements. For each test, the coil instrumentation is changed slightly. The instrumentation changes include installing additional thermocouples at the circuit outlets, running the experiment with the coil flipped over so that the first circuit becomes the last circuit, and replacing the rubber tubing connections between the circuit inlets and coil header. All of these test results are expected to be well within the estimated uncertainty range.

5.5.1. Overall Flat Fin Data

Besides the row-by-row data, Rich also presented an overall j-factor correlation for the entire coil. In this test, there are also enough measurements to derive the overall j-factor, therefore the overall j-factor data are also verified against Rich's data.

Before deriving the overall j-factor, the heat balance between the air side and the

water side is verified. It should be within ±5% to be suitable for data reduction. The heat balance is calculated by:

$$HB = \frac{\dot{Q}_{air} - \dot{Q}_{w}}{\dot{Q}_{avg}} \times 100\% \tag{5.44}$$

where $\dot{Q}_{avg}$ is the average capacity of the air and water sides. Figure 5.4 shows the heat balance for all the measured data collected for the five Rich coil experiments. The data show that the heat balance is relatively independent of the Reynolds number and are well within the ±5% heat balance criterion typically required for j-factor correlations.

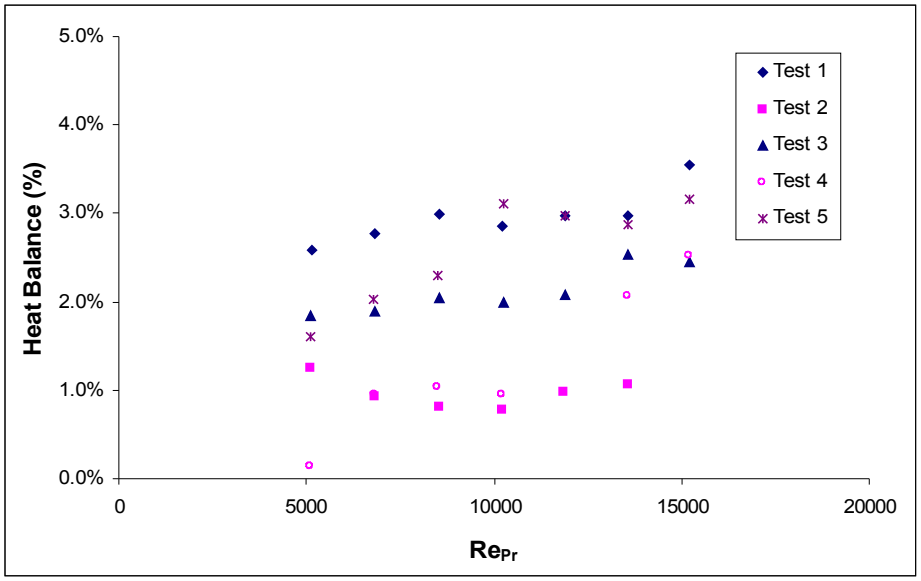

Figure 5.4 Heat balance between air and water measurements.

The derived overall j-factor data are presented in Figure 5.5 along with Rich's data (1975). Figure 10.1 in the Appendix shows the same comparison in terms of heat transfer coefficient. Uncertainty bars have been added to the figures to show the accuracy of the derived data. All of the derived data compare well with Rich's data. Rich's data lie within the uncertainty intervals of the current test data. In addition, the figure also shows that the current data are repeatable even though they are collected over

a period of time for different instrument and coil configurations. Although Rich used a different test facility and his data were derived using a different procedure, the result shows that the current test facility and data reduction procedure are valid and are able to replicate the overall coil j-factor presented by Rich.

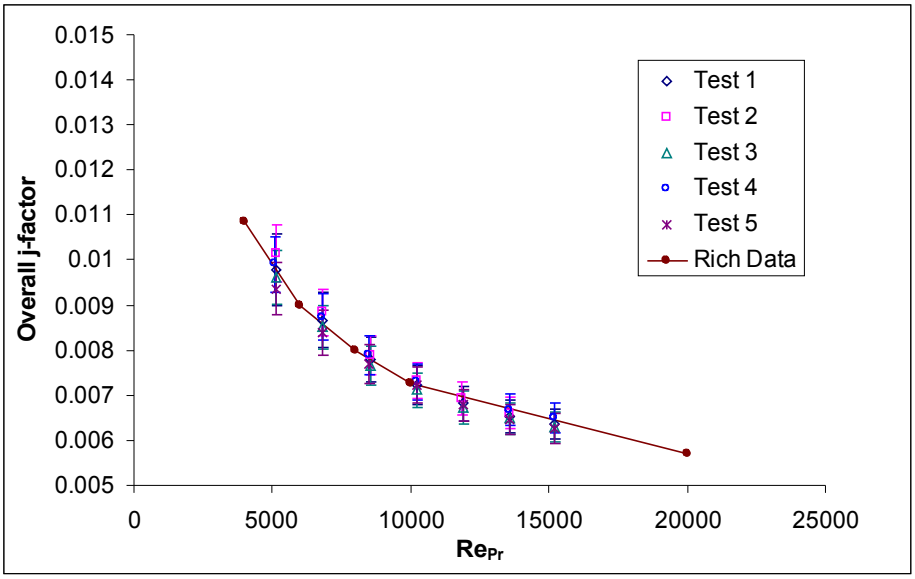

Figure 5.5 Flat fin overall j-factor verification.

5.5.2. Row-by-Row Flat Fin Data

The row-by-row j-factors can be calculated either starting from the 1st row along the air flow direction or starting from the last row into the air flow direction. In this data reduction, the calculation starts from the coil outlet. The air to water heat imbalance is distributed to each row according to the method presented in Section 5.1. Since the calculation is into the air flow direction, it should calculate an entering air temperature at the first row that matches the measured air temperature entering the coil. Figure 5.6 shows the temperature difference between the calculated and measured values. Both temperatures agree well with each other. All temperature differences are less then ±0.5 K. The temperature difference seems independent of the Reynolds number. Rather, it is

related to the air to water heat balance. Figure 5.4 and Figure 5.6 show that a better air to water heat balance gives a smaller temperature difference.

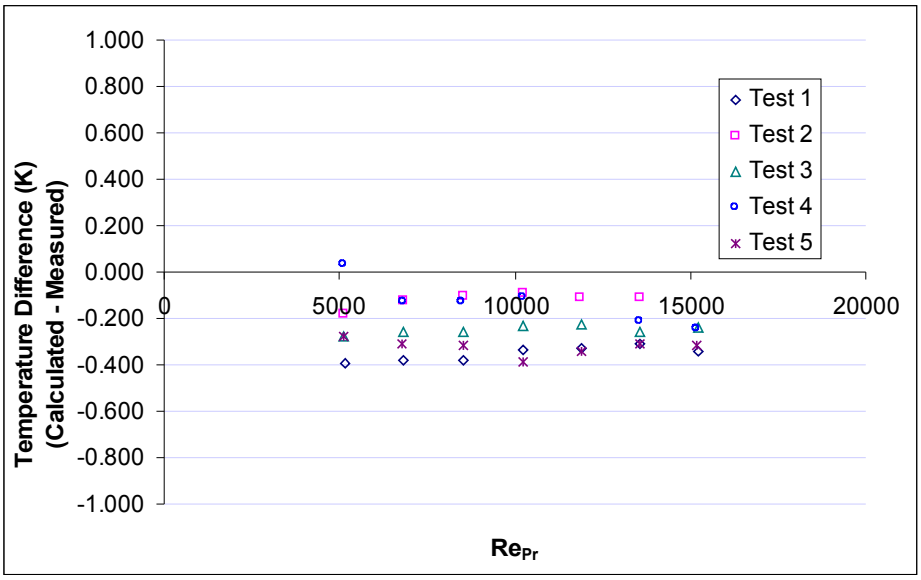

Figure 5.6 Calculated and measured air temperature difference at the first row inlet.

The derived row-by-row j-factors for all five tests are shown in Figures 5.7 to 5.10 for row 1 to row 4, respectively. The estimated uncertainties of the derived j-factors and Rich's data are also presented in the figures. Figures 10.2 to 10.5 in the Appendix show the same comparison with respect to heat transfer coefficient. Note that the uncertainty interval increases from row 1 to row 4 because the temperature change from row 1 to row 4 becomes smaller. Most heat transfer takes place in the front rows. When the air reaches the back rows, there is not much heat transfer capacity left, therefore the temperature change is small. A smaller temperature change results in a larger uncertainty interval according to the uncertainty analysis in Section 5.4. The smallest temperature change in this experiment is about ±2 K.

The figures show that the derived data are repeatable despite the fact that they are obtained from different test facilities. Most of Rich's data lie within the uncertainty

interval of the current j-factor results. The current results tend to predict a lower j-factor at row 1 for low Reynolds numbers as shown in Figure 5.7.

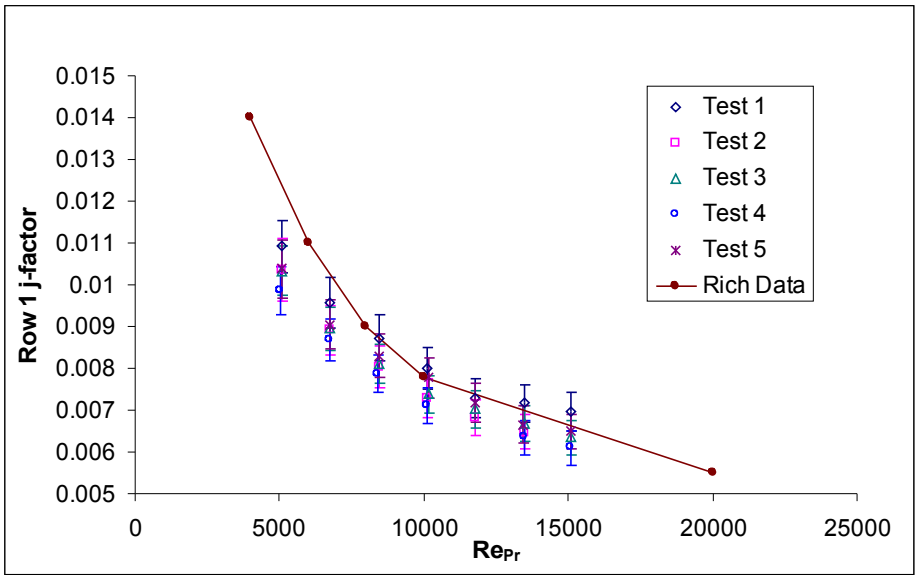

Figure 5.7 Flat fin row 1 j-factor verification.

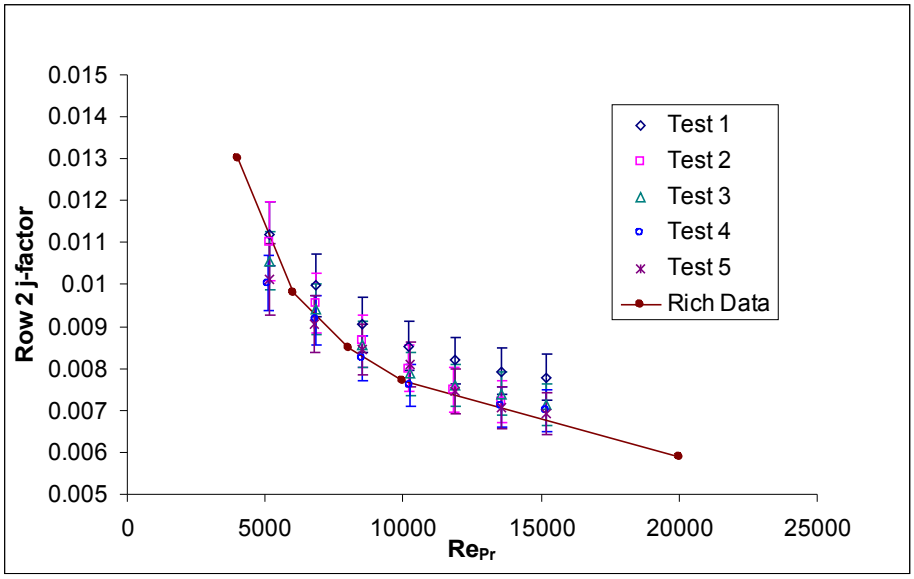

Figure 5.8 Flat fin row 2 j-factor verification.

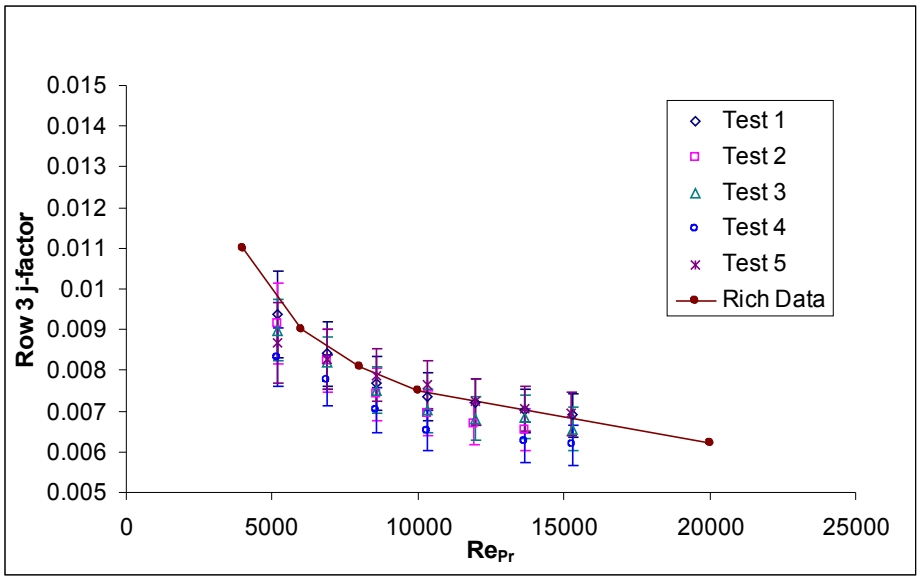

Figure 5.9 Flat fin row 3 j-factor verification.

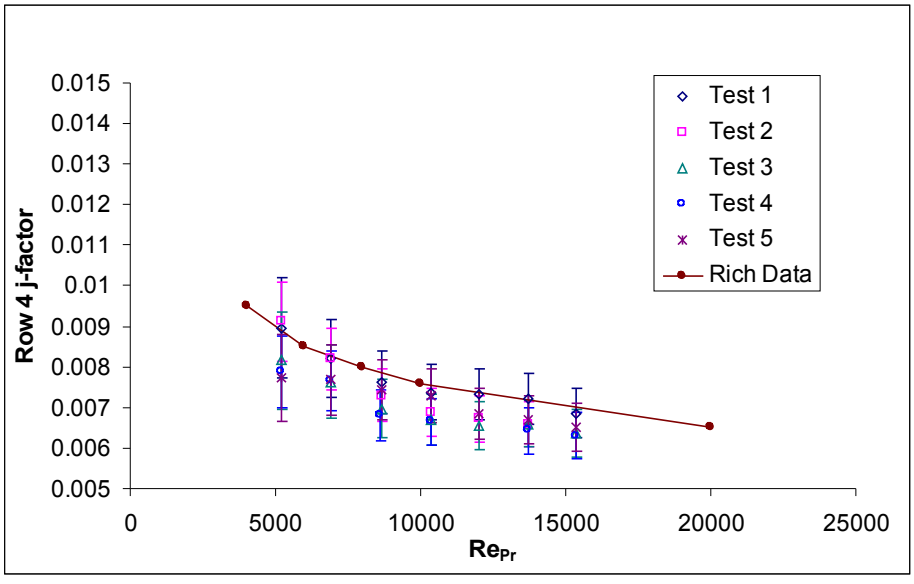

Figure 5.10 Flat fin row 4 j-factor verification.

The Test 1 data are the closest to Rich's data but its air to water heat balance is the highest as shown in Figure 5.4. It is believed that the row-by-row j-factor is more

sensitive to the air to water heat balance than the overall j-factor because the heat balance error is propagated to each row. The difference between the current data and Rich's data could be due to the fact that Rich did not report or account for the air to water heat balance in experimental data.

5.6. Louvered Fin Heat Transfer Coefficients

Row-by-row heat transfer data are collected for the louvered fin coils shown in Table 5.2. The same experimental method and data reduction procedures are applied to derive overall and row-by-row heat transfer coefficients for each test point. All of the measured data are within ±5% air to water side heat balance. Due to the fact that the heat transfer coefficient is proprietary, the heat transfer coefficients presented in this section are either normalized or scaled. The use of normalization or scaling only hides the actual values of the heat transfer coefficients, all of the characteristics of the heat transfer coefficients preserve. Figure 5.11 shows an example of the normalized row-by-row j-factors for Rich's data (1975). The j-factor for each row is normalized by the overall j-factor of the coil. Note that all the characteristics of the j-factor are preserved. The first row has the highest heat transfer coefficient at low Reynolds numbers but the last row has the highest heat transfer coefficient at high Reynolds numbers. The same approach is used to present the row-by-row j-factors for the louvered fins in this section.

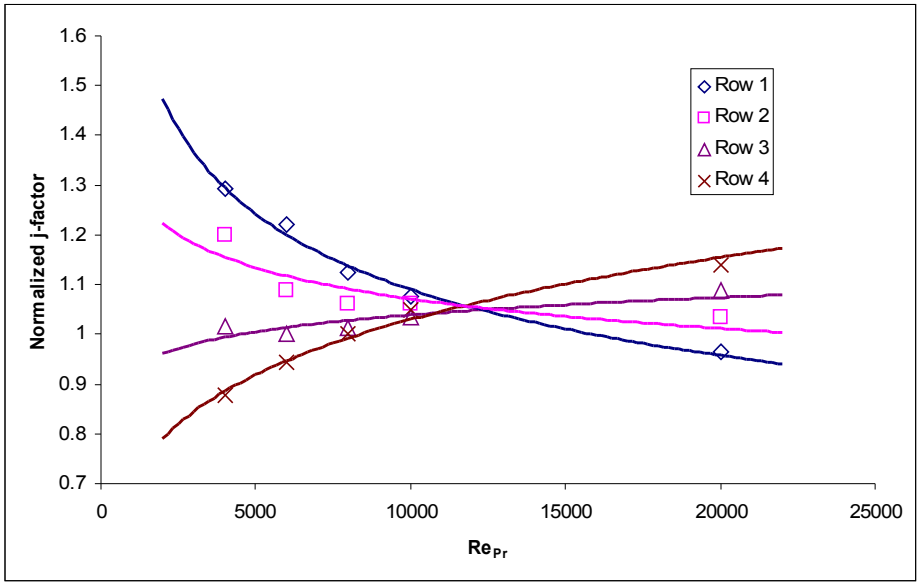

Figure 5.11 Normalized row-by-row j-factor for Rich's data (1975).

5.6.1. Overall Louvered Fin Data

Figure 5.12 shows the overall j-factors for all six louvered fin coils. The figure shows that the j-factors tend to "level off" in the low Reynolds number range. This louvered fin characteristic is due to the transition from "duct flow" to "boundary layer flow" as reported in the literature (Davenport 1983; Achaichia and Cowell 1988; Webb 1994; and Chang *et al.* 1995). For louvered fin coils, the "duct flow" and "boundary layer flow" are defined by Webb (1994) as:

- Duct flow: Axial flow through the fin array bypassing the louvers.
- Boundary layer flow: Parallel flow through the louvers.

At low Reynolds numbers, the hydraulic resistance for "duct flow" is smaller than that for the "boundary layer flow" through the louvers. For "duct flow", the air bypasses the louvers and results in a lower heat transfer coefficient. As the Reynolds number

increases, the hydraulic resistance for "duct flow" is increased and the air travels through the louvers. As a result, air mixing between air passages increases and the heat transfer coefficient also increases.

The fin density effect is also shown in Figure 5.12. Note that the j-factor decreases with increasing fin density (Coils 1 to 6) at low Reynolds number. As the Reynolds number increases, the j-factor becomes independent of the fin density. The effect of fin density is also due to the "duct flow" effect, since the air bypasses more louvers for the high fin density coil (Wang *et al.* 1998). For high Reynolds numbers, the "boundary layer flow" takes over and the j-factor is independent of the fin density. The fin density effect agrees with the experimental results from Wang *et al.* (1998).

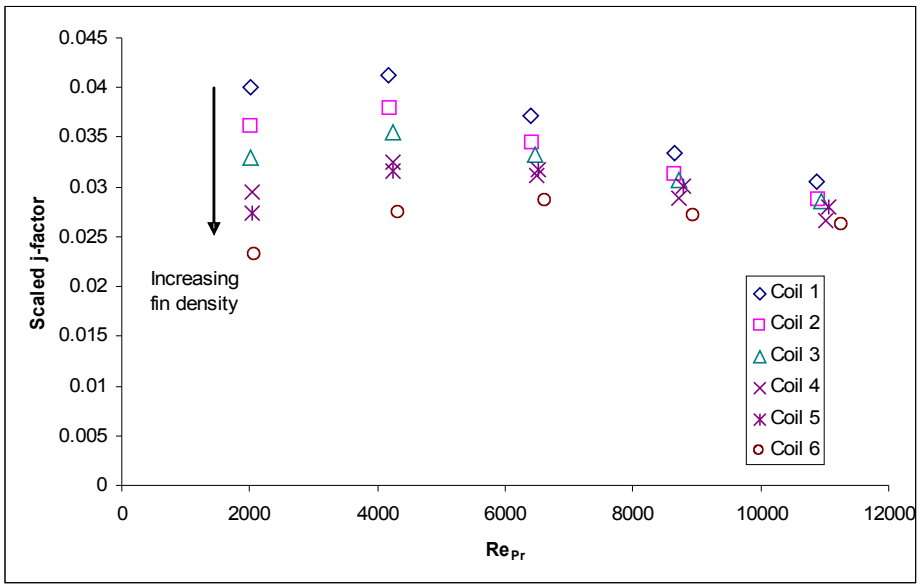

Figure 5.12 Scaled overall louvered fin j-factors.

The overall j-factor correlations are also compared to the best available louvered fin correlation (Wang *et al.* 1999b). The Wang *et al.* correlation is a general louvered fin correlation that was developed based on the heat transfer data from five different louvered fin types. However, the louvered fin tested in this research was not included in

their correlation development. Therefore the current correlation is not expected to match the Wang *et al.* correlation exactly, but they should be similar. Figure 5.13 shows the comparison between the current data and the Wang *et al.* correlation data. The comparison is presented in terms of the ratio of the current j-factor to the Wang *et al.* j-factor. For clarity, only the j-factor ratios for the minimum, intermediate, and maximum fin densities (Coils 1, 4, and 6) are shown.

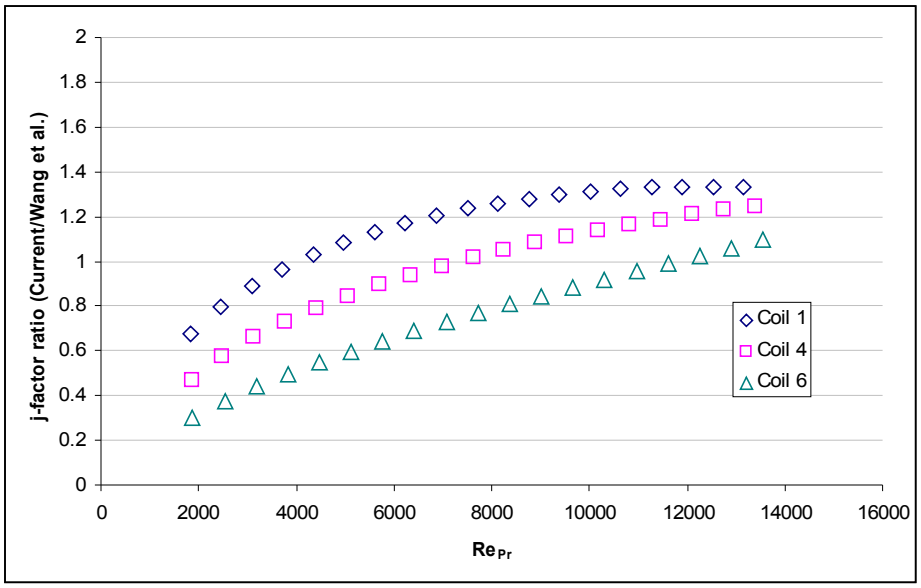

Figure 5.13 Comparison of current j-factor correlation to the Wang *et al.* (1999b) correlation.

The comparison shows that the current correlation tends to predict higher j-factors than the Wang *et al.* correlation for the high Reynolds number range. This is likely due to the fact that the current fin type has more louvered area than the fin types used by Wang *et al.*. Since there are two flow regimes (duct flow and boundary layer flow), it is possible that increasing the number of louvers would reduce the j-factor for duct flow and increase the j-factor for boundary layer flow. In addition, Wang *et al.* showed that their j-factor data are significantly scattered at low Reynolds numbers compared to the high Reynolds number data.

5.6.2. Row-by-Row Louvered Fin Data

The overall louvered fin j-factors are used to normalize the row-by-row louvered fin j-factors. Figure 5.14 shows the normalized row-by-row j-factors for Coil 1. The j-factors for other coils are similar and are shown in the appendix. Note that the louvered fin row-by-row j-factors have similar characteristics compared to Rich's flat fin data (Figure 5.11). Note that the y-axis scales for Figures 5.11 and 5.14 are different because not only the fin densities of both coils are different, the fin thickness, tube diameter and tube spacings are also different. If all of these parameters are the same, the flat fins are expected to have more row-by-row effect compared to the louvered fins.

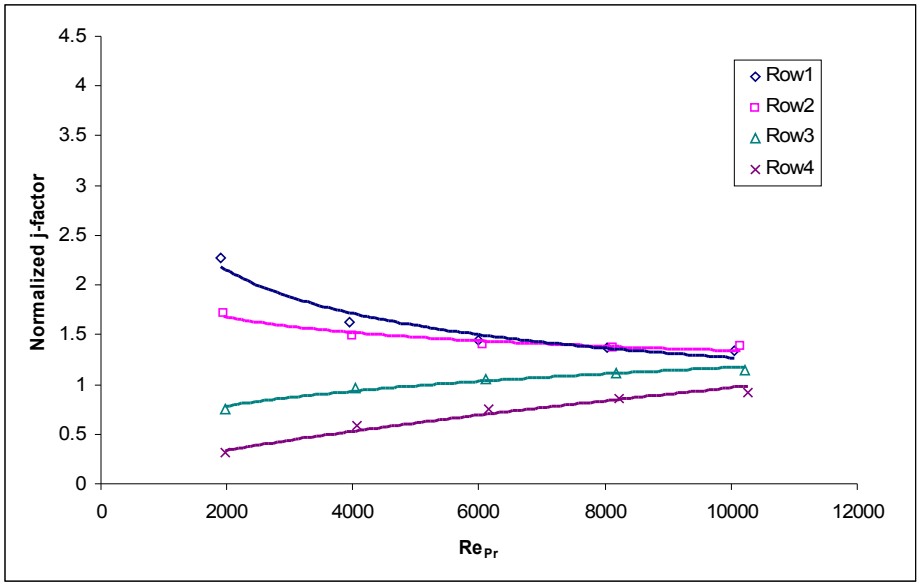

Figure 5.14 Coil 1 normalized row-by-row j-factor.

At low Reynolds number, Webb (1994) shows that because of the "duct flow" effect, the air bypasses the louvers and there is an entrance length effect at the front rows. This pseudo entrance length effect is a little different from the classical thermal entrance length effect because the air flow is interfered by the louvered fin geometry. However, the flow characteristic is analogous in this "duct flow" region. As a result, the heat

transfer coefficients at the front rows are higher than its fully developed value. But as the Reynolds number increases, the air travels through the louvers. There is more air mixing between flow passages but no more entrance length effect. The row-by-row heat transfer coefficients merge together.

The entrance length effect can be verified by plotting the row-by-row j-factors in terms of Nusselt number and entrance length:

$$Nu = j \cdot Re_{D_h} Pr^{1/3} \tag{5.45}$$

$$x^+ = \frac{n \cdot P_r / D_h}{Re_{D_h} Pr} \tag{5.46}$$

where n is the row number. Figure 5.15 shows the row-by-row Nusselt numbers plotted against the entrance length for Coil 1.

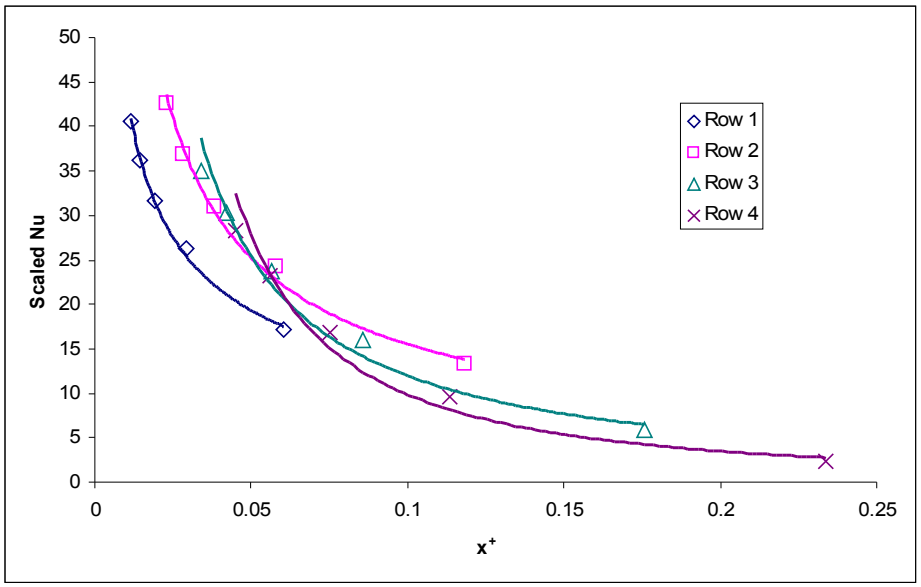

Figure 5.15 Coil 1 scaled row-by-row Nusselt number.

The same plots for other coils are shown in the appendix. Note that the entrance length effect is clearly shown. Most of the data are still in the developing region. The data at

row 4 are closest to fully developed where the heat transfer coefficient is relatively low.

5.7. Correlation Development

5.7.1. Row-by-Row Correlations

Although the row-by-row heat transfer curves (e.g. Figure 5.15) can be directly used in heat exchanger calculations, they are for a specific fin density only. Since the collected row-by-row heat transfer data sets cover a range of fin densities, they can be used to develop correlations that account for fin density effects. Although these correlations are not necessarily applicable to other louvered fin designs, the development of these correlations is useful in identifying likely correlation parameters and forms. General heat transfer correlations presented in the literature usually have the following formulation (Briggs and Young 1963; Gray and Webb 1986; Kayansayan 1993; Chang and Wang 1996; Wang *et al.* 2000; Kim and Bullard 2002):

$$h' = n_1 v'^{n_2} \prod_{i=1}^{N_{X'}} X_i'^{n_{i+2}} \tag{5.47}$$

where h' is a dimensionless heat transfer coefficient; v' is a dimensionless velocity; X' is dimensionless heat exchanger parameters, $N_{x'}$ is the number of heat exchanger parameters, and n_1, n_2, ... are empirical coefficients. The previous section illustrates the influence of the entrance length effect on the row-by-row coefficients. The pseudo entrance length was therefore selected as the dimensionless velocity for the proposed correlation. Since fin density is the only heat exchanger parameter being changed in the experiment, a correlation of the following form is proposed:

$$Nu = n_1 (x^+)^{n_2} \left(\frac{P_f}{P_{f,reference}} \right)^{n_3} \tag{5.48}$$

where n_1, n_2 and n_3 are empirical coefficients to be determined by the parameter estimation method (Jin and Spitler 2002). $P_{f,reference}$ is an arbitrary reference fin density to make the second parenthesis on the right hand side dimensionless. It is equal to 591 fins.m^{-1} for this correlation. Since Nu and x^+ are also dimensionless, the resulting empirical coefficients n_1, n_2 and n_3 are unit independent. Note that Equation (5.48) is a simplified version of Equation (5.47) because the fin density is the only heat exchanger parameter being changed. If heat transfer data for other coil parameters are available, the coil parameters can be introduced to the correlation according to the form of Equation (5.47).

Figure 5.16 shows the reproduction of Figure 5.12 in terms of Nusselt number and pseudo entrance length, where the pseudo entrance lengths for these 4-row coils are defined as:

$$x^+ = \frac{4 \cdot P_r / D_h}{Re_{D_h} Pr} \tag{5.49}$$

Note that the fin density effect is relatively insignificant on the Nu-x^+ plot because the fin density is accounted for by the hydraulic diameter in the pseudo entrance length equation. For instance, at Re_{Pr} = 2000, x^+ = 0.24 and Nu = 7.98 for a fin density of 512 fins.m^{-1}, but x^+ = 0.55 and Nu = 3.08 for a fin density of 787 fins.m^{-1}. The Nu-x^+ plot stretches out the data on a single curve which favors correlation development. Figure 5.16 also shows the estimation curves predicted by Equation (5.48). The curves predict the data very well and show a consistent trend with the measured data. The empirical coefficients for these curves are determined by minimizing the sum of the squared error between the measured

and estimated Nusselt numbers (Jin and Spitler 2002), i.e.:

$$min\,(SSE) = min \sum_{i=1}^{N} \left(\frac{Nu_{est} - Nu_{mea}}{Nu_{mea}} \right)^2 \tag{5.50}$$

where N is the number of data points. Table 5.4 shows the resulting empirical coefficients. The same procedures are used to develop the Nusselt number correlation for each row. Each row shares the same formulation, i.e. Equation (5.48), but has different empirical coefficients as shown in Table 5.4. Since the Nusselt number correlations are based on empirical data, they are suitable for the coil geometry shown in Table 5.2 and the application ranges shown with Table 5.4.

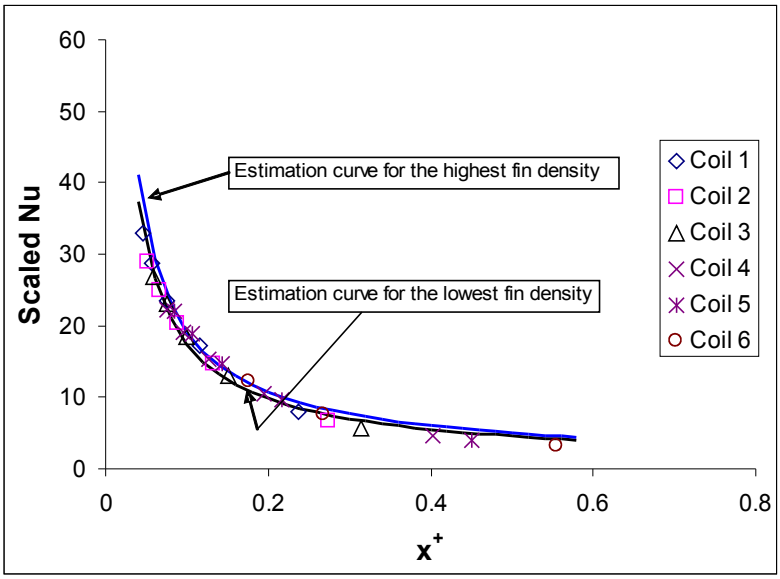

Figure 5.16 Overall Nusselt number correlations.

To minimize the error due to the number of significant digits in the coefficients, three significant digits are used so that no more than 0.1% error is introduced to the resulting Nusselt. The value of n_1 is directly proportional to the Nusselt number. Row 1 is expected to have the highest heat transfer coefficient in the current application range,

therefore n_1 is the largest for row 1. n_2 accounts for the entrance length effect. It has negative value because the entrance length is inverse proportional to the Reynolds number. Row 1 has the largest n_2 because the front row has the strongest entrance length effect. n_3 accounts for the fin density effect and it is the largest for row 4. It is due to the fact that the entrance length effect at row 4 is small and the fin effect dominates. The overall coefficient is lower than the first row but higher than the last row, therefore n_1, n_2 and n_3 of the overall coefficient are bounded by the row 1 and row 4 values.

Table 5.4 Empirical coefficients for the Nusselt number correlation, Equation (5.48).

Applications	n_1	n_2	n_3
Overall	0.843	-0.833	0.216
Row 1	3.678	-0.531	0.007
Row 2	2.613	-0.742	0.321
Row 3	1.293	-1.024	0.809
Row 4	0.707	-1.258	1.151

Application ranges: $0.012 < x^+ < 0.555$
$512 \text{ fins.m}^{-1} \le P_f \le 787 \text{ fins.m}^{-1}$
$1 \le N_r \le 4$

Figures 5.17 and 5.18 show the correlation curves compared to the measured data for row 1 and row 4, respectively. Similar figures for row 2 and row 3 are shown in Figures 10.16 and 10.17, respectively in the Appendix. At row 1 (Figure 5.17), the estimation curves for the lowest and highest fin densities are almost identical. The fin density effect is not significant. However, the entrance length effect dominates at the front rows where the heat transfer data are still in the developing region, therefore each x^+ predicts a unique Nusselt number.

Note that the data are more scattered for the back rows. The difference between the lowest and highest fin density curves becomes more apparent as the row number

increases. At row 4 (Figure 5.18), for a given x^+, different Nusselt numbers are predicted by different fin density curves. This is because the flow at row 4 is close to being fully developed (e.g. Figure 5.15). The entrance length effect is not as dominant as it is at row 1. As a result, the fin density effect becomes apparent.

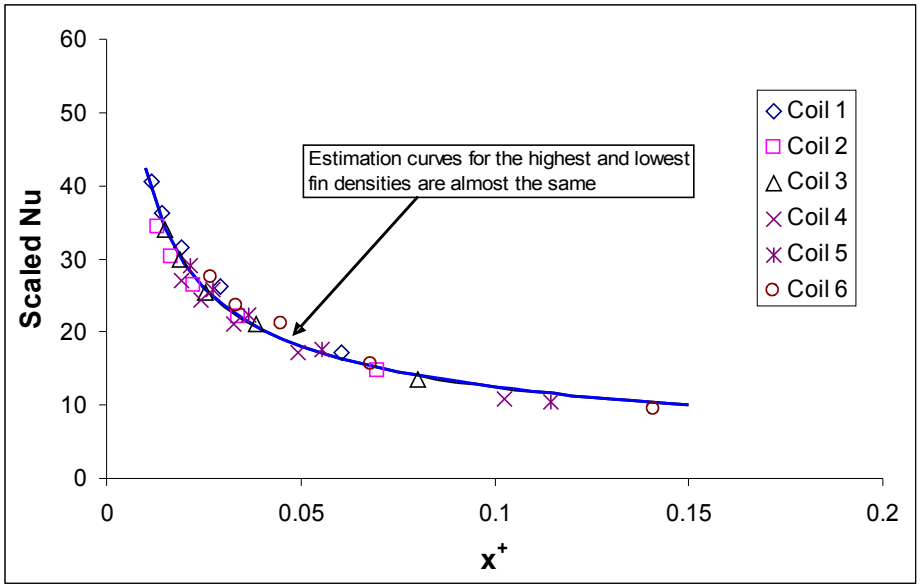

Figure 5.17 Row 1 Nusselt number correlations.

Figure 5.19 compares experimentally determined Nusselt numbers with calculated Nusselt number by Equation (5.48). Both row-by-row and the overall heat transfer data are compared and 150 data points are used for this validation. About 87% of the data are within the ±10% error band and 94% of the data are within the ±15% error band. The error appears higher at low Nusselt numbers where the measurement uncertainties are also high. Overall, the validation result is satisfactory.

Since there is an entrance length effect in heat exchanger coils, the air side heat transfer coefficient varies row-by-row. This section shows that a Nusselt number correlation in the form of Equation (5.47) can be used to model the entrance length effect and predict the row-by-row heat transfer coefficients. A row-by-row correlation, i.e.

Equation (5.48) based on a range of fin density is developed.

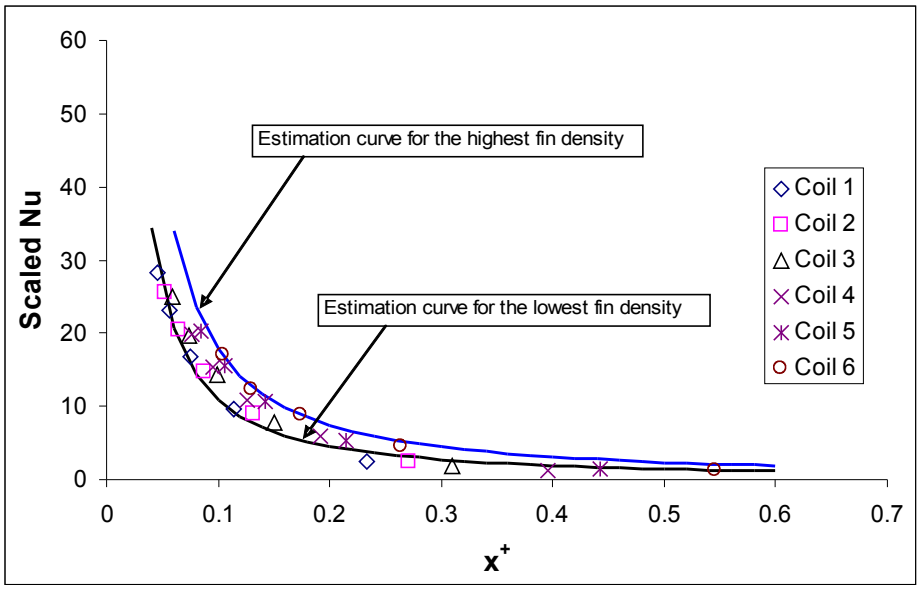

Figure 5.18 Row 4 Nusselt number correlations.

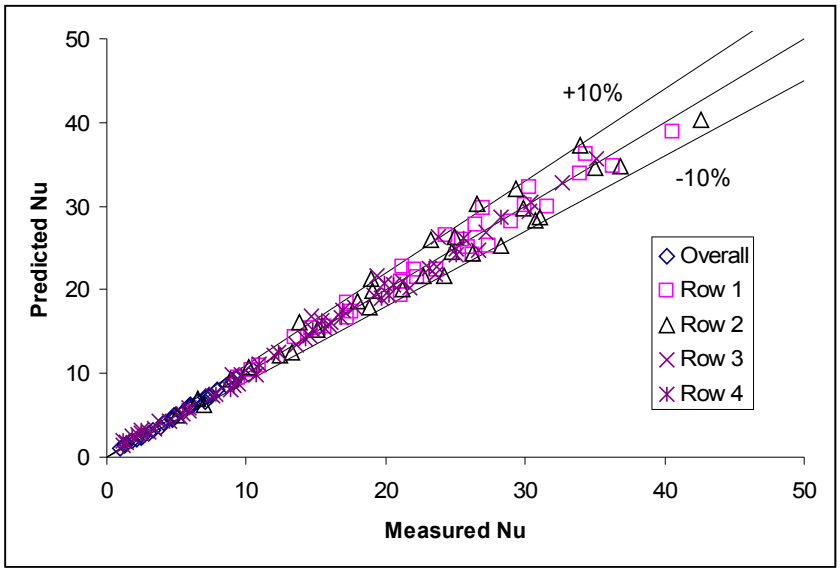

Figure 5.19 Validation of the Nusselt number correlations.

However, the application range of this correlation is limited. In order to extend the application range, more heat transfer data from different coil geometries are needed. The

data can be applied to the correlation development method in this section to develop more generalized row-by-row correlations.

5.7.2. Correlation Conversion

Since louvered fin coils are commonly used in the industry, but only the overall heat transfer correlations have been published in the literature, it is useful to break down the overall louvered fin correlations into the row-by-row forms for more accurate heat exchanger calculations. A conversion method is developed based on the available experimental data. This method is intended to provide a "framework" and demonstrates the feasibility of the conversion. The empirical coefficients in this section may not necessarily be applicable to other fin types.

In order to use the conversion method to predict the row-by-row coefficients, the conversion correlation should be similar to the form of the row-by-row correlation. Equation (5.51) shows the formulation of the conversion method. Note that it is very similar to the row-by-row correlation, Equation (5.48). The overall Nusselt number *Nu*, the pseudo entrance length, and the fin density are the correlating parameters for the row Nusselt number Nu_r conversion.

$$Nu_r = n_4 \, Nu \cdot (x^+)^{n_5} \left(\frac{P_f}{P_{f,reference}} \right)^{n_6} \tag{5.51}$$

The row number is accounted for by the pseudo entrance length as defined in Equation (5.46). Since this conversion method is generalized for a range of fin densities, the fin density term is also included in this formulation. Similar to Equation (5.48), the reference fin density is used to make last parenthesis dimensionless. The same reference

value of 591 fins.m^{-1} is used in this formulation. The empirical coefficients n_4, n_5 and n_6 are determined by minimizing the sum of squared errors between the two Nusselt numbers calculated by conversion estimation and measurement as show in Equation (5.50). The same measured Nusselt numbers used in the previous section are used to perform the parameter estimation. Table 5.5 shows the results from the parameter estimation. The coefficients are used with Equation (5.51) to convert overall Nusselt numbers to row-by-row Nusselt numbers. Three significant digits are used because they do not introduced more than 0.1% error to the resulting Nusselt number. Note that since the same measured data are used to derive the empirical coefficients, the application ranges for Equation (5.51) are the same as Equation (5.48). Since both equations are similar, n_4, n_5, and n_6 are analogous to the n_1, n_2, and n_3 of Table 5.4, respectively. However, since n_4, n_5, and n_6 are used for converting overall to row-by-row coefficients and the overall coefficient is bounded by the front and back row coefficients, they have different signs at different row numbers.

Figure 5.20 compares the estimated and measured row-by-row Nusselt numbers. Similar to the row-by-row correlation, i.e. Equation (5.48), most of the estimation data are within the ±10% error band. This is expected because both Equations (5.48) and (5.51) have similar formulation and the same measured data are used in the parameter estimations.

The conversion result shows that the conversion from overall to row-by-row heat transfer correlations is feasible. If both correlations have the same formulation, the conversion estimation can be as accurate as the original row-by-row correlation. However, the empirical coefficients presented in this section are used for specific fin type

and coil geometry. The original correlation, Equation (5.48) is still preferred at the moment.

Table 5.5 Empirical coefficients for the Nusselt number conversion, Equation (5.51).

Applications	n_4	n_5	n_6
Row 1	15.700	0.339	-0.239
Row 2	5.883	0.112	0.075
Row 3	1.923	-0.197	0.583
Row 4	0.781	-0.456	0.952

Application ranges: $0.012 < x^+ < 0.555$
$512 \text{ fins.m}^{-1} \le P_f \le 787 \text{ fins.m}^{-1}$
$1 \le N_r \le 4$

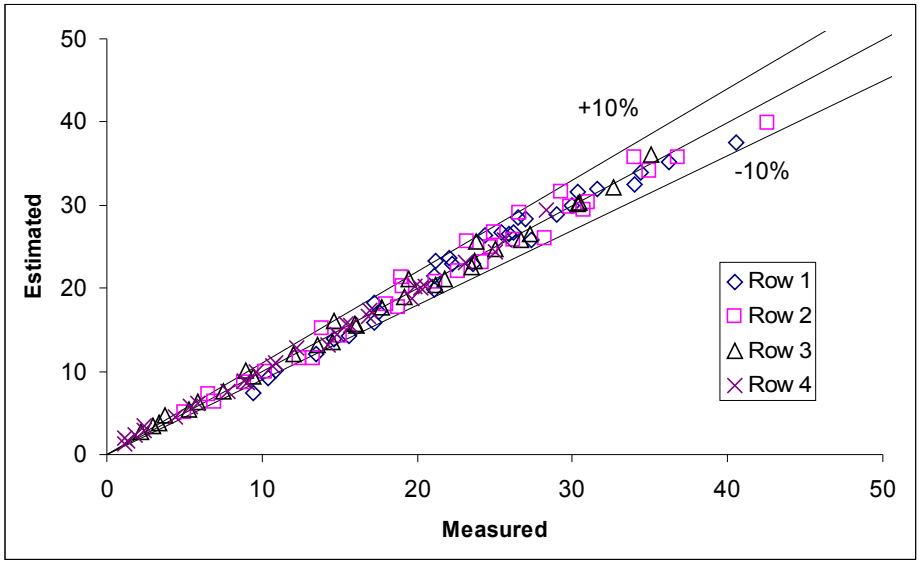

Figure 5.20 Validation of the Nusselt number conversions.

This chapter shows the experimental facility for developing overall and row-by-row heat transfer correlations are very similar. If the coil tubes are circuited row-by-row, more row-by-row heat transfer data can be collected. The entire conversion framework presented in this section should be able to apply to other fin types and coil geometries. To make the conversion method more usable, it is recommended that more experimental data for a wider range of coil geometries be used to derive the conversion correlation.

5.8. Evaluation of Row-by-Row Louvered Fin Heat Transfer Coefficients for System Simulation

In Section 4.7, the system simulation results with flat fin overall and row-by-row correlations are compared. The comparison shows that for the tested range of air flow rates, the overall correlation underpredicts the system capacity by 7% to 13% compared to the row-by-row correlation. Since the row-by-row and overall louvered fin coefficients have been developed in this chapter, the same system simulation comparison with louvered fins is presented in this section to evaluate the louvered fin effect. Besides the coil geometry, the same system configuration shown in Table 4.3 and the same range of boundary conditions are used to run this simulation. Table 5.6 shows the coil specifications for this test. Note that the coil specifications are changed to the louvered fin coils that have been tested in this experiment.

Table 5.6 Coil specifications for the evaluation of row-by-row louvered fin coefficients.

Parameters	Condenser	Evaporator
Coil width (m)	1.4	0.5
Coil height (m)	1	1
No. of rows	1	2 to 4
No. of tubes per row	39	39
No. of circuits	3	3
Tube OD (mm)	10	10
Tube ID (mm)	9.4	9.4
Tube spacing (mm)	25.4	25.4
Row spacing (mm)	22	22
Tube type	Smooth	Smooth
Fin thickness (mm)	0.099	0.099
Fin density ($fins.m^{-1}$)	551	551 to 591
Fin type	Louver	Louver

A range of row numbers and fin densities are used in the simulation to include the coil geometry effects in the comparison. Three circuits are used in each coil because of the smaller tube diameter to prevent excessive refrigerant pressure drop. The same coil circuitry shown in Figure 4.15 are used for these coils.

Figures 5.21 and 5.22 compare the simulated system capacities using overall and row-by-row coefficients for different number of rows and fin densities, respectively. As shown in the previous section, the uncertainty of the air side heat transfer correlation is ±10%, which only contributes to about ±0.07% variation in the simulated capacities. The capacity difference in the figures is calculated by:

$$\dot{Q}_{diff} = \frac{\left|\dot{Q}_{rbr} - \dot{Q}_{overall}\right|}{\dot{Q}_{overall}} \times 100\,\% \tag{5.52}$$

Figure 5.21 shows that the capacity difference can be as high as 6% for a 2-row coil. It tends to increase even higher at lower air flow rates. As a result, the error due to the use of overall heat transfer correlation in system simulation can be significant. The figure also shows that as the coil row number increases, the capacity difference decreases. This is due to the fact that most heat transfer takes place at the front rows (the pseudo entrance length effect); the amount of heat transfer in the back rows is not as significant and the heat transfer error due to the use of overall correlation is smaller.

Figure 5.22 shows the effect of fin density for the same simulation. Note that the capacity difference can be as high as 6.5% for the lowest fin density coil. The difference will be higher for lower fin densities or air flow rates. When the fin density increases or the air flow rate increases, the difference becomes smaller. This agrees with the louvered fin analysis in section 5.6. At low fin densities and air flow rates, "duct flow" dominates

and the row-by-row effect is significant, and "boundary layer flow" dominates at high fin densities and air flow rates, the difference between the overall and row-by-row correlations are smaller.

The evaluation results show that strong entrance length and duct flow effects are likely to cause significant error when overall heat transfer correlations are used instead of row-by-row correlations. Flat fin coils exhibit duct flow throughout because there are no cuts on the flat fin surface. As a result, the duct flow effect is even stronger than for the louvered fin coils. Section 4.7 shows that the capacity difference between the overall and row-by-row correlations are higher for flat fin coils. The higher capacity difference shown in the flat fin simulation is also due to the difference in Reynolds numbers. Although the test air flow rates are the same for both flat and louvered fin simulations, the coil dimensions are different. For the coil dimensions of the louvered fin test, the Reynolds number range is:

$$2400 < Re_{Pr} < 5500$$

which is higher than that in the flat fin test ($1300 < Re_{Pr} < 3000$). Figure 5.14 shows that as the Reynolds number increases, all of the heat transfer coefficients tend to converge and the row-by-row effect becomes less significant.

This section shows that the row effect for louvered fin coils is particularly important at low Reynolds numbers, low fin densities and few coil rows. Although the row-by-row correlations are based on a narrow Reynolds number range, they do cover the typical range for heat pump coils. The new louvered fin row-by-row correlations are used in the next chapter for model validation.

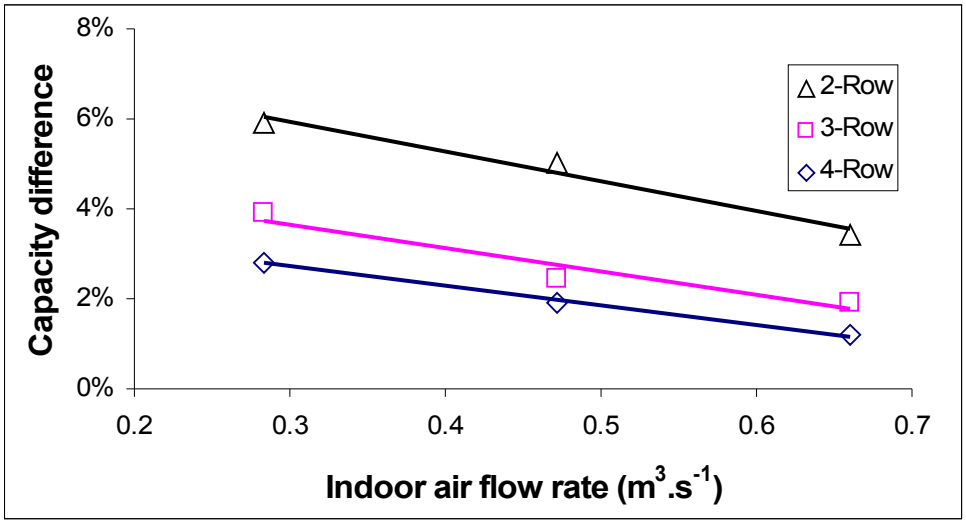

Figure 5.21 Comparison of row-by-row and overall louvered fin heat transfer coefficients for different number of rows with 551 fins.m^{-2} fin density.

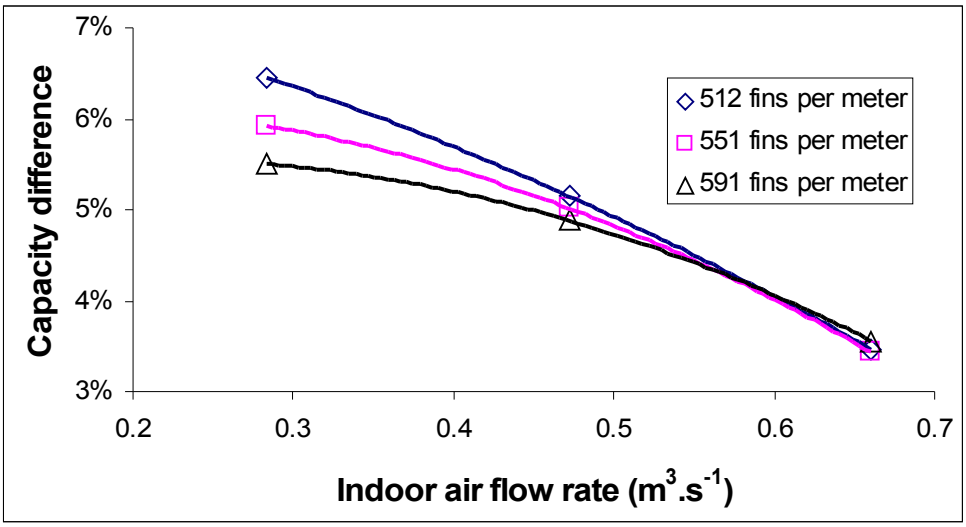

Figure 5.22 Comparison of row-by-row and overall louvered fin heat transfer coefficients for different fin densities with 2-row coils.

6. MODEL VALIDATIONS

6.1. Experiment for Model Validations

Heat pump performance data were collected under various boundary conditions as a part of the York-OCAST project (Weber 2003; Tang 2005). Figure 6.1 shows the schematic for the test facility. A 3-ton unitary heat pump system was used in this experiment.

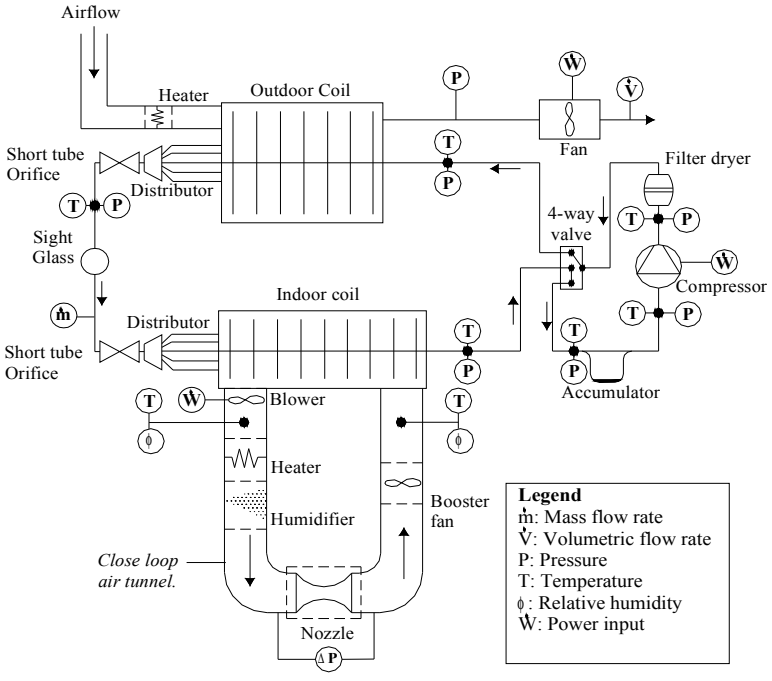

Figure 6.1 Schematics of system experiment (cooling mode operation).

This unit is a single compressor R-22 system. It has a 2-row outdoor and a 3-row indoor coils. Both coils are made of copper tubing and aluminum louvered fins. There are 5

circuits in each coil. The circuits in the outdoor coil are identical in length and design as shown in Figure 6.2, while the circuits in the indoor coil are rather complicated with different circuiting in each branch as shown in Figure 6.3. Table 6.1 lists the dimensions of both coils. Two short tube orifices are used as expansion device in this heat pump system. The one for cooling operation has a 2-mm inside diameter. The other, for heating operation, has a 1.7-mm inside diameter.

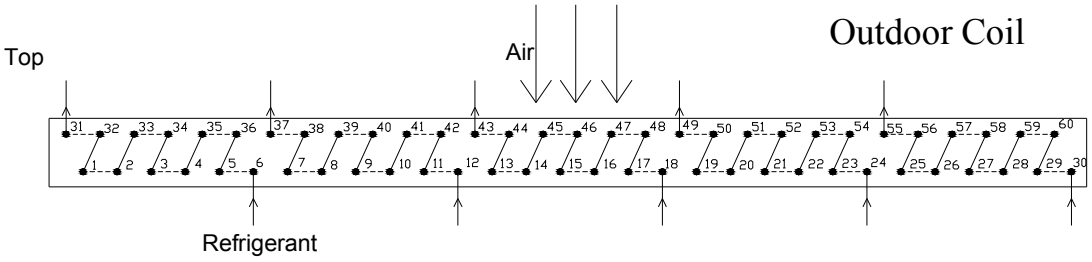

Figure 6.2 Outdoor coil circuitry (Hidden lines indicate invisible side).

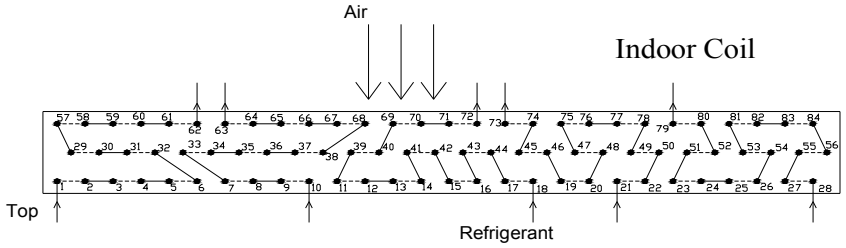

Figure 6.3 Indoor coil circuitry (Hidden lines indicate invisible side).

The air side, refrigerant side, and electrical side measurements were collected at various key locations around the heat pump system as shown in Figure 6.1. Table 6.2 lists all instruments used for the measurements. All instruments were calibrated prior to their use; the uncertainties are also listed in the table. Refrigerant temperatures were approximated by tube surface temperature with thermocouples glued on the tubing surface with highly conductive epoxy. The surface thermocouples were also insulated to minimize the effect of surrounding air temperature. Air temperatures were measured by

thermocouples that were radiation shielded to minimize the radiation exchange between the thermocouple beads and other nearby heat transfer surfaces. Weber (2003) described a detailed uncertainty analysis for this test facility and instrumentation. The uncertainty of measured capacity for the indoor coil and outdoor coil is within ±5% from this instrumentation. The power measurement uncertainty is within ±0.4%.

Table 6.1 Coil geometry.

Geometry	Indoor Coil	Outdoor Coil
Tube outside diameter (after expansion)	10.2 mm	10.2 mm
Tube inside diameter (after expansion)	10.0 mm	10.0 mm
Tube spacing (vertical)	25.4 mm	25.4 mm
Tube spacing (horizontal)	22 mm	22 mm
Coil width (finned length)	0.6 m	1.4 m
Coil height	0.7 m	0.8 m
Fin density	591 fins.m^{-1}	787 fins.m^{-1}
Fin thickness	0.099 mm	0.099 mm

Table 6.2 Instruments and uncertainties for the system tests.

Location	Measurement	Instrument	Uncertainty
Refrigerant Side	Temperature	T-type thermocouples	±0.1 °C
	Pressure	Pressure transducers	±0.13%
	Mass flow rate	Coriolis flow meter	±0.1%
Indoor Air Side	Dry bulb temperature	T-type thermocouples	±0.1 °C
	Relative humidity	Solid state humidity sensor	±2% RH
	Volumetric flow rate	Nozzle and pressure transducers	±1%
Outdoor Air Side	Dry bulb temperature	T-type thermocouples	±0.1 °C
	Volumetric flow rate	Hot wire velocity transducer	±0.5%
Electric	Current	Current transducer	±0.25%
	Voltage	Voltage transducer	±0.25%

The air side boundary conditions for the heat pump can be changed using the following equipment. A variable electric heater with capacity up to 15 kW was used to

adjust the indoor loop air temperature. Different nozzles were used in the indoor loop to alter the air flow rate entering the indoor coil. A humidifier with a maximum capacity up to 5.4 $kg.hr^{-1}$ was used to control the air moisture in the indoor loop. Electric heaters with a maximum capacity of 12 kW were used to obtain the desired outdoor side temperature.

6.2. Test Conditions

A range of experimental data is collected by Tang (2005) for model validations. The heat pump was tested in cooling mode operation where the indoor coil is an evaporator and the outdoor coil is a condenser. The ARI Standard 210/240 (2003) and the manufacturer's catalog were used as guidelines to design the test conditions for this experiment. The ARI steady state rating condition was the baseline case for the test matrix. For this test condition, the outdoor coil entering air temperature is 35 °C dry bulb, the indoor coil entering air temperature is 26.7 °C dry bulb and 19.4 °C wet bulb or 52% relative humidity at the local atmospheric pressure. Since the indoor and outdoor air volumetric flow rates are not specified in the standard, 35 $m^3.min^{-1}$ and 50 $m^3.min^{-1}$ air volumetric flow rates were used for the indoor and outdoor coils, respectively. The 35 $m^3.min^{-1}$ indoor flow rate is the mid range value of the catalog data and the 50 $m^3.min^{-1}$ outdoor flow rate is the rated flow rate that comes with the test system.

Three parameters, the indoor entering dry bulb temperature, the indoor volumetric flow rate, and the outdoor entering dry bulb temperature were varied in the tests. Table 6.3 shows the test conditions for this experiment. For each test, only one of the parameters was changed from the baseline condition. Due to the limitation of the test facility, the extreme conditions such as high indoor air flow rate, relative humidity, and

outdoor temperature were not included.

Table 6.3 Matrix for model validation (52% indoor relative humidity, 50 $m^3.min^{-1}$ outdoor flow rate).

Parameter change	Indoor entering dry bulb temperature	Indoor volumetric flow rate	Outdoor entering dry bulb temperature
Indoor temperature[1]	21 to 29 °C	35 $m^3.min^{-1}$	35 °C
Indoor flow rate[1]	27 °C	22 to 38 $m^3.min^{-1}$	35 °C
Outdoor temperature[2]	27 °C	35 $m^3.min^{-1}$	28 to 46 °C

1-Includes ARI steady state rating condition
2-Includes ARI steady state rating, dry coil, and maximum conditions.

Measured data were taken every one minute until steady state was achieved. The 10-minute average values after reaching steady state condition were collected for model validation. These measured data are used to validate the models at both component and system levels. Since the error of individual models may have a cumulative effect on the overall system simulation (Domanski and Didion 1983), the system level validation can reveal the integrated performance of the component models.

Totally 15 data points are taken for different boundary conditions. They are presented in terms of test numbers in the following sections. The meanings of the test numbers are:

- Tests 1 to 5: Increasing of outdoor air temperature
- Tests 6 to 10: Increasing of indoor air temperature
- Tests 11 to 15: Increasing of indoor air flow rate

6.3. Component Level Validation

In the component level validation, both air side and refrigerant side boundary conditions to the component model are directly from measured data in order to validate

each component model individually. The predicted outputs are compared to the measured data to assess the model accuracy. The major component models: compressor, short tube orifice, condenser, and evaporator are validated one-by-one as discussed in the following sections.

6.3.1. Compressor

The compressor model calculates the refrigerant mass flow rate and power consumption. It takes the suction and discharged saturation temperatures, and the suction superheat as the boundary condition inputs. Figure 6.4 shows the boundary conditions for the compressor model validation. The saturation temperatures are derived from the pressure measurements and local atmospheric pressure using REFPROP 6.01 (McLinden *et al.* 1998). Their measurement uncertainties are about ±0.2 K. The superheat is relatively constant for all of the test conditions. It is calculated by the pressure and temperature measurements at the compressor suction and its uncertainty is about ±0.25 K as shown in the figure. The heat pump system was run in cooling mode, therefore the outdoor coil is a condenser and the indoor coil is an evaporator. As the outdoor air temperature increases (Tests 1 to 5), the heat pump operates at higher discharge saturation temperature. The suction saturation temperature also increases slightly with the discharge saturation temperature. A similar trend is shown for the variations of indoor temperature (Tests 6 to 10), where the suction saturation temperature increases with the indoor air temperature, and the discharge saturation temperature increases slightly with the suction saturation temperature. The increase of indoor air flow (Tests 11 to 15) has similar effect to the increase of indoor air flow rate, it increases the average temperature across the evaporator. As a result, both the suction and discharge saturation

temperatures increase.

In addition to the boundary conditions, the model also requires the mass flow rate and power coefficients provided by manufacturer to perform the calculations. Each compressor has its unique coefficients. The compressor used in this heat pump is the Copeland ZR34K3-PFV. Table 6.4 lists the mass flow rate and compressor coefficients for this compressor. The compressor manufacturer claims that the accuracy of the coefficients are within ±5%. Note that if the mass flow rate and power are calculated from these coefficients, the units are $lbm.hr^{-1}$ and W, respectively. The calculated mass flow rate is converted to metric unit in this validation.

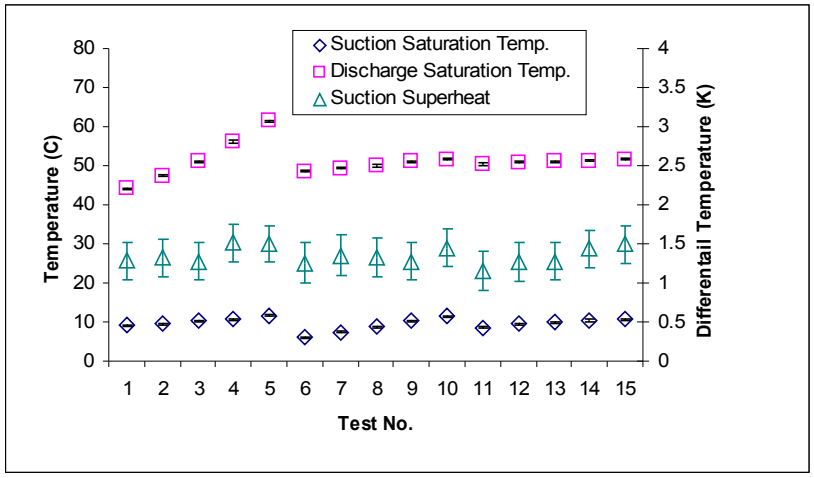

Figure 6.4 Boundary conditions for compressor model validation.

With all the inputs specified, the compressor model is run to predict the mass flow rates and power consumptions. Since the model prediction also depends on the uncertainties of the input data, an sensitivity analysis is conducted for the compressor model. Figure 6.5 shows the sensitivity of the mass flow rate and power consumption with respect to the input data. Each input parameter is perturbed by its measurement uncertainty as shown in the figure. Test 14 is the ARI rating condition and is used as the

baseline case for the uncertainty analysis. Note that the saturation temperatures are the most sensitive parameters to the compressor model but the uncertainties are relatively small. On the other hand, the uncertainty of the superheat is relatively high but its sensitivity is small. The propagated uncertainties to the predicted mass flow rate and power consumption are less than ±0.5% and ±0.25%, respectively, which are lower than the ±5% uncertainty of the compressor coefficients.

Table 6.4 Coefficients for the Copeland compressor ZR34K3-PFV.

No.	Mass flow rate	Power
1	216.9967	15.04447
2	4.735195	-2.17454
3	0.277542	30.12571
4	0.034808	-0.005012
5	0.006066	0.032241
6	-0.004003	-0.210031
7	0.00027	0.000338
8	-7.69E-05	-0.000422
9	-1.18E-05	-0.000143
10	1.72E-06	0.001267

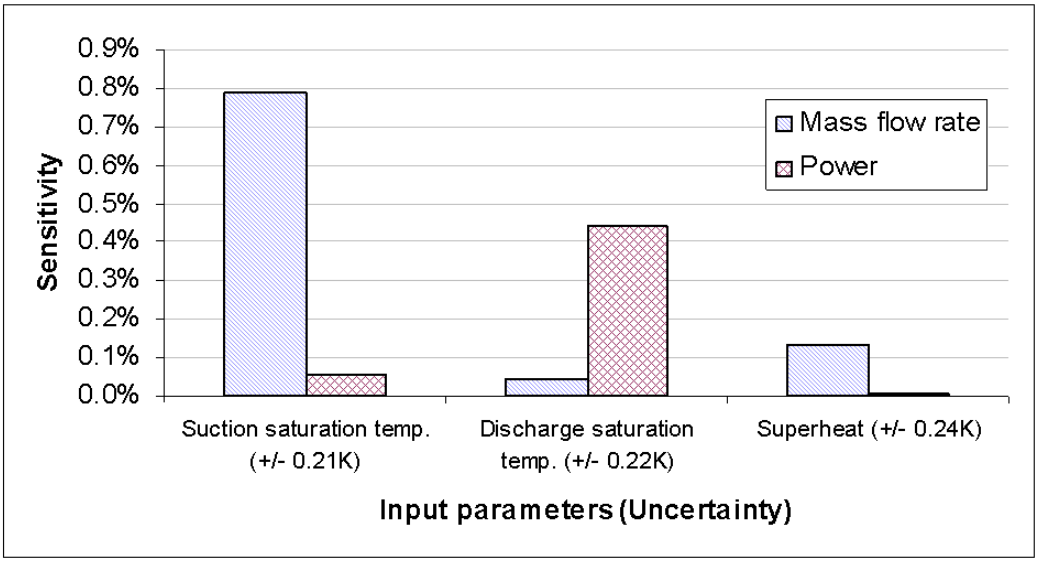

Figure 6.5 Sensitivity analysis for the compressor model.

Figure 6.6 shows the predicted mass flow rate along with the measured values. Note that the small bars in the figure represent the uncertainties due to measurements. The uncertainty of the measured data is ±0.1%. The measured mass flow rates show an increasing trend for all test conditions because the increasing suction temperatures as shown in Figure 6.4. The validation shows that the model is able to predict this trend consistently with the experimental data. A majority of the data points are slightly underpredicted by the model, however all of the data points are within ±5%.

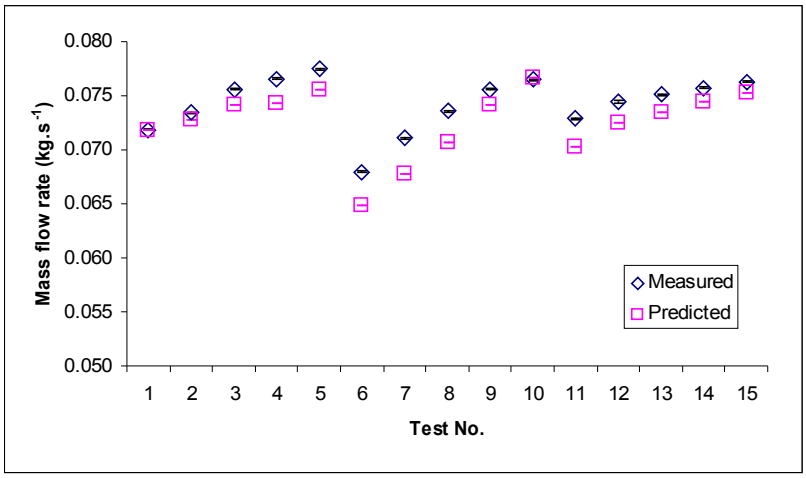

Figure 6.6 Compressor model validation: Mass flow rate.

The validation of the power consumption is shown in Figure 6.7. The measured data show that the power consumption is relatively constant for Tests 6 to 15 because they have relatively constant discharge to suction pressure (or saturation temperature) ratios. On the other hand, the pressure ratio increases more significantly for the Tests 1 to 5 and hence the change in power consumption is more obvious. All of the predicted data are in excellent agreement with the measured values. The difference between the measured and predicted data is well within ±5%. Considering the uncertainties of the measurements and compressor coefficients, the compressor model predictions are

satisfactory.

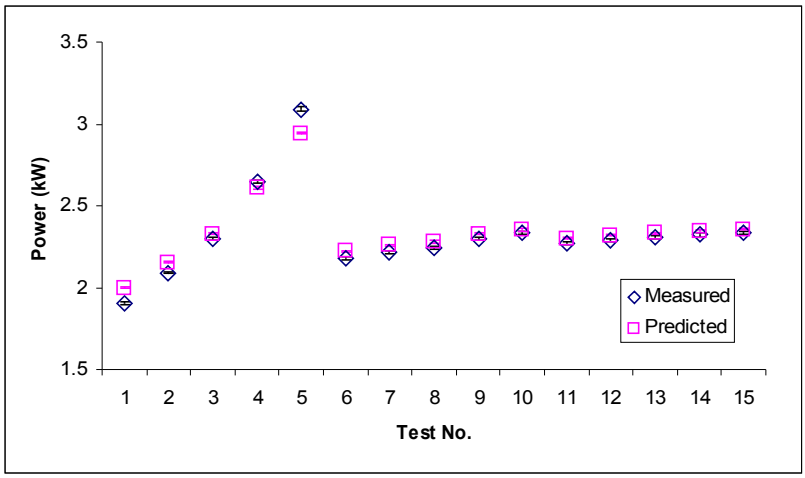

Figure 6.7 Validation of compressor model: Power consumption.

6.3.2. Short Tube Orifice

The short tube orifice model calculates the refrigerant mass flow based on the short tube geometry and boundary conditions. Figure 6.8 shows the boundary conditions for the model validation. Only the inlet refrigerant pressure and subcooling are required for the model. The uncertainties for the pressure and subcooling are about ±0.13% and ±0.15 K, respectively. Note that the inlet pressure changes in the same way as the discharge saturation temperature for the same reasons discussed above. The measured data show that the subcooling decreases with increasing outdoor temperature (Tests 1 to 5) because the temperature driving potential between the refrigerant and air sides are decreased, and result in less heat transfer capacity. But when the indoor air temperature (Tests 6 to 10) or the air flow rate (Tests 11 to 15) increases, the indoor coil capacity increases, and therefore the subcooling also increases accordingly.

Figure 6.9 shows the sensitivity of the inlet pressure and subcooling to the refrigerant mass flow rate. The input parameters are perturbed by their measurement

uncertainties as shown in the figure. Note that the model is slightly more sensitive to the inlet subcooling. However, due to the measurement uncertainties are small, the propagated uncertainty in predicted mass flow rate is less than ±0.2%.

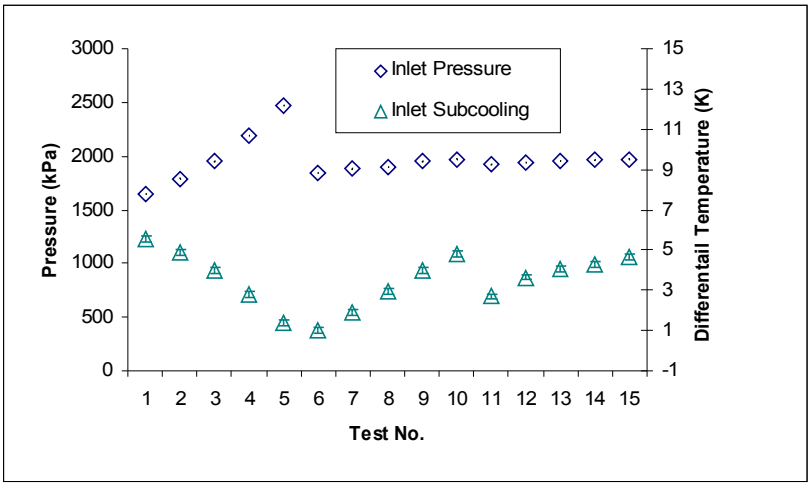

Figure 6.8 Boundary conditions for short tube orifice model validation.

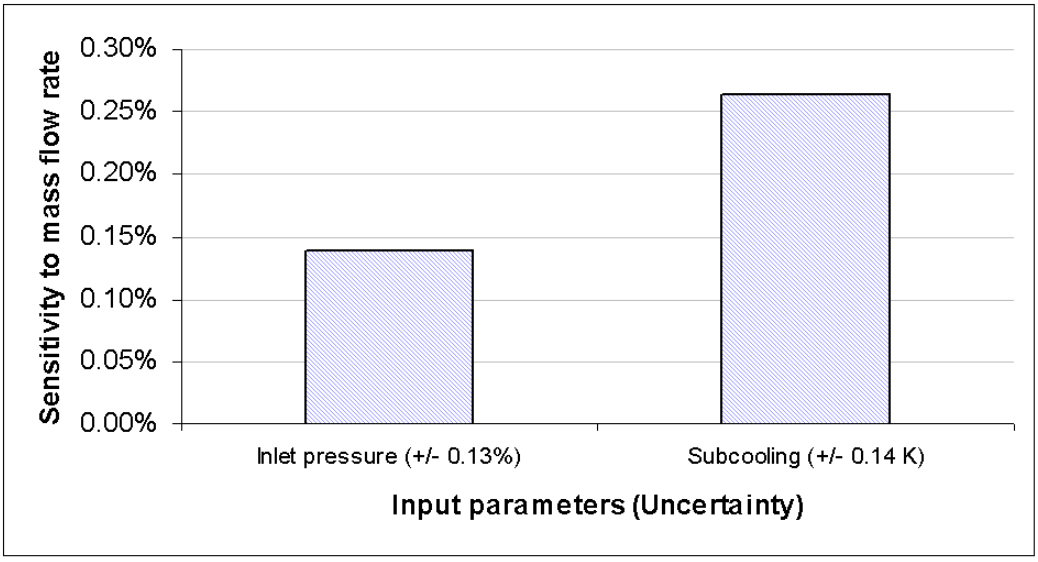

Figure 6.9 Sensitivity analysis for the short tube model.

Figure 6.10 shows the validation results for the short tube orifice model. The

same measured mass flow rate data used in the compressor validation are shown in this figure. It shows that the orifice model is able to predict the measured data very well. The model tends to overpredict the measured data slightly but all of the data are still well within ±5%, which is also less than the ±10% model accuracy (Payne and O'Neal 2004).

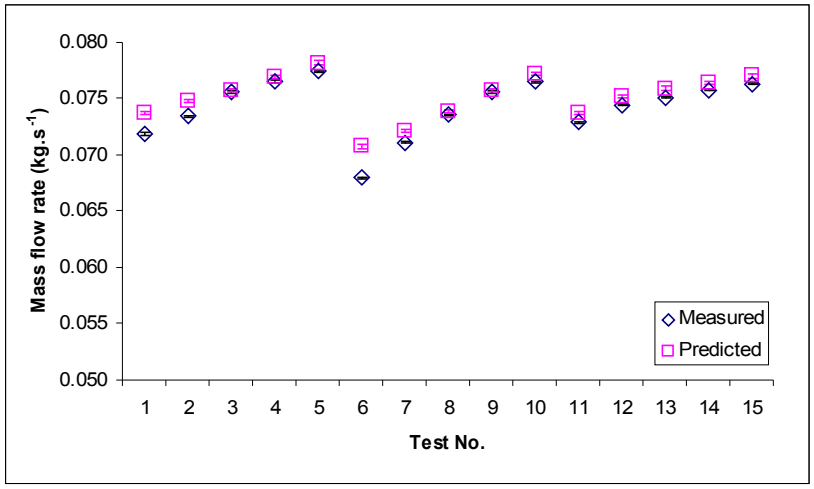

Figure 6.10 Validation of short tube orifice model.

6.3.3. Condenser

The condenser model calculates the heat transfer capacity based on the air and refrigerant side inlet conditions. The air side boundary conditions are the same as the outdoor test conditions in this experiment, while the refrigerant side boundary conditions are shown in Figure 6.11. The measurement uncertainties are ±0.13% and ±0.1 K for the pressure and temperature, respectively. Again, the figures show the trend of the inlet pressure follows the trend of discharge saturation temperature, and the increase in inlet refrigerant temperature is due to the increase in inlet pressure. In addition to the inlet pressure and temperature, the condenser model also requires the refrigerant mass flow

rate as an input. The measured mass flow rates shown in Figure 6.6 or Figure 6.10 are used for this validation.

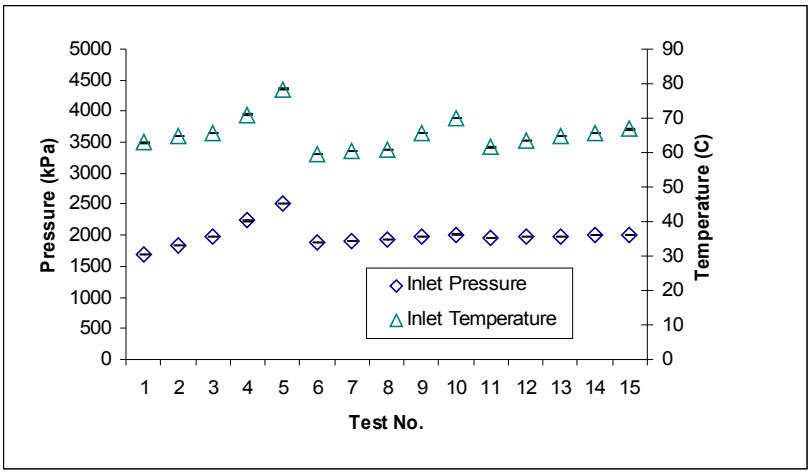

Figure 6.11 Boundary conditions for condenser model validation.

Figure 6.12 shows the sensitivity of the condenser capacity to the input parameters. All of the input parameters are perturbed by their uncertainties as shown in the figure. Note that the air side parameters dominates. The air side dry bulb temperature is the most dominant term, followed by the air flow rate. The uncertainties in input parameters contribute to about ±0.3% uncertainty in predicted capacity.

Figure 6.13 shows the comparison of the predicted capacities to the measured capacities. The measured capacities shown in the figure are the average of the air and refrigerant side capacities. The heat balance between the air and refrigerant sides is within the ±5% range for all measured data. Note that the measured capacities follow the trend of the measured subcooling as in shown in Figure 6.8. More subcooling indicates higher capacity. The uncertainties for measured and predicted data from experiment are also shown in the figure.

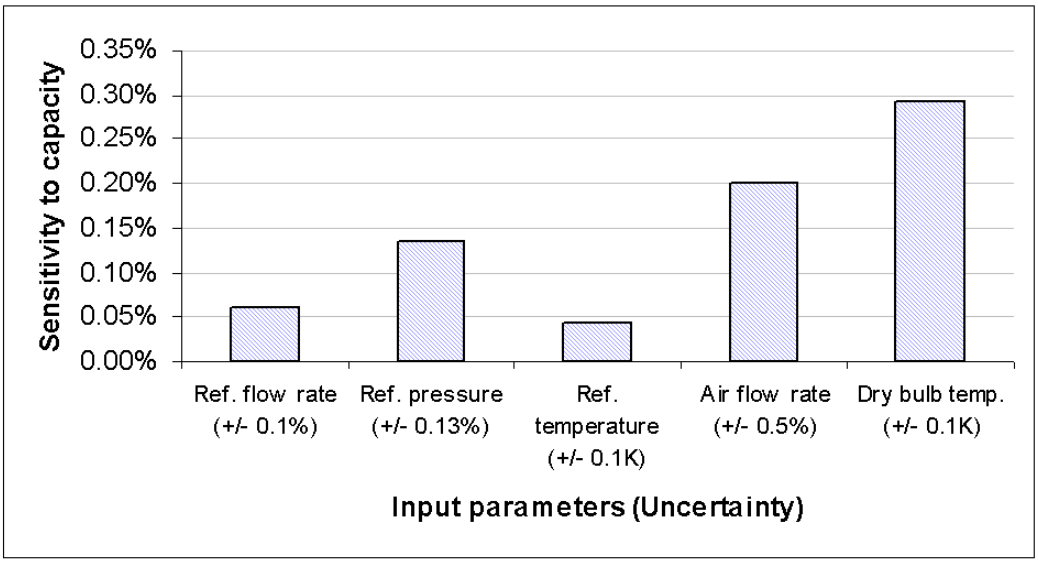

Figure 6.12 Sensitivity analysis for the condenser model.

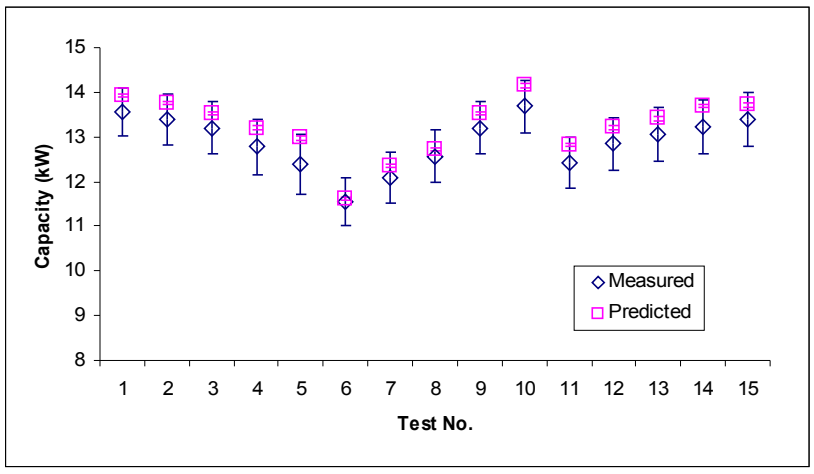

Figure 6.13 Validation of condenser model.

The validation results show that the condenser model is able to predict the capacity very well. Although the model tends to overpredict the measured capacity, all the data points are within the ±5% uncertainty interval (Weber 2003). The air side Reynolds number for this validation is only about 1700, which is considered low enough to have significant coil row effect according to the previous analysis. However, since the

use of row-by-row correlations has that accounted for in this validation, the results are satisfactory.

6.3.4. Evaporator

Similar to the condenser model, the evaporator model calculates the capacity from the inlet air and refrigerant side conditions. The air side conditions are simple to apply because they are the same as indoor conditions of the test matrix. However, the refrigerant side inlet conditions are not as straightforward. Since the inlet conditions to the evaporator are two-phase, a state point cannot be determined by pressure and temperature measurements only. In this validation and also in the later system level simulation, it is assumed that the refrigerant enthalpy does not change from the expansion device inlet to the evaporator inlet, therefore the enthalpy at the expansion device inlet is used for the evaporator model input. However, the enthalpy alone is not enough to determine the inlet refrigerant state. Either the refrigerant temperature or pressure is needed. Neither of them is measured in this experiment because there is a distributor at the evaporator inlet. Pressure and temperature changes across the distributor are not well defined and they would introduce other measurement uncertainties. Therefore, in this validation, an iteration scheme is used to run the evaporator model. Since the evaporator outlet pressure was measured, the evaporator model is run iteratively by adjusting its inlet pressure until its outlet pressure matches the measured value.

Figure 6.14 shows the refrigerant side input data for the evaporator model. Uncertainty bars are also shown in the figure. The measurement uncertainties for the outlet pressure and inlet enthalpy are ±0.13% and ±6.3 $kJ.kg^{-1}$, respectively. The trends of the outlet pressure and inlet enthalpy are due to the same reasons for the changes in

suction saturation temperature and subcooling, as discussed before. Refrigerant mass flow rate is also an input to the evaporator model. The measured mass flow rates shown in Figure 6.6 or Figure 6.10 are used to run the model.

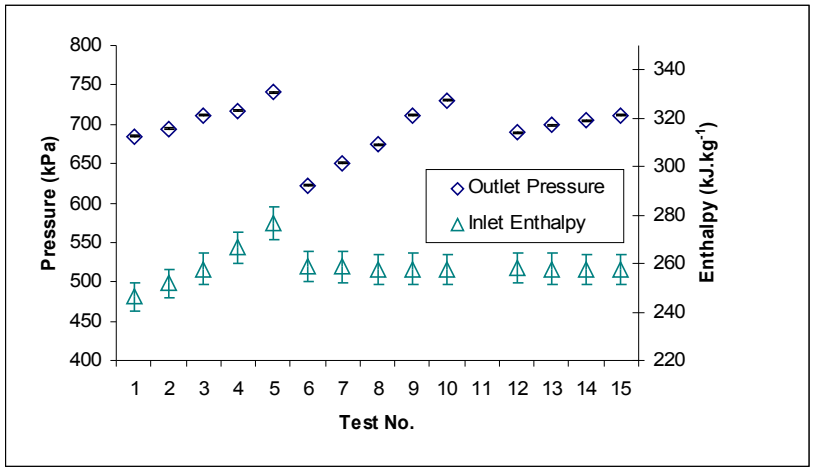

Figure 6.14 Boundary conditions for evaporator model validation.

Figure 6.15 shows the sensitivity of the evaporator capacity with respect to the input parameters. All of the input parameters are perturbed by their measurement uncertainties. The figure shows that the relative humidity is the most sensitive parameter because of the wet surface heat transfer at the evaporator and its relatively high measurement uncertainty. Refrigerant inlet enthalpy is the second most sensitive parameter because of its high uncertainty. On the contrary to the condenser model, the air dry bulb temperature is the least sensitive parameter because the wet surface heat transfer dominates and the measurement uncertainty for dry bulb temperature is relatively small. Due to the high sensitivity and uncertainty in relative humidity, the propagated uncertainty in predicted capacity also increases. It is about ±3% in this validation.

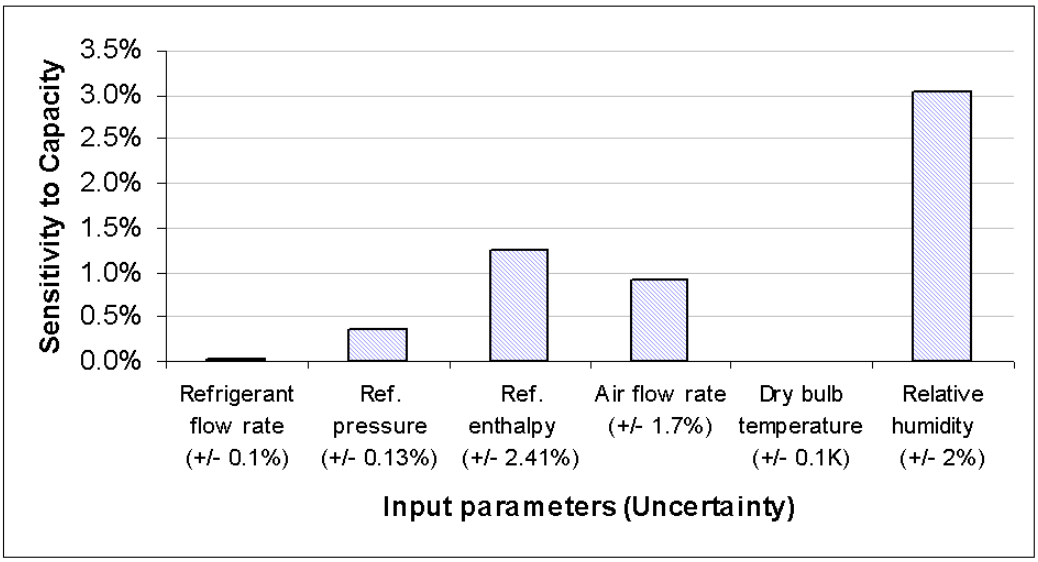

Figure 6.15 Sensitivity analysis for the evaporator model.

Figure 6.16 shows the measured and predicted capacities for all test conditions. The measured capacities are also the average values from the air and refrigerant side measurements. Only the data with less than ±5% heat balances are shown. Note that the lowest indoor flow rate point (Test 11) is discarded because its heat balance is more than ±6% (ARI 2003). The high heat balance is likely due to air leakage from the indoor air loop where the small air flow nozzle causes high duct pressure for this test. All the measured capacities follow the same trend as the condenser capacities.

With all the uncertainties taken into account, the validation results are satisfactory and are able to follow the same trend as the measured data. Although the air side Reynolds number is quite low and only ranges from 2400 to 3400 in this validation, the use of row-by-row correlations has the row effect accounted for in this validation. All of the data are within the uncertainty interval.

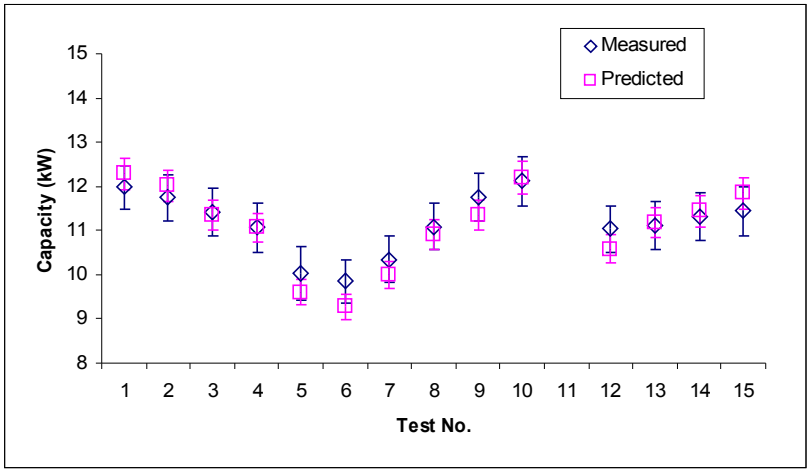

Figure 6.16 Validation of evaporator model.

6.4. System Level Validation

In the component level validation, all of the component models predicted satisfactory results against the experimental data. However, they are all based on the measured inputs and there are still some deviations between the predicted and measured data. In the system level validation, all of the components are linked together. The outputs of one model are the inputs to other models. As a result, the deviations in the components level validation may be accumulated or canceled out. This effect can only be validated in terms of system level simulation. The following system parameters, which are of interest to heat pump designers, are used for this validation.

- Saturation temperatures
- System capacity
- Sensible heat ratio (SHR)
- Coefficient Of Performance (COP)

Due to the uncertainties in the system charge calculation, Shen *et al.* (2006) suggested that the best way to validate a system level simulation is to specify subcooling and superheat as the boundary conditions. The "Orifice and TXV Design" calculation is used in this validation. Besides the subcooling and superheat, this simulation requires air side inputs that are the same as the test matrix in this experiment. In order to eliminate the modeling uncertainties, the interconnecting pipe temperature changes and compressor heat loss are also inputs to the simulation. The piping temperature changes are measured in this experiment and the compressor heat loss is calculated as follows:

$$\dot{Q}_{net} = \dot{W}_{cmp,act} - \dot{m}_{cmp,act}(i_{ref,out} - i_{ref,in}) \tag{6.1}$$

where the compressor power, mass flow rate, inlet and outlet enthalpies are all measured in this experiment. Table 6.5 summarizes all refrigerant side inputs for this validation. Notice that there are negative values for the compressor heat loss. The negative sign means a heat gain to the compressor. It is due to the fact the compressor loads are much less for these conditions, and consequently the power consumption of the compressor is less. In addition, since the compressor is located at the condenser coil outlet, the hot air leaving the coil is higher than the compressor case temperature at these test conditions.

Figure 6.17 shows the sensitivity analysis for the system simulation in terms of the input parameters. The uncertainties of the input parameters are also shown in the figure and are used for perturbations in the sensitivity calculations. Note that the most sensitive parameters are the evaporator relative humidity and suction line temperature change respectively for the air side and refrigerant side. Since this analysis is based on a cooling mode simulation, the impact of the evaporator relative humidity is high, as discussed in the evaporator validation. In consequence, the sensitivity of relative

humidity also propagates to other system parameters like sensible heat ratio and COP. On the refrigerant side, since the suction temperature change has direct impact to the suction saturation temperature, it is the most sensitive parameter. The impact to the suction saturation temperature also propagates to the refrigerant mass flow as shown in the compressor validation, which in turn affects the system capacity, sensible heat ratio and COP.

Table 6.5 Refrigerant side boundary conditions for system level validation.

Test No.	ΔT_{sub} (K)	ΔT_{sup} (K)	ΔT_{sucln} (K)	ΔT_{disln} (K)	ΔT_{liqln} (K)	$\dot{Q}_{net}$ (%)
1	5.5	4.1	2.8	-5.8	-2.1	-8.7%
2	4.9	2.7	1.4	-5.9	-2.5	-3.4%
3	4.0	2.0	0.7	-5.6	-3.1	8.2%
4	2.8	2.1	0.6	-5.9	-3.7	15.1%
5	1.4	2.3	0.8	-6.4	-4.2	18.6%
6	1.0	2.0	0.7	-5.4	-3.7	21.4%
7	1.9	2.1	0.7	-5.3	-3.5	20.9%
8	2.9	1.9	0.5	-5.1	-3.2	20.2%
9	4.0	2.0	0.7	-5.6	-3.1	8.2%
10	4.8	2.3	0.9	-6.2	-2.8	-3.8%
12	3.7	1.7	0.5	-5.1	-2.8	15.6%
13	4.1	1.8	0.5	-5.3	-3.4	11.6%
14	4.3	1.8	0.3	-5.5	-3.1	9.2%
15	4.6	1.9	0.4	-5.7	-3.5	6.3%

The measurement uncertainties in input parameters propagate to the simulation results. For the simulation outputs presented in this section, the uncertainties for capacity, sensible heat ratio, COP, suction and discharge saturation temperatures are ±0.4%, ±0.46%, ±0.36%, ±1.3 K and ±0.5 K, respectively.

With all the refrigerant side parameters specified, only the saturation temperatures are needed to determine the vapor compression cycle on the pressure-enthalpy diagram, given that the pressure drops across the coils and interconnecting pipes are relatively small. The saturation temperatures also determine the refrigerant mass flow rate and

compressor power consumption from the compressor model. Therefore, the saturation temperatures are the most important parameters in the system level simulation.

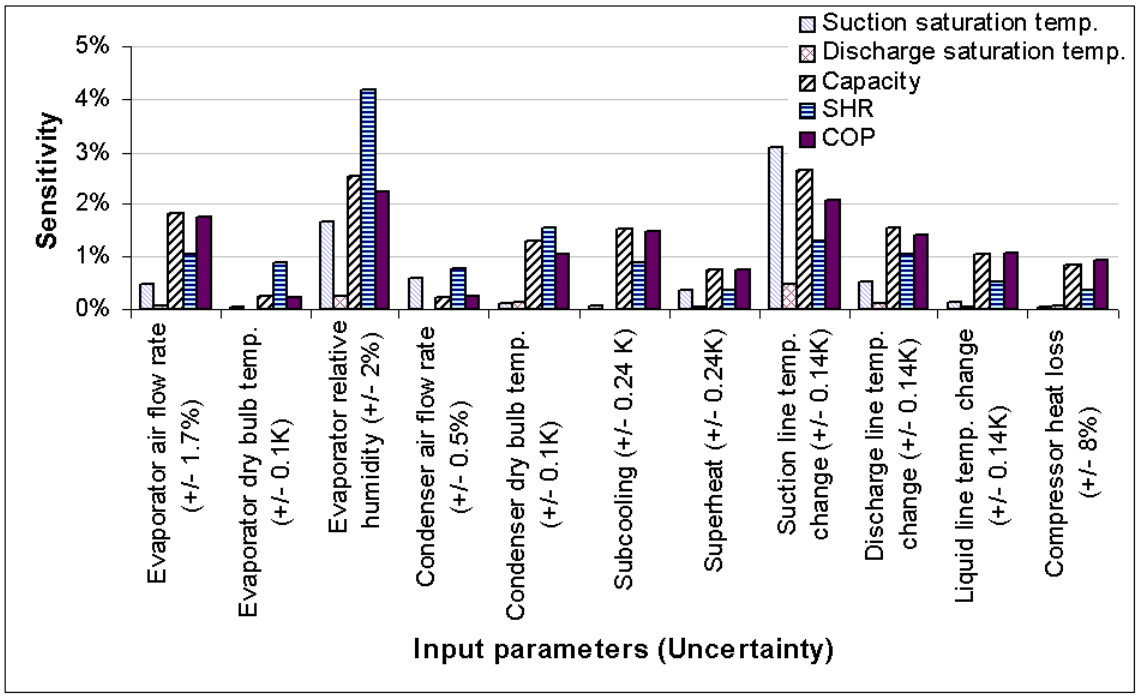

Figure 6.17 Sensitivity analysis for the system simulation.

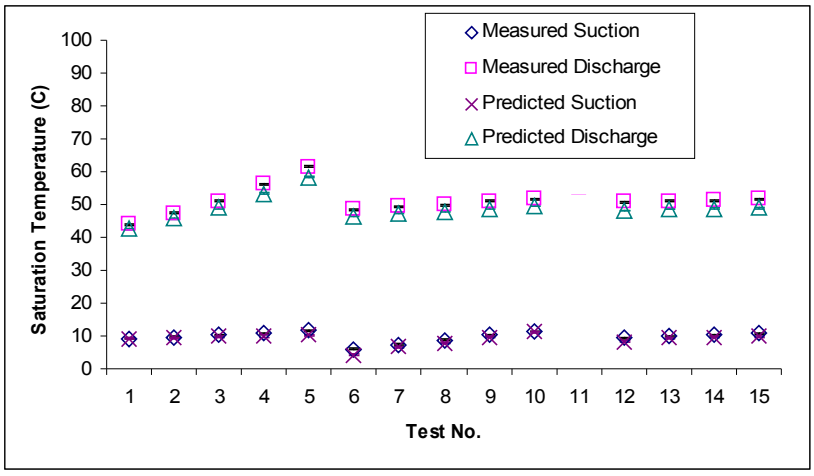

Figure 6.18 System level validation: Saturation temperatures.

Figure 6.18 shows the validation results for the saturation temperatures, where both discharge and suction saturation temperatures are compared. The Test 11 data are discarded in this system level validation as previously discussed. Note that measurement uncertainties do not introduce significant error in the simulation results. The simulation is able to predict the saturation temperatures very well. All of the predicted data are able to follow the trends of the experimental data. The saturation temperature validation results are satisfactory. All of the predicted results show less than ±5% error.

Figure 6.19 shows the system capacity validation. Note that the capacities shown in the figure do not include the heat generated from the indoor fan motor. The heat generated from the fan motor is input to the simulation and therefore it is not included. Since the system was run in cooling mode, the measured data shown in the figure are identical to the measured capacities in the evaporator model validation. Note that uncertainty bars for measurement and simulation are also presented in the figure. The figure shows that the simulation is able to predict the measured data very well. All of the predicted data are able to follow the trend of the measured data and are within the uncertainty interval of the measurements.

The component integration effect can be also seen from Figure 6.19. Compared to the evaporator model validation (Figure 6.16), the simulated capacities in the system level are slightly different. It is due to the difference in refrigerant side boundary conditions, the system level simulation predicted different saturation temperatures, this difference propagates to the system capacities. But since the predicted saturation temperatures agree very well with the measured values, the change in system capacity is small.

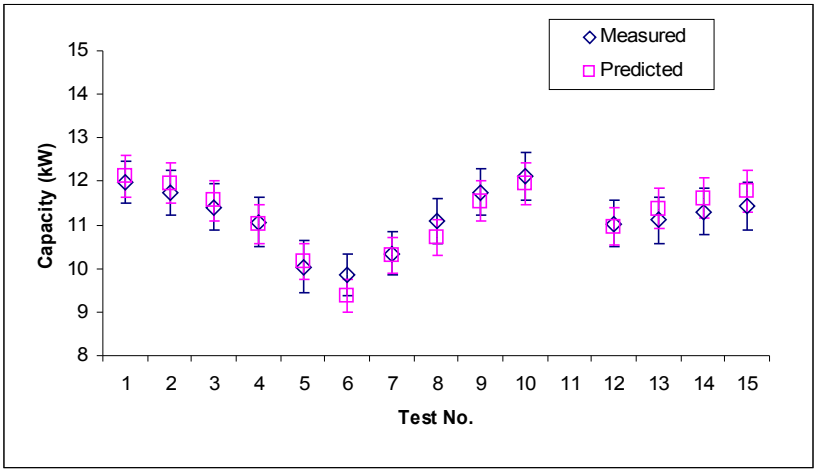

Figure 6.19 System level validation: System capacity.

Figure 6.20 compares the measured and predicted sensible heat ratio. The sensible heat ratio is defined as the ratio of sensible to total system capacities. Similar to the system capacity validation, the data shown in the figure do not include any fan motor heat. Since the high sensitivity and uncertainty of the relative humidity, the uncertainty in the simulation results is also high. The figure shows that the sensible heat ratio increases with outdoor air temperature (Tests 1 to 5) because the refrigerant temperature increases at the indoor coil and results in higher coil surface temperature.

Dehumidification only occurs when the coil surface temperature is lower then the incoming dew point temperature. The increase in coil surface temperature lessens the dehumidification and results in higher sensible heat ratio. For Tests 6 to 10, since only the indoor dry bulb temperature increases and the relative humidity is constant, the increase in dry bulb temperature increases the entering dew point temperature. As a result, the dehumidification increases and the sensible heat ratio decreases. Increasing the indoor air flow rate (Tests 12 to 15) increases the refrigerant temperature at the indoor coil, increases the coil surface temperature, and decreases the sensible heat ratio. The

simulations are able to predict all of these trends consistently.

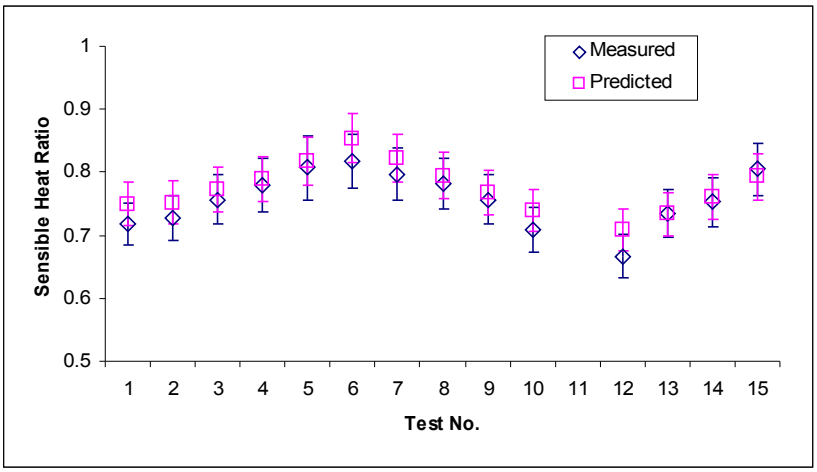

Figure 6.20 System level validation: Sensible heat ratio.

The sensible heat ratio validation also shows that the Harms *et al.* (2003) dehumidification model is able to predict accurate results. Although the dry surface air side correlations are used for these validations, the predicted results are satisfactory. All of the predicted sensible heat ratios are within the uncertainty level compared to the measured data.

The final system parameter validated in the system level validation is the system COP. It is defined as the ratio of energy supply to energy input. However, the COP defined in this validation is the ratio of system capacity to compressor power consumption. The power consumptions by the indoor and outdoor fans are not included because they are inputs to this simulation. Figure 6.21 shows the validation results for the system COP. Note that the COP decreases with increasing outdoor temperature (Tests 1 to 5) because the system capacity decreases but the power consumption increases as discussed before. On the other hand, the COP increases for Tests 6 to 15 because both the system capacity and power consumption increase in these conditions. The increase in

system capacity is slightly more significant than power consumption and therefore the COP increases. With all the measurement uncertainties, the validation results show that the simulations are able to predict the measured data reasonably well. All predicted data are able to follow the trend of the measured data and their differences are less then ±0.5 COP. Overall, the COP validation is satisfactory.

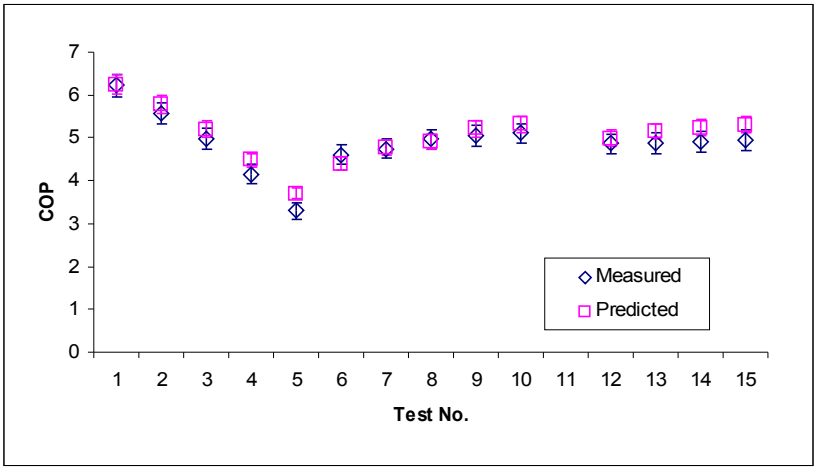

Figure 6.21 System level validation: COP.

The component and system level validations show that the developed models are able to predict the system performance accurately. Although the earlier evaluation sections showed that the coil row effect is significant at low Reynolds numbers, the use of row-by-row correlations in the simulation have that accounted for. The validation results show that the row-by-row louvered fin correlations developed in this research can be used in the system simulation to predict satisfactory results.

6.5. Validation with Additional Data

Although the validation results in the previous sections are promising, they are based on a single system configuration. In order to generalize the validation results,

additional data were collected at the York laboratory in Norman, Oklahoma. Thirty one different systems are used to extend the validation as shown Table 6.6. A range of system configurations are included, i.e. package systems, split systems, heat pumps (HP), and air conditioners (A/C). These systems are charged with either R22 and R410A. The system size ranges from 2 to 20 tons of capacity. The systems with less than 6½ ton capacity have only one compressor. Others are dual compressor systems with two compressors operate simultaneously. The heat exchangers in these systems include 1 to 4-row coils and have fin density from 512 to 787 fins.m^{-1}.

Test data were collected according to the ARI standard 210/240 (2003). The test data included 26 different boundary conditions as shown in Table 6.7. Both cooling and heating data were included for this validation. These conditions were applied to different systems as shown in Table 6.8. Note that the air volumetric flow rates for these conditions are also shown in the table. The complete set of systems and boundary conditions yields 112 additional data sets that can be used for model validation. The same component and system level validations are performed with these additional data sets as shown in the previous sections.

Table 6.6 York data system configuration.

No.	Type	Ton	Ref.	Compressor	Indoor Coil		Outdoor Coil	
1	Package A/C	2	R22	Bristol H29B20UABCA	No. of rows	3	No. of rows	2
					Face area	0.34	Face area	0.85
					Fin density	512	Fin density	591
2	Package A/C	3	R22	Bristol H29B30VABCA	No. of rows	3	No. of rows	2
					Face area	0.34	Face area	0.85
					Fin density	512	Fin density	591
3	Package A/C	3.5	R22	Bristol H20J353ABCA	No. of rows	3	No. of rows	2
					Face area	0.43	Face area	1.05
					Fin density	512	Fin density	591
4	Package A/C	4	R22	Bristol H20J403ABCA	No. of rows	3	No. of rows	2
					Face area	0.51	Face area	1.49
					Fin density	512	Fin density	591

No.	Type	Ton	Ref.	Compressor	Indoor Coil		Outdoor Coil	
5	Package A/C	5	R22	Bristol H23R513ABCA	No. of rows	3	No. of rows	2
					Face area	0.51	Face area	1.49
					Fin density	512	Fin density	591
6	Package HP	3	R22	Bristol H21J32BABCA	No. of rows	4	No. of rows	2
					Face area	0.43	Face area	1.05
					Fin density	512	Fin density	591
7	Package HP	3.5	R22	Bristol H21J38BABCA	No. of rows	4	No. of rows	2
					Face area	0.51	Face area	1.49
					Fin density	512	Fin density	591
8	Package HP	4	R22	Bristol H23C453ABCA	No. of rows	4	No. of rows	2
					Face area	0.51	Face area	1.49
					Fin density	512	Fin density	591
9	Package HP	5	R22	Bristol H23R513ABCA	No. of rows	4	No. of rows	2
					Face area	0.51	Face area	1.49
					Fin density	512	Fin density	591
10	Split A/C	15	R22	Bristol H20R943DBL	No. of rows	3	No. of rows	2
					Face area	0.85	Face area	1.15
					Fin density	512	Fin density	630
11	Split A/C	20	R22	Copeland ZR125KC-TF5	No. of rows	3	No. of rows	2
					Face area	1.05	Face area	1.52
					Fin density	630	Fin density	630
12	Package A/C	7.5	R410A	Bristol H83C383DBDA	No. of rows	3	No. of rows	2
					Face area	0.49	Face area	1.10
					Fin density	591	Fin density	787
13	Package A/C	8.5	R410A	Bristol H83R413DBDA	No. of rows	4	No. of rows	2
					Face area	0.61	Face area	1.35
					Fin density	591	Fin density	787
14	Package A/C	10	R410A	Bristol H83R513DBDA	No. of rows	4	No. of rows	2
					Face area	0.61	Face area	1.35
					Fin density	591	Fin density	787
15	Package A/C	12.5	R410A	Copeland ZP67KCE-TF5	No. of rows	4	No. of rows	2
					Face area	0.61	Face area	2.21
					Fin density	591	Fin density	591
16	Package A/C	3	R22	Bristol H20J293ABCA	No. of rows	3	No. of rows	2
					Face area	0.47	Face area	1.57
					Fin density	512	Fin density	709
17	Package A/C	4	R22	Bristol H20J383ABCA	No. of rows	4	No. of rows	2
					Face area	0.47	Face area	1.57
					Fin density	512	Fin density	709
18	Package A/C	5	R22	Bristol H23R543ABCA	No. of rows	4	No. of rows	2
					Face area	0.47	Face area	1.57
					Fin density	512	Fin density	709
19	Package HP	6.5	R22	Bristol H20R753DBYA	No. of rows	3	No. of rows	1
					Face area	1.23	Face area	2.70
					Fin density	512	Fin density	787
20	Package HP	12.5	R22	Bristol H20R753DBYA	No. of rows	4	No. of rows	2
					Face area	0.61	Face area	1.35
					Fin density	591	Fin density	787
21	Package A/C	7.5	R22	Bristol H28A383DBLA	No. of rows	3	No. of rows	1
					Face area	0.49	Face area	1.35

No.	Type	Ton	Ref.	Compressor	Indoor Coil		Outdoor Coil	
					Fin density	591	Fin density	787
22	Package A/C	10	R22	Bristol H29A503DBLA	No. of rows	3	No. of rows	2
					Face area	0.61	Face area	1.35
					Fin density	591	Fin density	787
23	Package HP	6.5	R410A	Bristol H83C363DBDA	No. of rows	3	No. of rows	2
					Face area	0.49	Face area	1.10
					Fin density	591	Fin density	787
24	Package HP	7.5	R410A	Copeland ZP42K5E-TF6	No. of rows	3	No. of rows	2
					Face area	0.49	Face area	1.10
					Fin density	591	Fin density	787
25	Package HP	8.5	R410A	Bristol H83R443DBDA	No. of rows	4	No. of rows	2
					Face area	0.61	Face area	1.35
					Fin density	591	Fin density	787
26	Package HP	10	R410A	Bristol H83R513DBDA	No. of rows	4	No. of rows	2
					Face area	0.61	Face area	1.35
					Fin density	591	Fin density	787
27	Package HP	12.5	R410A	Bristol H83R686DBDA	No. of rows	4	No. of rows	2
					Face area	0.61	Face area	2.21
					Fin density	591	Fin density	787
28	Package A/C	2.5	R410A	Copeland ZPS26K4E-PFV	No. of rows	3	No. of rows	2
					Face area	0.41	Face area	1.19
					Fin density	591	Fin density	787
29	Package A/C	2	R410A	Copeland ZPS26K4E-PFV	No. of rows	3	No. of rows	2
					Face area	0.41	Face area	1.19
					Fin density	591	Fin density	787
30	Package A/C	3	R22	Bristol H20J323DBL	No. of rows	2	No. of rows	2
					Face area	0.47	Face area	1.57
					Fin density	512	Fin density	709
31	Package A/C	5	R22	Bristol H23R583DBE	No. of rows	4	No. of rows	2
					Face area	0.47	Face area	1.57
					Fin density	512	Fin density	709

Face are is in m^2; Fin density is in $fins.m^{-1}$; A/C – Air conditioner; HP – Heat pump

Table 6.7 York data boundary conditions.

No.	Mode	Indoor dry bulb temp. (ºC)	Indoor wet bulb temp. (ºC)	Outdoor dry bulb temp. (ºC)	Outdoor wet bulb temp. (ºC)
1	Cooling	26.7	12.2	27.8	-
2	Cooling	26.7	12.8	18.3	-
3	Cooling	26.7	12.8	27.8	-
4	Cooling	26.7	13.3	18.3	-
5	Cooling	26.7	13.9	23.9	-
6	Cooling	26.7	13.9	29.4	-
7	Cooling	26.7	13.9	35.0	-
8	Cooling	26.7	13.9	46.1	-
9	Cooling	26.7	16.7	29.4	-
10	Cooling	26.7	16.7	46.1	-
11	Cooling	26.7	19.4	12.8	-
12	Cooling	26.7	19.4	18.3	-
13	Cooling	26.7	19.4	19.4	-
14	Cooling	26.7	19.4	27.8	-
15	Cooling	26.7	19.4	29.4	-
16	Cooling	26.7	19.4	35.0	-
17	Cooling	26.7	19.4	46.1	-
18	Cooling	26.7	22.2	18.3	-
19	Cooling	26.7	22.2	23.9	-
20	Cooling	26.7	22.2	29.4	-
21	Cooling	26.7	22.2	35.0	-
22	Cooling	26.7	22.2	46.1	-
23	Heating	12.8	-	8.3	6.1
24	Heating	21.1	-	8.3	6.1
25	Heating	26.7	-	8.3	6.1
26	Heating	21.1	-	15.6	12.8

Table 6.8 Test conditions for the York systems.

Data set no.	System No.	Indoor flow rate ($m^3.min^{-1}$)	Outdoor flow rate ($m^3.min^{-1}$)	Condition no.
1	1	22.65	62.30	14
2	1	22.65	62.30	16
3	2	33.98	79.29	14
4	3	33.98	79.29	16
5	3	33.98	79.29	14
6	4	38.23	101.94	16
7	4	38.23	101.94	14
8	5	46.72	101.94	16
9	5	46.72	101.94	14
10	6	33.98	80.70	14
11	6	33.98	80.70	24
12	7	39.64	101.94	16
13	7	39.64	101.94	14
14	8	42.48	101.94	16
15	8	42.48	101.94	14

Data set no.	System No.	Indoor flow rate ($m^3.min^{-1}$)	Outdoor flow rate ($m^3.min^{-1}$)	Condition no.
16	9	48.14	101.94	16
17	9	48.14	101.94	14
18	10	84.95	164.24	16
19	10	106.19	164.24	17
20	10	106.19	164.24	8
21	11	113.27	218.04	16
22	11	113.27	218.04	6
23	11	113.27	218.04	7
24	11	113.27	218.04	8
25	11	113.27	218.04	20
26	11	113.27	218.04	9
27	11	113.27	218.04	21
28	11	113.27	218.04	22
29	11	113.27	218.04	17
30	11	113.27	218.04	10
31	11	84.95	218.04	17
32	11	84.95	218.04	15
33	12	31.86	96.28	15
34	13	48.14	124.59	16
35	13	48.14	124.59	11
36	14	48.14	124.59	15
37	15	70.79	198.22	16
38	15	70.79	198.22	17
39	16	33.98	117.51	16
40	16	33.98	117.51	14
41	16	33.98	117.51	1
42	17	45.31	117.51	16
43	17	45.31	117.51	14
44	17	45.31	117.51	1
45	18	50.97	117.51	14
46	18	50.97	117.51	3
47	19	36.81	192.55	16
48	19	36.81	192.55	15
49	19	36.81	192.55	24
50	19	73.20	192.55	26
51	20	87.78	124.59	15
52	20	87.78	124.59	24
53	20	65.10	124.59	24
54	20	70.77	124.59	25
55	20	70.79	124.59	24
56	20	53.01	124.59	24
57	20	70.65	124.59	23
58	20	70.82	124.59	26
59	21	53.80	96.28	15
60	22	56.63	124.59	16
61	22	70.79	124.59	15
62	23	45.31	96.28	15
63	23	45.31	96.28	24
64	23	46.17	96.28	24

Data set no.	System No.	Indoor flow rate ($m^3.min^{-1}$)	Outdoor flow rate ($m^3.min^{-1}$)	Condition no.
65	23	36.78	96.28	24
66	23	36.81	96.28	23
67	23	27.61	96.28	24
68	23	36.81	96.28	24
69	23	36.78	96.28	25
70	24	53.80	96.28	15
71	24	53.80	96.28	24
72	24	53.15	96.28	24
73	24	42.40	96.28	23
74	25	46.72	96.28	16
75	25	59.47	96.28	15
76	25	60.19	96.28	24
77	25	48.34	96.28	26
78	26	52.39	96.28	16
79	26	52.39	96.28	24
80	26	70.79	96.28	17
81	27	56.63	198.22	16
82	27	87.78	198.22	15
83	27	87.78	198.22	24
84	27	70.54	198.22	23
85	27	70.40	198.22	25
86	27	52.80	198.22	24
87	27	86.89	198.22	24
88	28	28.32	67.96	21
89	28	28.32	67.96	18
90	28	28.32	67.96	4
91	28	28.32	67.96	13
92	29	19.82	67.96	12
93	29	19.82	67.96	18
94	29	19.82	67.96	20
95	30	33.98	117.51	16
96	30	33.98	117.51	3
97	30	33.98	117.51	14
98	30	28.32	117.51	14
99	31	48.14	117.51	16
100	31	56.63	117.51	2
101	31	56.63	117.51	16
102	31	56.63	117.51	5
103	31	56.63	117.51	9
104	31	56.63	117.51	15
105	31	56.63	117.51	20
106	31	56.63	117.51	19
107	31	56.63	117.51	18
108	31	56.63	117.51	21
109	31	70.79	117.51	15
110	31	42.48	117.51	16
111	31	42.48	117.51	15
112	31	48.14	117.51	16

6.5.1. Component Level Validation

The York data sets did not include all the measurements shown in Table 6.2. For example, refrigerant mass flow rate is one of the key inputs for the component level validation but most of the York data do not include this measurement. When refrigerant mass flow rate is not available, compressor coefficients are used to estimate the refrigerant mass flow rate. Other differences between the data presented in section 6.3 and the York data is discussed in the following sections.

6.5.1.1. Compressor

Compressor coefficients for mass flow rate and power consumption are obtained from the manufacturers' websites according to the model numbers shown in Table 6.6. Only the data for systems 28 to 31 have mass flow rate measurements, and there are totally 25 data points in this validation set. The input data for this validation set are shown in Table 10.1 in the Appendix. Figure 6.22 compares the predicted mass flow rates versus the measured values. Note that the mass flow rate amongst the systems are different because of varying system sizes and boundary conditions. System 29 has the lowest capacity and the lowest mass flow rates, and System 31 has the highest flow rates and the highest capacity. All of the data agrees well with the predicted values. The differences are within ±5% which is the uncertainty of the compressor coefficients.

Figure 6.23 shows the validation results for compressor power consumption. All 112 data points are included in this validation set. The power consumption ranges from 1 kW to 13 kW for all systems and boundary conditions. The compressor model is able to predict the measured data within ±5%.

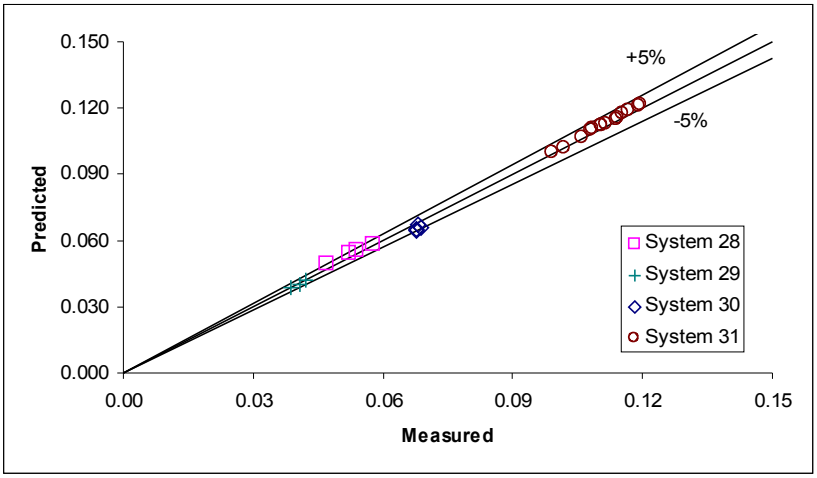

Figure 6.22 Compressor model validation with the York data: Mass flow rate ($kg.s^{-1}$).

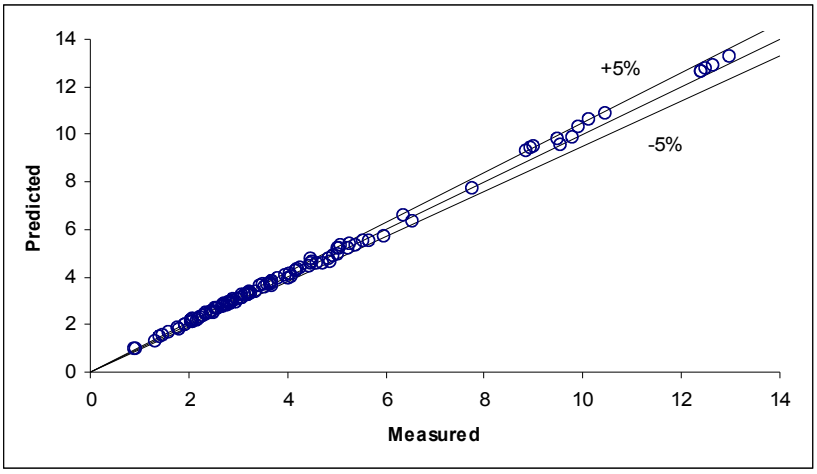

Figure 6.23 Compressor model validation with the York data: Power (kW).

6.5.1.2. Short Tube Orifice

In order to validate the short tube orifice model, the measured refrigerant mass flow rate is needed. However, amongst the data with mass flow rate measurements, only System 31 uses the short tube orifice as expansion device. As a result, only 4 points are

validated with the York data. Table 10.2 in the Appendix shows the input data for this validation set. The validation results are presented in tabular format in Table 6.9. Note that the boundary condition numbers correspond to the numbers in Table 6.7. The measured data are relatively constant for all 4 conditions. All of the predicted data match the measured data within ±5%.

Table 6.9 Short tube model validation with the York data System 30.

Boundary condition no.	Indoor air flow rate ($m^3.min^{-1}$)	Measured ref. flow rate ($kg.s^{-1}$)	Predicted ref. flow rate ($kg.s^{-1}$)	% difference
3	33.98	0.065	0.068	4.6%
14	33.98	0.066	0.069	4.5%
14	28.32	0.065	0.068	4.6%
16	33.98	0.067	0.068	1.5%

6.5.1.3. Condenser

The York data do not include the outdoor coil leaving air temperature. If the system is an air conditioner, the outdoor coil is a condenser. Since the leaving air temperature is unknown, the refrigerant side capacity is used for this validation. However, if the system is a heat pump and operates in heating mode, the indoor coil is a condenser. Both air and refrigerant capacities are measured. The average capacity with ±6% air to refrigerant heat balance (ARI 2003) is used for these heating conditions. Air side boundary conditions for this validation set are shown in Table 6.8. Refrigerant side boundary conditions are shown in Table 10.3 in the Appendix. Figure 6.24 compares the predicted and measured capacities. All 112 data points are included. The capacity ranges from 9 to 50 kW. A few data points are outside the ±5% range. This could be due to the uncertainty in the refrigerant flow rate, which is calculated based on compressor

coefficients, propagated to the capacity calculation. Overall, the validation result is satisfactory and a majority of the data are within the ±5% range.

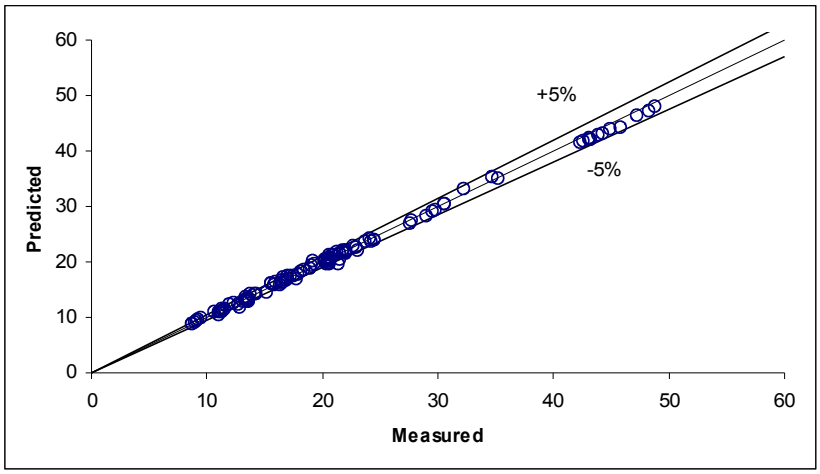

Figure 6.24 Condenser model validation with the York data: Capacity (kW).

6.5.1.4. Evaporator

Since the outdoor coil leaving air temperature is not measured for the York data, the refrigerant side capacity is used for this validation when the system operates at heating mode. For cooling conditions, the average capacity between the air and refrigerant is used. Only the data with less then ±6% heat balance are used according to ARI standard 210/240 (2003). Air side boundary conditions for this validation set are shown in Table 6.8 and refrigerant side boundary conditions are shown in Table 10.4 in the Appendix. Figure 6.25 shows the evaporator model validation result. The capacity ranges from 8 to 41 kW for these systems and boundary conditions. Note that only a few data points are outside the ±5% difference which could be the result of uncertainty in the refrigerant flow rate. Most of the predicted data agree with the measured data within ±5%.

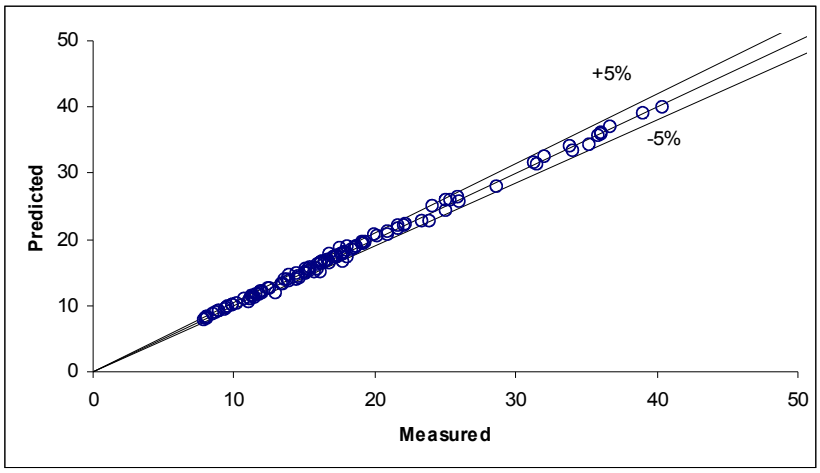

Figure 6.25 Evaporator model validation with the York data: Capacity (kW).

6.5.2. System Level Validation

The system level validation follows the procedure presented in section 6.4. For duo systems, with two compressors operating on two separate refrigerant loops, only one of the systems is simulated. The measured capacity used for this validation is the average of air and refrigerant side capacities. Air side capacity is half of the total system capacity from the measurement. Refrigerant side capacity is derived from refrigerant side measurements from one of the systems.

The same "Orifice and TXV Design" calculation is used for this validation. Table 6.8 shows the air side input data and Table 10.5 in the Appendix shows the refrigerant side input data for this validation. The validation results are presented in terms of saturation temperatures, system capacity, sensible heat ratio, and coefficient of performance as shown in Figures 6.26 to 6.29, respectively. The suction saturation temperature ranges from -6 ºC for the heating condition to 12 ºC for the high ambient outdoor temperature cooling condition. A high percentage error would be misleading for the small saturation temperatures even though the absolute temperature difference is less

then ±2 K. Therefore, the validation results for the saturation temperatures are presented in terms of temperature difference as shown Figure 6.26. The temperature difference is plotted against the test numbers in Table 6.8. Both saturation and discharge saturation temperatures are shown in the figure. The difference between the predicted and measured data points are bounded by the ±2 K lines.

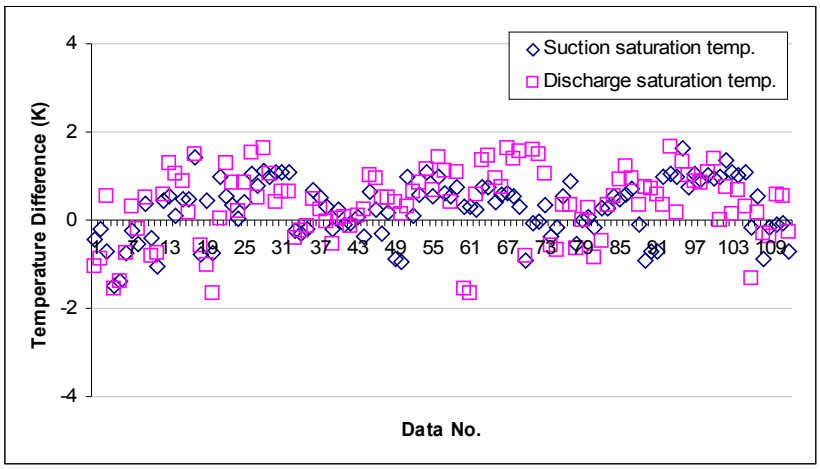

Figure 6.26: System level validation with the York data: Saturation temperature difference between predicted and measured data.

Figure 6.27 shows the validation results for the system capacity. Since the data include both cooling and heating conditions, the system capacities shown in the figure include both cooling and heating capacities. As a result, the data are different from the evaporator validation (Figure 6.25) where only cooling capacities are shown. Figure 6.27 shows that the capacity ranges from 8 to 41 kW which are the lowest and highest capacities in cooling mode. Besides the difference due to the heating capacities, the cooling capacity results are slightly different from the evaporator validation. It is because different saturation temperatures are used for these validations, the system level simulation predicted slightly different saturation temperatures and the resulting capacities are different. However, the difference in saturation temperatures do not contribute

significant error and the system capacity validation result is satisfactory. Almost all of the data points are within ±5%.

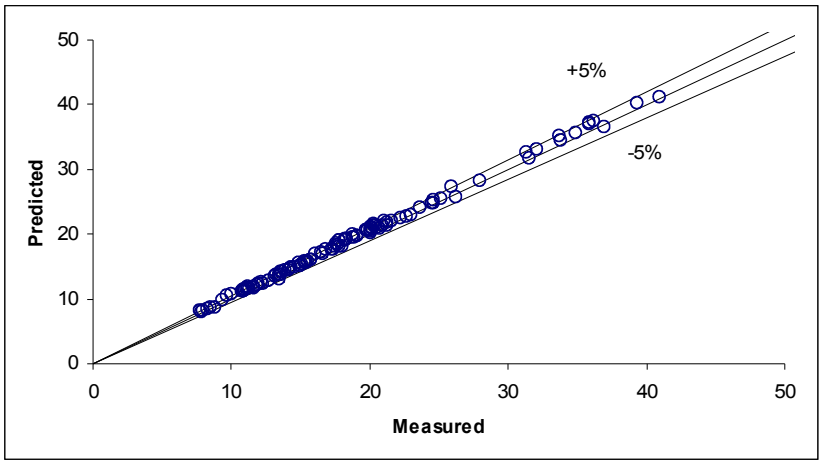

Figure 6.27 System level validation with the York data: System capacity (kW).

Figure 6.28 shows the validation result for the sensible heat ratio. The data points include test conditions that range from humid to dry conditions (SHR from 0.5 to 1). The dry conditions include data points from dry cooling conditions and heating conditions. Most of the data points for this validation are around 0.62 to 0.81 SHR, which include the 0.7 SHR that is the typical value at the ARI rating condition. The figure shows that the simulation slightly over predicted the sensible capacity for a few high humidity points. This error may also be due to experimental uncertainty. Overall, the simulation predicted satisfactory result. Almost all of the data points are well within the ±5% lines.

Figure 6.29 compares the predicted coefficient of performance to the measured data. The data points range from 2.5 to 9 COP. The low COP points represent high outdoor ambient temperatures at cooling mode, and the high COP points are the low outdoor ambient temperatures. All of the heating points have about 4 to 4.5 COP. The

figure shows that predicted data match the measured data very well. Since the saturation temperatures and system capacity validations are satisfactory, the error in the compressor power consumption calculated by the saturation temperatures is small and the predicted data are able to match measured data within ±0.5 COP.

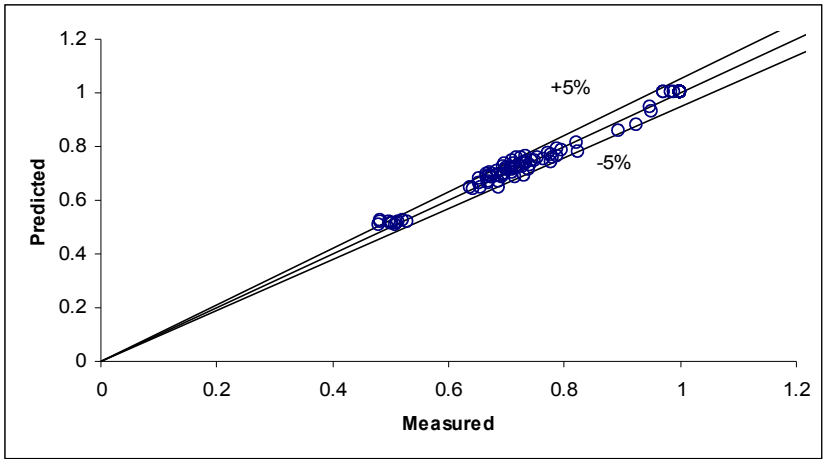

Figure 6.28 System level validation with the York data: Sensible heat ratio.

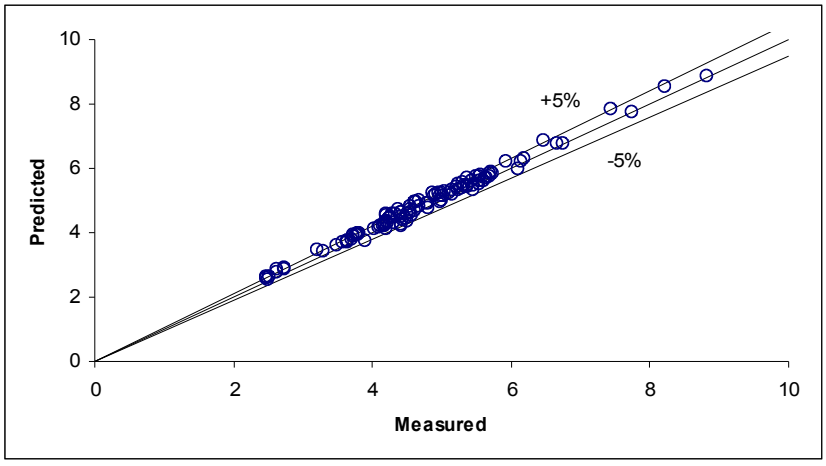

Figure 6.29 System level validation with the York data: COP.

7. SUMMARY AND RECOMMENDATIONS

7.1. Summary of Results

A computer program has been developed to help heat pump manufacturers simulate design and off-design operating conditions of their equipment. Use of the program is expected to reduce the cost to obtain system performance data from the test room. The program integrates the best available component models in a successive substitution solver and includes a novel heat exchanger circuit design algorithm and experimentally measured row-by-row air side heat transfer coefficients. In addition, the program includes a method to easily update pure refrigerant and refrigerant mixture properties using the NIST database.

Specific results of this research are summarized as follows:

- A new heat pump simulation program has been developed. It has an empirical compressor model (ARI 1999), a segment-by-segment heat exchanger model, and a semi-empirical short tube orifice model (Payne and O'Neal 2004). The segment-by-segment heat exchanger model, which calculates the saturation temperature locally at each segment, is able to account for the temperature glide characteristic in refrigerant mixtures. The component models are integrated in this simulation program to meet different calculation needs for system design and simulation. Systems with either a short tube orifice or a TXV can be simulated by

this program.

- The nodal admittance formulation (Vlach and Singhal 1993) is proposed to handle the complex heat exchanger problem. Previous circuit models either have limitations regarding circuit patterns or required boundary conditions. The proposed circuiting algorithm relaxes these constraints and provides a more flexible simulation environment for circuit design. A model evaluation shows that the proposed method is able to simulate different coil circuitries and differentiate between circuit performance.

- A new table format is presented to accommodate both pure refrigerant and refrigerant mixtures. The table look-up method is used in this simulation program because it is more efficient compared to the REFPROP calling routines (Domanski 1999). But due to the temperature glide in refrigerant mixtures, there are two different saturation pressures at a given saturation temperature. The new table format generalizes the difference between pure refrigerants and refrigerant mixtures without the need to change the calling syntax in the program. As a result, new refrigerant can be easily added to the program as long as the table format is consistent.

- A new set of louvered fin row-by-row heat transfer correlations have been experimentally developed and analyzed. Pseudo entrance length and Nusselt number are used in the correlations to account for the entrance length effect in the row-by-row heat transfer coefficients. The correlations can be used for 1 to 4-row coils with fin density from 512 fin.m^{-1} to 787 fin.m^{-1}, and are able to able to predict the measured data within ±10% difference.

The row-by-row correlations can be easily applied to the segment-by-segment heat exchanger model. These new louvered fin row-by-row correlations are implemented in the heat exchange model to account for the coil row effect. For louvered fin coils, the row effect is relatively insignificant compared to flat fins. However the difference in system capacity predicted by the row-by-row correlation can be as high as 6.5% compared to the capacity predicted by the overall correlation. The row effect is particularly noticeable at low Reynolds numbers and low fin densities.

- A conversion method to convert overall heat transfer correlation to row-by-row correlation is introduced. The conversion correlations are also based on the pseudo entrance length and Nusselt number formulation to account for the entrance length effect.

- The simulation program has been validated using the experimental data obtained in the York-OCAST project (Weber 2003; Tang 2005). The validation was conducted in terms of component and systems levels. At the component level, the heat pump components (compressor, condenser, short tube orifice, and evaporator) were validated individually with measured inputs. The models are able to predict the refrigerant mass flow rate, power consumption, and coil capacities accurately. All predicted data are able to follow the trend of experimental data, and the differences are within ±5%.

  At the system level, all components are linked together to simulate the system performance. The inputs to one component model are the outputs from other components. Simulated saturation temperatures, system capacity, sensible heat

ratio, and COP are compared to the experimental data. The validation results show that the integral effect of the component models is minimal. The accurate prediction at the component level is propagated to the system level. All of the predicted data are within ±5% compared to the experimental data. The predicted COP's are within ±0.5 compared to the measured values.

- The simulation program has also been validated using additional data provided by the York International Unitary Product Group. One hundred and twelve different data sets that include 26 different boundary conditions and 31 different system configurations were used. Component and system level validation tests were conducted with satisfactory results. The differences in refrigerant mass flow, compressor power consumption, condenser and evaporator capacities, and sensible heat ratio are all within ±5%. The saturation temperature differences are within ±2 K and the COP differences are within ±0.5 for all data points.

7.2. Recommendations for Future Work

Although the validation results showed that the new simulation program is able to accurately predict heat pump performance over a wide range of operating conditions and configurations, there are still limitations in terms of input data and assumptions in this simulation program. A list of recommendations with respect to the simulation capabilities are summarized as follows:

- *Row-by-row heat transfer correlations:* Row-by-row heat transfer data are still rare in the literature. The current row-by-row heat transfer correlations and conversion method are for a specific louvered fin type. Only the fin density effect

was included in this study. The louvered geometry effect, such as the louver angle, louver pitch, and number of louvers, etc. can be also brought into the picture to generalize the correlations and conversion method.

- *Heat transfer from interconnecting pipes:* Currently, the heat transfer from interconnecting pipes are accounted for by inputting the temperature change across each interconnecting pipe to the simulation. The heat transfer can directly alter the boundary conditions especially for the "Orifice Design Calculation" where the subcooling and superheat are specified. If this heat transfer is not taken into account, the simulation solution will converge to different saturation temperatures and the resulting capacity will be off too. It is particularly important for the suction line because it is the most sensitive refrigerant side input parameter to the system simulation. For the experimental data in this research, the refrigerant was single-phase in the interconnecting pipes and the heat transfer could be estimated by the temperature measurement. However, if the refrigerant is two-phase, the temperature measurement can not be used to estimate the heat transfer anymore. It would be desirable to be able to calculate the heat transfer from the interconnecting pipes based on the ambient condition.

- *Compressor heat loss:* Similar to the heat transfer from interconnecting pipes , the compressor heat loss is also an input to the simulation. It can affect the entire system simulation if it is not taken into account. If refrigerant side measurements are available, the compressor heat loss can be estimated from the refrigerant side. However, refrigerant side measurements are not always available for general simulation. An accurate compressor heat loss model from the air side is desirable.

The model can be based on the compressor operating condition, location of the compressor, and its surrounding temperature.

- *Multi-system simulation:* For high tonnage systems, there are often more than one compressor. The compressors may operate on different refrigerant loops or on the same loop. The systems with multiple compressors on a single loop are advantageous from a control's point of view. The simulation capacity could be extended to simulate such systems.

- *Refrigerant data*: The model validations only include two refrigerants, i.e. R22 and R410A. However, systems with other refrigerants (e.g. R407C) are also available in the industry. The simulation program is capable of simulating different kinds of refrigerant because of the flexibility of the REFPROP table. Experimental data with other refrigerants are needed to extend the validation scope of this simulation program.

- *Fan power consumptions*: The measured power consumption of the indoor and outdoor fans are inputs to the current simulation program. However, they may not be immediately known to the system design engineers because they are related to the fan location, coil geometry, and the geometry of the system compartment. A CFD analysis can be used to determine the power consumptions for the heat pump simulation program. This can be done separately from the simulation program because the indoor and outdoor fan power consumptions are kept constant during simulation.

8. REFERENCE

Aaron, D.A. and Domanski, P.A. (1990). "Experimentation, analysis, and correlation of refrigerant-22 flow through short tube restrictors." ASHRAE transactions. Vol. 1 (2), pp. 729-742.

Achaichia, A. and Cowell, T.A. (1988). "Heat transfer and pressure drop characteristics of flat tube and louvered plate fin surfaces." Exp. thermal and fluid sci., 1, pp. 147-157.

ARI (1999). "Positive displacement refrigerant compressor and compressor units." ARI standard 540. Air-conditioning and refrigeration institute. Arlington, Virginia.

ARI (2003). "Unitary air-conditioning and air-source heat pump equipment." ARI standard 210/240. Air-conditioning and refrigeration institute. Arlington, Virginia.

ARI (2004). "Performance rating of liquid-line driers." ARI standard 710. Air-conditioning and refrigeration institute. Arlington, Virginia.

ASHRAE (2000). "Laboratory method of testing fans for aerodynamic performance rating." ANSI/ASHRAE Standard 51. Atlanta, Georgia: American Society of Heating, Refrigerating and Air-Conditioning Engineers, Inc.

ASHRAE (2005). "ASHRAE Handbook - Fundamentals". Atlanta, GA: American Society of Heating, Refrigerating and Air-Conditioning Engineers, Inc.

ASHRAE (2006). "ASHRAE Handbook – Refrigeration". Atlanta, GA: American

Society of Heating, Refrigerating and Air-Conditioning Engineers, Inc.

Baustian, J.J.; Pate, M.B.; and Bergles, A.E. (1986). "Properties of oil-refrigerant liquid mixtures with applications to oil concentration measurement: Part I – Thermophysical and transport properties." ASHRAE transactions, 92(1a), pp. 55-73.

Bell, K. (2006). Personal communications.

Brandemuehl, M. (1993). "HVAC2 Toolkit: Algorithms and Subroutines for Secondary HVAC Systems Energy Calculations". Atlanta, Georgia: American Society of Heating, Refrigerating and Air-Conditioning Engineers, Inc.

Briggs, D.E. and Young, E.H. (1963). "Convective heat transfer and pressure drop of air flowing across triangular pitch banks of finned tube." Chem. Engng. Prog. Sym. Series, 59(41), pp. 1-10.

Bristol (2006). Personal communications.

Buckingham, E. (1914). "On physically similar systems: Illustrations of the use of dimensional equations." Physical Review, 4(4), pp. 345-376.

Chang, W.R.; Wang, C.C.; Tsi, W.C.; and Shyu, R.J. (1995). "Air side performance of louver fin heat exchanger." In proceedings of the 4th ASME/JSME thermal engineering joint conference, 4, 367-372.

Chartrand, G. (1985). "Introductory Graph Theory." New York: Dover, p. 218.

Chen, Y.; Halm, N.P.; Groll, E.A. and Braun, J.E. (2002a). "Mathematical modeling of scroll compressors – part I: compressor process modeling." International journal of refrigeration. Vol. 25, pp. 731-750.

Chen, Y.; Halm, N.P.; Groll, E.A. and Braun, J.E. (2002b). "Mathematical modeling of

scroll compressors – part II: overall scroll compressor modeling." International journal of refrigeration. Vol. 25, pp. 751-764.

Choi, J.Y.; Kedzierski, M. and Domanski, P.A. (1999). "A generalized pressure drop correlation for evaporation and condensation of alternative refrigerants in smooth and microfin tubes." NISTIR 6333. National Institute of Standard and Technology, Gaithersburg, MD.

Copeland (2006). Personal communications.

Crawley, D.B., Lawrie, L.K., Pedersen, C.O., Liesen, R.J., Fisher, D.E., Winkelmann, F.C. and Buhl, W.F. (1998). "EnergyPlus: The New Generation Energy Simulation Program Beyond BLAST and DOE-2." ASES Passive Conference, Albuquerque, New Mexico, Boulder, Colorado.

Gray, D.L. And Webb, R.L. (1986). "Heat transfer and friction correlations for plate finned-tube heat exchangers having plain fins." Proc. 8th heat transfer conference, pp. 2745-2750.

Cremaschi, L. (2004). "Experimental and theoretical investigation of oil retention in vapor compression systems." Ph.D. Dissertation, University of Maryland, College Park, MD.

Cremaschi, L. (2006). Personal communications.

Dabiri, A. E. and Rice, C. K. (1981). "A Compressor Simulation Model with Corrections for the Level of Suction Gas Superheat." ASHRAE Transactions, Vol. 87, Part 2, pp.771-782.

Davenport, C.J. (1983). "Correlation for heat transfer and flow friction characteristics of

louvered fin." AIChE symposium series, 79 (225), pp. 19-27.

Dittus, F.W. And Boelter, L.M.K. (1930). University of California, Berkeley, Publications on Engineering, Vol. 2, p. 443.

Dobson, M.K. (1994). "Heat transfer and flow regimes during condensation in horizontal tubes." University of Illinois at Urbana-Champaign, ACRC TR-57.

Domanski, P.A. (1991). "Simulation of an evaporator with nonuniform one-dimensional air distribution." ASHRAE transactions, 97(1), pp. 793-802.

Domanski, P.A. (1999). "Finned-tube evaporator model with a visual interface." International congress of refrigeration, 20th IIR/IIF proceedings. Sydney, Australia.

Domanski, P.A. and Didion, D. (1983). "Computer modeling of the vapor compression cycle with constant flow area expansion device." Building science series 155. National Bureau of Standards, Washington, D.C.

Eckels, S.J.; Doerr, T.M.; Pate, M.B. (1994a). "In-tube heat transfer and pressure drop of R-134a and ester lubricant mixtures in a smooth tube and a micro-fin tube: part II-condensation." ASHRAE Transactions, v 100, n 2, pp. 283-294.

Eckels, S.J.; Doerr, T.M.; Pate, M.B. (1994b). "In-tube heat transfer and pressure drop of R-134a and ester lubricant mixtures in a smooth tube and a micro-fin tube: part I-evaporation." ASHRAE Transactions, v 100, n 2, pp. 265-282.

Eckels, S.J.; Doerr, T.M. and Pate, M.B. (1998a). "A comparison of the heat transfer and pressure drop performance of R-134a-lubricant mixtures in different diameter smooth tubes and micro-fin tubes." ASHRAE transactions. Vol. 104(1).

Ellison, R.D.; Creswick, F.A. and Jackson, W.L. (1981). "A computer model for air

cooled refrigerant condensers with specified refrigerant circuiting." ASHRAE transactions. Vol. 87(1), pp. 1106-1124.

Fischer, S. K., Rice, C. K. and Jackson, W. L. (1998). "The Oak Ridge Heat Pump Model: Mark III Version Program Documentation." ORNL/TM-10192. Oak Ridge, TN.

Ganguli, A. and Breber, G. (1988). "Row effects in finned tube banks." HTRI report ESG-14, Heat transfer research, Inc., College Station, TX.

Chang, Y.J. and Wang, C.C. (1996). "Air side performance of brazed aluminum heat exchangers." Journal of enhanced heat transfer, 3(1), pp. 15-28.

Gnielinski, V. (1976). "New equation for heat and mass transfer in turbulent pipe and channel flow." Int. Chem. Eng. 16. pp. 359-368.

Graham, D.M.; Kopke, H.R.; Wilson, M.J.; Yashar, D.A.; Chato, J.C.; and Newell, T.A. (1998). "An investigation of void fraction in the stratified annular/intermittent flow regions in smooth, horizontal tubes." ACRC TR-144, Air conditioning and refrigeration center, University of Illinois, Urbana-Champaign, IL.

Gray, D.L. and Webb, R.L. (1986). "Heat transfer and friction correlations for plate finned-tube heat exchangers having plain fins." ASME Proc. Of 8th Int. heat transfer conference. San Francisco: CA.

Halici, F.; Taymaz, I.; Gunduz, M. (2001). "The effect of the number of tube rows on heat, mass and momentum transfer in flat-plate finned tube heat exchangers." Energy, 26, pp. 963-972.

Harms, T.M.; Groll, E.A. and Braun, J.E. (2003). "Accurate charge inventory modeling

for unitary air conditioners." HVAC&R research. Vol. 9(1), pp. 55-77.

Holman, J.P. (1971). "Experimental methods for engineers, 2nd ed." New York, NY: McGraw-Hill, Inc.

Incropera, F.P. and DeWitt, D.P. (1996). "Introduction to heat transfer, 3rd ed." New York, NY: John Wiley & Sons, Inc.

Jensen, M.K. and Jackman, D.L. (1984). "Prediction of nucleate pool boiling heat transfer coefficients of refrigerant-oil mixtures." Journal of heat transfer, 106(1), pp. 184-190.

Jiang, H.; Aute, V. and Radermacher, R. (2002). "A user-friendly simulation and optimization tool for design of coils." Proceedings of international refrigerant conference at Purdue University.

Jiang, H.; Aute, V.; and Radermacher, R. (2006). "CoilDesigner: A general-purpose simulation and design tool for air-to-refrigerant heat exchangers." International journal of refrigeration, 29, pp. 601-610.

Jin, H. and Spitler, J.D. (2002). "A Parameter Estimation Based Model of Water-To-Water Heat Pumps for use in Energy Calculation Programs." ASHRAE Transactions. 108(1): 3-17.

Kayansayan, N. (1993). "Heat transfer characterization of flat plain fins and round tube heat exchangers." Experimental thermal and fluid science, 6, pp. 263-272.

Kim, M.H. and Bullard, C.W. (2001). "A simple approach to thermal performance analysis of small hermetic reciprocating compressors." ASHRAE transactions. Vol. 107(1), pp. 109-119.

Kim, M.H. and Bullard, C.W. (2002). “Air side performance of brazed aluminum heat exchangers under dehumidifying conditions.” International journal of refrigeration, 25, pp. 924-934.

Kim, Y. and O'Neal, D.L. (1994). “Two-phase flow of R22 through short tube orifices.” ASHRAE transactions. Vol. 100(1), pp. 323-334.

Kim, Y., O'Neal, D.L. and Yuan, X. (1994). “Two-phase flow of HFC-134A and CFC-12 through short tube orifices.” ASHRAE transactions. Vol. 100(2), pp. 582-591.

Kline, S.J. and McClintock, F.A. (1953) “Describing uncertainties in single sample experiments.” Mechanical Engineering, 75, pp. 3-12.

Knight, J. (2005). Personal communications.

Lee, G.H. (2002). “Performance simulation of scroll compressors. Proceedings of the institution of mechanical engineers, part A: Journal of power and energy.” Vol. 21 (2), pp. 169-180.

Liang, S.Y.; Wong, T.N. and Nathan, G.K. (1998). “Study of refrigerant circuitry of evaporator coils with a distributed simulation model.” The proceedings of 7th international refrigeration conference. Purdue University. West Lafayette: IN.

Liaw, J.S., Liu, M.S., Wei, C.Z., Yang, B.C., and Wang, C.C. (2002). “Computer modeling for small air-conditioning systems capable of handling complex circuitry.” ASHRAE transactions. Vol. 108(2), pp. 613-626.

McLinden, M.O.; Klein, S.A.; Lemmon, E.W. and Peskin, A.P. (1998). “REPROP Thermodynamic and Transport Properties of Refrigerants and Refrigerant Mixtures.” NIST standard database 23, version 6.01, Gaithersburg, MD.

McQuiston, F. C., Parker, J. D. and Spitler, J.D. (2000). “Heating, ventilating, and air conditioning – analysis and design, 4th Ed.” New York, NY: John Wiley & Sons, Inc.

Mei, V.C. (1982). “Short tube refrigerant restrictors.” ASHRAE transactions, 88(2), pp. 157-168.

Mullen, C.E.; Bridges, B.D.; Porter, K.J.; Hahn, G.W. and Bullard, C.W. (1998) “Development and validation of a room air-conditioning simulation model.” ASHRAE transactions, 104(2), pp. 389-397.

Paliwoda, A. (1992). “Generalized method of pressure drop calculation across pipe components containing two-phase flow of refrigerants.” Int. j. of refrigeration. 15(2) pp. 119-125.

Payne, W.V. and O'Neal, D.L. (1998). “Mass flow characteristics of R407C through short-tube orifice.” ASHRAE transactions. Vol. 104(1A), pp. 197-209.

Payne, W.V. and O'Neal, D.L. (1999). “Multiphase flow of refrigerant 410A through short tube orifices.” ASHRAE transactions. Vol. 105(2), pp. 66-74.

Payne, V. and O'Neal, D.L. (2004). “A mass flow rate correlation for refrigerants and refrigerant mixtures flowing through short tubes.” HVAC&R Research, 10(1), pp. 73-87.

Pirompugd, W.; Wongwises, S. and Wang, C.C. (2005). “A tube-by-tube reduction method for simultaneous heat and mass transfer characteristics for plain fin-and-tube heat exchangers in dehumidifying conditions.” Heat and Mass Transfer, 41, pp. 756-765.

Popovic, P. and Shapiro, H.N. (1995). “Semi-empirical method for modeling a

reciprocating compressor in refrigerant systems." ASHRAE transactions. Vol. 101(2) pp. 367-382.

Ragazzi, F. and Pedersen, C.O. (1991). "Modular-based computer simulation of an air-cooled condenser." ACRC technical report 07. University of Illinois, Urbana, IL.

Rich, D. G. (1975). "Effect of the number of tube rows on heat transfer performance of smooth plate fin-and-tube heat exchangers." ASHRAE transactions. Vol. 81(1), pp. 307-319.

Rossi, T. and Braun, J.E. (1995). "Computer models for the development, evaluation, and implementation of fault detection and diagnostic methods for HVAC equipment." Technical Report HL95-13, Ray W. Herrick Laboratories, Purdue University, W. Lafayette, IN, USA.

Schein, C. and Radermacher, R. (2001). "Scroll compressor simulation model. Journal of engineering for gas turbines and power." Vol. 123, pp. 217-225.

Schmidt, ThE. (1949). "Heat transfer calculations for extended surfaces." Refrig. Eng., pp. 351-357.

Shen, B. and Groll, E.A. (2005). "A critical review of the influence of lubricants on the heat transfer and pressure drop of refrigerants – Part II: Lubricant influence on condensation and pressure drop." HVAC&R research, 11(4), pp. 511-526.

Shen, B.; Braun, J.E. and Groll, E.A. (2006). "A method for tuning refrigerant charge in modeling off-design performance of unitary equipment." HVAC&R research, 12(3), pp. 429 - 449.

Souza, A.L., Chato J.C., Wattelet, J.P. and Christoffersen, B.C. (1993). "Pressure drop

during two-phase flow of pure refrigerants and refrigerant-oil mixtures in horizontal smooth tubes." American society of mechanical engineerings, heat transfer division publication, 243, pp. 35-41.

Sporlan (1998). "Thermostatic expansion valves: Selective thermostatic charges. Bulletin 10-10." Sporlan valve company, Washington, MO.

Sporlan (1999). "Refrigerant distributors: For all direct expansion multi-circuit evaporators with versatile interchangeable nozzle. Bulletin 20-10." Sporlan valve company, Washington, MO.

Tandon, A. (1999). "Object-oriented modeling of vapor compression systems and components". M.S. Thesis. The University of Maryland, College Park, MD.

Tang C.C. (2005). "Modeling packaged heat pumps in a quasi-steady energy simulation program." M.S. Thesis. Oklahoma State University, Stillwater, OK.

Vardhan, A. and Dhar, P.L. (1998). "A new procedure for performance prediction of air conditioning coils." International journal of refrigeration. Vol. 21(1), pp. 77-83.

Vlach, J. and Singhal, K. (1993). "Computer methods for circuit analysis and design." 2nd ed. Van Nostrand Reinhold. New York.

Wang, C.C.; Chi, K.Y.; and Chang, Y.J. (1998). "An experimental study of heat transfer and friction characteristics of typical louver fin-and-tube heat exchangers." Int. J. of heat and mass transfer, 41(4-5), pp. 817-822.

Wang, C.C.; Jang, J.Y.; Lai, C.C. And Chang, Y.J. (1999a). "Effect of circuit arrangement on the performance of air-cooled condensers." International journal of refrigeration. 22, pp. 275-282.

Wang, C.C., Lee, C.J., Chang, C.T. and Lin, S.P. (1999b). “Heat transfer and friction correlation for compact louvered fin-and-tube heat exchangers.” International journal of heat and mass transfer. 42, pp. 1945-1956.

Wang, C.C.; Chi, K.Y.; and Chang, C.J. (2000). “Heat transfer and friction characteristics of plain fin-and-tube heat exchangers, part II: Correlation.” International journal of heat and mass transfer, 43, pp. 2693-2700.

Wang, C.C., Lin, Y.T. and Lee, C.J. (2000a). “An airside correlation for plain fin-and-tube heat exchangers in wet conditions.” International journal of heat and mass transfer. Vol. 43, pp. 1869-1872.

Wang, C.C; Webb, R.L. and Chi, K.Y. (2000b). “Data reduction for air-side performance of fin-and-tube heat exchangers.” Experimental fluid and thermal science, 21, pp. 218-226.

Wang, C.C., Hwang, Y.M. and Lin, Y.T. (2002). “Empirical correlations for heat transfer and flow friction characteristics of herringbone wavy fin-and-tube heat exchangers.” International journal of refrigeration. 25, pp. 673-680.

Wang, C.C. (2006). Personal communications.

Wattelet, J.P. (1990). “Heat transfer flow regimes of refrigerants in a horizontal-tube evaporator.” University of Illinois at Urbana-Champaign, ACRC TR-55.

Webb, R.L. (1994). “Principles of enhanced heat transfer.” John Wiley & Sons, Inc. New York, NY.

Weber, N.A. (2003). “Performance Effects of Air Velocity Profiles in a Residential Heat Pump.” M.S. Thesis, Oklahoma State University, Stillwater, OK.

Weber, N.A. (2005). Personal communications.

Winandy, E. and Lebrun, J. (2002a). “Scroll compressor using gas and liquid injection: experimental analysis and modelling.” International journal of refrigeration. Vol. 25, pp. 1143-1156.

Winandy, E.; Saavedra, O.C.; Lebrun, J. (2002b). “Simplified modelling of an open-type reciprocating compressor.” International journal of thermal sciences. Vol. 41, pp. 183- 192.

Wilson, E.E. (1915). “A basis for rational design of heat transfer apparatus.” ASME transactions, 37, pp. 47-70.

Yang, Z.H. (1999). “Study on effect of tube pitch and row for air-cooled heat exchangers: Data and method improvement.” HTRI Report AC-10, Heat transfer research, Inc. College Station, TX.

Yang, Z.H. (2002). “Development of incremental row correction factors for air-cooled heat exchangers.” HTRI Report AC-12, Heat transfer research, Inc. College Station, TX.

Yokozeki, M.A. (1992). “Solubility and viscosity of refrigerant-oil mixtures.” Proceedings of international refrigeration conference at Purdue University, pp. 335-340.

Zivi, S.M. (1964). “Estimation of steady-state steam void-fraction by means of the principle minimum entropy production.” ASME transactions, Journal of heat transfer, series C, Vol. 86, pp. 247-252.

9. BIBLIOGRAPHY

9.1. Air Side Heat Transfer and Pressure Drop

El-Din, M.M.S. (1997). "Performance analysis of partially-wet fin assembly. Applied thermal engineering." Vol. 18(5), pp. 337-349.

Hong, K.T. and Webb, R.L. (1996). "Calculation of fin efficiency for wet and dry fins." HVAC&R research. 2(1), pp. 27-41.

Liang, S.Y.; Wong, T.N. and Nathan, G.K. (2000). "Comparison of one-dimensional and two-dimensional models for wet-surface fin efficiency of a plate-fin-tube heat exchanger." Applied thermal engineering. Vol. 20, pp. 941-962.

Lin, Y.T.; Hsu, K.C.; Chang, Y.J. and Wang, C.C. (2001). "Performance of rectangular fin in wet conditions: visualization and wet fin efficiency." Journal of heat transfer, transaction of ASME. Vol. 123, pp. 827-836.

Rosario, L. and Rahman, M.M. (1999). "Analysis of heat transfer in a partially wet radial fin assembly during dehumidification." International journal of heat and fluid flow. Vol. 20, pp. 642-648.

Wang, C.C.; Lin, Y.T. and Lee, C.J. (2000). "Heat and momentum transfer for compact louvered fin-and-tube heat exchangers in wet conditions." International journal of heat and mass transfer. Vol. 43, pp. 3443-3452.

Webb, R.L. (1990). “Air-side heat transfer correlations for flat and wavy plate fin-and-tube geometries.” ASHRAE transactions. Vol. 96(2), pp. 445-559.

Wu, G. and Bong, T.Y. (1994). “Overall efficiency of a straight fin with combined heat and mass transfer.” ASHRAE transactions. Vol. 100(1). 367-374.

Yan, W.M. and Sheen, P.J. (2000). “Heat transfer and friction characteristics of fin-and-tube heat exchangers.” International journal of heat and mass transfer. Vol. 43, pp. 1651-1659.

9.2. Airflow Maldistribution

Aganda, A.A.; Coney, J.E.R. and Sheppard, C.C. (2000). “Airflow maldistribution and the performance of a packaged air conditioning unit evaporator.” Applied thermal engineering. Vol. 20, pp. 515-528.

Chwalowski, M.; Didion, D.A. and Domanski, P.A. (1989). “Verification of evaporator computer models and analysis of performance of an evaporator coil.” ASHRAE transactions. Vol. 95(1), pp. 1229-1237.

Domanski, P.A. (1991). “Simulation of an Evaporator with non-uniform one-dimensional air distribution.” ASHRAE transactions. Vol. 97(1), pp. 783-802.

Lee, J. and Domanski, P.A. (1997). “Impact of Air and Refrigerant Maldistributions On the Performance of Finned-Tube Evaporators With R-22 and R-407C.” DOE/CE/23810-81; Final Report. National Institute of Standards and Technology. Gaithersburg, MD.

9.3. Charge

Baroczy, C.J. (1965). “Correlation of liquid fraction in two-phase flow with application to liquid metals.” Chemical engineering progress symposium series. Vol. 61(57), pp. 179-191.

Farzad, M. (1990). “Modeling the effects of refrigerant charging on air conditioner performance characteristic for three expansion devices.” Ph.D. dissertation, Texas A&M University. College station, TX.

Hughmark, G.A. (1962). “Holdup in gas-liquid flow. Chemical engineering progress.” Vol. 58(4), pp. 62-65.

Premoli, A.; Francesco, D.D. and Prina, A. (1971). “A dimensional correlation for evaluating two-phase mixture density.” La Termotecnica. Vol. 25(1), pp. 17-26.

Rice, C.K. (1987). “The effect of void fraction correlation and heat flux assumption on refrigerant charge inventory predictions.” ASHRAE transactions. Vol. 93(1), pp. 341-367.

Smith, S.L. (1969). “Void fraction in two-phase flow: a correlation based upon an equal velocity head model.” Proceedings of instrumentation mechanical engineers. London. Vol. 184(1), no. 36, pp. 627-664.

Tandon, T.N.; Varma, H.K. and Gupta, C.P. (1985). “A void fraction model for annular two-phase flow.” International journal of heat and mass transfer. Vol. 28(1), pp. 191-198.

9.4. Compressor

Stouffs, P.; Tazerout, M. and Wauters, Pierre (2001). "Thermodynamic analysis of reciprocating compressors." International journal of thermal sciences. Vol. 40, pp. 52-66.

Winandy, E.; Saavedra, O.C. and Lebrun, J. (2002). "Experimental analysis and simplified modelling of a hermetic scroll refrigeration compressor." Applied thermal engineering. Vol. 22, pp. 107-120.

9.5. Dehumidification

Aganda, A.A.; Coney, J.E.R.; Farrant, P.E.; Sheppard, C.G.W. and Wongwuttanasatian, T. (2000). "A comparison of the predicted and experimental heat transfer performance of a finned tube evaporator." Applied thermal engineering. Vol. 20, pp. 499-513.

ARI (2001). "Forced-circulation air-cooling and air-heating coils, ARI standard 410." Air-conditioning and refrigeration institute. Arlington, Virginia.

Bryan, W.L. (1962). "Heat and mass transfer in dehumidifying extended surface coils." ASHRAE transactions. Vol. 68, pp. 237-247.

Chuah, Y.K.; Hung, C.C. and Tseng, P.C. (1998). "Experiments on the dehumidification performance of a finned tube heat exchanger." HVAC&R research. Vol. 4(2), pp. 167-178.

Braun, J.E.; Klein, S.A. and Mitchell, J.W. (1989). "Effectiveness models for cooling towers and cooling coils." ASHRAE Transactions. Vol. 95(2), pp. 164-174.

Ding, X.; Eppe, J.P.; Lebrun, J. and Wasacz, M. (1991). "Cooling coil models to be used in transient and/or wet regimes. Theoretical analysis and experimental validation." System simulation in buildings-Proceedings of the third international conference, pp. 405-437.

Elmahdy, A.H. and Mitalas, G.P. (1977). "A Simplified model for cooling and dehumidifying coils for use in calculating energy requirements for buildings." ASHRAE transactions. Vol. 83(2), pp. 103-117.

Horuz, I.; Kurem, E. and Yamankaradeniz, R. (1998). "Experimental and theoretical performance analysis of air-cooled plate-finned-tube evaporators." International communications in heat and mass transfer. Vol. 25(6), pp. 787-798.

LeRoy, J.T.; Groll, E.A. and Braun, J.E. (1998). "Computer model predictions of dehumidification performance of unitary air conditioners and heat pumps under extreme operating conditions." ASHRAE Transactions, vol. 104(2), pp. 773-788.

Myers, R.J. (1967). "The effect of dehumidification on the air side heat transfer coefficient for a finned-tube coil." MS thesis, University of Minnesota.

Oskarsson, S.P.; Krakow, K.I. and Lin, S. (1990). "Evaporator models for operation with dry, wet, and frosted finned surfaces part I: heat transfer and fluid flow theory." ASHRAE Transactions, vol. 96(1), pp. 373-380.

Oskarsson, S.P.; Krakow, K.I. and Lin, S. (1990). "Evaporator models for operation with dry, wet, and frosted finned surfaces part II: evaporator models and verification." ASHRAE Transactions, vol. 96(1), pp. 381-392.

Threlkeld, J.L. (1970). "Thermal environmental engineering, 2nd ed." New York:

Prentice-Hall.

Wang, C.C.; Hsieh, Y.C. and Lin, Y.T. (1997). “Performance of plate finned tube heat exchangers under dehumidifying conditions.” Journal of heat transfer, transaction of ASME. Vol. 119, pp. 109-117.

9.6. Expansion Device

Ibrahim, G.A. (1998). “Theoretical investigation into instability of a refrigeration system with an evaporator controlled by a thermostatic expansion valve.” The Canadian journal of chemical engineering. Vol. 76, pp. 722-727.

Mithrarathne, P.; Wijeysundera, N.E. and Bong, T.Y. (2000). “Dynamic simulation of a thermostatically controlled counter-flow evaporator.” International journal of refrigeration. Vol. 23, pp. 174-189.

Smith L.D. (1978). “Influence of the expansion device on the performance of a residential air conditioning unit.” University of Illinois at Urbana-Champaign, MS thesis. Urbana, IL.

Sporlan (2001). “Thermostatic expansion valves: theory of operation, application and selection. Bulletin 10-9.” Sporlan valve company, Washington, MO.

Wei, C.S.; Lin, Y.T. And Wang, C.C. (2000). “A performance comparison between coiled and straight capillary tubes.” Heat transfer engineering, 21(2), pp. 62-65.

9.7. Heat Exchangers

Hawlader, M.N.A.; Chou, S.K.; Chua, K.J.; Ho, J.C. and Mujumadar, A.S. (2001). “On

the steady-state modelling of a two-stage evaporator system." International journal of energy research. Vol. 25, pp. 859-880.

Theerakulpisut, S. and Priprem, S. (1997). "Modeling cooling coils." International communications in heat and mass transfer. Vol. 25(1), pp. 127-137.

Wu, X.M. and Webb, R.L. (2002). "Thermal and hydraulic analysis of a brazed aluminum evaporator." Applied thermal engineering. Vol. 22, pp. 1369-1390.

Casson, V.; Cavallini, A.; Cecchinato, L.; Col, D.D.; Doretti, L.; Fornasieri, E.; Rossetto, L. and Zilio, C. (2002). "Performance of finned coil condensers optimized for new HFC refrigerants." ASHRAE transactions. HI-02-1-3.

Corberan, J.M. and Melon, M.G. (1997). "Modelling of plate finned tube evaporators and condensers working with R134A." International journal of refrigeration. Vol. 21(4), pp. 273-284.

Judge, J. and Radermacher, R. (1997). "A heat exchanger model for mixtures and pure refrigerant cycle simulations." International journal of refrigeration. Vol. 20(4), pp. 244-255.

Kim, M.H. and Bullard, C.W. (2000). "Development of a microchannel evaporator model for a CO2 air-conditioning system." Energy. Vol. 26, pp. 931-948.

9.8. Heat Pump Models

Cecchini, C. and Marchal, D. (1991). "A simulation model of refrigerating and air-conditioning equipment based on experimental data." ASHRAE transactions. Vol. 97(2), pp. 388-393.

Dabiri, A.E. (1982). “A steady state computer simulation model for air-to-air heat pumps.” ASHRAE transactions. TO-82-8.

Domanski, P.A. and McLinden, M.O. (1992). “A simplified cycle simulation model for the performance rating of refrigerants and refrigerant mixtures.” International journal of refrigeration. Vol. 15(2), pp. 81-88.

Hamilton, J.F. and Miller, J.L. (1990). “A simulation program for modeling an air-conditioning system.” ASHRAE transactions. Vol. 96(1), pp. 213-221.

Jin, H. (2002). “Parameter estimation based models of water source heat pumps.” Ph.D. dissertation, Oklahoma State University, Stillwater, OK.

Lee, G.H. and Yoo, J.Y. (2000). “Performance analysis and simulation of automobile air conditioning system.” International journal of refrigeration. Vol. 23, pp. 243-254.

LeRoy, J.T.; Groll, E.A. and Brauns, J.E. (2000). “Evaluating the Accuracy of PUREZ in Predicting Unitary Equipment Performance.” ASHRAE transactions. Vol. 106(1), pp. 200- 215.

9.9. Miscellaneous

ASHRAE (2004). “ASHRAE Handbook - HVAC Systems and Equipment”. Atlanta, GA: American Society of Heating, Refrigerating and Air-Conditioning Engineers, Inc.

Stoecker, W.F. And Jones, J.W. (1982). “Refrigeration and air conditioning”. New York: McGraw-Hill, Inc.

York (n.d.). “Champion Plus – Single package heat pumps, BHH018 thru 060, 1-1/2 thru 5 nominal tons, 12 SEER.” Unitary Product Group, York international, Norman, OK.

9.10. Refrigerant Side Heat Transfer and Pressure Drop

Chen, I.Y.; Yang, K.S.; Chang, Y.J. and Wang, C.C. (2001). "Two-phase pressure drop of air-water and R410A in small horizontal tubes." International journal of multiphase flow. Vol. 27, pp. 1293-1299.

Chitti, M.S. and Anand, N.K. (1996). "Condensation heat transfer inside smooth horizontal tubes for R-22 and R-32/125 mixtures." HVAC&R research. Vol. 2(1), pp. 79-100.

Choi, J.; Chung, J.T.; and Kim, Y. (2004). "A generalized correlation for two-phase flow of alternative refrigerants through short tube orifices." International journal of refrigeration, 27, pp. 393-400.

Eckels, S.J.; Doerr, T.M. and Pate, M.B. (1998b). "Heat transfer and pressure drops for R-134a and an ester lubricant mixture in smooth tube and a micro-fin tube." ASHRAE transactions. Vol. 104(1).

Eckels, S.J. and Pate, M.B. (1990). "A comparison of R-134a and R-12 in-tube heat transfer coefficients based on existing correlations." ASHRAE transactions. Vol. 96(1), pp. 256-265.

Eckels, S. J. and Tesene, B.A. (1999). "A comparison of R-22, R134a, R-410a, and R-407c condensation performance in smooth and enhanced tubes: Part I, heat transfer." ASHRAE transactions. SE-99-4-3.

Eckels, S. J. and Tesene, B.A. (1999). "A comparison of R-22, R134a, R-410a, and R-407c condensation performance in smooth and enhanced tubes: Part II, pressure drop." ASHRAE transactions. SE-99-4-4.

Eckels, S.J. and Unruh, B.J. (1999). “Local heat transfer coefficients during condensation of R-22 and R-32/R-125 mixtures.” HVAC&R research. Vol. 5(1), pp. 59-76.

Gidwani, A.; Ohadi, M.M. and Salehi, M. (1998). “In-tube condensation of refrigerant and refrigerant-oil mixtures – A review of most recent work.” ASHRAE transactions. Vol. 104(1).

Kattan N, Thome, J.R. and Favrat D. (1998). “Flow boiling in horizontal tubes: part 3 – development of a new heat transfer model based on flow pattern.” Journal of heat transfer, transaction of ASME. Vol. 120, pp. 156-165.

Kaushik, N. and Azer, N.Z. (1990). “A general pressure drop correlation for condensation inside internally finned tubes.” ASHRAE transactions. Vol. 96(1), pp. 242-248.

Kim, D. and Ghajar, A.J. (2002). “Heat transfer measurements and correlations for air-water flow of different flow patterns in a horizontal pipe.” Experimental Thermal and Fluid Science, 25, pp. 659-676.

Nitheanandan, T.; Soliman, H.M. and Chant, R.E. (1990). “A proposed approach for correlating heat transfer during condensation inside tubes.” ASHRAE transactions. Vol. 96(1), pp. 230-241.

Pierre, B. (1964). “Flow resistance with boiling refrigerants-Part I”. ASHRAE Journal, 6(9), pp. 58-65.

Shah, M.M (1977). “General correlation for heat transfer during subcooled boiling in pipes and annuli.” ASHRAE transactions. 83(1), pp. 202-217.

Shah, M.M. (1979). “A general correlation for heat transfer during film condensation inside pipes.” International Journal of heat and mass transfer. 88, pp 185-196.

Wang, C.C.; Chiang, C.S. and Yu, J.G. (1998). “An experimental study of in-tube evaporation of R-22 inside a 6.5-mm smooth tube.” International journal of heat and fluid flow. Vol. 19, pp. 259-269.

Wang, C.C., Shieh, W.Y., Chang, Y.J. and Yang, C.Y. (1998). “Nucleate boiling performance of R-22, R-123, R-134A, R-410A, and R-407C on smooth and enhanced tubes.” ASHRAE transactions. 104(1)

Zurcher, O.; Thome, J.R. and Favrat, D. (1998). “In-tube flow boiling of R-407C and R-407C/Oil Mixtures Part I: Microfin tube.” HVAC&R research. Vol. 4(4), pp. 347-372.

Zurcher, O.; Thome, J.R. and Favrat, D. (1998). “In-tube flow boiling of R-407C and R-407C/Oil Mixtures Part II: Plain tube results and predictions.” HVAC&R research. Vol. 4(4), pp. 373-399.

10. APPENDIX

10.1. Verification of Flat Fin Heat Transfer Coefficients

Rich (1975) only presented j-factor data in his paper. The local air temperature between rows are unknown. Rich's heat transfer coefficients presented below are derived from Rich's j-factors and standard air properties for the closest approximation.

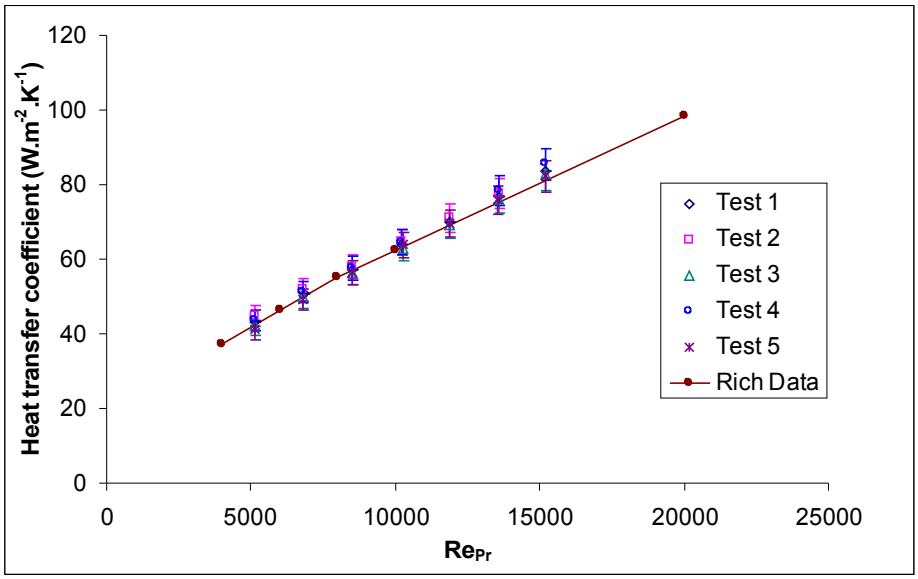

Figure 10.1 Overall heat transfer coefficients.

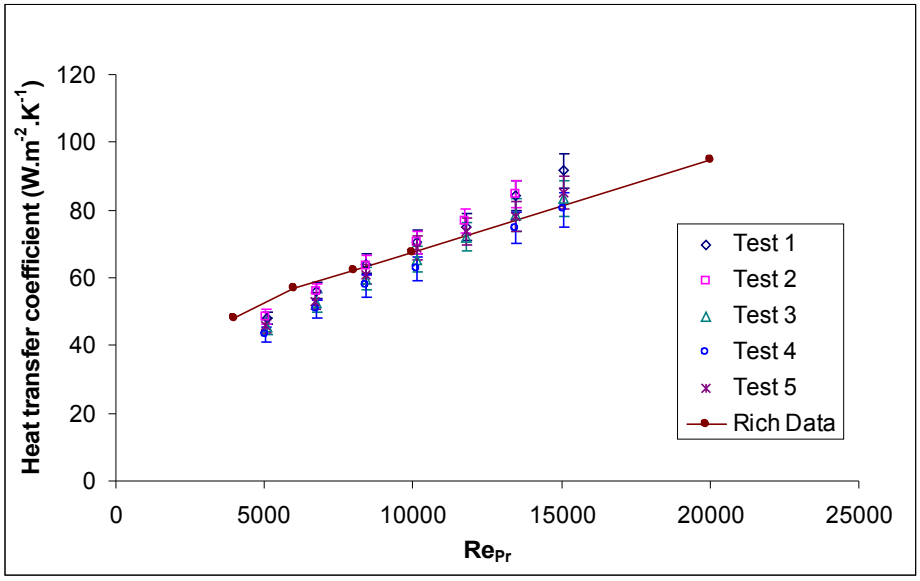

Figure 10.2 Row 1 heat transfer coefficients.

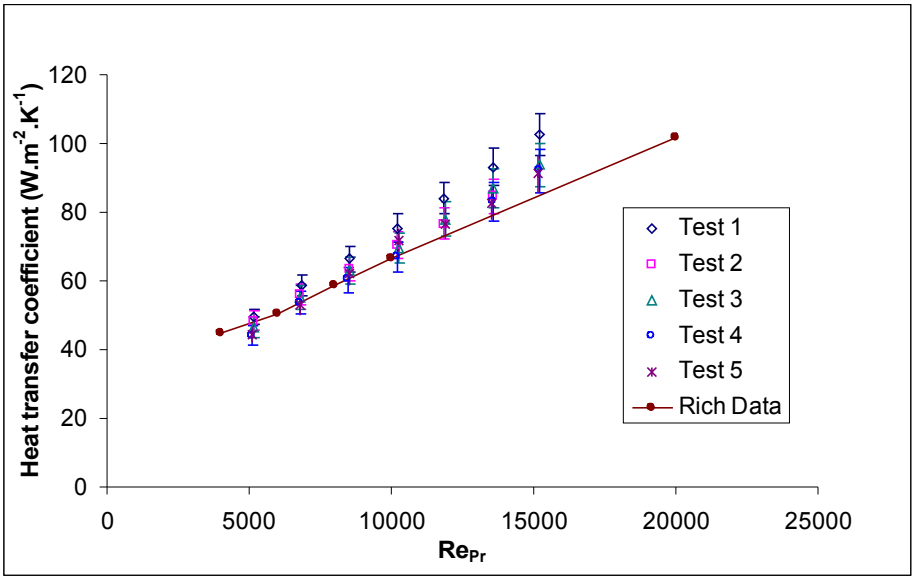

Figure 10.3 Row 2 heat transfer coefficients.

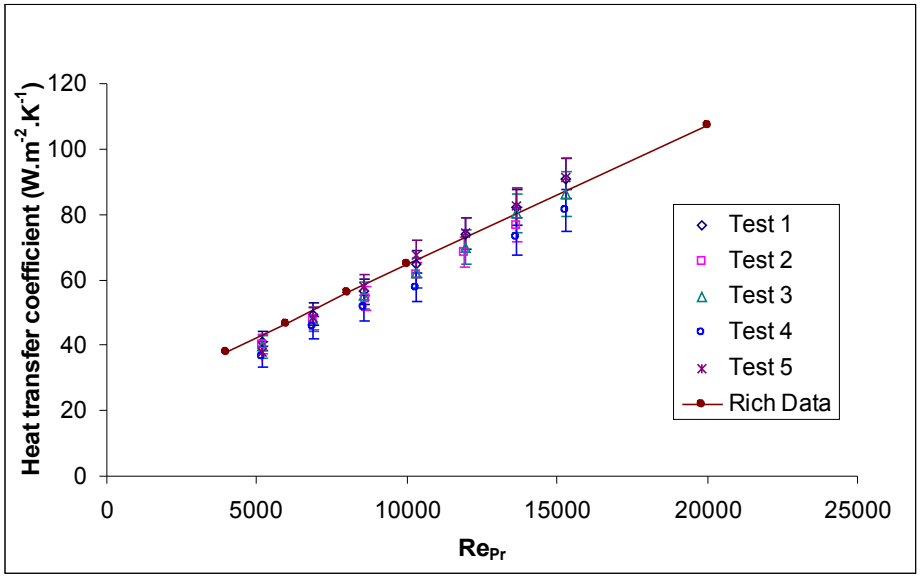

Figure 10.4 Row 3 heat transfer coefficients.

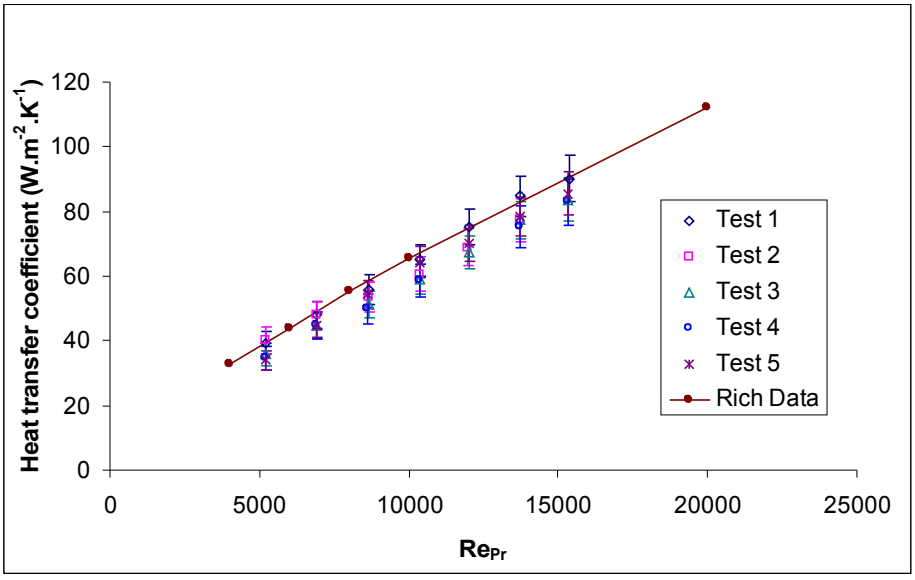

Figure 10.5 Row 4 heat transfer coefficients.

10.2. Louvered Fin Normalized Row-By-Row j-factors

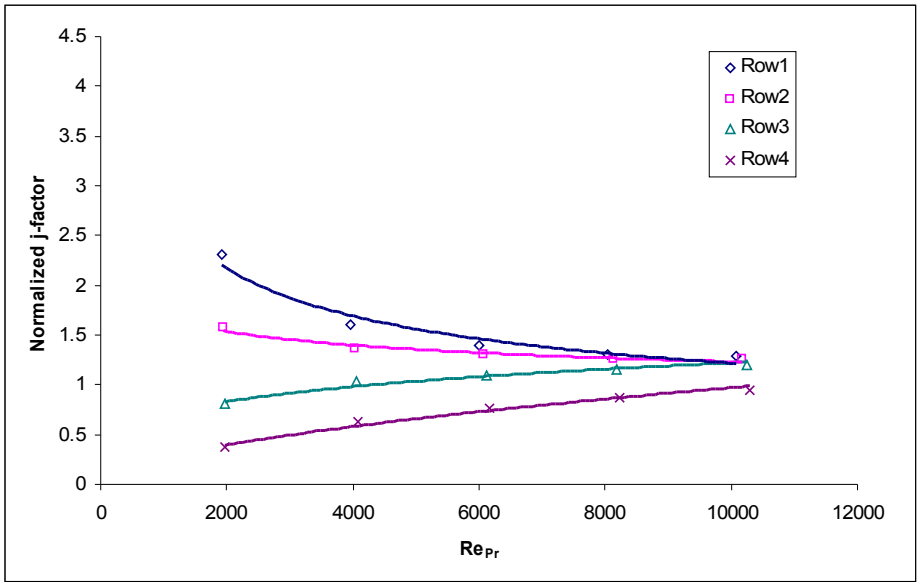

Figure 10.6 Coil 2 normalized row-by-row j-factor.

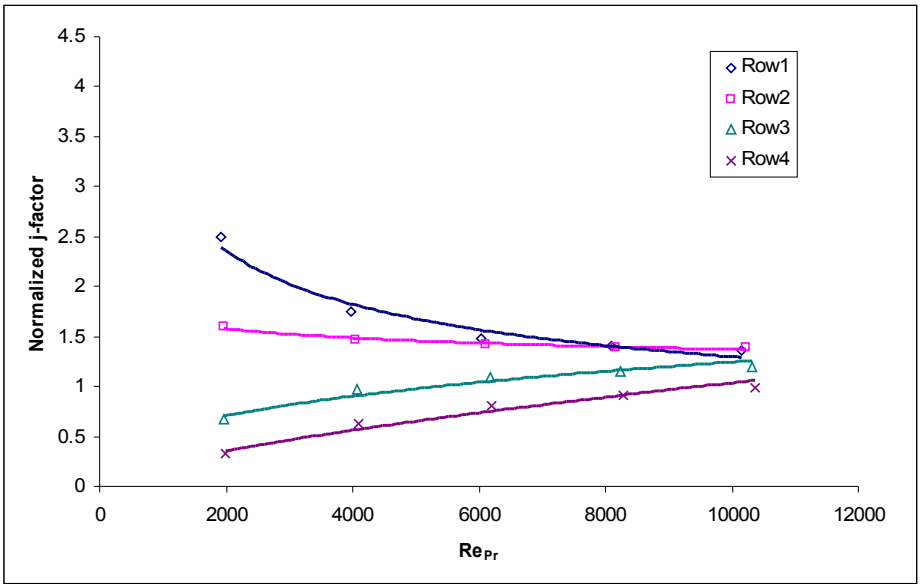

Figure 10.7 Coil 3 normalized row-by-row j-factor.

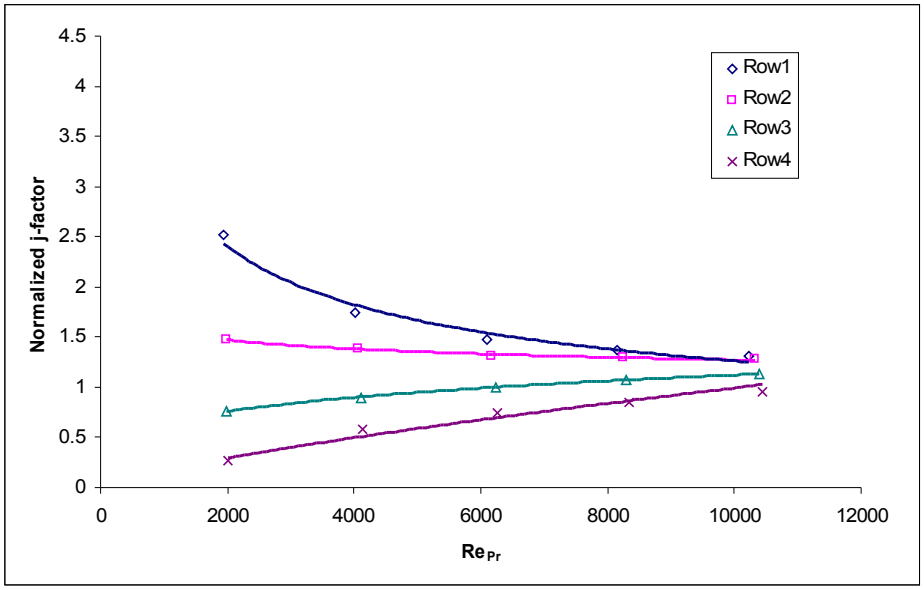

Figure 10.8 Coil 4 normalized row-by-row j-factor.

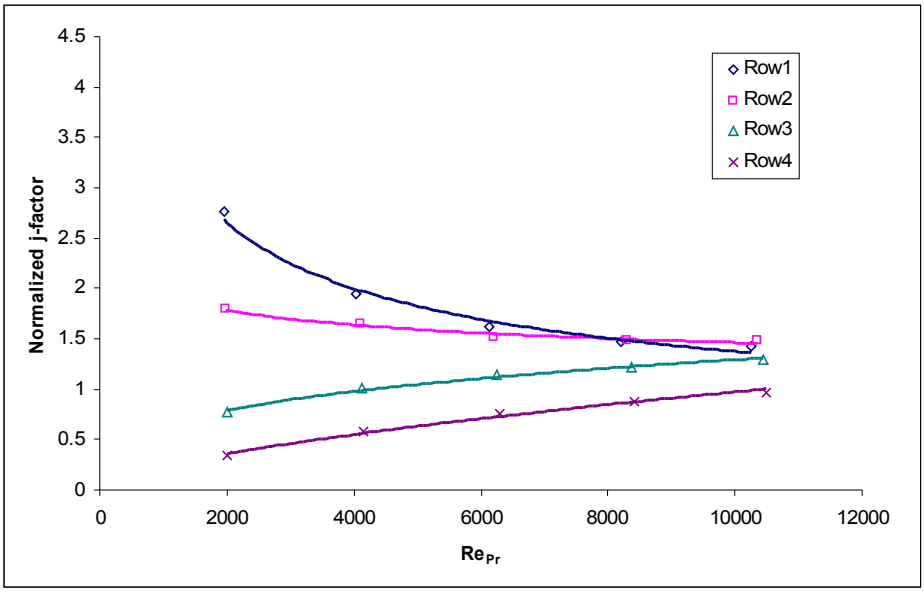

Figure 10.9 Coil 5 normalized row-by-row j-factor.

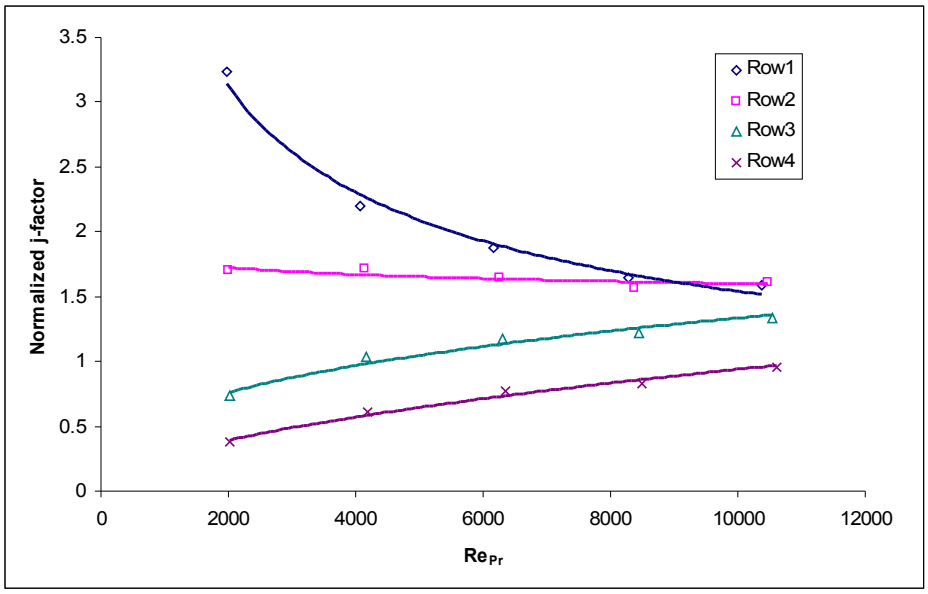

Figure 10.10 Coil 6 normalized row-by-row j-factor.

10.3. Louvered Fin Scaled Row-By-Row Nusselt Number

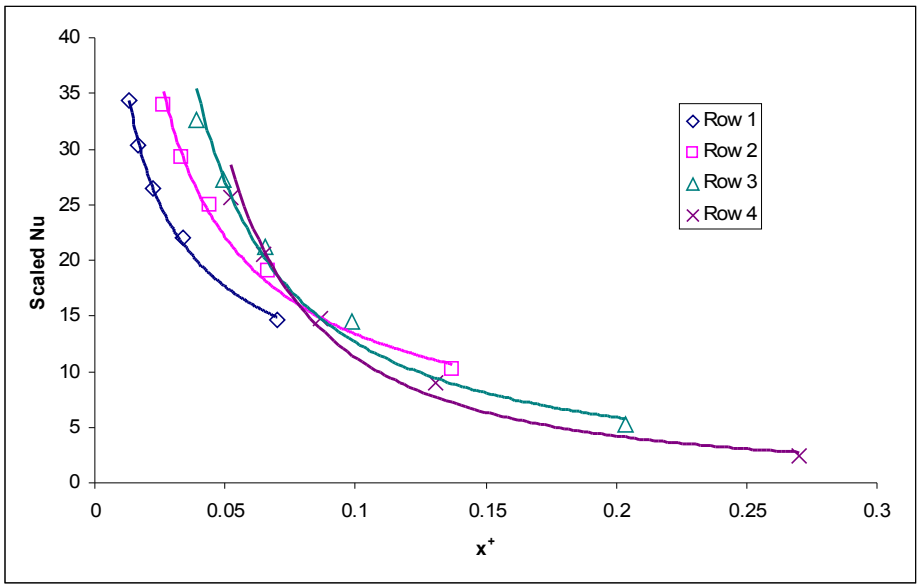

Figure 10.11 Coil 2 scaled row-by-row Nusselt number.

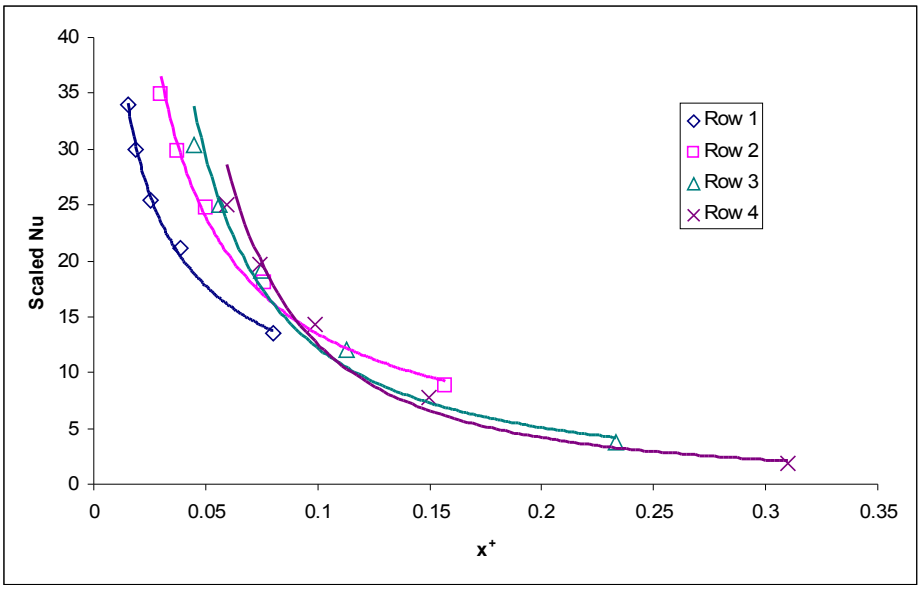

Figure 10.12 Coil 3 scaled row-by-row Nusselt number.

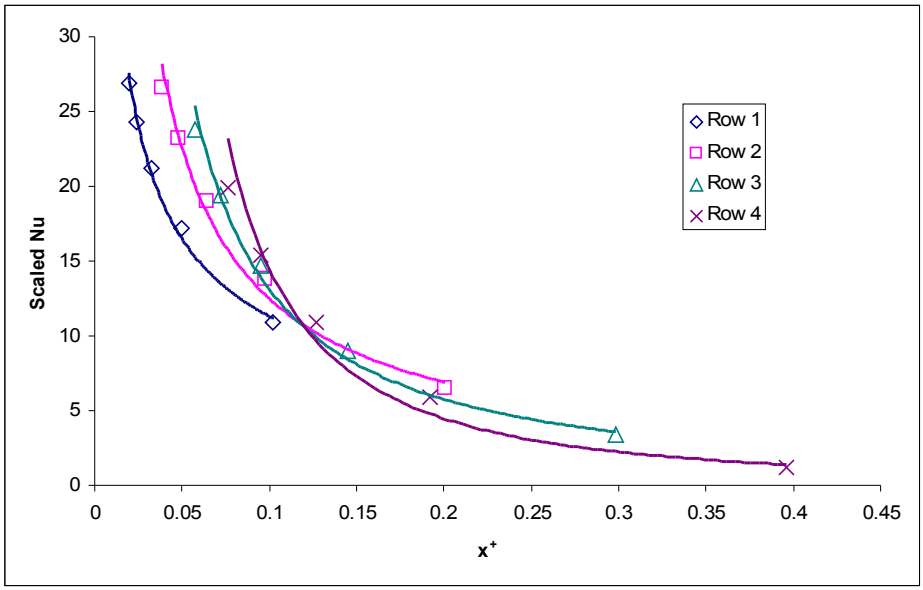

Figure 10.13 Coil 4 scaled row-by-row Nusselt number.

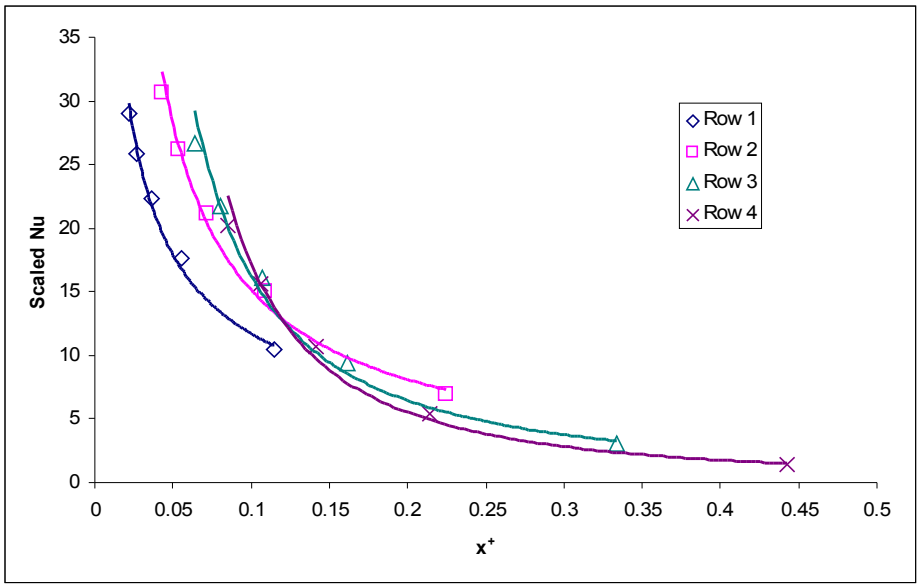

Figure 10.14 Coil 5 scaled row-by-row Nusselt number.

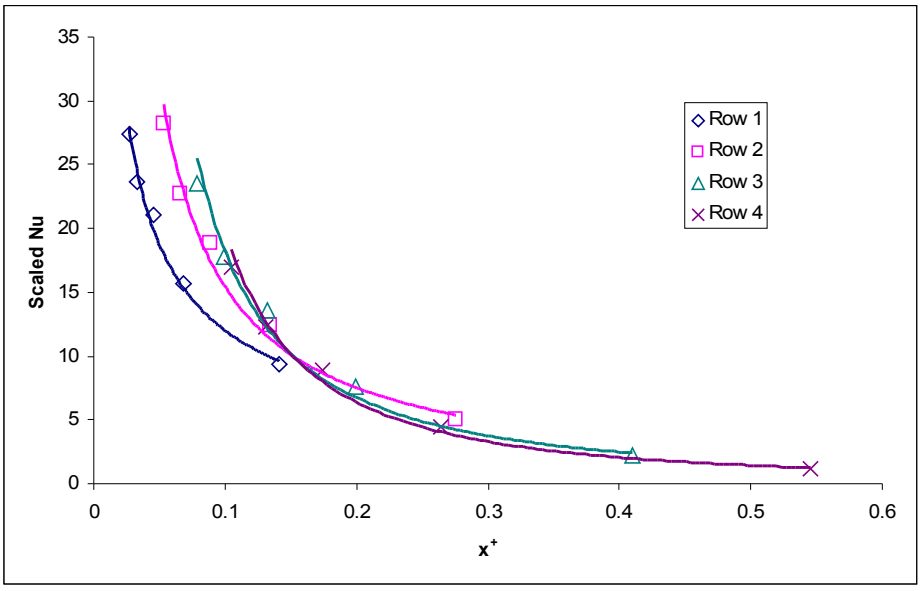

Figure 10.15 Coil 6 scaled row-by-row Nusselt number.

10.4. Nusselt Number Correlations

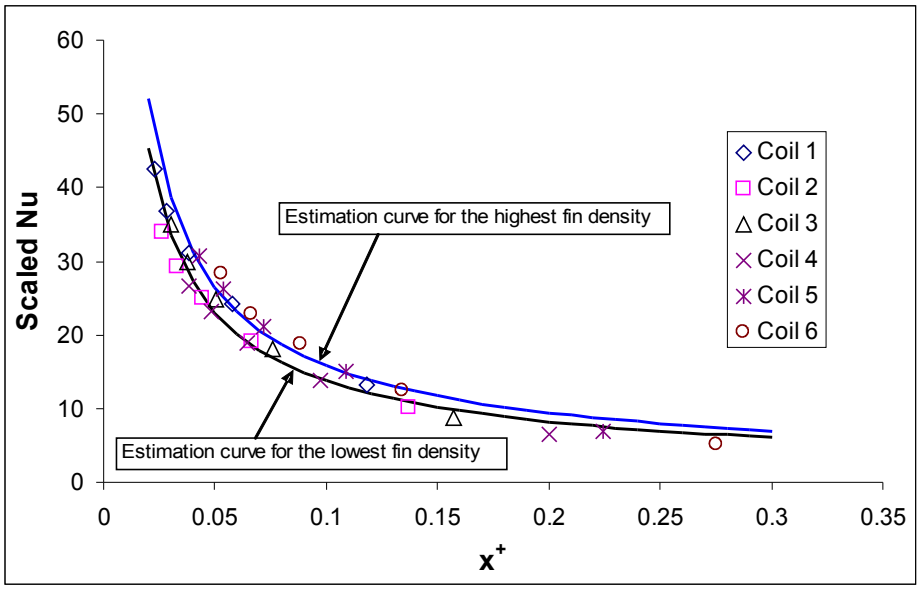

Figure 10.16 Row 2 Nusselt number correlations.

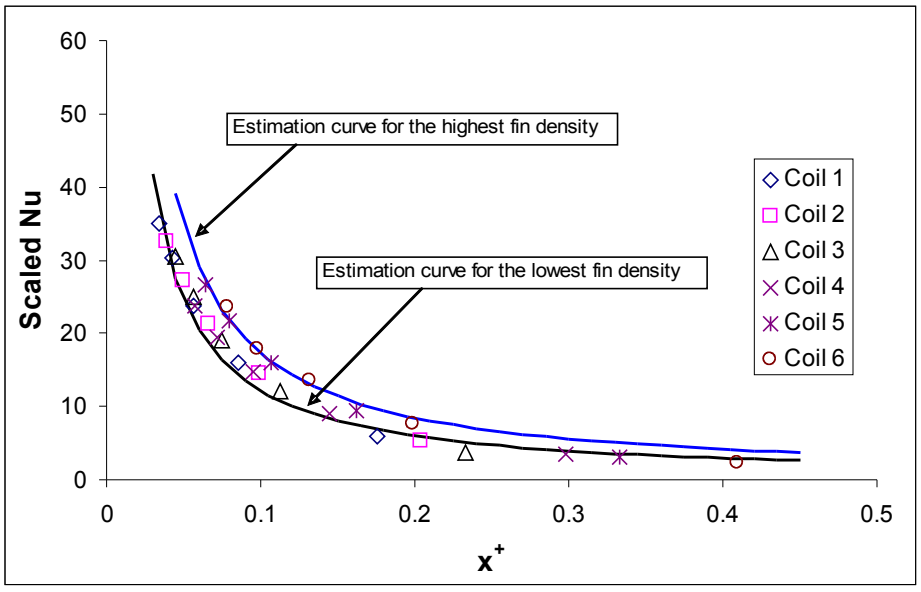

Figure 10.17 Row 3 Nusselt number correlations.

10.5. York Data Boundary Conditions

Table 10.1 Boundary conditions for compressor model validation.

Data set no.	Suction Saturation temp. (°C)	Discharge saturation temp. (°C)	Suction superheat (K)
1	10.7	45.9	3.2
2	8.6	39.0	13.8
3	9.2	39.3	18.8
4	10.8	48.8	12.1
5	8.7	42.0	17.3
6	9.5	47.2	12.1
7	7.6	40.4	15.8
8	10.1	50.6	5.5
9	8.3	43.6	11.3
10	9.5	42.0	15.0
11	-0.9	38.5	6.5
12	10.3	46.0	10.7
13	8.3	38.4	17.7
14	9.9	45.9	15.6
15	8.0	38.5	18.3
16	9.8	48.0	8.4
17	8.2	40.5	8.3
18	7.7	52.2	10.6
19	9.3	63.8	10.3
20	6.7	62.8	10.9
21	5.3	50.8	15.9
22	2.2	44.6	15.5
23	3.0	50.1	16.1
24	4.6	60.8	15.8
25	6.8	47.3	15.6
26	2.7	45.0	16.0
27	5.1	61.2	15.7
28	3.0	45.2	15.7
29	7.3	52.2	15.5
30	8.9	62.9	15.0
31	6.7	61.7	15.2
32	4.3	60.8	15.4
33	9.3	41.0	4.3
34	12.2	44.4	5.9
35	11.6	39.1	6.7
36	10.5	41.0	6.2

Data set no.	Suction Saturation temp. (°C)	Discharge saturation temp. (°C)	Suction superheat (K)
37	10.5	45.4	5.4
38	11.7	55.3	3.7
39	10.7	42.2	7.4
40	8.6	34.6	14.6
41	6.8	34.2	7.1
42	11.2	43.8	8.4
43	9.3	36.5	16.6
44	7.7	35.9	10.3
45	8.3	38.5	6.3
46	5.5	37.5	5.9
47	9.2	54.1	5.8
48	8.3	49.3	9.4
49	-3.3	38.6	13.1
50	-1.7	40.0	19.0
51	8.7	46.6	9.6
52	-3.7	37.5	10.9
53	-3.3	41.0	10.3
54	-2.4	45.2	6.7
55	-3.6	39.9	10.6
56	-2.8	43.9	9.0
57	-6.6	30.9	12.1
58	-2.0	41.4	14.3
59	9.4	43.4	11.3
60	8.8	47.4	15.5
61	6.7	42.0	18.3
62	10.7	39.7	11.8
63	-0.4	40.0	6.0
64	0.1	36.9	4.5
65	6.8	42.8	4.5
66	-0.4	32.0	4.5
67	0.6	43.7	4.3
68	0.6	39.7	4.4
69	1.1	45.0	4.2
70	11.3	41.9	5.3
71	0.3	43.3	5.8
72	0.2	39.0	5.0
73	-0.4	34.2	5.2
74	11.8	48.1	6.1
75	12.0	43.6	10.4
76	-0.2	36.4	4.6
77	5.5	41.6	4.8
78	11.1	50.1	4.3

Data set no.	Suction Saturation temp. (°C)	Discharge saturation temp. (°C)	Suction superheat (K)
79	12.5	59.0	14.2
80	-0.9	39.9	6.0
81	9.1	44.5	5.4
82	9.9	39.4	8.4
83	-2.0	38.1	6.9
84	-2.7	32.3	6.7
85	-1.3	45.9	6.8
86	-1.6	43.8	6.6
87	-2.1	38.2	6.9
88	7.6	41.3	11.2
89	4.3	33.7	4.1
90	6.3	34.1	13.9
91	5.8	34.1	13.6
92	7.0	46.3	8.5
93	3.3	28.7	8.5
94	8.0	46.8	8.1
95	2.8	34.2	8.5
96	5.2	40.0	8.1
97	7.5	41.0	7.7
98	9.7	41.8	11.7
99	8.6	36.2	13.7
100	7.5	30.6	15.6
101	10.0	47.7	11.6
102	8.3	41.5	8.0
103	6.4	46.4	8.4
104	5.9	40.6	8.0
105	7.0	46.4	8.5
106	12.1	46.4	9.5
107	9.8	30.1	10.6
108	5.8	28.9	7.9
109	9.5	38.6	8.8
110	8.8	26.7	9.2
111	10.3	27.3	10.8
112	11.8	38.3	10.2

Table 10.2 Boundary conditions for short tube model validation.

Data set no.	Inlet pressure (kPa)	Inlet subcooling (K)
88	1521.0	2.2
89	1261.0	3.8
90	1274.5	4.7
91	1275.0	4.4

Table 10.3 Refrigerant side boundary conditions for condenser model validation.

Data set no.	Ref. mass flow rate ($kg.s^{-1}$)	Inlet pressure (kPa)	Inlet temperature (°C)
1	0.049	1767.5	74.3
2	0.045	1497.2	70.3
3	0.068	1508.2	72.6
4	0.078	1891.6	83.1
5	0.074	1611.0	79.2
6	0.087	1801.9	77.2
7	0.083	1532.4	72.3
8	0.108	1944.7	72.2
9	0.100	1646.8	69.2
10	0.069	1590.3	65.6
11	0.048	1473.1	45.8
12	0.087	1751.6	70.0
13	0.081	1451.7	67.8
14	0.091	1772.3	77.4
15	0.085	1484.8	70.2
16	0.106	1857.8	74.3
17	0.102	1553.0	64.2
18	0.179	2040.7	88.6
19	0.182	2633.5	106.4
20	0.166	2578.8	108.1
21	0.220	1977.5	93.5
22	0.203	1711.5	86.4
23	0.205	1946.8	94.3
24	0.210	2471.9	109.4
25	0.233	1823.7	86.3
26	0.205	1729.3	87.0
27	0.213	2489.3	109.5
28	0.207	1735.9	86.9
29	0.234	2044.5	92.9
30	0.240	2583.7	106.7
31	0.225	2516.3	107.7
32	0.208	2470.1	109.6
33	0.081	2459.0	61.0

Data set no.	Ref. mass flow rate (kg.s^{-1})	Inlet pressure (kPa)	Inlet temperature (°C)
34	0.095	2677.9	66.7
35	0.093	2358.4	60.5
36	0.113	2468.9	62.3
37	0.148	2744.9	69.8
38	0.153	3446.7	82.1
39	0.070	1608.9	67.2
40	0.066	1331.0	64.7
41	0.065	1318.6	58.1
42	0.088	1672.3	67.2
43	0.083	1397.9	65.8
44	0.082	1379.3	60.2
45	0.110	1478.6	63.8
46	0.101	1442.7	64.0
47	0.153	2125.2	82.8
48	0.147	1905.4	80.7
49	0.100	1508.3	78.2
50	0.103	1557.9	85.3
51	0.149	1780.6	73.5
52	0.099	1431.3	71.8
53	0.101	1566.3	76.7
54	0.105	1733.0	78.7
55	0.100	1523.3	75.7
56	0.103	1675.8	80.3
57	0.092	1203.7	64.9
58	0.104	1579.7	80.3
59	0.086	1668.3	77.0
60	0.103	1826.7	86.4
61	0.097	1605.3	82.3
62	0.078	2390.7	61.2
63	0.054	2405.9	66.6
64	0.057	2235.6	60.2
65	0.072	2574.1	64.4
66	0.056	1972.2	52.8
67	0.057	2635.5	71.1
68	0.057	2396.3	64.4
69	0.058	2716.9	72.7
70	0.095	2514.9	58.6
71	0.066	2607.2	71.2
72	0.067	2356.3	63.4
73	0.066	2089.4	56.3
74	0.101	2918.2	54.4
75	0.099	2620.3	61.2

Data set no.	Ref. mass flow rate (kg.s^{-1})	Inlet pressure (kPa)	Inlet temperature (°C)
76	0.069	2209.4	59.7
77	0.084	2503.1	64.4
78	0.115	3060.2	70.2
79	0.108	3749.7	92.9
80	0.077	2394.2	65.6
81	0.142	2675.5	65.7
82	0.145	2368.0	61.4
83	0.099	2305.3	64.3
84	0.098	1991.5	57.0
85	0.100	2782.4	76.0
86	0.100	2647.2	72.8
87	0.099	2313.5	64.4
88	0.067	1587.4	72.7
89	0.065	1316.9	58.2
90	0.066	1329.4	67.0
91	0.065	1331.4	66.4
92	0.112	1776.7	75.2
93	0.102	1130.5	52.9
94	0.115	1795.6	74.9
95	0.100	1315.5	60.2
96	0.107	1515.8	66.8
97	0.115	1551.8	66.3
98	0.121	1585.0	69.8
99	0.117	1381.3	64.8
100	0.113	1193.8	59.9
101	0.122	1835.2	77.8
102	0.119	1582.5	66.4
103	0.111	1781.8	75.0
104	0.110	1549.8	66.9
105	0.112	1779.9	75.1
106	0.058	2816.6	74.9
107	0.054	1887.8	55.4
108	0.047	1832.7	53.3
109	0.052	2340.8	64.8
110	0.039	1731.2	48.6
111	0.041	1755.1	49.6
112	0.042	2318.3	63.2

Table 10.4 Refrigerant side boundary conditions for evaporator model validation.

Data set no.	Ref. mass flow rate ($kg.s^{-1}$)	Outlet pressure (kPa)	Inlet enthalpy ($kJ.kg^{-1}$)
1	0.049	695.3	248.0
2	0.045	652.6	236.9
3	0.068	662.9	236.5
4	0.078	698.1	250.2
5	0.074	655.3	238.4
6	0.087	674.0	249.0
7	0.083	636.0	237.1
8	0.108	685.7	245.1
9	0.100	651.9	234.2
10	0.069	687.7	239.0
11	0.048	503.0	242.3
12	0.087	700.8	249.6
13	0.081	666.4	239.6
14	0.091	691.9	249.8
15	0.085	654.0	238.9
16	0.106	692.6	250.3
17	0.102	660.9	237.2
18	0.179	645.8	254.6
19	0.182	691.6	271.4
20	0.166	637.3	269.8
21	0.220	618.6	249.5
22	0.203	563.1	241.0
23	0.205	575.4	248.7
24	0.210	604.2	264.2
25	0.233	650.4	243.6
26	0.205	568.1	241.2
27	0.213	609.4	264.2
28	0.207	575.5	241.5
29	0.234	655.3	250.5
30	0.240	683.7	266.2
31	0.225	642.1	264.5
32	0.208	595.8	263.4
33	0.081	1062.1	257.8
34	0.095	1156.1	265.0
35	0.093	1138.4	255.4
36	0.113	1107.8	255.9
37	0.148	1100.1	267.4
38	0.153	1147.8	287.7
39	0.070	698.8	245.4
40	0.066	652.6	234.3
41	0.065	616.7	235.1

Data set no.	Ref. mass flow rate (kg.s^{-1})	Outlet pressure (kPa)	Inlet enthalpy (kJ.kg^{-1})
42	0.088	712.6	243.5
43	0.083	669.1	233.9
44	0.082	637.4	234.2
45	0.110	647.1	236.5
46	0.101	594.0	236.0
47	0.153	709.5	245.9
48	0.147	692.9	238.9
49	0.100	466.6	243.6
50	0.103	497.3	244.5
51	0.149	692.6	245.2
52	0.099	463.4	239.3
53	0.101	475.8	244.8
54	0.105	487.9	250.2
55	0.100	470.9	243.3
56	0.103	482.1	249.0
57	0.092	424.6	231.7
58	0.104	501.2	244.2
59	0.086	675.7	241.9
60	0.103	665.4	247.0
61	0.097	624.6	239.8
62	0.078	1118.7	263.7
63	0.054	799.4	259.1
64	0.057	817.4	255.4
65	0.072	1009.7	268.4
66	0.056	820.1	249.2
67	0.057	830.5	269.1
68	0.057	826.3	260.8
69	0.058	834.6	269.3
70	0.095	1133.1	259.3
71	0.066	821.5	261.6
72	0.067	824.9	254.9
73	0.066	822.9	248.1
74	0.101	1173.8	271.5
75	0.099	1173.1	261.3
76	0.069	804.3	252.7
77	0.084	967.0	261.8
78	0.115	1167.6	270.2
79	0.108	1227.6	299.1
80	0.077	781.5	250.6
81	0.142	1109.0	265.0
82	0.145	1134.5	255.0
83	0.099	794.6	252.1

Data set no.	Ref. mass flow rate ($kg.s^{-1}$)	Outlet pressure (kPa)	Inlet enthalpy ($kJ.kg^{-1}$)
84	0.098	776.7	243.8
85	0.100	813.2	265.7
86	0.100	806.3	263.4
87	0.099	795.3	252.4
88	0.067	647.8	246.2
89	0.065	584.8	234.3
90	0.066	616.9	233.8
91	0.065	609.8	234.1
92	0.112	643.2	243.4
93	0.102	572.8	221.6
94	0.115	662.8	243.7
95	0.100	563.7	228.4
96	0.107	605.8	235.3
97	0.115	649.9	236.2
98	0.121	699.5	236.4
99	0.117	675.7	229.3
100	0.113	648.8	222.3
101	0.122	711.4	244.1
102	0.119	669.5	236.7
103	0.111	630.8	243.5
104	0.110	621.3	236.1
105	0.112	645.1	243.4
106	0.058	1158.3	258.7
107	0.054	1089.5	228.7
108	0.047	961.3	229.3
109	0.052	1073.0	244.9
110	0.039	1055.2	228.1
111	0.041	1102.0	228.2
112	0.042	1150.9	247.6

Table 10.5 Refrigerant side boundary conditions for system level validation.

Data set no.	ΔT_{suc} (K)	ΔT_{sup} (K)	ΔT_{sucln} (K)	ΔT_{disln} (K)	ΔT_{liqln} (K)	Heat loss (%)
1	6.1	3.2	0.0	0.0	0.0	12.9%
2	7.7	13.8	0.0	0.0	0.0	30.2%
3	6.6	18.8	1.8	0.0	-0.2	27.8%
4	5.6	12.1	0.0	0.0	0.0	15.5%
5	7.2	17.3	0.0	0.0	0.0	17.8%
6	2.8	12.1	2.1	-4.8	-0.4	16.1%
7	4.3	15.8	1.4	-5.3	-0.5	16.1%
8	7.9	5.5	3.6	-2.9	-0.3	23.4%
9	8.7	11.3	4.5	-3.4	-0.3	23.3%

Data set no.	ΔT_{suc} (K)	ΔT_{sup} (K)	ΔT_{sucln} (K)	ΔT_{disln} (K)	ΔT_{liqln} (K)	Heat loss (%)
10	8.7	15.0	0.0	0.0	0.0	44.4%
11	3.3	6.5	1.2	-13.3	0.0	42.1%
12	4.0	10.7	8.6	-6.6	1.0	17.6%
13	4.1	17.7	2.7	-7.2	1.5	17.2%
14	3.3	15.6	3.1	-6.4	0.2	11.0%
15	4.4	18.3	2.0	-6.6	0.4	12.9%
16	5.2	8.4	5.9	-7.4	-0.1	5.7%
17	7.8	8.3	5.8	-5.0	-0.1	12.1%
18	6.2	10.6	1.1	0.0	-1.5	12.1%
19	6.1	10.3	1.4	0.0	-0.4	13.8%
20	6.5	10.9	1.7	0.0	-0.4	14.0%
21	7.4	15.9	2.0	0.0	-0.1	17.6%
22	7.4	15.5	2.3	0.0	-0.4	16.3%
23	7.4	16.1	3.2	0.0	-0.3	17.0%
24	7.1	15.8	4.6	0.0	-0.2	18.2%
25	7.0	15.6	0.8	0.0	0.2	17.3%
26	7.6	16.0	1.6	0.0	-0.2	17.3%
27	7.5	15.7	4.1	0.0	-0.2	18.3%
28	7.5	15.7	1.7	0.0	-0.1	16.8%
29	7.2	15.5	1.6	0.0	0.1	18.3%
30	6.9	15.0	3.2	0.0	-0.3	20.0%
31	7.3	15.2	3.6	0.0	-0.5	18.8%
32	7.7	15.4	4.7	0.0	-0.5	18.1%
33	5.1	4.3	-0.1	-1.5	-0.3	14.7%
34	4.4	5.9	-1.2	0.0	0.0	18.6%
35	4.3	6.7	-1.2	0.0	0.0	18.2%
36	5.3	6.2	0.4	0.0	-0.1	17.4%
37	4.1	5.4	1.0	0.0	0.0	11.7%
38	3.5	3.7	0.7	0.0	0.0	11.4%
39	4.4	7.4	5.7	-1.3	-2.4	17.0%
40	5.1	14.6	1.7	-1.6	-1.6	18.8%
41	4.1	7.1	6.0	-1.3	-1.9	17.7%
42	7.0	8.4	7.2	0.0	-3.2	27.8%
43	7.0	16.6	2.2	0.0	-2.5	30.8%
44	6.1	10.3	3.8	0.0	-2.7	28.6%
45	6.3	6.3	2.2	0.0	-0.8	13.2%
46	6.0	5.9	3.1	0.0	-0.9	12.3%
47	14.9	5.8	2.1	-2.7	0.0	10.8%
48	15.6	9.4	2.9	-2.5	0.0	9.5%
49	2.3	13.1	1.3	-2.6	0.0	11.8%
50	2.9	19.0	1.3	-2.5	0.0	9.6%
51	5.6	9.6	1.6	-3.4	0.0	16.6%

Data set no.	ΔT_{suc} (K)	ΔT_{sup} (K)	ΔT_{sucln} (K)	ΔT_{disln} (K)	ΔT_{liqln} (K)	Heat loss (%)
52	4.1	10.9	4.2	-4.1	0.0	15.5%
53	3.6	10.3	4.2	-4.0	0.0	14.1%
54	3.6	6.7	3.3	-4.1	0.0	15.2%
55	3.7	10.6	4.3	-3.8	0.0	14.6%
56	3.3	9.0	4.0	-3.8	0.0	13.8%
57	3.8	12.1	3.3	-3.8	0.0	17.4%
58	4.5	14.3	3.4	-3.7	0.0	14.7%
59	7.2	11.3	-0.7	-2.3	0.0	9.0%
60	6.3	15.5	-0.7	-3.2	0.0	5.2%
61	6.3	18.3	-0.7	-3.5	0.0	6.7%
62	1.0	11.8	0.8	-5.8	-0.2	17.0%
63	4.0	6.0	2.7	-2.6	-0.9	103.3%
64	3.1	4.5	2.4	-1.8	-1.2	20.8%
65	1.3	4.5	1.2	-1.4	-0.7	19.4%
66	1.5	4.5	1.4	-1.8	-0.7	21.8%
67	2.2	4.3	2.4	-2.2	-1.2	18.6%
68	2.8	4.4	2.4	-2.2	-1.2	18.9%
69	3.4	4.2	2.8	-2.6	-1.3	17.4%
70	3.9	5.3	1.2	-5.3	-0.8	9.7%
71	5.8	5.8	2.8	-3.0	0.0	11.6%
72	4.9	5.0	2.4	-2.3	-0.9	12.8%
73	3.9	5.2	1.8	-2.2	-0.8	14.2%
74	3.5	6.1	3.3	-18.5	-0.3	13.4%
75	5.4	10.4	1.1	-9.5	-0.3	13.6%
76	3.7	4.6	2.2	-2.8	-1.0	16.3%
77	3.5	4.8	1.3	-2.3	-0.8	13.0%
78	6.7	4.3	1.5	-3.1	-0.3	18.0%
79	1.9	14.2	1.8	-3.9	-0.7	18.7%
80	8.2	6.0	2.7	-4.9	-4.0	13.6%
81	1.3	5.4	0.4	-2.4	0.6	114.2%
82	1.3	8.4	-0.1	-2.6	0.5	16.3%
83	5.5	6.9	2.1	-3.6	-0.8	103.6%
84	4.4	6.7	1.4	-3.1	-0.7	15.1%
85	5.7	6.8	2.4	-3.6	-1.0	15.1%
86	4.8	6.6	2.1	-3.6	-0.9	14.8%
87	5.4	6.9	2.1	-3.6	-0.8	15.0%
88	2.2	11.2	3.2	-1.3	-2.2	16.1%
89	3.8	4.1	3.4	-1.1	-2.3	13.5%
90	4.7	13.9	1.3	-1.4	-2.0	14.6%
91	4.4	13.6	1.6	-1.6	-2.0	15.1%
92	7.6	8.5	3.6	-0.1	-2.5	19.2%
93	6.3	8.5	1.8	-0.2	-1.9	20.7%

Data set no.	ΔT_{suc} (K)	ΔT_{sup} (K)	ΔT_{sucln} (K)	ΔT_{disln} (K)	ΔT_{liqln} (K)	Heat loss (%)
94	7.7	8.1	2.7	-0.2	-2.7	18.9%
95	7.0	8.5	2.6	-0.3	-2.3	19.7%
96	7.4	8.1	2.5	-0.2	-2.4	19.1%
97	7.2	7.7	1.4	-0.2	-2.3	19.2%
98	7.5	11.7	0.4	-0.2	-2.2	19.9%
99	7.3	13.7	-0.1	-0.3	-1.9	20.9%
100	7.0	15.6	-0.6	-0.4	-1.6	22.1%
101	8.0	11.6	0.4	-0.1	-2.6	19.7%
102	7.2	8.0	0.9	-0.2	-2.4	19.7%
103	7.7	8.4	3.7	-0.3	-2.6	19.6%
104	7.3	8.0	2.5	-0.3	-2.3	19.1%
105	7.7	8.5	3.6	-0.3	-2.6	18.8%
106	10.1	9.5	-0.5	-1.2	-1.0	10.9%
107	11.4	10.6	-0.3	-1.2	-0.9	12.8%
108	10.2	7.9	1.5	-1.2	-0.9	11.5%
109	10.4	8.8	-0.3	-0.8	-0.9	12.7%
110	9.1	9.2	-1.3	-1.2	-0.8	15.2%
111	9.5	10.8	-1.5	-1.2	-0.8	16.8%
112	8.8	10.2	-1.7	-1.2	-0.8	14.1%

VITA

IP SENG IU

Candidate for the Degree of
Doctor of Philosophy

Dissertation: DEVELOPMENT OF AIR-TO-AIR HEAT PUMP SIMULATION PROGRAM WITH ADVANCED HEAT EXCHANGER CIRCUITRY ALGORITHM

Major Field: Mechanical Engineering

Biographical:

Personal Data: Born in Macau, Macau SAR (a Portuguese colony back then), China on November 18, 1976. Raised in the friendly neighborhood of Fai Chi Kei up to the age of 13. The youngest son of Oi Lin Vong and the late Son Iu.

Education: Received Bachelor of Science degree in Electromechanical Engineering from the University of Macau, Macau SAR, China in June 1999. Received Master of Science degree in Mechanical Engineering from Oklahoma State University, Stillwater, OK, USA in December 2002. Completed the requirements for the Doctor of Philosophy degree with a major in Mechanical Engineering at Oklahoma State University, Stillwater, OK, USA in May 2007.

Experience: Worked at the Department of Forestry at Oklahoma State University as a graduate research assistant, Summer 2001. Worked at York International Unitary Product Group/A Johnson Controls Company as a summer intern, 2005 and 2006. Worked at the Department of Mechanical Engineering, Oklahoma State University as a graduate research assistant, 2000 to 2007.

Professional Memberships: American society of Heating, Refrigerating and Air-Conditioning Engineers (ASHRAE); The honor society of Phi Kappa Phi

Name: Ip Seng Iu Date of Degree: May 2007

Institution: Oklahoma State University Location: Stillwater, Oklahoma

Title of Study: DEVELOPMENT OF AIR-TO-AIR HEAT PUMP SIMULATION PROGRAM WITH ADVANCED HEAT EXCHANGER CIRCUITRY ALGORITHM

Pages in Study: 239 Candidate for the Degree of Doctor of Philosophy

Major Field: Mechanical Engineering

Scope and Method of Study: The purpose of this study was to develop a heat pump simulation program that is capable of simulating complex heat exchanger circuits. A segment-by-segment heat exchanger model has been developed in this research. When modeling the heat exchanger circuitries, local air side and refrigerant side boundary conditions for each heat exchanger segment are necessary information to account for the heat transfer and pressure drop changes. Refrigerant flow distribution in the coil circuits are determined by the flow resistance in each circuit. A novel circuiting algorithm that relaxes the constraints of previous models has been proposed to determine the refrigerant flow distribution. As reported in the literature, air side heat transfer coefficients vary row-by-row in multi-row heat exchangers. An experimental procedure that covers a range of fin densities has been conducted to develop row-by-row heat transfer correlations for louvered fin coils. The heat pump simulation program, with the proposed circuitry algorithm and developed row-by-row correlations integrated, has been validated at both component and system level simulations. The validation is based on a range of experimental data that cover different boundary conditions and system configurations.

Findings and Conclusions: The results of the row-by-row heat transfer experiment showed that there is thermal entrance length effect in the row-by-row heat transfer data. Heat transfer dominates at the front rows because the data are in the developing region. The louvered fin heat transfer data also confirm that there is a transition between “duct flow” and “boundary layer flow”. The row effect is particularly significant for duct flow and developing region. However, it is always ignored in overall heat transfer correlations. Simulation results with overall and row-by-row correlations showed that the simulated capacity difference can be as high as 6.5%. The difference can be higher if there is no boundary layer flow in the heat exchangers, such as flat fins. Validation results of the simulation program are satisfactory. A majority of the simulated heat exchanger capacities, sensible heat ratio, compressor power consumptions, and refrigerant mass flow rates are within ±5% difference. Saturation temperatures and coefficient of performance are within ±2K and ±0.5, respectively.

ADVISER'S APPROVAL: Daniel Fisher